Searching for electrolytes and electrodes for CO2 reduction below 300 °C

Vico, Federica

Publication date:
2015

Document Version
Publisher's PDF, also known as Version of record

Searching for electrolytes and electrodes for CO_2 reduction below 300 °C

Federica Vico

Department of Energy Conversion and Storage
Ph.D. Thesis, May 2015

DTU Energy
Department of Energy Conversion and Storage

Abstract

Electrochemical CO_2 reduction research is driven by the desire to reduce reliance on fossil fuels and lower greenhouse gas emissions. The conversion of CO_2 into fuels and chemicals using energy derived from a renewable source, such as wind or solar, could replace the use of fossil fuels.

This thesis uses the knowledge derived from earlier investigations on electrolysis techniques as the foundation for an exploratory work to find acceptable materials and fabricate an electrochemical cell able to produce hydrocarbons and alcohols directly from reduction of CO_2 and steam. The operating conditions should be between 200 – 300 ^{0}C and at elevated pressure in the range of 20 – 30 bar. The temperature range is chosen according to the thermal stability of the hydrocarbons produced by conversion of CO_2. The electrochemical performance of the fabricated cells was evaluated using electrochemical impedance spectroscopy and chronoamperometry, while the gas analysis was carried out via gas chromatography.

The initial part of the study focused on electrolyte materials in order to identify a promising candidate to be implemented in the full cells. Some proton conducting materials, such as Y-doped $BaZrO_3$-$BaCeO_3$ solid solutions and K-doped $BaZr_{1-x}Y_xO_{3-\delta}$ were evaluated. $BaCe_{0.5}Zr_{0.4}Y_{0.1}O_{3-\delta}$ would have been the best electrolyte candidate because of its low resistivity in high pH_2O ($2 \cdot 10^{-3}$ S/cm) even at temperatures as low as 240 °C. However, the instability in the acidic CO_2 gas atmosphere hinders practical application for carbon dioxide reduction at high pressure. K-doped $BaZr_{1-x}Y_xO_{3-\delta}$ was successfully synthesized by hydrothermal technique, but the conductivity recorded in high pH_2O and at 240 °C was too low ($3 \cdot 10^{-5}$ S/cm) to be considered as a suitable electrolyte.

A literature survey showed that most CO_2 reduction studies were performed in aqueous potassium bicarbonate ($KHCO_3$) and with a copper metal catalyst. Therefore, it was decided to investigate the electrocatalytic activity of copper foam in aqueous media at ambient conditions for electrochemical reduction of CO_2. The measurements were conducted at Stanford University – Chemical Engineer Department, where it was possible to utilize an experimental setup which ensures high sensitivity for minor products from the CO_2 reduction reaction. Seven products were identified with the copper foam electrode tested to -0.98 V vs. RHE. H_2, formate and CO were the main products observed and in particular the faradaic efficiency of H_2 was ca. 90 %. The highest current density that could be sustained with this setup was about -20 mA/cm^2. Therefore, it was decided to develop a new cell that could operate at higher current densities, pressures and temperatures.

A foam based CO_2 conversion cell with gas diffusion electrodes and a ceramic porous structure in which the liquid electrolyte is immobilized by capillary forces was developed and tested up to 20 bar and to a maximum temperature of 50 °C. Potassium carbonate was selected as aqueous electrolyte and various concentrations of this electrolyte were immobilized in a ceramic porous matrix at both ambient and elevated temperatures and pressures. Copper and silver metal foams were tested as cathode. Nickel metal foam was chosen as anode. When copper was used as electrocatalyst, a high faradaic efficiency for the evolution of H_2, i.e. between 92 to 99 % was registered. The other products detected were CO and during one test also methane was identified. The performance of Ag cathode metal foam confirmed its higher selectivity for CO_2 reduction to

CO. The formation of passive oxide layers and the subsequent degradation of nickel foam electrodes affected the electrochemical performance and the stability of the cells negatively.

Resumé på dansk

Forskning i elektrokemisk reduktion af CO_2 er motiveret af ønsket om at reducere afhængigheden af fossile brændsler og mindske udledningen af drivhusgasser. Med omdannelsen af CO_2 og vand til brændsler og nyttige kemikalier ved hjælp af fornybar energi, f.eks. vind og sol, kan fossile brændsler erstattes helt med CO_2 neutrale syntetiske brændsler.
Denne afhandling anvender viden, der stammer fra tidligere forskning og udvikling af elektrolyseteknikker, som grundlag for et eksplorativt arbejde med henblik på at finde brugbare materialer og at fremstille en elektrokemisk celle, der i stand til at producere kulbrinter og alkoholer direkte fra reduktion af CO_2 og vanddamp under driftsbetingelser mellem 200 - 300 ^{0}C og ved forhøjet tryk på 20 – 30 atm. Temperaturområdet er valgt i overensstemmelse med den termiske stabilitet af kulbrinter fremstillet ved omdannelse af CO_2. Reaktionshastigheden for dannelse af produkterne stiger med øget tryk. Den elektrokemiske ydeevne af de fremstillede celler blev undersøgt ved anvendelse af elektrokemisk impedans spektroskopi og kronoamperometri, mens gasanalysen blev udført ved hjælp af gaskromatografi.
De indledende undersøgelser var fokuseret på elektrolytmaterialer med det formål at identificere den bedste kandidat, der ville kunne bruges i hele celler. Nogle protonledende materialer, såsom Y-doterede $BaZrO_3$-$BaCeO_3$ faststof opløsninger og K-doteret $BaZr_{1-x}Y_xO_{3-\delta}$ blev undersøgt. $BaCe_{0.5}Zr_{0.4}Y_{0.1}O_{3-\delta}$ ville have været den bedste elektrolytkandidat på grund af dens lave modstand i høj pH_2O ($2 \cdot 10^{-3}$ S / cm), selv ved lave temperaturer som 240 °C hvis ikke dens manglende stabilitet i sur CO_2-gas atmosfære forhindrede dens praktiske anvendelse til kuldioxid reduktion ved højt tryk. K-doteret $BaZr_{1-x}Y_xO_{3-\delta}$ blev succesfuldt syntetiseret ved hjælp af hydrotermal syntese, men ledningsevnen der blev målt ved høj vanddamptryk og ved 240 °C var for lav ($3 \cdot 10^{-5}$ S/cm) til at materialet kunne komme i betragtning som en egnet elektrolyt.
En litteraturundersøgelse viste, at de fleste undersøgelser CO_2-reduktion blev udført i vandigt kaliumbikarbonat ($KHCO_3$) og med kobbermetal katalysator. Det blev derfor besluttet at undersøge den elektrokatalytiske aktivitet af kobberskum i vandig opløsning ved stuetemperatur og atmosfæretryk for elektrokemisk reduktion af CO_2. Målingerne blev udført på Stanford University - Chemical Engineering Department, hvor det var muligt at anvende en forsøgsopstilling, der sikrede høj følsomhed for produkter med lav udbytte fra CO_2-reduktionsreaktionen. Syv produkter blev identificeret ved forsøg med kobberskumelektroden, der blev polariseret til -0,98 V vs. RHE. H_2, $HCOO^-$ og CO blev observeret som hovedprodukter, og især H_2 udviste en høj Faradayisk effektivitet på ca. 90 %. Den højeste strømtæthed, der kunne opnås med denne opstilling, var ca. -20 mA/cm^2. Derfor blev det besluttet at udvikle en ny celle, som kunne operere ved højere strømtætheder, tryk og temperaturer.
Alkaliske elektrolyseceller, der er baseret på metalskum, og som kan omdanne CO_2 og vand til brændsler, blev fremstillet. De var konstrueret af gasdiffusionselektroder og en keramisk porøs struktur, i hvilken den flydende elektrolyt blev immobiliseret ved hjælp af kapillære kræfter. Cellerne blev testet op til 20 bar og en maksimum temperatur på 50 °C. En vandig opløsning af

kaliumkarbonat blev valgt som elektrolyt. Kobber og sølv metalskum blev testet som katode, da de er velkendte elektrokatalysatorer for CO_2-reduktion. Nikkel metalskum blev valgt som anode. Når kobberskum blev anvendt som elektrokatalysator, blev en høj Faradayisk effektivitet, 92 til 99 %, for udviklingen af H_2 registreret. Det andet påviste produkt var CO og under en enkelt test blev metan også identificeret. Ydeevnen af Ag metalskumkatoden bekræftede den højere selektivitet af CO ved reduktion af CO_2 på Ag. Dannelsen af et passivt oxidlag på nikkel og den efterfølgende nedbrydning af nikkelskumelektroden påvirkede den elektrokemiske ydeevne og stabilitet af cellerne negativt.

Acknowledgements

First of all I would like to thank my supervisor, Mogens B. Mogensen, for his help, his ideas and patience in teaching, and his enormous and contagious curiosity. I am very thankful for his support and his wise suggestions during these three years.
It was a pleasure to listen to and discuss together with him, not only about scientific topics.

I am especially grateful to my co-supervisor Christodoulos Chatzichristodoulou for his work on the high pressure and temperature measurement setup, for his collaboration, for his brilliant ideas and his comments on my manuscripts.
Also, my second co-supervisor and section leader, Peter Holtappels should be acknowledged for his contribution during my "monthly meetings".

Frank Allebrod, Jonathan Hallinder, Alberto Lapina and Davide Ippolito were precious colleagues and friends during these three years. I am very thankful for their time and their helpful advices.
They managed to cheer me up and support me during the difficult moments of this journey.
We had really good time together.
I would like to thank also my office mates and colleagues Ragnar Kiebach and Jimmy Nielsen. It has been a pleasure to share the office with you.

Ebtisam Abdellahi and Jens Borchsenius should be named and granted in representation of all the technicians and laboratorians, because without their help this work would not have been possible.

I would like to thank Prof. Thomas Jaramillo and Prof. Anders Nilsson for hosting me in the SUNCAT group at SLAC, Stanford. In particular, I am grateful to Kendra Kuhl and Toru Hatsukade for introducing me to a new experimental setup, for the interesting and useful discussion on the CO_2 reduction process.

I would like to thank Simone, Andreas, Iva, Arianna, Kristian, Carlo, Sune, Lisa, Philip and Pia for their precious friendship during these last years.

I am very grateful to my family, because since I was young they have given me the possibility and the freedom to travel and to experience different cultures. I feel very lucky for it.

This work was carried out as a part of the "Catalysis for Sustainable Energy" (CASE), initiative funded by the Danish Ministry of Science, Technology and Innovation.

TABLE OF CONTENTS

Chapter 7

CO_2 reduction on electrochemical cells using gas diffusion electrodes at elevated pressure…85

Part IV

Chapter 8

Overall Discussion and Conclusions……126

List of Figures

Fig. 3.7. SEM micrograph of the fractured cross section of the BCZY541 pellet after exposure to high steam partial pressure during conductivity testing (sequence 1).

Fig. 3.8. SEM micrograph of the fractured cross section of: a) just sintered BCZY262 cell and b) BCZY262 cell tested under the two sequences of the high partial pressure test. Note: the magnifications are different as indicated by the scale bars. These pellets had a density of 93%.

Fig. 3.9. SEM micrograph of the fractured cross section of the BCZY262 cell tested under high steam partial pressure. This pellet was only 85 % dense.

Fig. 3.10. Nyquist plot recorded for BCZY541 at 240 °C and Ptot = 50 bar, with a gas mixture of pH_2 = 2.5 bar, pH_2O = 10 bar and pN_2 = 37.5 bar.

Fig. 3.11. **a)** Nyquist plots at different acquisition times and **b)** conductivity relaxation of the BCZY541 cell at 240 °C and Ptot = 50 bar, following the gas composition change from pH_2O = 10 bar (□), to pH_2O = 25 bar (■, ★ , ▲ , ●) in 5 vol.% H_2 in N_2.

Fig. 3.12. Conductivity dependence on increasing pH_2O at 240 ^{0}C at 50 bar in a wet mixture of 5 vol.% H_2 in N_2 and during the ramp down phase for BCZY541 cell. Closed and open symbols are used to distinguish between equilibrated and non-equilibrated values, respectively. The total conductivity at 10 mbar for the three compounds is compared with extrapolated and measured literature data

Fig. 3.13. Conductivity dependence on pCO_2 at 240 ^{0}C in the gas mixture: 50 vol.% CO_2, 5 vol.% H_2 and 45 vol.% N_2. The total pressure was between 1 bar and 50 bar. The pH_2O values given on top are the calculated equilibrium values of the gas mixture at 240 ^{0}C.

Fig.4.1. XRD of (a) as synthesized powders of BKZY91 prepared by hydrothermal synthesis, (b) powders of BKZY91 sintered at 1550 °C with added 0.1 wt% of Si powder as standard reference and (c) powders of BZY91 sintered by solid state reactive sintering at 1550 °C with added 0.1 wt% of Si powder as standard reference. The Si peaks position is indicated with dotted lines in pattern b) and c)

Fig.4.2. XRDs for the pellets of (a) BZY91, (b) BKZY91, (c) BCZY541 after the conductivity test in ambient pressure and various temperatures. Platinum peaks are due to traces of Pt paint (contained in the electrodes) left on the material after testing.

Fig. 4.3. XRDs for the pellets of (a) BZY91 and (b) BKZY91 after the conductivity test at 240 °C in high pH_2O and in high pCO_2.

Fig. 4.4. SEM images of as synthesized $Ba_{1-x}K_xZr_{0.9}Y_{0.1}O_{3-\delta}$ powders obtained a hydrothermal treatment of 72 h at 200 °C.

List of Tables

List of Abbreviations

AC	Alternating Current
AEC	Alkaline Electrolysis Cell
BET	Brunauer–Emmett–Teller
EIS	Electrochemical Impedance Spectroscopy
CA	ChronoAmperometry
CV	Cyclic Voltammetry
DFT	Density Functional Theory
FE	Faradaic Efficiency
FobAEC	Foam based Alkaline Electrolysis Cell
GC	Gas Chromatograph
GLS	Gas Liquid Separator
HF	High Frequency
Hz	Hertz
IF	Intermediate Frequency
LF	Low Frequency
MHz	Mega Hertz
NMR	Nuclear Magnetic Resonance
OCV	Open Circuit Voltage
PEM	Proton Exchange Membrane
PLD	Pulse Laser Deposition
PTFE	PolyTetraFluorEten
Q	Constant phase element
R_s	Serial resistance
R_p	Polarization resistance
SEM	Scanning Electron Microscope
SOEC	Solid Oxide Electrolytic Cell
SPCEC	Solid Proton Conducting Electrolysis Cell
TCD	Thermal Conductivity Detector
TEM	Tunneling Electron Microscope
XPS	X-ray Photoelectron Spectroscopy
Y	Admittance
YSZ	Yttrium Stabilized Zirconia
Z	Impedance
ε	Energy efficiency

Part I

INTRODUCTION

Chapter 1
Introduction and Motivation

1.1 The energy challenge

The interest in electrocatalytic conversion of CO_2 into fuels and chemicals is connected to concerns about climate changes. By using renewable or nuclear energy for the conversion process, it is possible to create hydrocarbon products in a way that does not contribute to anthropogenic CO_2 emissions. It is not the scope of this work to go into detail on the discussion on climate changes. However, it is pertinent to include some literature on the topic in order to elucidate the scale of the challenges. According to Petit et al.[1], there is a correlation between the atmospheric CO_2, CH_4 and temperature levels. Data on these levels until 420 000 years before present (bp) were obtained by analysing an ice core that was drilled near the Vostok station in Antarctica. In this time period, it was found that the atmospheric CO_2 concentration varied between 210 and 300 ppm. In comparison, the atmospheric CO_2 concentration was measured to be 403.3 ppm in April 2015.[2] The results obtained from the Vostok ice core is shown in Fig. 1.1. The labelling on the bottom horizontal axis denotes the number of years before present.

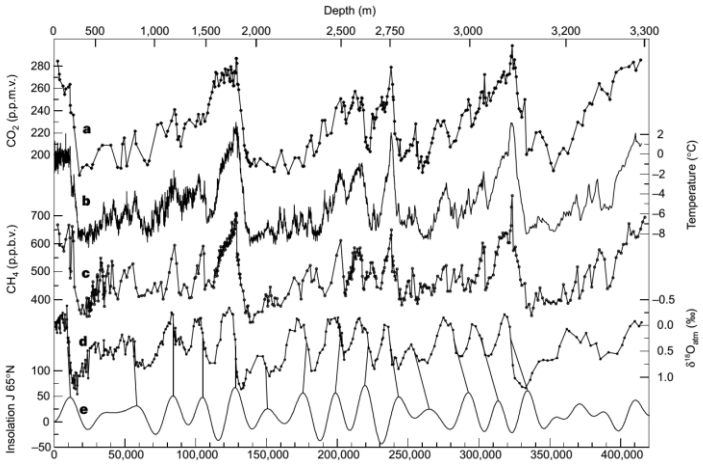

Fig. 1.1. Data obtained from the Vostok ice core on the CO_2, CH_4 and temperature levels in the atmosphere in the past 420 000 years. Adapted from [Petit et al.[1]]

The increasing atmospheric CO_2 concentration has been linked to the consumption of fossil fuels. Emissions of CO_2 can be mitigated by displacing fossil fuels with renewable energy. However, according to the International Energy Outlook report from the U.S. Department of Energy[3] it is expected that the demand for energy will increase greatly from present until 2050. In their report they predict an increase in the consumption of renewable, nuclear and fossil fuels over the entire time period as shown in Fig.1.2. With such a development, a stronger contribution on the atmospheric CO_2 concentration from consumption of fossil fuels can be expected in the coming decades.

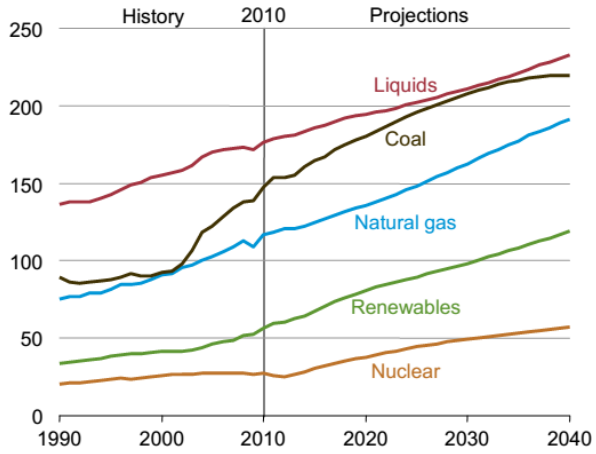

Fig. 1.2. Trend of the world energy consumption by fuel type, from 1990 – 2040. Y-scale is in quadrillion Btu. (US Department of energy) [2].

The worldwide mix of primary fuels used to generate electricity has deeply changed over the past four decades[2]. Coal represents still the fuel most widely utilized in electricity generation, although generation from nuclear power increased rapidly from the 1970s through the 1980s, and natural gas-fired generation grew rapidly in the 1980s, 1990s, and 2000s.

Since the beginning of the early 2000s, high fossil fuel prices together with concerns about the environmental consequences of greenhouse gas emissions lead to a growing interest in developing alternatives to fossil fuels for electricity generation, such as nuclear power and renewable energy sources. According to the International Energy outlook the renewable energy sources are the fastest-growing sources of electricity generation (Fig. 1.3). In particular, nonhydropower renewable resources are the fastest-growing sources of new generation in the outlook, in both OECD and non-OECD regions. Nonhydropower renewables, which accounted for 4 percent of the generation market in 2010, increase their share of the market to 9 percent in 2040, with much of the growth coming from wind generation.

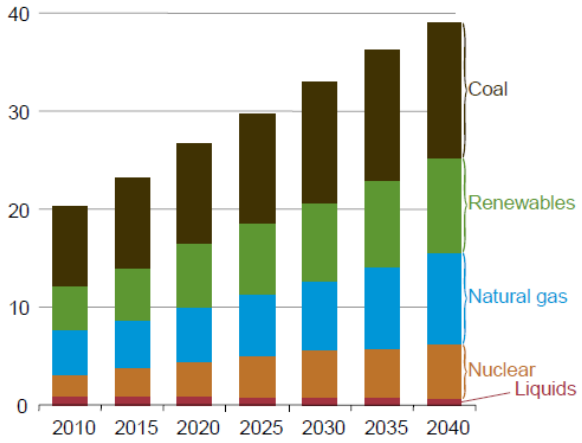

Fig. 1.3. World net electricity generation by fuel, 2010-2040. Y-scale unit is trillion kWh. (US Department of energy) [2].

In particular with the EU 2020 goals[4], the European Union is aiming to increase up to 20% the share of renewable energy in the total energy mix by 2020. Figures 1.4 to 1.7 show the market share of renewable energy in Denmark and the European Union in year 2010 and their respective goals for year 2020. All the Figures were originally published in the "Renewable Energy Projections" in the National Renewable Energy Action Plans of the European Member States in 2011[4]. The planned increase in Denmark from 21.9 % to 30 % is expected to be achieved largely by increased production of bio- and wind energy. The empty part of the pie charts shown in Fig. 1.4 and Fig 1.5 indicates the missing renewable energy production in order to reach the year 2020 goals which are shown in Fig 1.6 and Fig 1.7.

Denmark

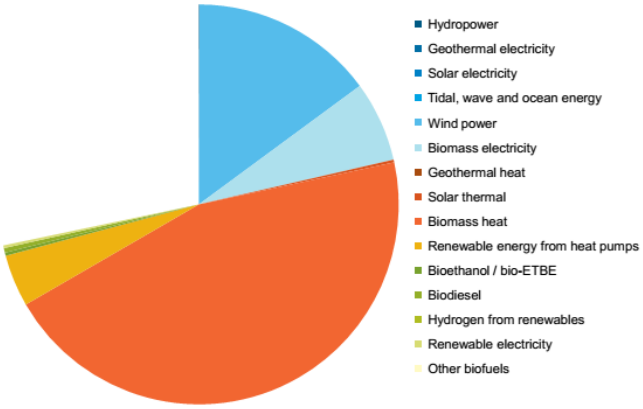

Fig. 1.4. Renewable energy share in Denmark in 2010 was 21.9%.

European Union

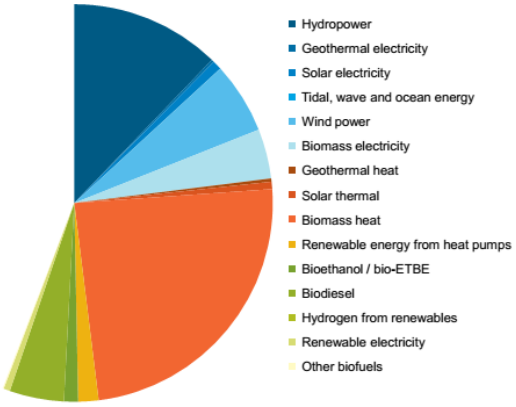

Fig.1.5. Renewable energy share in the European Union in 2010 was 11.6%.

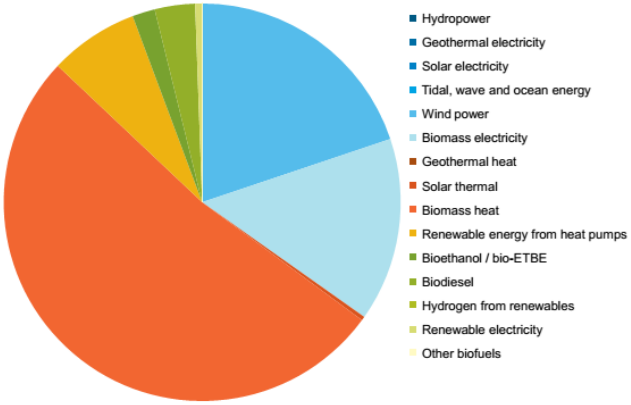

Fig. 1.6. Renewable energy target for Denmark in 2020 is 30%.

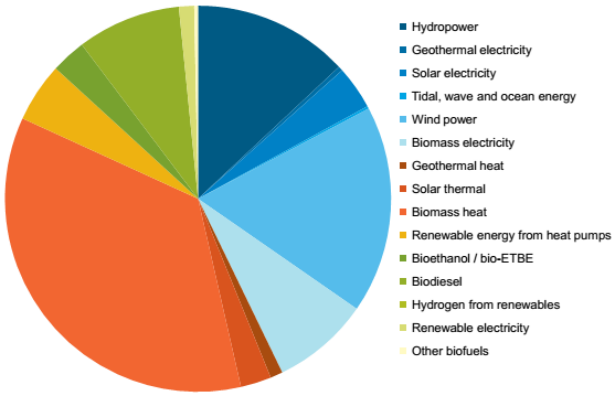

Fig. 1.7. Renewable energy target for the European Union in 2020 is 20%.

The availability of solar photovoltaic and on- and offshore wind power depends on seasonal and hourly weather conditions which does not follow consumer demand. Significant amounts of excess renewable energy will most likely start to emerge with continued expansion of the production infrastructure for wind and solar energy. The excess periods will occur when the output from photovoltaic cells and wind energy far exceeds consumer demand. In other periods, the output of solar and wind energy will be only a fraction of the maximum production capacity and non-

renewable or stored energy from periods of excess production will be required. This behaviour has to some degree been observed already. For example, in Germany in 2013 the average rate of electricity consumption was 64 GW and the largest over- and undersupply was 15 and 9 GW, respectively[5]. Electric energy from periods of excess production can be stored in systems that can be charged and hold energy that later can be discharged as electrical energy. Examples of this are pumped hydro, flywheels, compressed air and batteries. An alternative is to convert excess electric energy into energy carriers such as heat, hydrogen or hydrocarbons and alcohols that can be discharged outside the electrical power system and used for other applications.

With electrocatalytic processes, one possibility is to convert the hydrocarbon combustion products (H_2O and CO_2) back into hydrocarbon fuels. It is possible to gather CO_2 directly from the atmosphere or to collect it from large single point sources of emission. By using renewable electrical energy for the conversion process, it is possible to use hydrocarbons as energy carriers in an energy system that does not contribute to anthropogenic CO_2 emissions. A possible scheme over how this can be done is shown in Fig. 1.8.

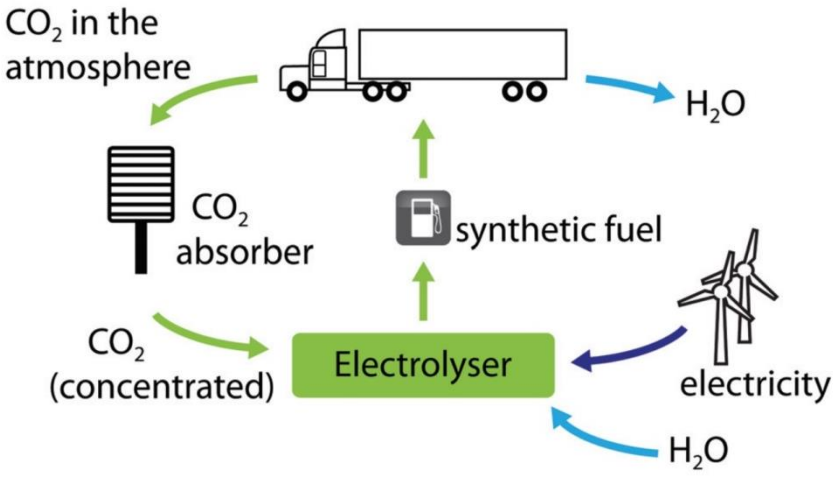

Fig. 1.8. A possible scheme for a hydrocarbon fuel cycle that does not contribute to anthropogenic CO_2 emissions. Originally published by Mogensen et al.[6]

The ambitions regarding the use of electro catalytic processes for production of hydrocarbon fuels and chemicals does not need to be limited to only using excess electricity for the production process. According to Nocera et al.[7], the global average rate of energy consumption in 2002 was 13.5 TW. Conservative estimates project the global rate of energy consumption to be 28-35 TW in 2050. In an extreme example, if a population of 9 billion people in 2050 consumes the same amount of energy per person as today's average in the U.S., then the power demand will be over 100 TW. The estimated practically available amounts of power from biomass, nuclear, wind and hydroelectric are about 9, 8, 2 and 1.4 TW, respectively. The continuous power influx from the sun to the earth is about $1.2 \cdot 10^5$ TW. With photovoltaic cells with an efficiency of 10%, it would be necessary to use less than 0.2% of the surface of the earth for solar energy production in order to obtain an amount of electrical energy equal to today's total energy consumption. From this, it appears that the sun is also a readily available renewable source of energy that is large enough to

satisfy expected future energy needs. Because of this, the development of processes for conversion of electric energy into other energy carriers and also chemicals could become essential in order to allow the creation of a sustainable energy future that permits a high standard of living for a wider part of the global population.

1.2 Production of hydrogen and synthetic fuels

1.2.1 Heterogeneous catalysis

Heterogeneous catalysis is already commercially used to convert coal and natural gas into liquid hydrocarbons. These processes are abbreviated as CTL, GTL or BTL when the feedstock is coal, natural gas or biomass, respectively. Since the only major difference between these processes is the feedstock, they are commonly referred to as X-to-liquids (XTL) processes in order to include all processes in one term. In XTL processes, a feedstock is converted into synthesis gas (CO_2 + CO + H_2) which later can be converted into methanol, olefins, dimethyl ether (DME) or paraffin. Ammonia can also be made from synthesis gas if a water gas shift reactor is used to convert the CO into H_2 which can be mixed with N_2 for the Haber-Bosch process. All of these processes consist of two or three steps that are the production of synthesis gas, conversion of synthesis gas into intermediate or final products and if necessary final upgrading to products. For the low temperature Fischer-Tropsch process the intermediate product is a hydrocarbon wax that is solid at ambient conditions and that needs to be upgraded to final products through hydrocracking. In the methanol synthesis process the intermediate product is a mixture of water and methanol that needs to be separated in a distillation process. Table 1 shows the major products in heterogeneous catalysis processes with synthesis gas.

Table 1.1. Heterogeneous catalysis reactions for production of hydrocarbons or ammonia from synthesis gas or a mixture of N_2 and H_2.

Main reactions	
Paraffins	$n\mathrm{CO} + (2n+1)\mathrm{H_2} \rightarrow \mathrm{C_nH_{2n+2}} + n\mathrm{H_2O}$
Olefins	$n\mathrm{CO} + 2n\mathrm{H_2} \rightarrow \mathrm{C_nH_{2n}} + n\mathrm{H_2O}$
Water-gas-shift (WGS)	$\mathrm{CO + H_2O} \rightarrow \mathrm{CO_2 + H_2}$
Oxygenates	$n\mathrm{CO} + 2n\mathrm{H_2} \rightarrow \mathrm{C_nH_{2n+2}O} + (n\text{-}1)\mathrm{H_2O}$
DME	$2\mathrm{CH_3OH} \rightarrow \mathrm{C_2H_6O + H_2O}$
Methanol	$\mathrm{CO_2 + 3H_2} \rightarrow \mathrm{CH_3OH + H_2O}$
Haber-Bosch	$\mathrm{N_2 + 3H_2} \rightarrow \mathrm{2NH_3}$

One step processes for conversion of methane directly into liquids does exist. One example of this is a process that uses a Mo/H-ZSM5 catalyst for conversion of CH_4 directly into a mixture consisting mainly of solid carbon, naphthalene and benzene[8]. Since the two latter products are toxic and have a limited marked these products also need further processing in order to make mass market products.
It is also possible to make synthetic natural gas (SNG) from synthesis gas. This reaction was discovered in 1913 by Sabatier and Senderens who used a nickel catalyst to carry out the reaction. With the Sabatier process it is possible to make methane from other hydrocarbon feedstocks such as biomass, coal and oil via synthesis gas.

$$CO + 3H_2 \rightarrow CH_4 + H_2O$$

1.2.2 Electrolysis cells

Electrolysis is an efficient technology for converting electrical and thermal energy into chemical energy stored in fuels, by passing an electric current through two electrodes separated by an electrolyte. Various kinds of electrolyser cells have been developed and are currently under improvement. The different cells are often defined and classified by their electrolyte materials. The electrolyte can be liquid like an alkaline solution as it is for alkaline electrolyser cells (AEC), or an acid solution as it is for phosphoric acid and sulphuric acid electrolysis cells. On the other hand, the electrolyte can be solid like a polymer as it is for polymer electrolyte membrane cells (PEMEC), or a solid oxide as it is for solid oxide electrolysis cells (SOEC) or a proton conductor as for solid proton conducting electrolysis cells (SPC-EC)[9]. The overall electrolysis reaction of H_2O and/or CO_2 is a sum of two half-cell reactions, which take place at each of the two electrodes. The reduction of reactants or intermediates occurs at the cathode electrode, while the oxidation occurs at the anode electrode. The operating conditions of the various electrolyser cells are related to the properties and characteristics of the electrolytes used.

1.2.2.1 Low-temperature electrolysis

Alkaline water electrolysis cells are the most commonly used electrolysers and are already commercially available. The electrode reactions are:

Cathode: $4\ H_2O\ (l) + 4\ e^- \rightarrow\ 2\ H_2\ (g) + 4\ OH^-\ (aq)$

Anode: $4\ OH^-\ (aq) \rightarrow\ O_2\ (g) + 2\ H_2O\ (l) + 4\ e^-$

The conventional electrolyte is a 30 wt% KOH solution and the operating temperature is ~80 ^{0}C. A proton conducting membrane is used to separate the two electrodes to avoid crossover of evolved gases. Nickel electrodes are applied in most commercial alkaline electrolyzers[10]. In order to electrochemically split H_2O it is necessary to apply a voltage that exceeds a minimum that can be determined by thermodynamics. At 25 °C and 1 atm pressure of the reactants, this is 1.23 V for water splitting. Typically, it is necessary to apply a greater potential in order to electrochemically split water at a feasible rate. The difference between the thermodynamically necessary potential to drive the reaction and the applied voltage is typically referred to as the overpotential. Several factors contribute to the necessary overpotential, but the typically largest contributing factor is the

reaction barriers related to the catalytic properties of the anode and the cathode. Alkaline electrolysers are usually operated at rather high cell voltages (1.7 – 1.9 V) to obtain an acceptable hydrogen production rate.

Co-electrolysis of H_2O and CO_2 related to alkaline electrolysis has been performed and is still under development using aqueous carbonate or bicarbonate electrolyte[11]. The electrochemical reduction of H_2O and CO_2 can produce synthesis gas, alcohols and hydrocarbons such as formate, methanol, methane and ethylene, depending on the cathode materials and cell parameters. The necessary thermodynamic potential for electrochemical conversion of CO_2 into hydrocarbons or alcohols is similar to that of hydrogen evolution. Some of the reactions that can occur on the cathode during CO_2 reduction along with their equilibrium potential are shown in Table 1.2. The electrochemical conversion of CO_2 into hydrocarbons involves several electron transfers and intermediates. It is also necessary to apply a large overpotential with currently available electrocatalysts.

Table 1.2. List of CO_2 reduction reactions with their corresponding equilibrium potentials[11].

CO_2 reduction half reactions			**E^0 vs. RHE**
$CO_2 + H^+ + 2e^-$	↔	$CO + H_2O$	-0.11 V
$CO_2 + 8H^+ + 8e^-$	↔	$CH_4 + 2H_2O$	+0.16 V
$2CO_2 + 12H^+ + 12e^-$	↔	$C_2H_4 + 4H_2O$	+0.07 V
$2CO_2 + 12H^+ + 12e^-$	↔	$C_2H_5OH + 3H_2O$	+0.08 V
$3CO_2 + 18H^+ + 18e^-$	↔	$C_3H_7OH + 5H_2O$	+0.09 V

Most of the studies performed at ambient conditions were focused on improving the product selectivity at an applied potential rather than maximizing energy efficiency or current density for lowering costs. Among all the catalysts tested for co-electrolysis of H_2O and CO_2, only copper electrode was identified to selectively produce methane, ethylene and other hydrocarbons over just hydrogen and carbon monoxide. The cathode reaction for methane is:

$$CO_2(aq) + 8H^+ + 8e^- \rightarrow CH_4\,(g) + 2H_2O\,(l)$$

while the electrochemical reaction at the anode is water oxidation:

$$H_2O\,(l) \rightarrow O_2\,(g) + 4H^+ + 4e^-$$

Instead, transition metals such as Au and Ag were found to selectively produce carbon monoxide over hydrocarbons and alcohols. CO_2 reduction is a difficult process since it involves many reactions steps and the overpotentials needed to selectively produce hydrocarbons or synthesis gas are at present too high for a commercially viable electrolyzer.

With a type of cell as shown in Fig. 1.9, a current density of 100 mA/cm^2 was achieved when applying a cell voltage of 3 V to produce a gaseous mixture of methane and hydrogen with traces of ethylene and carbon monoxide[12].

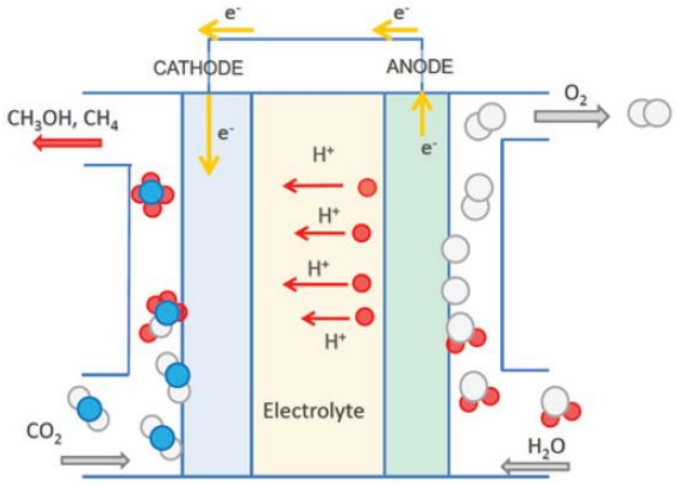

Fig. 1.9. Schematic representation of an electrolyser for bulk CO_2 reduction.

Advanced alkaline cells operating at elevated pressure and temperature might be modified and implemented to work more efficiently for H_2O electrolysis combined with catalytic CO_2 hydrogenation to hydrocarbons by using gas diffusion electrodes which enable higher current density. Promising results at high pressure have been obtained recently by E. J. Dufek[13] on silver catalyst. Electrochemical reduction of CO_2 using different transition metal catalysts and aqueous electrolytes is further described in Chapter 2.

Proton exchange membrane (PEM) electrolysis cells are generally operated at a similar temperature range of AEC (~ 60 to 80 ^{0}C) and are as well commercially available. A polymer membrane called Nafion is used as electrolyte. PEM cell electrodes are constituted by noble metals such as platinum or iridium and ruthenium oxides as electrocatalysts, which affect significantly the capital costs[14].
At the cathode, hydrogen evolution reaction takes place: $2H^+ + 2e^- \rightarrow H_2$. While at the anode water oxidation: $2H_2O\ (l) \rightarrow O_2\ (g) + 4H^+ + 4e^-$.

Only a few studies on PEM electrolysis cells for reduction of humidified CO_2 at the cathode and oxidation of pure water at the anode have been performed. Unfortunately, low current efficiencies for CO_2 reduction products were observed. Cook et al. reported ca. 2.6 % faradaic efficiency for methane on copper[15] (which is the best metal catalyst for CO_2 reduction to hydrocarbons), and < 1% on other metals such as nickel, silver and gold[16]. In these studies, hydrogen was reported to be the main product. Similar results were reported by C. Delacourt et al.[17] who used silver as catalyst and a cation-exchange membrane as electrolyte. It is reasonable to conclude that the acidity of the membrane could shift the cathode selectivity towards hydrogen evolution.

1.2.2.2 High-temperature electrolysis

Performing electrolysis at high temperature has both a thermodynamic advantage and an advantage in reaction rates. By increasing the temperature, a bigger contribution of heat and therefore a smaller contribution of electricity is required for the dissociation of the reactants. The high temperature leads to faster reaction kinetics, which allows to decrease the utilization of expensive catalyst materials. These aspects permit higher operational efficiency and higher current density.

Solid oxide electrolysis cells (SOECs) can operate for both steam electrolysis and co-electrolysis of steam and carbon dioxide. The electrode reactions are:

Cathode: $H_2O\ (g) + 2e^- \rightarrow\ H_2\ (g) + O^{2-}$

Or $\quad CO_2(g) + 2e^- \rightarrow\ CO\ (g) +\ O^{2-}$

Anode: $O^{2-} \rightarrow \frac{1}{2} O_2\ (g) + 2e^-$

The only products that can be formed during the co-electrolysis process are CO and H_2 (syngas), which can be used as reactants for hydrocarbons and alcohols synthesis via heterogeneous catalysis. The operating temperature of SOECs is between 750 – 900 ^{0}C and the cells are usually constituted by YSZ (yttria stabilized zirconia) electrolyte, Nickel-YSZ cathode and a LSM-YSZ anode, where LSM is lanthanum strontium manganite ($La_{1-x}Sr_xMn_yO_{3-\delta}$)[18,19].

Solid proton conducting electrolysis cells (SPCECs) have been mainly studied for electrolysis of water and recently it has been investigated the possibility of combining the electrolysis of water with electrochemical conversion of CO_2[20,21]. The electrolytes are proton conducting oxides, mainly based on $ABO_{3-\delta}$ type perovskites such as $SrCeO_3$, $BaZrO_3$ and $BaCeO_3$. The operating temperature is usually above 400 ^{0}C. The conductivity of cerates is higher than zirconates, however, zirconates exhibit a better chemical stability in CO_2, water and H_2 containing atmospheres. The conduction mechanism and other properties of this group of materials are further described in the Introduction part of Chapter 3 and 4. The reactions for water electrolysis taking place at the electrodes are oxidation of steam at the anode and hydrogen evolution at the cathode. Evolution of pure hydrogen at the cathode represents an advantage compared to SOECs, in which the hydrogen needs to be separated from the steam used as reactant. When both CO_2 and water is involved in the electrolysis process (co-electrolysis), the following electrode reactions can occur:

Anode: $2H_2O\ (g) \rightarrow\ O_2\ (g) + 4H^+ + 4e^-$

Cathode: $CO_2(g) + 2H^+ + 2e^- \rightarrow\ CO\ (g) +\ H_2O\ (g)$

$2H^+ + 2e^- \rightarrow\ H_2$

Using solid solutions of Y-doped $BaCeO_3$ and $BaZrO_3$ (i.e. $BaCe_{0.5}Zr_{0.3}Y_{0.16}Zn_{0.04}O_{3-\delta}$ or BCZYZ) as proton conducting electrolyte and an iron based composite as cathode electrode, K. Xie et al. [22] have demonstrated that at 650 ^{0}C it is possible to convert CO_2 into CO with a faradaic efficiency of 29.5 %, but also into methane with a faradaic efficiency of ca. 2.4%, following the reaction:

$$CO_2(g) + 8H^+ + 8e^- \rightarrow CH_4\,(g) + 2H_2O\,(g)$$

So far, most of the investigations on SPCEC have focused on exploring electrolyte materials, and only a few studies on the electrode materials and reactions have been published. The anode or fuel electrode is usually Ni-based (Ni-BCZY, Ni-BCZYZ) in similarity to SOEC. The cathode is generally perovskites based such as strontium-doped lanthanum ferrite partially substituted with cobalt (LSCF)[23] and strontium-doped lanthanum cobaltite (LSC)[24]. All the electrodes as in SOECs are gas diffusion electrodes. A schematic representation of this type of cell based on proton conducting electrolyte is shown in Fig. 1.10.

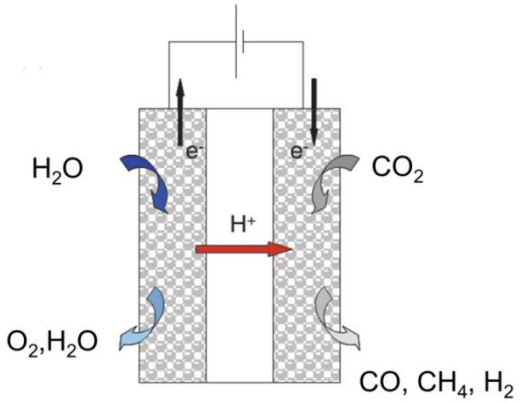

Fig. 1.10. Schematics of a proton conducting electrolyte based electrochemical cell that combine H_2O electrolysis and CO_2 reduction into hydrocarbons.

Recently an advanced alkaline electrolysis cell operating at high temperature and pressure has been developed and successfully tested[25]. This new type of alkaline electrolysis cell is based on metal foam gas diffusion electrodes (FobAEC) wherein the aqueous electrolyte (KOH) is immobilized in a porous ceramic structure, such as $SrTiO_3$. An illustration of such a cell with gas diffusion electrodes is shown in Fig. 1.11.

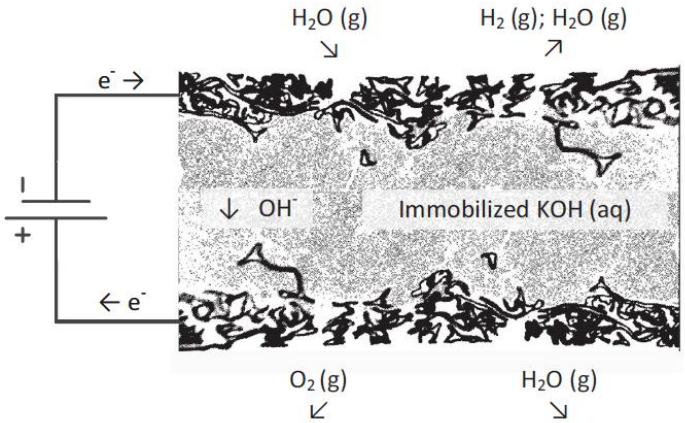

Fig. 1.11. Schematic representation of an alkaline electrolysis cell with aqueous KOH electrolyte immobilized in a porous matrix and gas diffusion electrodes. Originally published by F. Allebrod.[26]

The porous ceramic structure in which the liquid electrolyte is immobilized by capillary forces can be used as a combination of diaphragm and electrolyte. Such an electrolysis cell has been tested for temperatures above the boiling point of water, from 150 to 250 ^{0}C and total pressure up to 40 bar. Thus the electrolyte remains in the liquid phase due to the higher boiling point of the concentrated electrolyte based on KOH. The control of the pressure together with the temperature is fundamental, since too high pressure could cause condensation of steam, i.e. dilution of the electrolyte or flood the gas diffusion electrode, while too low pressure could lead to evaporation of the electrolyte and increase of its ohmic resistance. Allebrod et al.[27] who have developed this new design for alkaline cells, have also calculated –based on literature data- the phase transitions between the liquid and liquid + gas phase for water and KOH solutions as a function of pressure and temperature. Immobilizing the electrolyte in a ceramic porous matrix allows to use gas diffusion electrodes which prevents the formation of gas bubbles, usually responsible of increased ohmic losses and higher anodic and cathodic overpotentials due to reduced available electrode area[28]. The electrodes used were usually nickel foams as anode and Inconel foam as cathode. Using electrodeposited silver on nickel foam electrode a current density of -1 A/cm^2 has been measured at a cell voltage of 1.5 V, at 240 ^{0}C and 37 bar[25].

1.3 Thesis purpose and Outline

The main purpose of this thesis was to develop and characterize electrolyte materials and electrodes for production of hydrocarbons and/or alcohols via electrochemical reduction of CO_2. This should be carried out by taking into considerations the knowledge and the experience developed within the electrolysis technologies. During this chapter some well-established and more recent electrolysis technologies were presented and introduced. Low current densities due to slow electrode kinetics together with scarce catalyst selectivity are some of the drawbacks for the low temperature CO_2 conversion technologies, while the low stability of the produced hydrocarbons at elevated temperature represents a disadvantage for this process. Therefore it is necessary to design, develop and characterize a new electrochemical cell able to successfully form hydrocarbons directly by conversion of CO_2 with sufficient production rates.
The cells should run at intermediate temperature as 200 – 300 ^{0}C and elevated pressure.
The temperature range is chosen according to the thermal stability of hydrocarbons in order to produce synthetic fuels directly by conversion of CO_2. In addition, operating CO_2 reduction at intermediate temperature might avoid the need to utilize precious metals as catalysts. The advantages of performing the reduction at elevated pressure are manifold. Increasing the pressure increases the solubility of CO_2 according to Henry's law. In addition, a decrease in cell resistance will occur due to the frequency of reactants hitting the triple phase boundary, i.e. improved electrode kinetics and decreased diffusion resistance[29]. As a consequence, the reaction rate increases with higher pressure.

This thesis is divided in eight chapters which are grouped into four parts. The introductory Part I comprises two chapters explaining the purpose of this thesis, an introduction to the topic and relevant theoretical backgrounds and concepts. Part II and Part III contain 3 and 2 chapters presenting the experimental investigations on electrolytes and electrodes, respectively. Part II contains the studies performed on proton conducting materials, such as Y-doped $BaZrO_3$-$BaCeO_3$ solid solutions and K-doped $BaZr_{1-x}Y_xO_{3-\delta}$, where the main aim was to identify a proper electrolyte which could be implemented into full cells. Chapter 5 compares the different materials considered and explains the reason behind the choice of electrolyte to use in the third part of the thesis.

In Part III of the thesis the results of CO_2 reduction acquired with two different electrochemical cells and experimental setups are reported. In Chapter 6 is studied the electrocatalytic activity of copper foam in aqueous media and at ambient condition for electrochemical reduction of CO_2. It represents a fundamental study of the copper foam electrode. The measurements were conducted at the laboratory of Prof. Thomas F. Jaramillo (Stanford University – Chemical Engineer Department), where it was possible to utilize an experimental setup which ensures high sensitivity for minor products of CO_2 reduction reaction. In Chapter 7 are reported the description of the new designed electrochemical cell based on metal foam gas diffusion electrodes, able to reduce CO_2 in a single step process at elevated pressure. This chapter includes the results on the electrochemical performance and product selectivity of such newly designed cell. The electrocatalysts tested were copper and silver metal foams. Nickel metal foam was chosen as anode. The evaluation and characterization of both microstructure and surface elemental composition of the different parts of the cells are included.

Finally, the main conclusions of this work and the outlook are presented in Part IV - Chapter 8.

References

[1] J. R. Petit, J. Jouzel, D. Raynaud, N. I. Barkov, J.M. Barnola, I. Basile, M. Bender, J. Chappellaz, M. Davisk, G. Delaygue, M. Delmotte, V. M. Kotlyakov, M. Legrand, V. Y. Lipenkov, C. Lorius, L. Pepin, C. Ritz, E. Saltzmank & M. Stievenard, Nature, 399 (1999) 429-436.
[2] http://www.esrl.noaa.gov/gmd/ccgg/trends/ (accessed 30/05-2015)
[3] U.S. Energy Information Administration, Independent Statistics & Analysis, International Energy Outlook 2013, DOE/EIA – 0484 (2013).
[4] L.W.M. Beurskens, M. Hekkenberg, "Renewable Energy Projections" as published in the National Renewable Energy Action Plans of the European Member States, European Environment Agency, 2011.
[5] J. Mayer, «Electricity Spot-Prices and Production Data in Germany 2013», Fraunhofer Institute for Solar Energy Systems ISE, 2014.
http://www.ise.fraunhofer.de/de/downloads/pdf-files/aktuelles/boersenstrompreise-und-stromproduktion-2013.pdf (accessed 29/05-2015)
[6] M. Mogensen, F. Allebrod, J.R. Bowen, C. Chatzichristodoulou, M. Chen, S. D. Ebbesen, C. Graves, J. Hallinder, A. Hauch, P.V. Hendriksen, P. Holtappels, J. V.T. Høgh, S.H. Jensen, A. Lapina, P.L. Mollerup, X. Sun, 10th International workshop on Large-Scale Integration of wind power into Power System as well as on Transmission Networks for Offshore wind farms, ISBN: 978-3-9813870-3-2. (2011).
[7] a) N.S. Lewis and D.G. Nocera, Proceedings of the National Academy of Sciences of the United States of America, 103(43) (2006) 15729–15735. b) D.G. Nocera, 2006 Daedalus, 135(4) 112-115.

[8] R.W. Borry, Y. H. Kim, A. Huffsmith, J. A. Reimer and E. Iglesia, Journal of Physical Chemistry B, 103 (28) (1999) 5787-5796.
[9] S. D. Ebbesen, S. H. Jensen, A. Hauch and M.B. Mogensen, Chemical Reviews, 114(21) (2014) 10697-10734.
[10] P. Ragunathan, S. K. Mitra, M.G. Nayar, International Journal of Hydrogen Energy, 6(5) (1981) 487-496.
[11] Y. Hori, "Electrochemical CO_2 Reduction on Metal Electrodes", MODERN ASPECTS OF ELECTROCHEMISTRY No. 42, Edited by VAYENAS et al., Springer (NY) 2008
[12] M. Gattrell, N. Gupta, A. Co, Energy Conversion and Management, 48 (4) (2007) 1255-1265.
[13] E.J. Dufek, T. E. Lister, S. G. Stone, M.E. McIlwain , Journal of the Electrochemical Society, 159 (9) (2012) F514-F517.
[14] C.A. Linkous, H.R. Anderson, R.W. Kopitzke, G.L. Nelson, International Journal of Hydrogen Energy, 23 (1998) 525-529.
[15] R.L. Cook, R.C. MacDuff, A.F. Sammells, Journal of The Electrochemical Society, 135 (1988) 1470.
[16] R.L. Cook, R.C. MacDuff, A.F. Sammells, Journal of The Electrochemical Society, 137 (1990) 187.
[17] C. Delacourt, P. L. Ridgway, J. B. Kerr, J. Newman, Journal of the Electrochemical Society, 155(1) (2008) B42-B49.
[18] A. Ursúa, L. M. Gandia, P. Sanchis, Proceedings of the IEEE, 100 (2012) 410.
[19] S.H. Jensen, X. Sun, S.D. Ebbesen, R. Knibbe, M. Mogensen, International Journal of Hydrogen Energy, 35 (2010) 9544-9549.
[20] E. Ruiz-Trejo, J.T.S. Irvine, Solid State Ionics, 216 (2012) 36.
[21] E. Ruiz-Trejo, J.T.S. Irvine, Solid State Ionics, 252 (2013) 157.
[22] K. Xie, Y. Zhang, G. Meng, J.T.S. Irvine, Journal of Materials Chemistry, 21 (2011) 195.

[23] V. Kyriakou, C. Athanasiou, I. Garagounis, A. Skodra, M. Stoukides, Solid State Ionics, 225 (2012) 219.
[24] H. Iwahara, H. Uchida, I. Yamasaki, International Journal of Hydrogen Energy, 12 (1987) 73.
[25] F. Allebrod, C. Chatzichristodoulou, M.B. Mogensen, Journal of Power Sources, 229 (2013) 22-31.
[26] Frank Allebrod, "High Temperature and Pressure Alkaline Electrolysis", PhD Thesis, DTU Technical University of Denmark, Department of Energy, March 2013.
[27] F. Allebrod, C. Chatzichristodoulou, P.L. Mollerup, M.B. Mogensen, International Journal of Hydrogen Energy, 37 (2012) 16505.
[28] G. Kreysa and H. J. Kuelps, Journal of the Electrochemical Society, 128(5) (1981), 979–984.
[29] A. Momma, K. Takano, Y. Tanaka, T. Kato, A. Yamamoto, ECS Transaction, 57 (2013) 699.

Chapter 2
Electrochemical reduction of CO_2 in aqueous electrolytes.

This Chapter provides a description of the cell design used for CO_2 reduction in aqueous electrolytes. It includes a brief literature review on both the ionic conductivity of a suitable electrolyte and on the electrocatalytic properties of various transition metals for CO_2 reduction.

2.1 Cell concept

The main aim of this exploratory study was to develop and characterize electrolyte and electrode materials for electrochemical reduction of CO_2 into hydrocarbons and/or alcohols in a single device.

A temperature range between 200 to 300 ^{0}C and elevated pressure up to 50 bar are the target operating conditions, since several hydrocarbons are stable and reaction kinetics are improved at these conditions. There are no current electrochemical systems that can produce hydrocarbons at such temperatures and pressures. Because of this, investigation of promising and potentially suitable electrolytes and electrodes is needed.

The electrochemical cell consists of three main parts: anode, cathode and electrolyte.

Different classes of electrolytes, all having their optimal operating conditions are described in the literature. The electrolyte can be solid or liquid. However, aqueous electrolytes are known for their high conductivity at low temperatures[1]. As reported in Chapter 1, F. Allebrod et al.[2] developed a new alkaline steam electrolysis cell operating at temperatures and pressures up to 250 ^{0}C and 42 bar, respectively. By immobilizing the aqueous electrolyte (KOH) via capillary forces into a porous structure it was possible to use metal foam gas diffusion electrodes and to avoid the formation of bubbles at the electrodes.

Similarly P.L. Mollerup[3] investigated the potential of immobilized aqueous K_2CO_3 as a possible electrolyte for co-electrolysis of CO_2 and water at ca. 200 ^{0}C. This was done by studying the properties of pure aqueous K_2CO_3 and immobilized aqueous K_2CO_3 in two different porous ceramic matrixes. $KHCO_3$ is a well-known electrolyte for reduction of CO_2 [4,5].

Using K_2CO_3 (aq) as electrolyte leads to the following equilibrium reactions in the electrochemical cell:

$$H_2O + CO_3^{2-} \leftrightarrow OH^- + HCO_3^-$$

$$CO_2 + OH^- \leftrightarrow HCO_3^-$$

These equilibrium reactions can also be written as:

$$CO_2 + H_2O + CO_3^{2-} \leftrightarrow 2\,HCO_3^-$$

This indicates that increasing the partial pressure of CO_2 the equilibrium will be shifted to the right and therefore the amount of HCO_3^- ions will also increase. This also suggests that the CO_2 partial pressure can influence the possible charge carriers in the aqueous electrolyte.

P.L. Mollerup[3] calculated that the main charge carriers for 10wt% K_2CO_3 used in CO_2 atmosphere are most likely K^+ and HCO_3^-.

The anode reaction (water oxidation) can be written as:

$$2H_2O \leftrightarrow O_2 + 4e^- + 4H^+$$

Or

$$4OH^- \leftrightarrow O_2 + 4e^- + 2H_2O$$

While at the cathode CO_2 is reduced and H_2O is involved as proton donor (OH^-) since the electrochemical reactions occur in an aqueous solution. If the products are CO, methane or methanol the reactions are as follows:

$$CO_2 + H_2O + 2e^- \leftrightarrow CO + 2OH^-$$

$$CO_2 + 6H_2O + 8e^- \leftrightarrow CH_4 + 8OH^-$$

$$CO_2 + 5H_2O + 6e^- \leftrightarrow CH_3OH + 6OH^-$$

At the same potential as CO_2 reduction reaction occurs, it is also possible for water to be reduced to make hydrogen, which is a concurrent reaction:

$$2H_2O + 2e^- \leftrightarrow H_2 + 2OH^-.$$

The cell concept that was proposed for this study could consist of an immobilized aqueous electrolyte and electrocatalytic active gas diffusion electrodes for CO_2 fixation and O_2 evolution, respectively. A schematic representation is shown in Fig. 2.1.

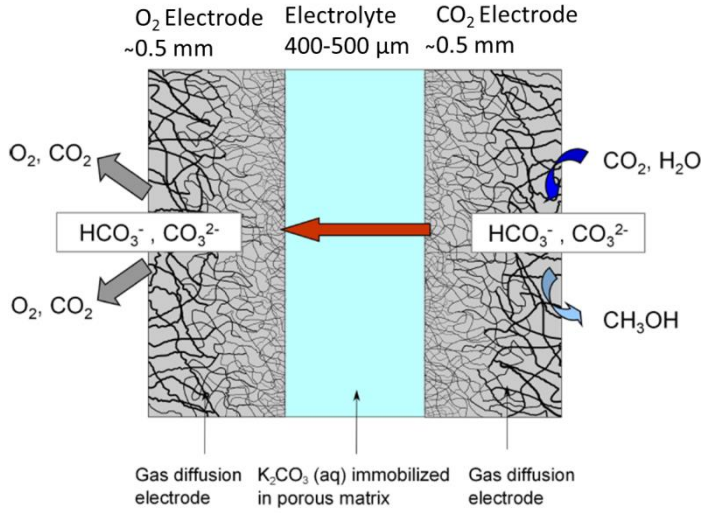

Fig. 2.1. Illustration of the suggested electrochemical cell with immobilized aqueous K_2CO_3 as electrolyte and with gas diffusion electrodes. The cathode is exposed to CO_2 and to the H_2O present in the electrolyte, while on the anode O_2 evolution takes place as well as some CO_2 formation. HCO_3^- and CO_3^- are the possible charge carriers. Adapted and modified from P. L. Mollerup[3].

2.1.1 Conductivity of aqueous and immobilized K_2CO_3

In order to use aqueous electrolytes at intermediate temperatures and elevated pressure it is important to know the ionic conductivity at different concentrations as a function of the operating conditions. The conductivity of 10-50 wt% aqueous K_2CO_3 at ambient conditions was measured by P.L. Mollerup [6] using the van der Pauw method in combination with electrochemical impedance spectroscopy (EIS) . Fig. 2.2 shows the comparison between the measured values and other published literature results [1,7]. The maximum conductivity was observed for a concentration of 30-40 wt%. P.L. Mollerup investigated also the conductivity of 5-30 wt% K_2CO_3 from ambient temperature up to 200 ^{0}C at 30 bar (Fig. 2.3). The conductivity showed a linear trend with temperature up to 100-120 ^{0}C. Conductivity values as high as 1.34 S/cm at ca. 170 ^{0}C for 30 wt% aqueous K_2CO_3 was measured. For higher temperature the conductivity of 30 wt% aqueous K_2CO_3 decreased to ca. 1 S/cm due to precipitation phenomenon.

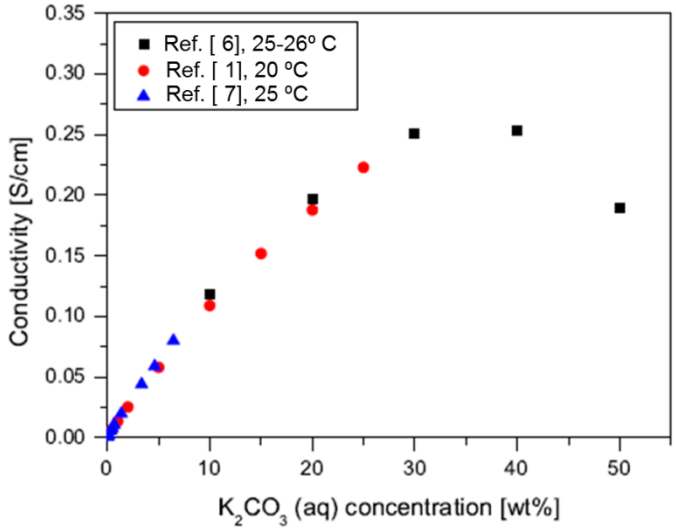

Fig. 2.2. Conductivity of 0.01-50 wt% K_2CO_3 at ambient temperature. Originally published by P.L. Mollerup et al. [6].

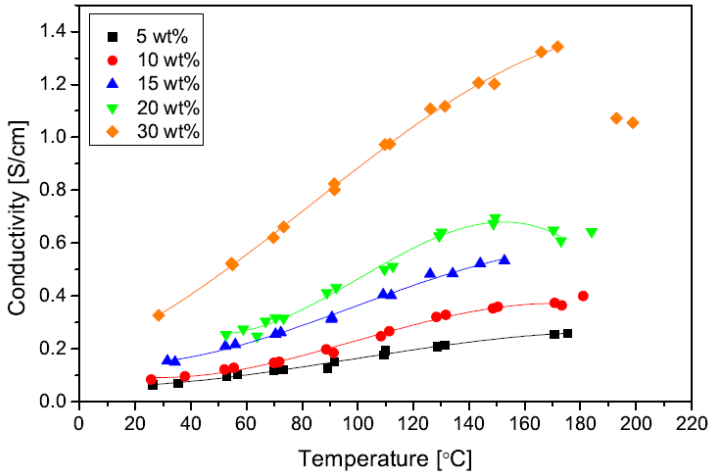

Fig. 2.3. Conductivity of 5-30 wt% aqueous K_2CO_3 from ambient temperature to 180-200 ^{0}C and at 30 bar. Originally published by P.L. Mollerup et al. [6].

Meso-porous solid pellets of $SrTiO_3$ and TiO_2 were synthesized and used to immobilize aqueous K_2CO_3. The conductivity at elevated temperature (up to 180 ^{0}C) and pressure (at 30-40 bar) of 10 wt% aqueous K_2CO_3 immobilized in $SrTiO_3$ and TiO_2 is shown in Fig. 2.4. For comparison, it is also reported the conductivity of pure aqueous 10 wt% K_2CO_3.

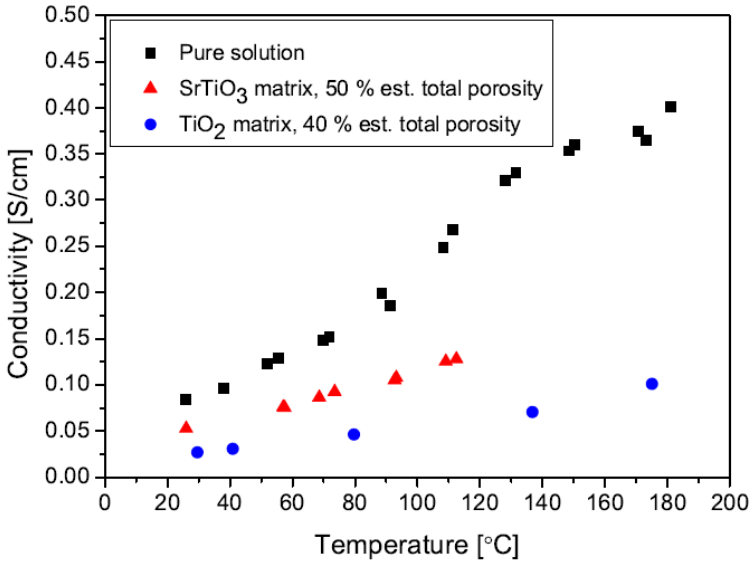

Fig. 2.4. Conductivity of 10 wt% aqueous K_2CO_3 both pure and immobilized in $SrTiO_3$ and TiO_2, from 25-185 ^{0}C. The initial pressure was 30 bar and kept constant during the test with $SrTiO_3$, while the pressure was allowed to increase with the temperature in the other tests. Originally published by P.L. Mollerup[3].

The conductivity increased with temperature and the conductivity of 10 wt% K_2CO_3 immobilized in $SrTiO_3$ were higher than for the same concentration of aqueous K_2CO_3 immobilized in TiO_2.
The difference in conductivity between 10 wt% aqueous K_2CO_3 immobilized in $SrTiO_3$ and TiO_2 pellets was explained by P.L. Mollerup[3] with the different estimated porosities of the two porous structures. $SrTiO_3$ pellets exhibited a smaller average pore size (ca. 55 nm) compared to TiO_2 pellets (ca. 200 nm). Therefore the capillary forces (ΔP), described by the Young–Laplace equation[8] (Eq. 2.1), were larger when using $SrTiO_3$ pellets. The higher the capillary forces the tighter the aqueous electrolyte is bound. a indicates the average pore radius, θ the contact angle and γ_{lv} the liquid-surface tension.

$$\Delta P = \frac{2\gamma_{lv}}{a} cos\theta \qquad \text{(Eq. 2.1)}$$

By decreasing the pore radius the capillary forces can be increased.
However the highest conductivity was registered for the pure aqueous 10 wt% K_2CO_3, due to the absence of the porous structure. By reducing the thickness of the ceramic matrix is possible to reduce the ohmic losses.

2.2 Electrocatalysts for CO_2 reduction

A key technological challenge fundamental to enable the conversion of CO_2 into value added products is the development of catalysts that are active and selective for this reaction. The desirable catalyst should reduce CO_2 at low overpotentials, generate selected products at high current densities with slow degradation and avoid the formation of unwanted byproducts. Many studies have focused on ways to increase the energy efficiency of CO_2 reduction reaction. The main contribution was given in 1985 by Hori et al.[4], when they discovered that methane and ethylene were the major products when copper metal was used as a catalyst at ambient conditions and in 0.1 M $KHCO_3$ aqueous electrolyte. Since then, a number of scientific articles[9,10,11,12,13] have compared the activity of different transition metals and found that the products of the CO_2 reduction reaction depend on the type of bond to the catalyst and the binding energy of CO, which is believed to be a fundamental intermediate in the reduction of CO_2, to the transition metal catalyst used. Table 2.1 shows literature data on the measured faradaic efficiencies with different metal electrodes. These results were obtained by applying a constant current density of -5 mA/cm^2 at ambient conditions and in 0.1 M $KHCO_3$ aqueous electrolyte and U is the electrode potential. The values of potentials are expressed vs reversible hydrogen electrode (RHE) scale by $V_{vs.RHE} = V_{vs.SHE} + 0.059 * pH_{(solution)}$. The RHE is a subtype of the standard hydrogen electrodes which differs from it by the fact that the measured potential takes into account the pH value of the electrolyte.

Table 2.1 Faradaic efficiencies of products in CO_2 reduction at various metal electrodes. Electrolyte: 0.1 M $KHCO_3$ T = 18 - 19°C, applied current density - 5 mA/cm^2 (Adapted and modified from Hori [13])

Metal	U V vs. RHE	**Faradaic Efficiency (%)**							
		CH_4	**C_2H_4**	**C_2H_5OH**	**C_3H_8O**	**CO**	**$HCOO^-$**	**H_2**	**Total**
Ni	-1.18	1.8	0	0	0	0	1	89	92
Fe	-0.57	0	0.1	0	0	0	0	95	95
Pt	-0.67	0	0	0	0	0	0	96	96
Ti	-1.20	0	0	0	0	tr	0	100	100
Pb	-1.23	0	0	0	0	0	97	5	102
Tl	1.20	0	0	0	0	0	95	6	100
In	-1.15	0	0	0	0	2	95	5	101
Sn	-1.08	0	0	0	0	7	88	5	100
Cd	-1.23	1.3	0	0	0	14	78	9	100
Au	-0.75	0	0	0	0	87	1	10	103
Ag	-0.97	0	0	0	0	81	1	12	98
Zn	-1.14	0	0	0	0	79	6	10	95
Pd	-0.80	2.9	0	0	0	28	3	26	95
Ga	-0.84	0	0	0	0	23	0	79	60
Cu	**-1.04**	**33.3**	**25.5**	**5.7**	**3**	**1.3**	**9**	**20**	**102**

Metals like Fe and Pt that bind CO strongly produce few products during the reduction, because they are poisoned by CO or other intermediates that form during the CO_2 reduction reaction. In particular, hydrogen is the main product observed from the competing water reduction.
The next group of metals as Sn, In, Pb, Cd successfully reduce CO_2, but does not have the possibility of breaking the carbon-oxygen bond, therefore, the major product is formate. This group of metals is the least active for hydrogen evolution. On the other hand, metals like Au, Ag and Zn that bind CO weakly produce mainly CO as a product, because when CO_2 is reduced to CO, the CO is released from the surface and does not keep reacting to form more reduced products such as alcohols and hydrocarbons. Cu metal is characterized by an intermediate binding energy for CO, which is claimed to be the reason for its almost exclusive ability to catalyze the formation of more reduced products that need more than a two electron reduction. The undesirable aspects of copper catalyst are in fact the variety of products it makes and the large overpotential. Furthermore, it is not yet well understood how to control the selectivity of the CO_2 reduction towards the most desired products like methanol and ethylene[13].

2.1.1 CO_2 electrochemical reduction on copper

Copper has been extensively studied as an electrocatalyst, since it is unique among the transition metals tried as an electrode for CO_2 reduction. Many studies[5,13] have correlated the catalytic activity and selectivity of copper to different parameters and reaction conditions, such as surface structure, working potential, temperature, working electrode and pressure.

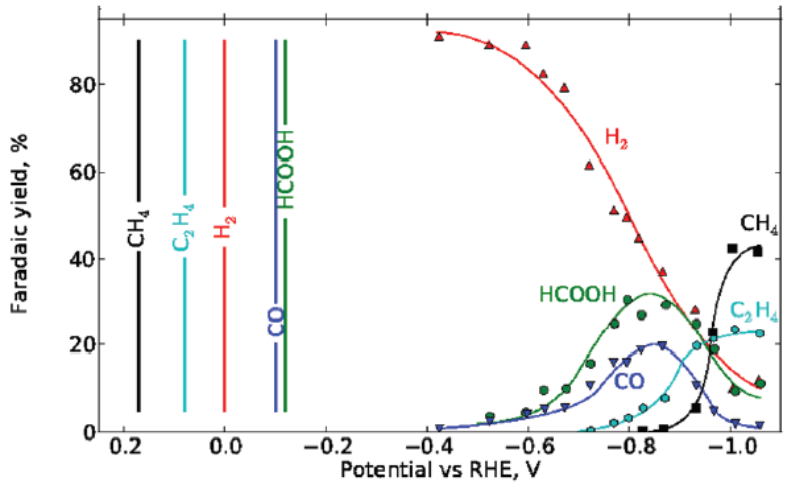

Fig. 2.5. Product distribution as a function of applied potential in the electrochemical reduction of CO_2 at a copper electrode in 0.1 M $KHCO_3$, measured by Y. Hori et al.[14] It is also reported the reversible potentials for formation of all the products form CO_2. Adapted by the originally published by A. Peterson et al.[16]

Hori et al.[14] firstly investigated the dependence of the product distribution on potential (Fig. 2.5). For potentials less negative than -0.4 V vs. RHE, hydrogen is the only detected product, while CO_2 electrochemical reduction occurred when larger overpotentials were applied. Formation of CO and formate takes place at ca. -0.6 V vs. RHE, achieving the highest Faradaic efficiencies at

around -0.85 V vs. RHE. Hydrocarbons formation, mainly ethylene and methane start to be produced at -0.7 V and -0.85 V vs. RHE, respectively. Ethylene formation reaches its maximum value at potentials around -0.9 vs. RHE, while at -1.0 vs. RHE methane is the predominant product with a faradaic efficiency of ca. 40%. The corresponding overpotential for producing high yields of hydrocarbons is in the range of 1.0 V to 1.2 V, which represents a significant energy loss.

K. Kuhl et al.[15] have recently reported new insights into the products distribution as a function of potential during the electrochemical reduction of CO_2 on a metallic copper foil surface. They developed an experimental methodology with high sensitivity for the quantification and identification of CO_2 electrochemical reduction products. Gas chromatography and nuclear magnetic resonance were used for the identification and quantification of gas and liquid products, respectively. They were able to identify sixteen reaction products in total, five of which were reported for the first time.

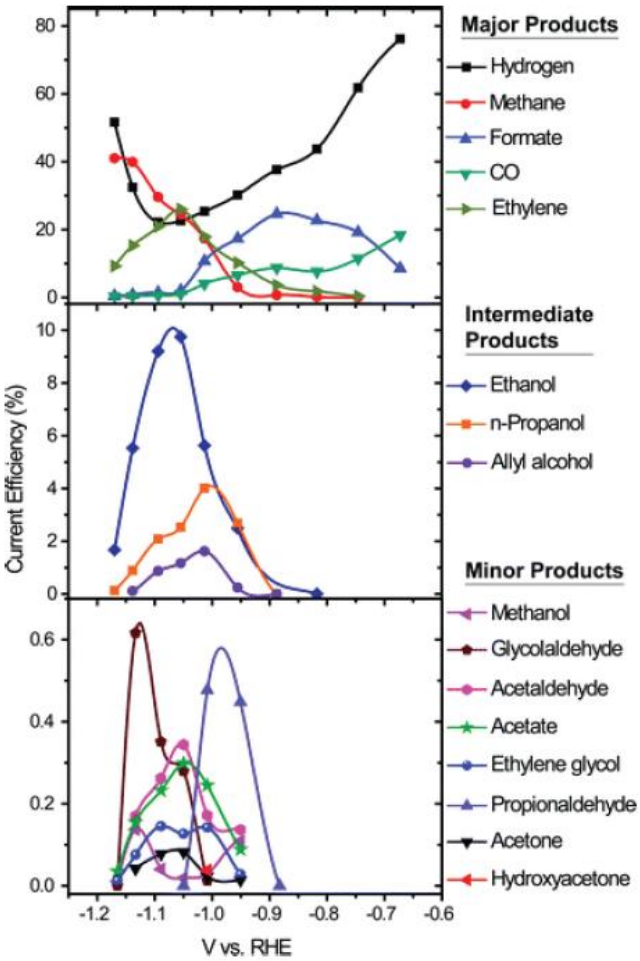

Fig. 2.6. Faradaic efficiency versus potential of the Cu electrode for each product as a function of potential is shown for major, intermediate and minor products. Originally published by K. Kuhl et al.[15].

Fig. 2.6 shows the distribution of the major CO_2 reduction products as a function of potential. It is possible to observe that the data are consistent with Y. Hori et al.[14] results. Apart from H_2, the products with the highest faradaic efficiency are the hydrocarbons methane and ethylene, while the remaining fourteen products are oxygenates, eleven of which are compounds with two or three carbon atoms. In addition, they observed a similar dependence on potential for those compounds with more than one carbon atom. Methane and ethylene are the dominant products of reaction. The onset potential for methane formation is at ca. -0.75 V vs. RHE. Ethylene shows the highest efficiency at -1.0 V vs. RHE, while the faradaic efficiency of methane increases when moving towards more negative potentials, such as -1.2 V vs. RHE. Their differing electrochemical behavior over the potential range indicates that they are characterized by different rate determining steps. The exact mechanism of CO_2 electrochemical reduction, in which hydrocarbons are produced, is still under debate. Density Functional Theory (DFT) was used to suggest the mechanism of methane formation on a Cu(211) model surface by A. A. Peterson et al.[16] The reaction steps corresponding to the lowest energy pathway for CO_2 reduction to methane are shown in Fig. 2.7. They identified that the key step in the formation of methane is the hydrogenation of the adsorbed CO to form adsorbed CHO at -0.74 V vs. RHE. From this potential, the hydrocarbon forming reaction pathways start. This value is in agreement with experimental onset potential for methane formation by Kuhl et al. [15].

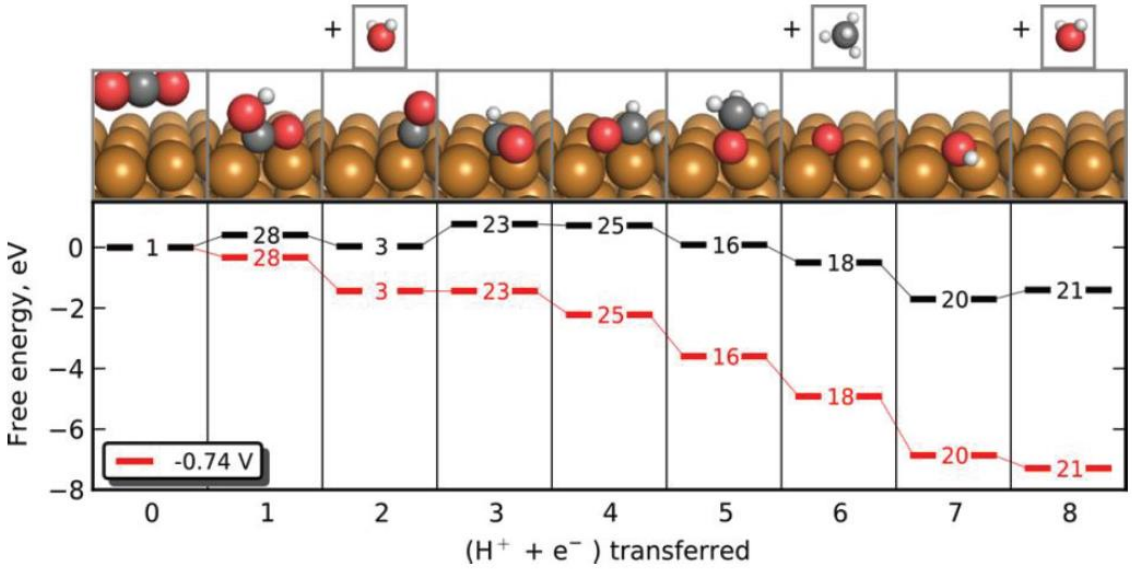

Fig. 2.7. Plot of Free energy versus number of transferred ($H^+ + e^-$) for a suggested CO_2 electrochemical reduction pathway for methane formation on Cu(211) model surface. The black and the red line show the free energy with 0 V and – 0.74 V vs. RHE applied potential, respectively. The numbers on the red and the black line are labels that refer to different states and are of no relevance here. The orange, red, black and white balls in the top of the figure symbolize Cu, O, C and H atoms, respectively. Originally published by A. Peterson et al.[16].

The crystal orientation of copper electrode is another factor that influences the product distribution, and many reviews and papers concerning this aspect have been published[17,18]. Hori et al.[19] observed that on stepped surfaces, like Cu(311), Cu(511) and Cu(711), the reaction occurs at lower potentials for a specific applied current density compared to the low indexed facets Cu(111) and Cu(100). In addition, they claimed that the crystal orientation influences the selectivity ratio between CH_4 and C_2H_4. On Cu(111) the faradaic efficiency for formation of methane was of 50.5%, while for ethylene was 8.8%. Conversely, the stepped surface Cu(711) showed only a low faradaic efficiency of 3.8% for methane and 51.6% for ethylene formation. Therefore stepped surfaces are more selective towards ethylene production, while terraces are more selective towards the formation of methane.

The reaction temperature also influences the product distribution[20]. CO_2 reduction was performed in the range of temperature between 0^0 and 40^0C and applying a constant current of 5 mA/cm^2 at a copper electrode. For decreasing temperature the faradaic efficiency for formate production was almost constant, hydrogen evolution and ethylene decreased while an increased efficiency of up to 65 % was observed for methane formation at 0^0 C[21]. Lower temperatures seem to influence not only the reaction rates, but also the adsorption equilibrium of the intermediate species and increase the CO_2 solubility. The concentration of CO_2 in the electrolyte could be enhanced by carrying out the electrochemical reduction under high CO_2 pressure.
Many studies have been done to investigate how the Faradaic efficiency and the selectivity of the reduction products are modified by increasing CO_2 pressure during the reduction on metal electrodes[22,23,24] and in particular on copper ones[25]. Hara et al. [25] tested the reduction of CO_2 on a copper electrode in aqueous 0.1 M $KHCO_3$ solution in an autoclave (limit of 100 atm). In this work the aqueous electrolyte was purified by pre-electrolysis and the copper wire cathode was electropolished. During the first part of the study, the applied current density was kept constant to 163 mA/cm^2 (galvanostatic configuration) and the CO_2 pressures was increased from 0 to 60 atm. Already at 10 bar the predominant reaction shifted from hydrogen to hydrocarbons with a 44 % of faradaic efficiency. Increasing the pressure at 20 atm, hydrocarbons decreased to ca 10% and formate and CO achieved a 30 % of current efficiency. At 30 bar formate was the main product, having a maximum of 54% of faradaic efficiency. Therefore, according to the authors by increasing the pressure less reduced CO_2 products were formed. Then, electrolysis measurements were carried out at constant pressure of 30 atm of CO_2 and varying the applied current density. The main products at 30 atm and current density up to 200 mA/cm^2 were formate and CO. By increasing the applied current density (and the electrode potential moved towards more negative values) hydrogen and hydrocarbons formation increased for current density between 600-700 mA/cm^2. This tendency in product selectivity is in line with that one observed by Hori et al.[13] at 1 atm of CO_2. However, the electrode potential for each product formed at 30 atm of CO_2 was more negative than that one at 1 atm. The authors claimed that the selectivity for reduction products formed was dependent on the electrode potential and also on the CO_2 pressure.
On the other hand, in Hara et al. [25] paper are reported the rates of CO_2 reduction and H_2 formation against electrode potential.

It is possible to see (Fig. 2.8) that for potentials more negative than -1.6 V vs Ag/AgCl the profile of the reaction rate of CO_2 is almost constant, while the H_2 one increases, suggesting the existence of mass transport limitations at higher overpotentials.
Under such conditions, where the current density is more or less independent of overpotential, the actual CO_2/Cu electrode overpotential as well as the actual electrolyte composition at the electrode/electrolyte interface might vary significantly.

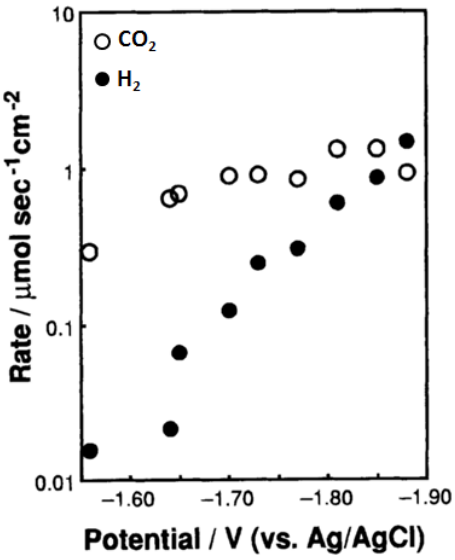

Fig. 2.8. Rates of total CO_2 reduction and H_2 formation under 30 atm of CO_2 with stirring electrolyte. (○) Rate of CO_2 reduction, (●) rate of H_2 formation. Originally published by Hara et al.[25]

2.1.2 CO_2 electrochemical reduction on silver

Metallic silver surfaces exhibit low activity for hydrogen evolution reaction and is characterized by a quite low CO binding energy, giving CO as the primary product in CO_2 reduction in aqueous media[26], [27]. M. Azuma et al.[20] reported that at lower temperature, i.e. 0 ^{0}C, the faradaic efficiency of CO together with $HCOO^-$ was enhanced. Some of the literature results obtained on Ag catalyst and in aqueous $KHCO_3$ electrolyte are summarized in Table 2.2.

Table 2.2 Literature overview of the faradaic efficiencies of CO, $HCOO^-$ and H_2 obtained during electrolysis on Ag electrodes at room temperature and pressure. The potentials are expressed vs. SHE.

Electrode	**Electrolyte**	**Faradaic efficiencies**	**Ref**
Ag-based GDEs	0.2 M $KHCO_3$	65-80 % CO and ca. 15 % $HCOO^-$ between -1.5 and -2.8 V vs SHE; current density is not given; H_2 efficiency not determined experimentally.	[28]
Ag planar electrode	0.5 M $KHCO_3$	61.4-89.9 % CO, 1.6-4.6 % $HCOO^-$, and 10.4-35.3 % H_2 at -1.4 V vs SHE, and 5 mA/cm^2.	[4]
Ag planar electrode	0.1 M $KHCO_3$	81.5 % CO, 0.8 % $HCOO^-$, and 12.4 % H_2 at – 1.37 V vs SHE and 5 mA/cm^2.	[29]
Ag planar electrode	0.05 M $KHCO_3$	30 % CO, 16 % $HCOO^-$, and 50 % H_2 at -1.96 V vs SHE; current density not given.	[20]
Ag planar electrode	0.1 M $KHCO_3$	64.7 % CO and 28 % H_2 at -1.4 V vs SHE and 1.5 mA/cm^2.	[26]
Ag planar electrode	0.5 M $KHCO_3$	15-20 % CO and 60-65 % H_2 at -1.8 V vs SHE; current density not given.	[30]

Recent work from T. Hatsukade et al. [31] provides a more detailed insight into the product distribution as a function of potential during the electrocatalytic CO_2 reduction on silver foil electrodes in aqueous electrolyte and ambient conditions.

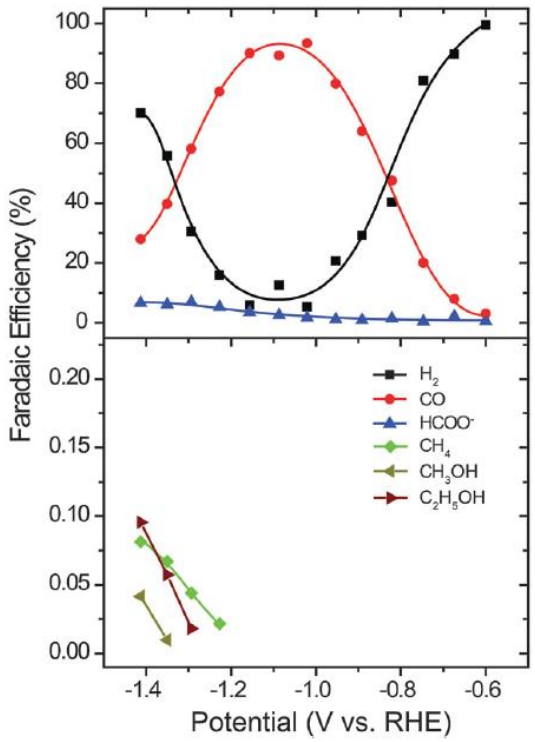

Fig. 2.9. Faradaic efficiency for each products detected as a function of potential. Originally published by T. Hatsukade et al[31].

The same highly sensitive electrochemical cell setup used by K. Kuhl allowed the detection of six different products, two of them reported for the first time. H_2 and CO are the major products detected and four different minor products were also observed: formate, methane, methanol and ethanol. In Fig. 2.9 the faradaic efficiency is reported as a function of the applied potential. Hydrogen and CO have a combined faradaic efficiency of 90 % over the potential range investigated. The evolution of hydrogen is dominant at the lowest (-0.6 V to -1 V vs RHE) and highest (-1.2 V to -1.4 V vs RHE) overpotential, while CO has its maximum in the intermediate (-1.0 V to -1.2 V vs RHE) overpotential. On the other hand, the faradaic efficiencies of the minor products increase with the overpotential. The onset potential (ca. -1.2 V vs RHE) for the formation of methane, methanol and ethanol is similar and according to the authors this might be due to similarities in their mechanistic pathways, and perhaps indicate a common rate-determining step.

The pressurized electrochemical reduction of CO_2 has been investigated on Ag electrode surface both at ambient temperature[20] and at 60^0 to 90^0 C[32]. The predominant reduction product is CO on Ag electrodes under high pressure, as is the case under a pressure of 1 atm. The faradaic efficiency for CO formation reaches 78.8% at a current density of 300 mA cm^{-2}, and is 34.9% at 600 mA cm^{-2} at 30 bar in 0.1 M $KHCO_3$ electrolyte. The faradaic efficiency for CO formation decreases with increasing current density. E. Dufek et al.[32] reported an initial study on the operation of an electrolysis cell for pressurized reduction of CO_2 able to generate syngas mixtures continuously at high current density. By using a gas diffusion silver electrode the amount of CO generated at 18.5 bar is five times higher than that observed at ambient pressure, with faradaic efficiency of ca. 90% observed at 350 mA/cm^2. At 18.5 bar and 60^0 C the faradaic efficiency for CO production was still ca. 90 % after one hour electrolysis test even applying a lower current density of 225 mA/cm^2.

References

[1] W. M. Haynes, Ed. CRC Handbook of Chemistry and Physics, 92nd ed.; CRC Press/Taylor and Francis: Boca Raton, FL.

[2] F. Allebrod, C. Chatzichristodoulou, M.B. Mogensen, Journal of Power Sources, 229 (2013) 22-31.

[3] Pia Lolk Mollerup, "New Electrolytes for CO_2 Electrolysis cells", Department of Energy Conversion and Storage, Technical University of Denmark, December 2012.

[4] Y. Hori, K. Kikuchi, S. Suzuki, Chemistry Letters, 14 (1985), 1695-1698.

[5] M. Gattrell, N. Gupta, A. Co, Journal of Electroanalytical Chemistry, 594 (2006), 1-19.

[6] P.L. Mollerup, A.S. Christiansen, N. Bonanos, M.B. Mogensen, Journal of new materials for electrochemical system, 16 (2013), 279-285.

[7] E.W. Washburn, Ed. International Critical Tables of Numerical Data, Physics, Chemistry and Technology (1st Electronic Edition); Knovel, 2003; Chapter VI, pp 259-256.

[8] S. Lowell, J.E. Shields, M.A. Thomas, M. Thommes, Characterization of Porous Solids and Powders: Surface Area, Pore Size and Density, 4th ed.; Springer New York, 2004.

[9] Handbook of Fuel Cells: Fundamentals, Technology and Application; Hori, Y., Ed.; VHC-Wiley: Chichester, 2003; Vol. 2.
[10] K. J. P Schouten,Y. Kwon, C.J.M. van der Ham, Z. Qin, M.T. M. Koper, Chemical Science, 2 (2011) 1902.
[11] M. Jitaru, D.A. Lowy, M. Toma, B. C. Toma, L. Oniciu, Journal of Applied Electrochemistry 27 (1997), 875.
[12] K. Watanabe, U. Nagashima, and H. Hosoya, Chemical Physics letters, 209 (1993) 109-110.
[13] Y. Hori, in Modern aspects of electrochemistry, ed. C. Vayenas, R. White, and M. Gamboa-Aldeco, Springer, New York, 2008, vol. 42, pp. 89-189.
[14] Y. Hori, A. Murata, R. Takahashi, Journal of the Chemical Society, Faraday Transactions 1: Physical Chemistry in Condensed Phases, 85 (1989) 2309.
[15] K. P. Kuhl, E. R. Cave, D. N. Abram and T. F. Jaramillo, Energy & Environmental Science, 5 (2012) 7050 – 7059.
[16] A. A. Peterson, F. Abild-Pedersen, F. Studt, J. Rossmeisl, J.K. Nørskov, Energy & Environmental Science 2010, 3, 1311.
[17] Y. Hori, I. Takahashi, O. Koga, N. Hoshi, Journal of Molecular Catalysis A, 199 (2003) 39.
[18] W. Tang, A. A. Peterson, J. K. Norskov, I. Chorkendorff, Phys. Chem. Chem. Phys.,14, 2012, 76.
[19] Y.Hori, I. Takahashi, O. Koga, N. Hoshi, The Journal of Physical Chemistry B, 106 (2001) 15.
[20] M. Azuma, K. Hashimoto, and M. Hiramoto, Journal of Electrochemical Society, 137, 1990, 1772.
[21] Y. Hori, K. Kikuchi, A. Murata, S. Suzuki, Chemistry Letters, (1986) 897-898.
[22] K. Hara, A. Kudo, and T. Sakata, Journal of Electroanalytical Chemistry, 391 (1995) 141.
[23] K. Hara, A. Kudo, T. Sakata and M. Watanabe, Journal of Electrochemical Society, 142 (1995) 57-59.
[24] A. Kudo, S. Nakagawa, A. tsuneto, T. Sakata, Journal of Electrochemical Society, 140 (1993) 1541-1545.
[25] K. Hara, A. Tsuneto, A. Kudo, and T. Sakata, Journal of Electrochemical Society, 141 (1994) 2097.
[26] H. Noda, S. Ikeda, Y. Oda, K. Imai, M. Maeda, and K. Ito, Bulletin of the Chemical Society of Japan, 63 (1990) 2459.
[27] K. Watanabe, U. Nagashima and H. Hosoya, Applied Surface Science, 75 (1994) 121-124.
[28] M. Shibata, K. Yoshida, N. Furuya, Journal of Electroanalytical Chemistry 442 (1998) 67.
[29] Y. Hory, H. Wakebe, T. Tsukamoto, O. Koga, Electrochemica Acta, 39 (1994) 1833.
[30] H. Yano, F. Shirai, M. Nakayama, K. Ogura, Journal of Electroanalytical Chemistry, 533 (2002) 113.
[31] T. Hatsukade, K.P. Kuhl, E.R. Cave, D.N. Abram, T.F. Jaramillo, Phys. Chem. Chem. Phys., 16 (2014) 13814- 13819.
[32] E.J. Dufek, T.E. Lister, S.G. Stone, M.E. McIlwain, Journal of Electrochemical Society, 159 (2012) 514-517.

Part II

ELECTROLYTES

Chapter 3
Phase stability and conductivity of $BaCe_{1-x-y}Zr_yY_xO_{3-\delta}$ at elevated partial pressures of H_2, H_2O and CO_2 at 240 ^oC[a]

The aim of Part II was to find suitable electrolyte materials for an electrochemical cell able to reduce CO2 at intermediate temperature and high pressure. This Chapter consists of an exploratory study on three different proton conducting materials, such as Y- doped $BaZrO_3$-$BaCeO_3$ solid solutions. The purpose was to investigate the conductivity and the phase stability of the different compounds.

Abstract

$BaCe_{1-x-y}Zr_yY_xO_{3-\delta}$ is a family of proton conductors with potential for use at intermediate temperatures. The conductivity of $BaCe_{1-x-y}Zr_yY_xO_{3-\delta}$ (x; y) = (0.1; 0.9) – (0.1; 0.4) – (0.2; 0.6) was studied with Electrochemical Impedance Spectroscopy at 240 ^{0}C at a total pressure of 50 bar in a wet mixture of 5 vol.% H_2 in N_2 (pH_2O = 10 mbar – 25 bar), and in a gas mixture of 50 vol.% CO_2, 5 vol.% H_2 and 45 vol.% N_2 with a gradual increase of the total pressure from 1 to 50 bar. Contrary to the compounds containing CeO_2, $BaZr_{0.9}Y_{0.1}O_{3-\delta}$ showed a gradual increase of one order of magnitude in conductivity with increasing pH_2O from 10 mbar to 5 bar. The compound with the highest cerium content, $BaCe_{0.5}Zr_{0.4}Y_{0.1}O_{3-\delta}$, exhibited the highest conductivity values at all conditions. Especially at high pH_2O a drastic increase in conductivity was observed, reaching a value of $2\cdot10^{-3}$ S/cm, the highest value ever reported for this type of compounds at low temperatures. Post-test phase analysis revealed that the chemical stability in H_2O and CO_2 increased with increasing ZrO_2 content and that phase separation was obstructed at high degrees of densification. Formation of CeO_2 and $BaCO_3$ was observed in the $BaCe_{0.5}Zr_{0.4}Y_{0.1}O_{3-\delta}$ electrolyte after exposure to elevated pH_2O and pCO_2.

[a] This chapter has been submitted to: *Solid State Ionics* in February 2015: F. Vico*, C. Chatzichristodoulou, M.B. Mogensen. Title: Phase stability and conductivity of $BaCe_{1-x-y}Zr_yY_xO_{3-\delta}$ at elevated partial pressures of H_2, H_2O and CO_2 at 240 ^{0}C.

3.1 Introduction

The electrochemical conversion of CO_2 for production of renewable hydrocarbon fuels is a research field of growing interest, as it can enable the use of carbon based fuels in a CO_2 neutral manner.[1]

Electrochemical CO_2 reduction at intermediate temperatures (T ~ 300 °C) can be advantageous as compared to room temperature operation, as it will increase the rate of thermally activated processes, thereby increasing the rate of CO_2 reduction. Elevated pressure can also have a positive influence on electrode activity, due to the increased impinging frequency of gaseous reactants on the electrode surface, while enhancing the thermodynamic stability of hydrocarbon products and offering a means to control product selectivity. Thus intermediate temperature and elevated pressure electrolysis represents a promising route for production of renewable hydrocarbons, as it can potentially lead to a system where hydrocarbons are produced in a single step process, selectively and at industrially feasible rates without the use of precious metals.

One of the challenges is to identify an electrolyte material that shows high conductivity and high mechanical and chemical stability over several years under these relatively extreme operating conditions. As an alternative to the oxide ion conducting electrolytes, widely used in solid oxide electrolysis cells (SOEC) and solid oxide fuel cells (SOFC), proton conducting doped perovskite oxides have been the subject of extensive investigation ever since Iwahara et al.[2] demonstrated their properties and potential. In particular, proton conducting perovskite oxides exhibit lower activation energy compared to oxide ion conductors, which makes them interesting candidates for intermediate temperature operation. These materials are termed high-temperature proton conductors (HTPCs), because their working temperatures (400 – 800 °C) are noticeably higher than the working temperatures of proton conducting polymers (~100 °C).

HTPCs have been considered very attractive electrolyte materials for high-temperature steam electrolysis[3] and more recently for reforming of hydrocarbon fuels by steam permeation in a protonic ceramic fuel cell[4]. Moreover, Irvine *et al.* have successfully demonstrated electrochemical reduction of CO_2, accompanied by formation of hydrocarbons and CO at 614 °C and atmospheric pressure in a proton conducting solid oxide electrolyser based on $BaCe_{0.5}Zr_{0.3}Y_{0.16}Zn_{0.04}O_{3-\delta}$ electrolyte[5].

HTPCs display proton conductivity when exposed to hydrogen and/or water vapor atmospheres[6]. This characteristic belongs to a restricted group of the oxides with perovskite-type structure ABO_3, where A and B denote two different cations with oxidation states yielding a sum of 6, e.g. 1 + 5, 2 + 4, and 3 + 3. Protonic conductivity is promoted by doping the B-site with a suitable acceptor element M, obtaining $AB_{1-x}M_xO_{3-\delta}$ where δ represents the oxygen deficiency per formula unit.

Substitution of the M acceptor dopant cations in the B site induces the formation of oxide-ion vacancies.[7] In Kröger-Vink notation:

$$2B_B^x + O_O^x + M_2O_3 \leftrightarrow 2M_B' + V_O^{\cdot\cdot} + 2BO_2 \qquad \text{(Eq. 3.1)}$$

Solid state hydration takes place upon exposure to water vapor according to the reaction:

$$H_2O\ (g) + V_O^{\cdot\cdot} + O_O^x \leftrightarrow 2OH_O^{\cdot} \qquad \text{(Eq. 3.2)}$$

Water in the gas phase dissociates into a hydroxide ion and a proton. The OH^- fills an oxygen vacancy, while the proton can establish a covalent bond with lattice oxygen. The reaction described by equation (3.2) is reversible, so the hydration or dehydration reaction can take place depending on the local partial pressure of steam and the value of the equilibrium constant. In addition, decreasing electronegativity difference between B and A facilitates hydration of the oxygen vacancies[8].

The mechanism which describes the incorporation of the protons and their diffusion in the perovskite structure has been extensively studied e.g. by Coors et al.[4,9]. They find that the proton migrates by the so called Grotthuss-type mechanism, which is based on the hopping of the proton from one oxide ion to a neighboring oxide ion.

Alkaline earth cerates ($ACeO_3$) and zirconates ($AZrO_3$) are the proton-conducting perovskite oxides that have received most attention, due to their high proton conductivity and good chemical stability, respectively. P. A. Stuart *et al.*[10] have analysed the conductivity of $BaCe_{0.9}Y_{0.1}O_{3-\delta}$ (BCY10) in the temperature range of 200-600 °C, and at 300 °C they reported a value of 10^{-3} S cm^{-1}. In general, cerate-based protonic conductors have a high conductivity but rather poor chemical stability. For example Y-doped barium cerate (BCY) powder degrades in atmospheres containing more than 9 vol.% of CO_2 in argon at temperatures below 750 °C, because the barium cerate is highly basic and it decomposes into CeO_2 and $BaCO_3$ or $Ba(OH)_2$ when it reacts with CO_2 and H_2O [11]. The instability towards water is related to the high solubility of water into the bulk structure of barium cerates[12, 13]. Instead CO_2 cannot dissolve or diffuse into the barium cerate lattice and therefore fully densified ceramics can be kinetically stable in CO_2 at temperatures below 700 ^{0}C, even if the carbonation is thermodynamically favored[14]. On the other hand, polycrystalline yttrium-doped barium zirconate has insufficient conductivity for practical applications, but a good chemical stability[14]. Although the bulk conductivity of Y-doped $BaZrO_3$ is higher than the bulk contribution of $BaCeO_3$-based oxides, barium zirconates are characterized by large grain boundary resistivity which limits the total conductivity[15].

One of the greater challenges for the perovskite-type proton conductors is an appropriate compromise between conductivity and chemical stability. Since $BaCeO_3$ and $BaZrO_3$ easily form solid solutions, it is possible to substitute a fraction of Ce in Y:$BaCeO_3$ with Zr to produce a solid solution that shows both reasonable proton conductivity and adequate chemical stability under the conditions required for practical applications[16], e.g. CO_2 reduction.

It is the aim of this exploratory work to examine the conductivity and chemical stability of selected compositions of $BaCe_{1-x-y}Zr_yY_xO_{3-\delta}$ as possible electrolytes for the electrochemical conversion of CO_2 into $C_xH_yO_z$ at elevated partial pressures of water vapour and of carbon dioxide and intermediate temperatures (T = 240 °C).

3.2 Experimental

3.2.1 Synthesis of pellets

$BaCe_{0.5}Zr_{0.4}Y_{0.1}O_{3-\delta}$ (BCZY541), $BaCe_{0.2}Zr_{0.6}Y_{0.2}O_{3-\delta}$ (BCZY262) and $BaZr_{0.9}Y_{0.1}O_{3-\delta}$ (BZY91) were synthesized by the solid state reaction method[17], using $BaCO_3$ (Alfa Aesar, 99.95% (metal basis)), ZrO_2 (Tosoh TZ-0), CeO_2 (Aldrich, 99.9%, trace of metal basis, <5 μm), and Y_2O_3 (Reacton, 99.99%). 1 wt% of NiO (Alfa Aesar, 99% (metal basis)) was added as a sintering additive. After drying, the precursors were weighed in molar ratios of 0.98 $BaCO_3$• (1-x-y) CeO_2• $yZrO_2$• xY_2O_3, resulting in a slightly A-site deficient perovskite. It is important to have a small A-site substoichiometry, because it is not possible to make an exact stoichiometric compound due to the uncertainty on the exact composition and on weighing of the raw materials. Thus, if the procedure aims for an A/B ratio equal to 1.000 then there is a risk that A/B > 1 in the perovskite, and as the AO with the big A-ion is very reactive towards H_2O and CO_2 this will destabilize the perovskite. By decreasing the A-site occupancy as much as possible, the AO activity is maximum reduced and the stability of the perovskite maximum increased. BO_2 will in general not react with CO_2 or H_2O, so small amounts of secondary phase will not be disadvantageous in any way. Throughout this work it will be indicated as $BaCe_{1-x-y}Zr_yY_xO_{3-\delta}$ because it is not exactly known how much A-site deficiency that may be induced in $BaCe_{1-x-y}Zr_yY_xO_{3-\delta}$, but most probably it will be less than 2 % of the A-sites. The dried powder mixtures were ground in a ball mill for 24 h with acetone. Afterwards a small quantity of binder, composed of PeO_x (Poly(2-ethyl-2-oxazoline)), acetone, and Kellox (fish oil) as dispersant were added to the mixture which was further ball milled for 6 h. After blending, the solutions were pan dried and the powders were sieved manually reducing them in particles size of diameter of 95 μm (160 mesh screen)[18]. The powder was pressed into cylindrical pellets by uniaxial pressing under a pressure of 60 MPa. The pellets were placed on NiO - YSZ substrates covered by calcined 8YSZ to prevent contamination and sintered in air at 1550 °C for 8 h. Each composition of BCZY was sintered separately. The obtained pellets had a diameter of 8 $\pm$ 0.1 mm and a thickness of 2 $\pm$ 0.1 mm after polishing.

After the solid state reactive sintering the three oxides showed a different relative density, varying mainly with the amount of Ce present in the structure. BCZY541 had the largest grain size after the sintering procedure and thus the BCZY541 powder had better sinterability as also observed by Fabbri *et al.*[14]. Synthesis of dense BCZY262 and BZY91 was more problematic. In particular, different degrees of densification were obtained between different batches. Table 3.1 lists the relative geometric densities of the electrolytes tested in cells of BCZY541, BCZY262 and BZY91.

Table 3.1. Relative density for the BCZY pellets prepared by solid state reactive sintering.

	BZY91	BCZY262	BCZY262	BCZY541
Relative density	90 %	85 %	93 %	95 %

3.2.2 Characterization

X-ray diffractograms (XRDs) were recorded using a Bruker D8 Advance, in order to determine the crystalline phases and exact cell parameters. The lattice parameters and unit cell volume were determined using both the software Diffrac.EVA and the Rietveld method (TOPAS 3.0), which was also used for structural refinement.

SEM imaging was carried out on fractured cross sections of tested and pristine pellets using a Zeiss SUPRA SEM. The fractured pellets were attached to a metal sample holder through a piece of carbon tape and coated with a thin layer of carbon using a sputter coater.
Electrochemical measurements were performed in a high pressure electrochemical test station (limit: 100 bar, 300 °C), described in detail elsewhere[19]. Preliminary experiments were carried out in the electrochemical rig in order to optimize the measurements on high impedance samples. In particular a dummy cell with high impedance was made to determine the capacitance of the setup, which was likely to influence the impedance spectra mainly at high frequency[20].
Cells for conductivity measurements were made by painting Pt-ink (Ferro 308a, fritless, platelets) on each side of the electrolyte disc samples and fired in air at 900 °C for 4 h.
The electrical conductivity measurements were performed by Electrochemical Impedance Spectroscopy (EIS) using a Gamry 3000 Reference potentiostat, in the frequency range of 0.1 Hz to 1 MHz and amplitude of 0.35 V.
The AC conductivity test was performed along two consecutive sequences, both at temperatures of 240 °C. During the sequence 1 the conductivity of the oxides was measured with a total pressure of 50 bar in a wet mixture of 5 vol.% H_2 in N_2 (pH_2O = 10 mbar – 2.5 bar – 5 bar – 10 bar – 25 bar). The first value of pH_2O was obtained by considering that pH_2O in the unhumidified H_2 and N_2 gases is estimated to be $\approx 2 \cdot 10^{-4}$ atm. [18] After sequence 1 the pressure was decreased to 1 bar and during sequence 2 the total pressure (P_{tot}) was gradually increased from 1 to 50 bar, *i.e.* P_{tot} = 1 bar, 2 bar, 3 bar, 4 bar, 5 bar, 10 bar, 15 bar, 20 bar, 25 bar, 50 bar. In this second part the conductivity measurements were carried out in a gas mixture composed of 50 vol.% CO_2, 5 vol.% H_2 and 45 vol.% N_2. The 85 % dense BCZY262 electrolyte was only exposed to a sequence 1 test.

A flushing time of several hours was allowed after every change of gas composition in order to exchange once the gases present in the reactor. The number of hours was estimated taking into account the volume of the autoclave, the P_{tot} and the flow rate of the gases. In addition, a hold time of three hours was used, during which impedance spectra were recorded every 15 minutes.

3.3 Results

3.3.1 Chemical stability in CO_2

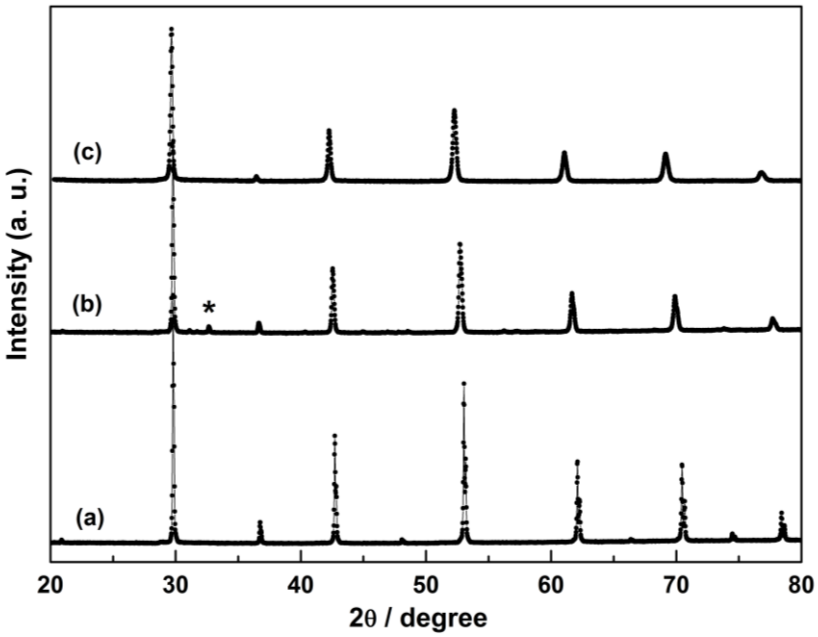

Fig. 3.1. XRD of (a) BCZY541, (b) BCZY262 and (c) BZY91, prepared by solid state reactive sintering at 1550 °C. * Indicates the phase Ba_2YNiO_5 (reflection (112)).

Table 3.2. Space group, lattice parameters and unit cell volume of sintered $BaCe_{1-x-y}Zr_yY_xO_{3-\delta}$ obtained through Diffrac.EVA.

Compound	Space Group	Lattice parameters [Å]	Unit cell Volume [$Å^3$]	Formula unit volume [$Å^3$]
BCZY541	Pmcn (orthorhombic)	a = 6.493 ± 0.002 b = 5.957± 0.002 c = 8.925± 0.003	344.95	86.23
BCZY262	Pmcn (orthorhombic)	a = 6.0352±0.0003 b = 6.0233±0.0003 c = 8.5144±0.0005	309.51	77.37
BZY91	Pm-3m (cubic)	a = 4.2091±0.0006	74.57	74.57

Fig. 3.1 shows the XRDs of $BaCe_{1-x-y}Zr_yY_xO_{3-\delta}$ after sintering. The lattice symmetry was found to be cubic (Pm-3m) for BZY91 and orthorhombic (Pmcn) for both BCZY262 and BCZY541. Table 3.2 lists the lattice parameters and the unit cell volume estimated from the XRD analysis done with the Rietveld refinement method. The lattice parameters of these oxides are in line with published data[21]. The volume per formula unit increased with increasing Ce content due to the bigger ionic radius of Ce^{4+} (0.87 Å) compared to the radius of Zr^{4+} (0.72 Å) in 6-fold coordination[22]. The chemical stability of the synthesized $BaCe_{0.5}Zr_{0.4}Y_{0.1}O_{3-\delta}$ (BCZY541) was tested firstly by high temperature XRD (HT-XRD) experiments under flowing CO_2 (1 bar) at 700 ^{0}C for 7 h and at 900 °C for 12 h.

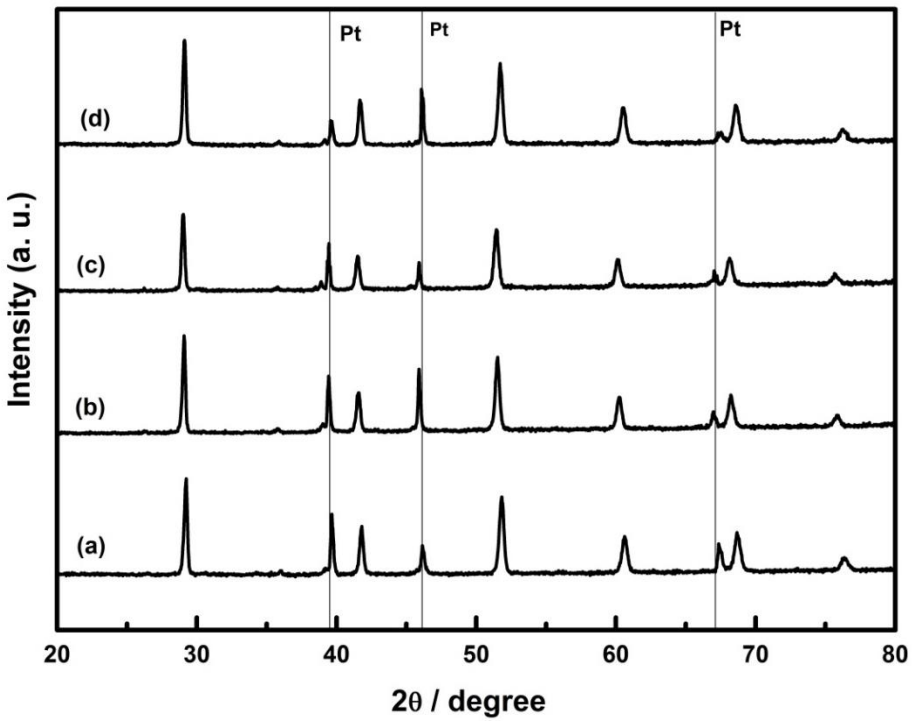

Fig. 3,2. XRDs of BCZY541 powders during exposure to CO_2 atmosphere at different temperatures. (a) 30 °C, (b) 700 °C after 7 h, (c) 900 °C after 12 h and (d) 30 °C after test. The extra peaks present are due to diffraction from the sample holder which is a Platinum foil.

Only the compound BCZY541 was investigated, because it is already well known from the literature[23,24] that compounds with lower amount of Ce do not react with acidic gases like CO_2 at 1 bar, as the thermo-chemical stability of Zr-substituted $BaCeO_3$ against CO_2 increases with increasing Zr-content. As Fig. 3.2 shows, the XRDs before and after the HT-XRD test coincide, indicating that BCZY541 is chemically stable in 1 bar CO_2 at $T \geq 700$ °C. Furthermore, XRD analysis was undertaken on the electrolytes of three cells (BZY91, BCZY262 and BCZY541) five days after the conductivity sequences 1 and 2 were completed (Fig. 3.3).

After high pressure conductivity tests the three cells were kept in air, at an average temperature of 20 °C. The BCZY541 electrolyte changed colour from black (Ni sintering aid effect) to white due to the carbonation reaction. This was noticed visually as soon as the sample was removed from the autoclave.
After one month of storage in air, the sample of BCZY541 heavily cracked and broke into small pieces. A part of them was ground and XRD was undertaken on the powder obtained. The BCZY262 and BZY91 samples did not exhibit any severe colour change or mechanical modification.

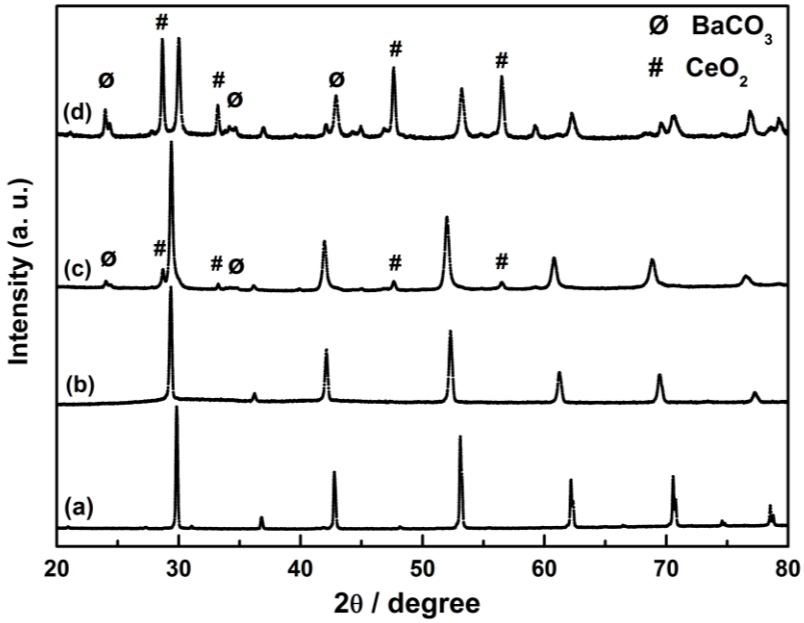

Fig. 3.3. XRDs for the pellets of (a) BZY91, (b) BCZY262, (c) BCZY541 five days after the conductivity test and (d) BCZY41 powder one month after the conductivity test at 240 °C. The BCZY541 sample is influenced by the carbonation reaction.

Fig. 3.3 shows the post-test XRDs which reveal the formation of CeO_2 (space group Fm-3m) and $BaCO_3$ (space group Pmcn) in the diffractogram (c) belonging to BCZY541 compound 5 days after the test. Conversely compounds BZY91 and BCZY262 remained unaffected. In particular, Fig. 3.3 shows also the XRDs taken on BCZY541 one month after the conductivity test. Structural refinement was done on both diffractograms (c) and (d) of Fig. 3.3. As Fig. 3.3 pattern (d) shows, the carbonation reaction of BCZY541 has further evolved with time at ambient conditions. The structural analysis done with Rietveld refinement method indicated that the perovskite phase changed from orthorhombic to cubic $BaZr_{x1}Y_{x2}O_{3-\delta}$, and at the same time the contribution given by $BaCO_3$ and CeO_2 significantly increased. The molar fractions of Zr and Y (x1, x2) were refined under the constraint that x1 + x2 = 1. The best refinement of the experimental data was obtained for x1 = 0.8 and x2 = 0.2. The refined results are summarized in Tables 3.3 and 3.4 for diffractograms (b) and (c), respectively.

Table 3.3. Structural refinement factors; lattice parameters, unit cell volume and quantities of BCZY541, CeO_2 and $BaCO_3$ five days after the high pressure conductivity test. The profile R value (R_p = 3.22), weighted profile R-factor (R_{wp} = 5.76) and Goodness of fit (GOF = 1.79) values were obtained.

	$BaCe_{0.5}Zr_{0.4}Y_{0.1}O_{3-d}$	CeO_2	$BaCO_3$
a(Å)	6.4934(21)	5.406(1)	5.3092(12)
b(Å)	5.9334(18)		8.915(2)
c(Å)	8.902(3)		6.4393(15)
V($Å^3$)	342.99	157.983	304.77
mol %	70	16	14

Table 3.4. Structural refinement factors; lattice parameters, unit cell volume and quantities of BCZY541, CeO_2 and $BaCO_3$ one month after the high pressure conductivity test. The profile R value (R_p = 2.65), weighted profile R-factor (R_{wp} = 4.75) and Goodness of fit (GOF = 1.79) values were obtained.

	$BaZr_{0.8}Y_{0.2}O_{3-\delta}$	CeO_2	$BaCO_3$
a(Å)	4.220(6)	5.407(1)	5.3094(11)
b(Å)			8.9145(19)
c(Å)			6.4395(14)
V($Å^3$)	75.1674	158.07	304.77
mol %	34	42	24

The XRDs of BCZY541 and BCZY262 which have been exposed to high partial pressure of steam (sequence 1 and following ramp down of pH_2O) and then preserved in air for five months are presented in Fig. 3.4. BCZY541 deteriorated less compared to the cell which was also tested in high partial pressure of CO_2. Indeed, the surface of the cell started to be covered by a thin white layer more than one month after the test ended. The bulk of the cell remained black and its X-ray diffractogram did not exhibit any secondary phases. In addition only few micro fractures were visible on the external area of the pellet. XRD was undertaken on the outermost surface of the cell after mechanical polishing in order to remove traces of the platinum electrode. Few minor peaks from 2θ equal to 24 ^{0} until 50 ^{0} were observed, which are related to $BaCO_3$. The main perovskite phase with orthorhombic symmetry is still notable. There is no evidence of crystalline forms of $Ba(OH)_2$.

BCZY262 did not display any visually observable mechanical change after the high pressure test. XRD was undertaken on powder obtained by grinding a piece of the bulk of the cell. Traces of $BaCO_3$ were observed by XRD (Fig. 3.4 pattern (b)) for 2θ equal to 24 ^{0}.

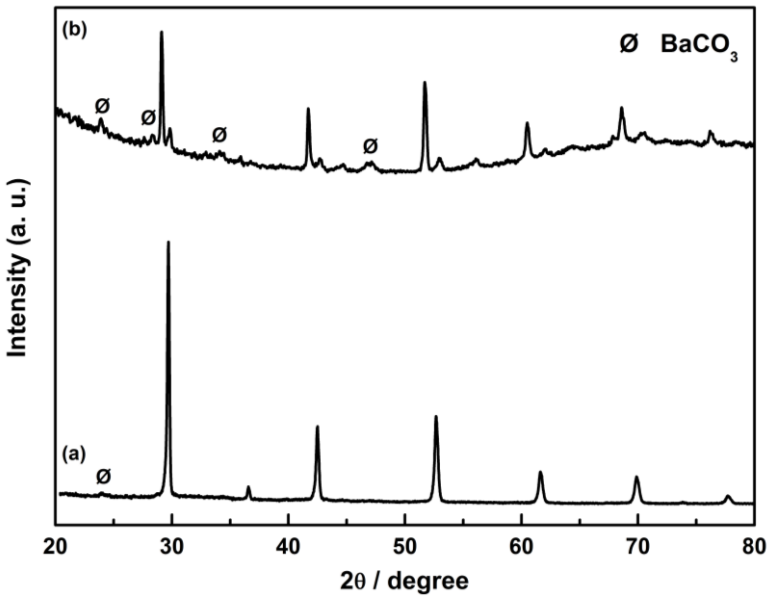

Fig. 3.4. XRDs for the pellets of (a) BCZY262 and (b) BCZY541 five months after the sequence 1 of the conductivity test at 240 °C. Both samples are characterized by formation of minor phases of $BaCO_3$ (Ø).

3.3.2 SEM

SEM images of BZY91 were taken on the fractured area situated near the free surface of the tested and untested pellets. The pristine pellet had a density of 90 % relative to the theoretical density. Both sintered specimens were made from the same powder batch. The morphology of fractured surfaces of BZY91 before and after the conductivity test does not show any significant change (Fig. 3.5 a) and 3.5 b)). This is in agreement with XRD results, showing stable phase composition.

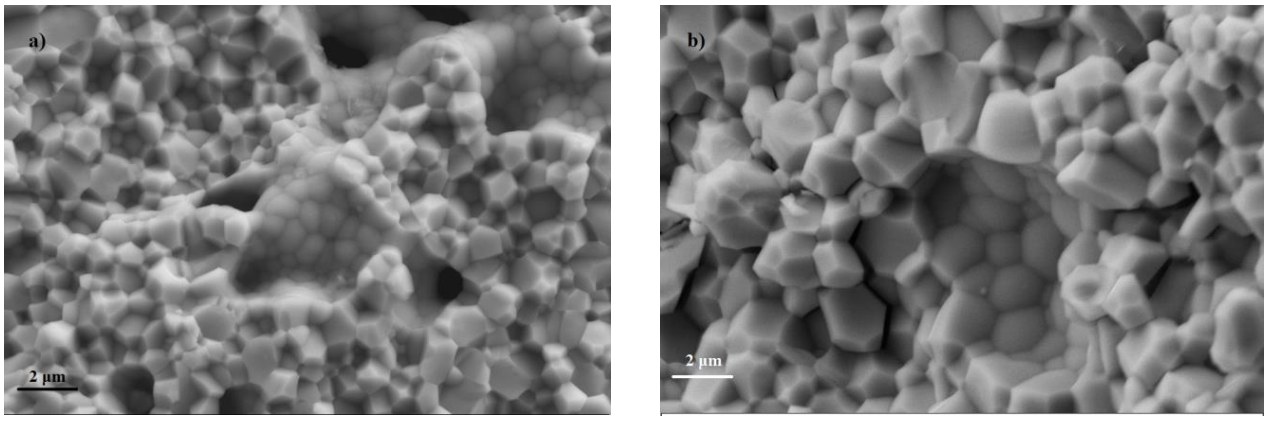

Fig.3.5. SEM micrograph of the fractured cross section of: a) freshly sintered BZY91 cell and b) BZY91 cell tested under the 2 sequences of the high pressure conductivity test.

The BCZY541 sintered pellets had a density of 98 % and SEM images indicated that a drastic structural change occurred during and after exposure to elevated partial pressures of H_2O and CO_2. The fractured cross section of the freshly sintered BCZY541 is shown in Fig. 3.6a. It is possible to notice a bigger grain size in BCZY541 than in the pellet with no cerium. Fig. 3.6b displays a SEM micrograph of the fractured surface of the BCZY541 cell one month after the conductivity test. The grain boundaries have changed. An about 500 nm thick layer has formed, composed of thin needle like grains, which cover the BCZY541 grains. This phenomenon has been detected uniformly over the entire cross section of the pellet.

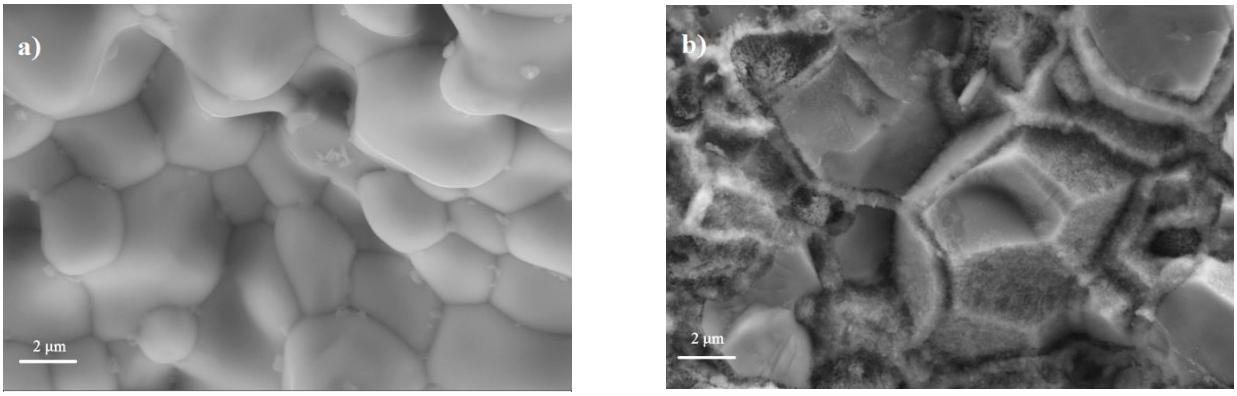

Fig. 3.6. SEM micrograph of the fractured cross section of: a) freshly sintered BCZY541 pellet and b) BCZY541 after exposure to elevated partial pressures of H_2O and CO_2 during the conductivity test.

Fig. 3.7 shows a SEM micrograph of the fractured surface of the BCZY541 specimen after elevated pH_2O exposure during the first sequence of the conductivity test and five months exposure to ambient conditions. The pellet was fractured just before carrying out the SEM analysis. Only the outermost layer (~300 µm) of the cell started to be affected by the hydration and carbonation reaction, while the interior of the pellet did not change its original morphology as observed by analysing the inner layers of the cell. The BCZY541 grains in Fig. 3.7 are only partially covered by needle like grains as opposed to what was seen previously in Fig.3. 6b.

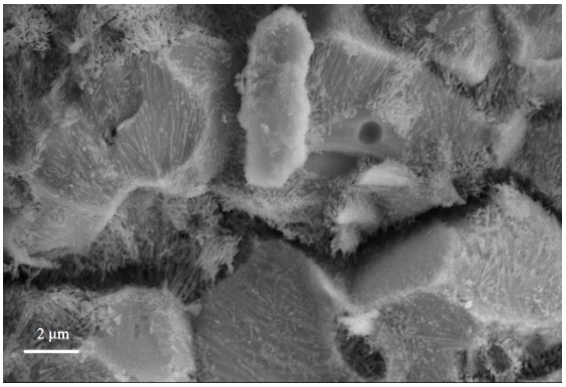

Fig. 3.7. SEM micrograph of the fractured cross section of the BCZY541 pellet after exposure to high steam partial pressure during conductivity testing (sequence 1).

No substantial difference in the grain morphology can be noticed when comparing the micrographs of the BCZY262 before and one month after the two sequences (Fig. 3.8a and Fig. 3.8b). On the other hand micro-fractures have been observed close to the external surface of the tested cell. These pellets had a density of 93%. Both images have been taken in the inner part of the fractured cells.

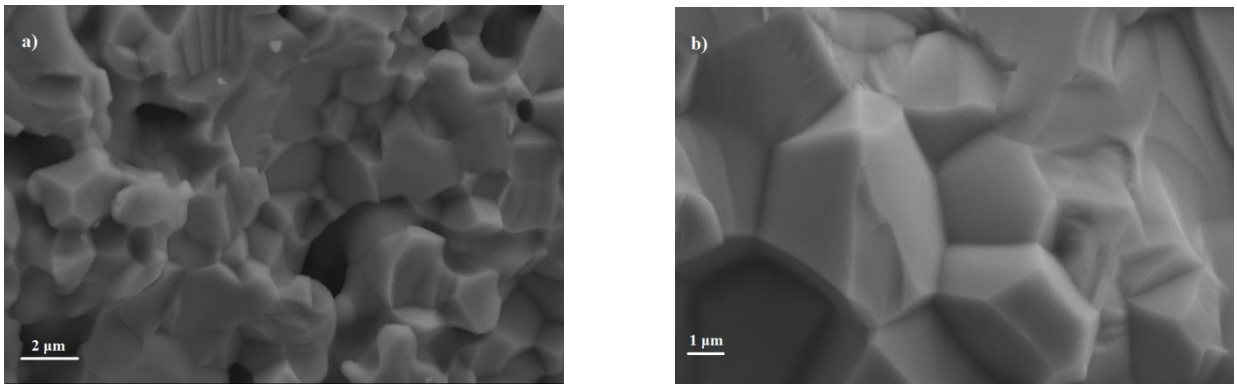

Fig. 3.8. SEM micrograph of the fractured cross section of: a) just sintered BCZY262 cell and b) BCZY262 cell tested under the two sequences of the high partial pressure test. Note: the magnifications are different as indicated by the scale bars. These pellets had a density of 93%.

Conversely, the BCZY262 measured under high steam partial pressure, meaning until the end of sequence 1, showed the presence of particles (~500 nm) attached to the grain boundaries (Fig.3. 9). This phenomenon coupled with micro fractures has been observed across the entire cross section of the cell. Analogously to what done with BCZY541, the images have been taken five months after the test. In this case the density of BCZY262 tested in high partial pressure of steam was 85 %.

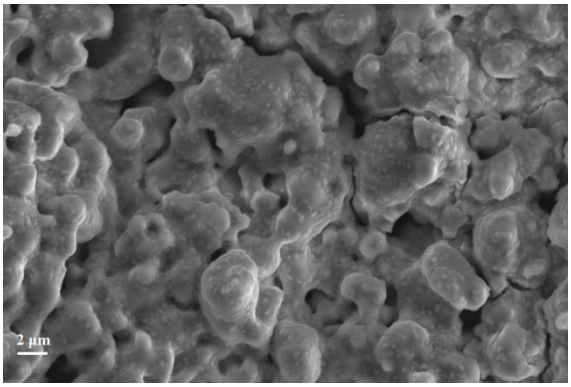

Fig. 3.9. SEM micrograph of the fractured cross section of the BCZY262 cell tested under high steam partial pressure. This pellet was only 85 % dense.

3.3.3 Conductivity measurements of BCZY

Fig. 3.10 shows one of the spectra of BCZY541 recorded at 240 ^{0}C with a pH_2O of 10 bar. The bulk and the grain boundary contributions are modelled by two (RQ) circuits in series and were analysed using the *brick layer model*[25]. The impedance of the Q element (constant phase element) is given by $Z_q = [Y_0(j\omega)^n]^{-1}$ and $0 < n < 1$[20]. The bulk resistance is determined from the high frequency semicircle (pseudocapacitance of $8 \cdot 10^{-10}$ F/cm^2), while the grain boundary resistance is deduced from the intermediate frequency semicircle (pseudocapacitance of $2.55 \cdot 10^{-8}$ F/ cm^2) and the electrodes contributions give rise to the two low frequency arcs (pseudocapacitance of 10^{-6} F/cm^2 and 10^{-4} F/cm^2). On all the BCZY541 impedance spectra it has been possible to distinguish the contribution of the bulk and of the grain boundary to the total electrolyte resistance.

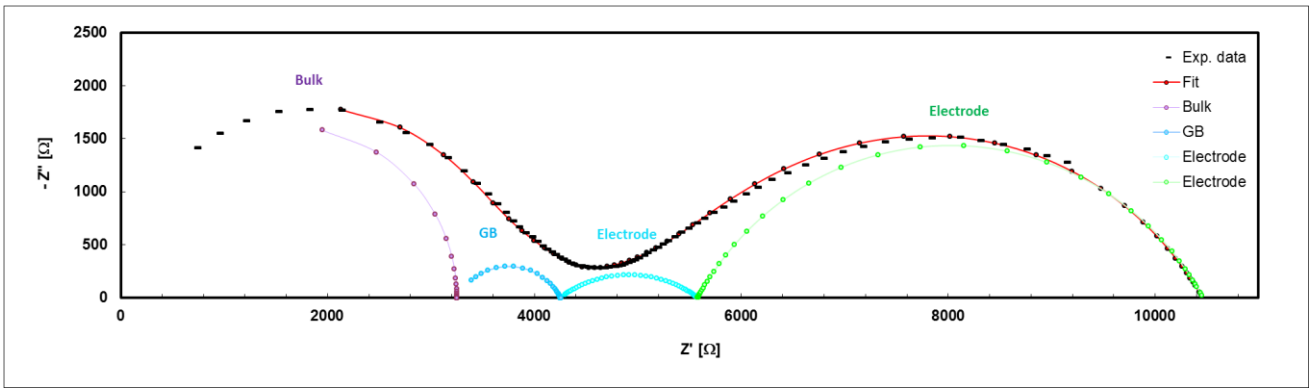

Fig. 3.10. Nyquist plot recorded for BCZY541 at 240 °C and Ptot = 50 bar, with a gas mixture of pH_2 = 2.5 bar, pH_2O = 10 bar and pN_2 = 37.5 bar.

It was possible to identify the contribution of the bulk and of the grain boundary on the impedance spectra acquired for the first three values of pH_2O for BCZY262 (i.e. 10 mbar, 2.5 bar and 5 bar) and for the last three values of pH_2O for BZY91 (i.e. 5 bar, 10 bar and 25 bar). For the remaining values of pH_2O, the ohmic resistance of BCZ262 and BZY91 cells was obtained by fitting the bulk

and grain boundary contributions with a single (RQ) semicircle in the high frequency part of the impedance spectra (pseudocapacitance of 10^{-9} F/ cm^2). The stray capacitance contribution has been subtracted from all the analysed impedance spectra[20]. The average error between fitted and measured data is less than 2%. As shown in Fig. 3.12, BCZY541 is characterized by an almost constant trend in total conductivity from 10 mbar ($8.5 \cdot 10^{-5}$ S/cm) to 10 bar of pH_2O ($1.1 \cdot 10^{-4}$ S/cm), followed by a sudden increase in conductivity by more than an order of magnitude with increasing steam content from 10 bar to 25 bar ($2 \cdot 10^{-3}$ S/cm). To confirm and understand this unexpected result, the conductivity test was repeated, recording impedance spectra during the last three hours of the flushing time (necessary to exchange once the gases in the autoclave between pH_2O of 10 bar and 25 bar), shown in Fig. 3.11b. Analogous trend in total conductivity was obtained.

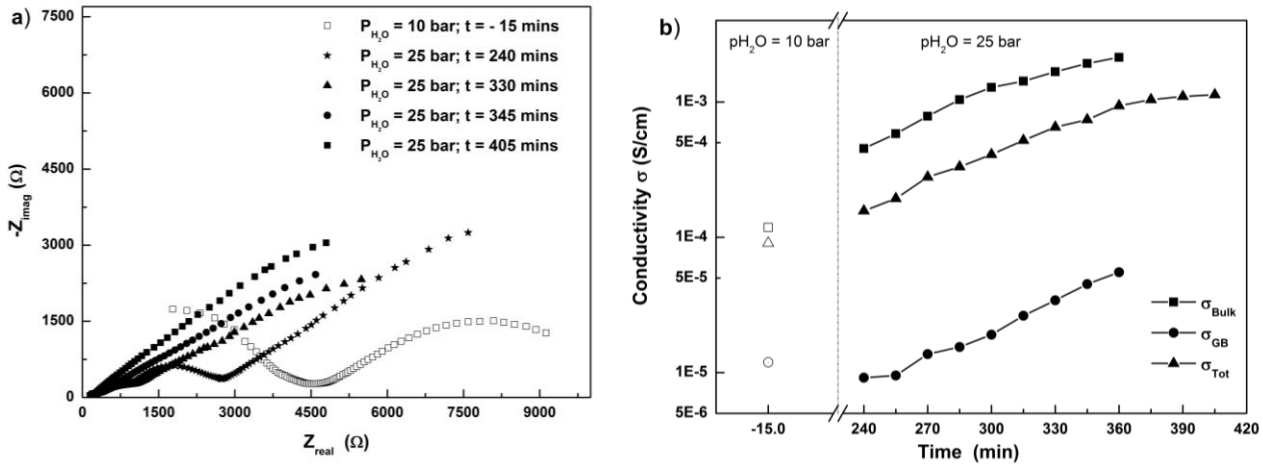

Fig. 3.11. **a)** Nyquist plots at different acquisition times and **b)** conductivity relaxation of the BCZY541 cell at 240 °C and Ptot = 50 bar, following the gas composition change from pH_2O = 10 bar (□), to pH_2O = 25 bar (■, ★, ▲, ●) in 5 vol.% H_2 in N_2.

In particular, the last recorded impedance spectra at pH_2O of 10 bar (t = - 15 minutes) and some of the spectra acquired during the last three hours of flushing at pH_2O = 25 bar are reported in Fig. 3.11a. Fig. 3.11b shows the corresponding bulk, specific grain boundary and total conductivity calculated from the spectra of Fig. 3.11a as a function of time. For the impedance measurements taken for t > 360 min it was not possible to separate the bulk and the grain boundary contribution from the total impedance. The first point for all the three curves in Fig. 3.11b refers to the last impedance spectra at pH_2O of 10 bar. Both the bulk and the specific grain boundary conductivity gradually increased by almost one order of magnitude during the three hours of measurements. The electrolyte resistivity approached equilibrium after t = 360 minutes as it reached a nearly constant value after that.

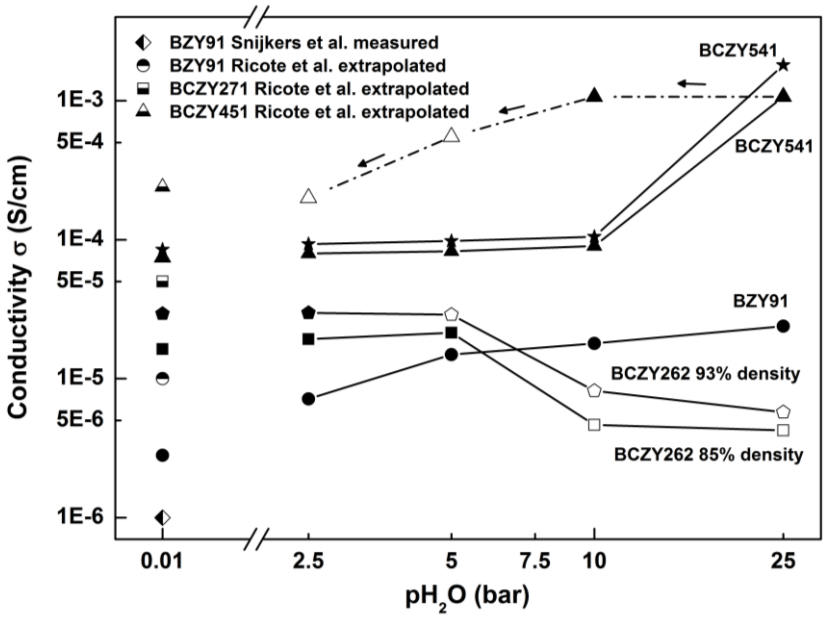

Fig. 3.12. Conductivity dependence on increasing pH_2O at 240 ^{0}C at 50 bar in a wet mixture of 5 vol.% H_2 in N_2 and during the ramp down phase for BCZY541 cell. Closed and open symbols are used to distinguish between equilibrated and non-equilibrated values, respectively. The total conductivity at 10 mbar for the three compounds is compared with extrapolated [26] and measured literature data[27].

The dependence of the conductivity of all the three electrolytes on H_2O partial pressure is shown in Fig. 3.12. The results obtained at 10 mbar of pH_2O are compared with extrapolated literature results of BCZY total conductivity, measured instead in a wet (pH_2O = 0.015 bar) mixture of 9% H_2 in N_2 at ambient pressure[26] and with one measured value of BZY91 tested in normal air with a relative humidity of 50% at room temperature[27]. The extrapolated conductivity values from Ricote *et al.* are higher due to differences in the macrostructure and in the density of the compounds. Conversely the conductivity of the measured BZY91 is lower due to the different sintering procedure which may lead to structural deviations. As expected, the conductivity increases with increasing content of cerium and the highest values of conductivity were obtained at elevated partial pressures of steam. In addition, BCZY541 was also tested during the ramp down phase of the steam partial pressure, as shown in Fig. 3.12. The hydration/dehydration process observed during the treatment in high pH_2O exhibited a strong hysteresis. The EIS spectra at pH_2O of 10 bar during the ramp down phase overlapped with those recorded at pH_2O = 25 bar along the last step of the sequence 1. The conductivity of BCZY541 did not change with time upon lowering pH_2O from 25 to 10 bar. For lower values of pH_2O, the conductivity started to decrease from 10^{-3} S/cm at pH_2O = 10 bar to $\approx 2 \cdot 10^{-4}$ S/cm at pH_2O = 2.5 bar. The impedance spectra acquired at pH_2O of 5 and 2.5 bar did not reach equilibrium over the three hours holding time, therefore indicated with open symbols in Fig. 3.12. The two Ce containing perovskites (BCZY262 & BCZY541) showed opposite trends in conductivity at the highest values of water vapour partial pressure (pH_2O = 5 to 25 bar), whereas for pH_2O < 5 bar the conductivity was pH_2O-independent for both compositions. Indeed BCZY262

showed a drastic conductivity drop of almost one order of magnitude with increasing steam content from 5 bar to 25 bar. Also in this case, the bulk conductivity was almost constant during the first three values of pH_2O ($\sigma_{bulk} \approx 1.6 \cdot 10^{-4}$ S/cm), while the specific grain boundary conductivity increased from $\approx 8.5 \cdot 10^{-6}$ S/cm at pH_2O of 10 mbar to $1.8 \cdot 10^{-5}$ S/cm at pH_2O of 5 bar. With further increasing steam partial pressure the conductivity decreased and kept deteriorating. Furthermore, the impedance spectra did not stabilize over the three hours holding time. This effect was reproduced for a separate BCZY262 cell tested only under sequence 1 and then during the ramp down phase, where the conductivity kept decreasing until it reached a value of almost 10^{-7} S/cm at $pH_2O$of 5 bar. The conductivity of BZY91 increased by almost one order of magnitude upon increasing steam partial pressure from 10 mbar to 25 bar. Analysis of the EIS data suggests that the hydration process affected to a higher extent the specific grain boundary conductivity of BZY91, which increased gradually from $\approx 8.7 \cdot 10^{-7}$ S/cm at pH_2O of 5 bar to $4.46 \cdot 10^{-6}$ S/cm at pH_2O of 25 bar. The bulk conductivity contribution, instead, was almost independent on pH_2O ($\sigma_{bulk} \approx 9.5 \cdot 10^{-5}$ S/cm).

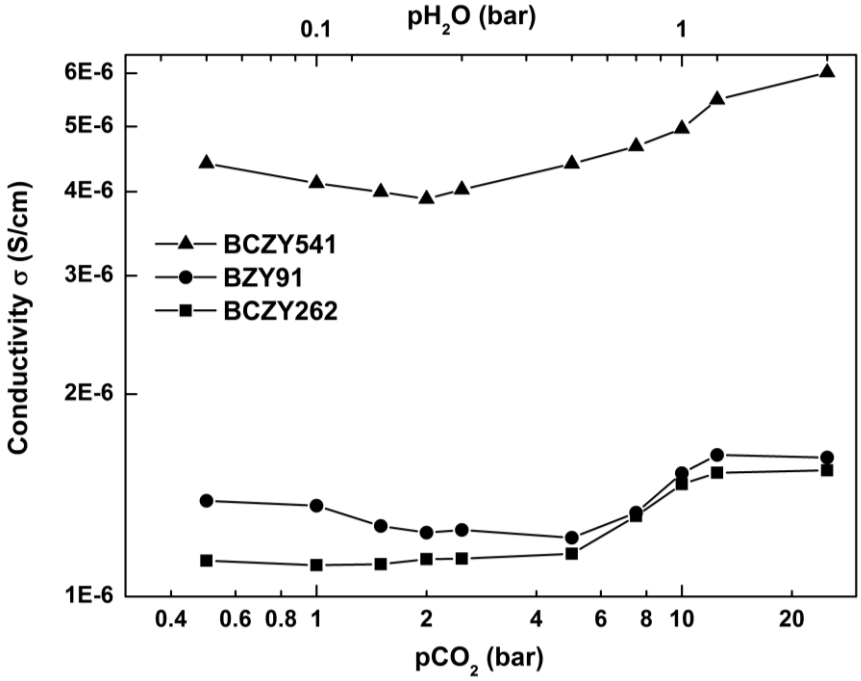

Fig. 3.13. Conductivity dependence on pCO_2 at 240 ^{0}C in the gas mixture: 50 vol.% CO_2, 5 vol.% H_2 and 45 vol.% N_2. The total pressure was between 1 bar and 50 bar. The pH_2O values given on top are the calculated equilibrium values of the gas mixture at 240 ^{0}C.

The dependence of the conductivity on CO_2 partial pressure is shown in Fig. 3.13. The conductivity values obtained in carbon dioxide rich atmospheres for the Ce containing samples, BCZY262 and BCZY541, were lower compared to the results obtained and plotted in Fig. 3.12. Nonetheless, it is interesting to observe that for low pCO_2 the conductivity is almost constant or slightly decreasing and then for higher pCO_2 (≈ 4 bar) it shows a mild increasing tendency.

3.4 Discussion

The modification of the grain boundaries in all three compounds, along with microstructural changes may help rationalize the conductivity trends in high partial pressure of steam.

The bulk conductivity of BCZY262 and BCZY541 was only weakly influenced by the increasing concentration of steam in the range between 10 mbar to 5 bar. This is in line with the anticipated complete hydration of BCZY at 240 °C and pH_2O > 10 mbar[28]. Upon increasing pH_2O from 10 bar to 25 bar the conductivity of BCZY541 increased by one order of magnitude showing values around $2 \cdot 10^{-3}$ S/cm (at 240 °C), which is usually obtained for the same compound at 400 °C in a steam partial pressure of 0.03 bar[14]. To the best of the authors' knowledge this is the highest proton conductivity ever reported for polycrystalline ceramic proton conductors at such low temperatures. Both the grain and the grain boundary conductivity increased by almost one order of magnitude (Fig. 3.11b). A possible explanation may be related to the modification of the phase composition and microstructure at the grain boundaries (as observed in SEM images of the tested cell), and in particular to the formation of a continuous conductive secondary phase around the grains. Structural refinement of the diffractogram of the tested cell revealed that the molar ratio between $BaCO_3$ (24 mol%) and CeO_2 (42 mol%) deviates substantially from unity (Table 3.4), which supports the hypothesis of formation of an amorphous secondary phase at the grain boundaries containing Ba, e.g. $Ba(OH)_2$, not detectable by XRD. In case of no amorphous $Ba(OH)_2$, the molar ratio of $BaCO_3$ to CeO_2, should indeed be almost equal to one, because barium zirconate cannot tolerate a large A-site non-stoichiometry[29]. In particular, a maximum 5% barium deficiency is the threshold for the formation of a single phase perovskite[30]. Why the grain bulk conductivity also increases with almost a decade is less clear, but probably a significant higher amount of H_2O has been absorbed – probably irreversibly forming $Ba(OH)_2$ - into both the grain boundaries and part of the grain bulk. This might also explain the continued reactivity of BCZY541 to $BaCO_3$ in air at room temperature (Fig. 3.3).

Surprisingly, the conductivity of BCZY262 above 5 bar of steam partial pressure decreased by almost one order of magnitude. This is believed to arise due to the formation of micro fractures on the outer layers of the electrolyte in the cell, as observed by SEM. Small amount of secondary phases (such as BaY_2NiO_5, $Ba(OH)_2$, CeO_2) and modification of the grain boundaries may be the cause of mechanical stress that lead to the formation of micro fractures. This hypothesis is further supported by the observed no equilibrated impedance spectra acquired at 10 and 25 bar of pH_2O and the irreversible deterioration of the conductivity of the tested cell when ramping down the pH_2O. In fact the conductivity was further deteriorated by about one order of magnitude after ramping down the pH_2O. In BCZY262 a minor amount of the secondary phase BaY_2NiO_5 has been observed, as also reported in a previous study[26]. According to Ricote *et al.*, the nickel added as sintering aid and the presence of this impurity phase did not influence the conductivity or the chemical and mechanical stability at atmospheric pressure. The crack formation in BCZY262 and not in BCZY541 might be due to a much slower diffusion of H_2O into BCZY262 than into BCZY541. This might make stresses in the surface region temporally bigger in BCZY262 and cause the crack formation.

Finally, the conductivity of BZY91 gradually increased from $2.8 \cdot 10^{-6}$ S/cm to $2.4 \cdot 10^{-5}$ S/cm with increasing pH_2O in the range 10 mbar – 25 bar. BZY91 is expected to be fully hydrated already at the beginning of the conductivity measurements at 240 °C and 10 mbar[28]. In particular, the grain boundary resistivity decreased for pH_2O > 10 mbar, resulting in the increase of the total conductivity, as the bulk conductivity was almost independent of pH_2O. The observed conductivity increase may again be explained by a change in the grain boundary structure under elevated pH_2O, influencing the space charge potential, and thereby the concentration of charge carriers in the space charge region. The positively charged grain boundary core of BZY91 is understood to be the cause of the well-known high grain boundary resistivity[31]. An analogous increase of BZY91 grain boundary conductivity was registered at 250 °C by Bohn and Schober [32] when increasing the pH_2O from 10^{-7} bar to $4 \cdot 10^{-2}$ bar, due to incorporation of H_2O. It should be noticed though that this pH_2O range is below that required for full hydration of the BZY91 bulk [28]. The compound with the highest Ce loading (BCZY541) exhibited under all conditions the largest conductivity values. This can be explained partly by the increasing grain boundary proton mobility with increasing Ce content[14] and partly by the difference in grain size between the oxides containing only Zr and the ones doped also with Ce. In particular, BCZY541 has grain sizes in the range 2 – 6 μm, while BZY91 around 1 μm. A bigger grain size leads to a smaller number of grain boundaries that the current must pass, ensuring a higher conductivity[33].

The impedance spectra of BCZY541 were stable during the three hours measuring time at each pH_2O of sequence 1. On the contrary, the conductivity values obtained along the ramp down phase of pH_2O were not equilibrated and were almost one order of magnitude higher compared to the results acquired while increasing the pH_2O in sequence 1. This aspect may be related to slower kinetics of the dehydration process at 240 °C.

The conductivity values obtained during sequence 2 were lower than the results obtained in high partial pressure of steam (Fig. 3.13). It is interesting to note that all three compounds exhibit a common trend as a function of carbon dioxide partial pressure. The conductivity is almost constant until 3 bar, then starts to increase and finally stabilizes at the highest CO_2 partial pressures. Residual amounts of steam from sequence 1 may still be present during sequence 2, due to the short transition time between the two sequences and the slow release of steam upon dehydration of the compounds. Moreover, platinum is active for the water gas shift reaction [34]. According to thermodynamic calculations performed with FactSage[35], the equilibrium partial pressure of steam with the gas mixture present at the electrode is 0.05 bar at 1 bar total pressure. Assuming ideal gas behaviour, the equilibrium partial pressure of steam increases gradually from 0.1 to 2.5 bar when the total pressure is raised from 2 to 50 bar, respectively. The increase in conductivity observed for pCO_2 > 3 bar can thus be related to the increasing amount of water vapour formed at the Pt electrodes.

The hydration process under high pH_2O and the exposure in elevated pCO_2 affected not only the conductivity, but also the chemical stability of the compounds containing Ce. Indeed, BCZY541 demonstrated chemical modifications after exposure to high pH_2O and pCO_2. After an additional five days exposure to ambient conditions, the orthorhombic symmetry of the BCZY541 was still present, but its decomposition had started to take place with the formation of $BaCO_3$ and CeO_2. The two former phases are then predominant in the same compound analysed one month after the high

pressure test, while the orthorhombic perovskite phase changed into a cubic perovskite phase, having an approximate composition of $BaZr_{0.8}Y_{0.2}O_{3-\delta}$. Indeed, $BaCeO_3$ and $BaCeO_3$ – based proton conductors can react with H_2O and decompose according to Eq. 3.3.

$$BaCe_{1-x}RE_xO_{3-d} + H_2O \rightarrow Ba(OH)_2 + Ce_{1-x}RE_xO_{2-\gamma} \quad \text{(Eq. 3.3)}$$

In the above equations RE is a rare-earth ion. Virkar *et al.*[13] studied the kinetics of this decomposition on 20 mol % Gd-doped $BaCeO_3$ and they observed formation of $Ba(OH)_2$ after seven days of exposure to 1 bar of water vapour at 200°C. Moreover $Ba(OH)_2$ can further react in the presence of CO_2, according to:

$$Ba(OH)_2 + CO_2 \rightarrow BaCO_3 + H_2O \quad \text{(Eq. 3.4)}$$

Therefore Eq. 3.3 and 3.4 can be used to explain the chemical decomposition process that occurred to BCZY compounds. $Ba(OH)_2$ may form under high partial pressure of steam, but when exposed to highly pressurized carbon dioxide (up to 25 bar of pCO_2) it reacts and transforms to $BaCO_3$. The time of exposure to atmospheric air after test influenced the decomposition of BCZY541 and the consequent formation of $BaCO_3$, CeO_2 and phase transition from orthorhombic to cubic. This is also confirmed by the SEM images taken on the tested cell which showed a clear difference in the grain boundaries compared to the pristine BCZY541 structure (Fig. 3.6b).

The results obtained for BCZY541 exposed only to high partial pressure of steam have been important to understand the kinetics of decomposition of the BCZY541 consequent to the sequence 1 and sequence 2. Indeed, formation of minor amounts of $BaCO_3$ has been observed in the diffraction pattern of BCZY541 taken on the external surface of the cell after the test in high partial pressure of steam (Fig. 3.4). Also, its SEM images have revealed the presence of different microstructures at the grain boundary, mainly on the outermost part of the cell. So the $Ba(OH)_2$, which could be formed near the surface of the BCZY541 electrolyte, may react with CO_2 when it gets in contact with air. The decomposition rate is nevertheless quite sluggish. Within five months after the test a thin white layer appeared on the external surface of the pellet and micro fractures started to affect its mechanical stability. Therefore a prolonged exposure time in high pCO_2 is necessary to affect the chemical stability of BCZY541. Conversely, BCZY541 did not show any chemical instability at 1 bar of CO_2 and T > 700 °C. In spite of the thermodynamic instability of $BaCeO_3$–based compounds in CO_2 containing atmospheres, sintered powders of $BaCeO_3$–based ceramics can be kinetically stable due to strong kinetic limitations in the range of temperatures between 500 and 850 °C.

The scarcely dense (85 %) cell of BCZY262 tested only in high partial pressure of steam showed the presence of particles (~500 nm) attached to the grain boundaries across the entire cross section of the cell (Fig. 3.9). Minor amounts of $BaCO_3$ were also observed by XRD (Fig. 3.4a). The formation of $Ba(OH)_2$ could be enhanced due to the higher porosity of the sample, which provoked fractures along the cell. On the other hand, the more dense BCZY262 (93 % density) tested also in elevated partial pressure of CO_2 exhibited micro fractures on the external layers but no modification in its inner morphology, suggesting that high density can kinetically limit the chemical

decomposition of the $BaCeO_3$–based proton conductors. Indeed, Colomban *et al.* observed that scarcely dense perovskite proton conductors can be affected by crumbling and chemical decomposition when treated under pH_2O = 80 bar and temperature of 300 °C.[36]
The addition of more zirconium into barium cerate played an important role concerning the chemical and mechanical stability. Indeed, BZY91 maintained its morphology and structure during the entire test confirming that the higher basicity of the cerates facilitates the reaction with an acidic gas as CO_2 and therefore the chemical instability.

3.5 Conclusions

The conductivity of $BaCe_{1-x-y}Zr_yY_xO_{3-\delta}$ (x; y) = (0.1; 0.9) – (0.1; 0.4) – (0.2; 0.6) electrolytes was studied in wet H_2/N_2 and in $CO_2/H_2/N_2$ gas mixtures at a total pressure of up to 50 bar and temperature of 240 °C for the first time. The highest conductivity values were found for the compound with the highest Ce content (BCZY541), reaching a value of 10^{-3} S/cm at pH_2O = 25 bar. The conductivity of BCZY262 and BCZY541 was almost constant in the pH_2O range from 10 mbar to 5 bar and 10 bar, respectively, in line with the anticipated fully hydrated state of the compounds under these conditions. Increasing pH_2O from 10 to 25 bar resulted in almost one order of magnitude increase in the conductivity of BCZY541. On the contrary, the conductivity of BCZY262 dropped irreversibly by one order of magnitude for pH_2O > 5 bar. These changes are most probably associated with the formation of $Ba(OH)_2$ at the grain boundaries, which enhances the conducting properties of the BCZY541 cell but decreases the conductivity of the BCZY262 cell due to the formation of micro-cracks. The resistivity of BZY91 gradually decreased by increasing pH_2O, which was found to arise from a positive influence of increasing pH_2O to the grain boundary conductivity of BZY91.
BCZY541 would have been the best electrolyte candidate because of its low resistivity in high pH_2O even at temperatures as low as 240 °C. However, the instability in the acidic CO_2 gas atmosphere hinders practical application for carbon dioxide reduction at high pressure. Nevertheless, BCZY541 is an interesting electrolyte candidate for elevated pressure steam electrolysis, but long term stability needs to be explored. BZY91 appears to be a suitable electrolyte for CO_2 reduction thanks to its stability and promising conductivity, which may possibly be further improved by additives that decrease the grain boundary resistivity.

References

[1] C. Graves, S.D. Ebbesen, M. Mogensen, K.S. Lackner, *Renewable and Sustainable Energy Reviews*, 15 (2011) 1-23.

[2] H. Iwahara, T. Esaka, H. Uchida and N. Maeda, *Solid State Ionics*, 3-4 (1981) 359.

[3] H. Iwahara, H. Uchida, I. Yamasaki, *International Journal of Hydrogen Energy*, 12 (2) (1987) 73-77.

[4] W. Grover Coors, *Journal of the Electrochemical Society*, 151 (7) (2004) A994-A997.

[5] K. Xie, Y. Zhang, G. Meng, J. T. S. Irvine, *Journal of Material Chemistry*, 21 (2011) 195.

[6] H. Iwahara, T. Esaka, H. Uchida and N. Maeda, *Solid State Ionics*, 11 (1983) 109-115.

[7] N. Bonanos, K.S. Knight and B. Ellis, *Solid State Ionics*, 79 (1995) 161-170.

[8] T. Norby, "Perovskite oxide for solid oxide fuel cells", Chapter 11, ed. T. Ishihara, 2009, Springer, p. 238.

[9] W. Grover Coors, *Solid State Ionics*, 178 (2007) 481 - 485.

[10] P. A. Stuart, T. Unno, J. A. Kilner, S. J. Skinner, *Solid State Ionics*, 179 (2008) 1120.

[11] N. Zakowsky, S. Williamson and John T. S. Irvine, *Solid State Ionics*, 176 (2006) 3019 – 3026.

[12] C. W. Tanner and A. V. Virkar, *Journal of the Electrochemical Society*, 143 (1996) 1386 – 1389.

[13] S. V. Bhide and A. V. Virkar, *Journal of the Electrochemical Society*, 146 (1999) 2038 – 2044. S.

[14] E. Fabbri, A. D. Epifanio, E.D. Bartolomeo, S. Licoccia, E. Traversa, *Solid State Ionics*, 179 (2008) 558.

[15] K.D. Kreuer, *Solid State Ionics*, 97 (1997) 1.

[16] K.H. Ryu, S.M. Haile, *Solid State Ionics*, 125 (1999) 355.

[17] J. Tong, D. Clark, L. Bernau, M. Sanders and R. O'Hayre, *Journal of Material Chemistry*, 20 (2010) 6333 – 6341.

[18]A. Lapina, C. Chatzichristodoulou, P. Holtappels and M. Mogensen, *Journal of the Electrochemical Society*, 161 (2014) 833-837.

[19] C. Chatzichristodoulou, F. Allebrod, and M. Mogensen, *Review of Scientific Instruments*, 84 (2013) 054101.

[20] J.R. MacDonald, E. Barsoukov, Impedance Spectroscopy, J. R. MacDonald, Wiley and Sons, Second Edition, New York, 2005.

[21] X. Ma, J. Dai, H. Zhang, D. E. Reisner, *Surface & Coatings Technology*, 200 (2005) 1252 – 1258.

[22] R.D. Shannon, *Acta Crystallographica* A 32 (1976) 751.

[23] S. Barison, M. Battagliarin, T. Cavallin, L. Doubova, M. Fabrizio, C. Mortalo', S. Boldrini, L. Malavasi and R. Gerbasi, *Journal of Materials Chemistry*, 18 (2008) 5120-5128

[24] S. Ricote, N. Bonanos, *Solid State Ionics*, 181 (2010) 694-700.

[25] J. R. Macdonald, *Solid State Ionics*, 13 (1984) 147.

[26] S. Ricote, N. Bonanos, A. Manerbino, W.G. Coors, *International Journal of Hydrogen Energy*, 37 (2012) 7954-7961.

[27] F.M.M. Snijkers, A. Buekenhoudt, J. Cooymans, J.J. Luyten, *Scripta Materialia*, 50 (5) (2004) 655.

[28] K.D. Kreuer, *Annual Review of Material Research*, 33 (2003) 333.

[29] D. Shima and S. M. Haile, *Solid State Ionics*, 97 (1997) 443.

[30] G. Ma, H. Matsumoto and H. Iwahara, *Solid State Ionics*, 122 (1999) 237.

[31] M. Shirpour, PhD thesis, University of Stuttgart, Germany (2011).

[32] H. G. Bohn and T. Schober, *Journal of the American Ceramic Society*, 83 (4) (2000) 768.

[33] S. M. Haile, G. Staneff, K.H. Ryu, *Journal of Material Science*, 36 (2001) 1149.

[34] I. Yati, M. Ridwan, G. E. Jeang, Y. Lee, J. Choi, C.W. Yoon, D. J. Suh and J. Ha, *Catalysis Communications*, 56 (2014) 11 -16.

[35] C. W. Bale, P. Chartrand, S.A. Degterov, G. Eriksson, K. Hack, R.B. Mahfoud, J. Melançon, A.D. Pelton, S. Petersen, Calphad 26 (2) (2002), 189 – 228.

[36] P. Colomban, O. Zaafrani, A. Slodczyk, *Membranes*, 2 (2012) 493 – 509.

Chapter 4
Hydrothermal synthesis and characerization of K-doped $BaZr_{0.9}Y_{0.1}O_{3-\delta}$.

Chapter 3 presented results for a number of proton conducting materials, i.e. $BaCe_{1-x-y}Zr_yY_xO_{3-\delta}$, tested at elevated partial pressures of water vapour and of carbon dioxide and intermediate temperatures (T = 240 °C). Only $BaCe_{0.5}Zr_{0.4}Y_{0.1}O_{3-\delta}$ exhibited conductivity above 10^{-3} S/cm in high steam partial pressure (pH_2O = 25 bar), but it did not show a sufficient chemical stability during the after tests analysis. Indeed, $BaZr_{0.9}Y_{0.1}O_{3-\delta}$ appeared to be a suitable electrolyte for CO_2 reduction thanks to its stability and promising conductivity. Therefore, it was decided that additional studies on yttrium doped barium zirconate based electrolyte were needed to improve the conductivity in high steam and carbon dioxide pressures at intermediate temperature. The main aim with this study was to evaluate if potassium doped BZY91 was suitable as an electrolyte material for an electrochemical cell for CO_2 reduction at intermediate temperature and high pressure.

Abstract

The effect of doping potassium on the A-site of $BaZr_{0.9}Y_{0.1}O_{3-\delta}$ for application as intermediate temperature proton conductor was studied. Potassium doped barium zirconates was synthesized for the first time by the hydrothermal method. The synthesis procedures of $Ba_{1-x}K_xZr_{0.9}Y_{0.1}O_{3-\delta}$ and its characterization by X-ray diffraction, inductively coupled plasma and scanning electron microscopy are presented. The sintering conditions were improved by adding 1 wt% ZnO during material synthesis. The actual composition of the electrolyte tested was $Ba_{0.92}K_{0.08}Zr_{0.9}Y_{0.1}O_{3-\delta}$. The conductivity was measured via electrochemical impedance spectroscopy as a function of temperature (from 790 °C to 275°C) and steam partial pressure (from pH_2O < 0.001 atm to 0.1 atm) in N_2/H_2O gas mixtures. $Ba_{0.92}K_{0.08}Zr_{0.9}Y_{0.1}O_{3-\delta}$ exhibited higher total conductivity compared to $BaZr_{0.9}Y_{0.1}O_{3-\delta}$ sintered by solid state reactive sintering. In particular, it showed higher specific grain boundary conductivity when the grain boundary and bulk contributions were distinguished by the analysis of the low temperature spectra. In addition, the conductivity of $Ba_{0.92}K_{0.08}Zr_{0.9}Y_{0.1}O_{3-\delta}$ exhibited higher values compared to $BaZr_{0.9}Y_{0.1}O_{3-\delta}$ during two consecutive sequences in high steam partial pressure and in high carbon dioxide pressure, as described in the previous chapter. After the test, X-ray diffraction and scanning electron microscopy analysis confirmed the chemical stability in high pressure of H_2O and of CO_2 for barium zirconate based materials.

4.1 Introduction

Electrolysers based on proton conducting electrolytes are of great interest for their potential to operate at intermediate temperatures (400-600 °C), compared to solid oxide electrolytic cells (SOECs) which require operating temperatures above 700 °C. Reducing the operating temperature can limit degradation phenomena, interfacial reactions among components, thermal expansion mismatches and can lower production costs. Proton conductors are viable electrolytes at intermediate temperatures because protons migrate more easily than oxygen ions at 400-600 °C, thus conductivities are high enough for technical applications. High protonic conduction is observed for several perovskite-type oxides, such as doped $BaCeO_3$, $BaZrO_3$, $SrCeO_3$ and $SrZrO_3$ [1, 2]. These materials are termed high-temperature proton conductors (HTPCs), because their working temperatures (400 – 600 °C) are noticeably higher than the working temperatures of proton conducting polymers (~100 °C). HTPCs have been considered very attractive electrolyte materials for high-temperature steam electrolysis[3] and more recently for reforming of hydrocarbon fuels by steam permeation in a protonic ceramic fuel cell[4]. One interesting application for proton conducting electrochemical cells operating at intermediate temperatures is electrochemical reduction of carbon dioxide at the cathode of a proton conducting solid oxide electrolyser based on $BaCe_{0.5}Zr_{0.3}Y_{0.16}Zn_{0.04}O_{3-\delta}$ electrolyte[5]. In Chapter 3 it has been already described the main properties and characteristics of high protonic conductivity and low chemical stability in CO_2 atmosphere of these perovskite-type oxides. Among HTPCs, barium zirconate-based electrolytes have been extensively studied because of their good chemical stability[6], also confirmed by the analysis in high pCO_2, as studied in Chapter 3. In particular, K. Kreuer[7] reported that $BaZr_{0.8}Y_{0.2}O_{3-\delta}$ is characterized by very high proton conductivity in the grain bulk, which results to be higher than that of the best oxygen ion conductors below 600 °C. On the other hand, Y-doped $BaZrO_3$ exhibits poor sinterability, small grain size (on average 1μm or smaller)[8] and high grain boundary resistivity[7]. Different approaches have been studied to reduce its grain boundary surface, *i.e.* annealing at high temperature[9] or using sintering aids[10]. In particular, the solid-state reacting sintering technique is often the method used to prepare dense Y-doped $BaZrO_3$ ceramics[11]. It consists of a single firing step of the precursors pressed in a pellet shape with the addition of small amount of sintering aid which helps perovskite phase formation and sintering. Recently, solution-based synthesis route such as the hydrothermal method have been developed to produce perovskite materials with controlled morphology and narrow particle-size distribution, in particular for $BaCeO_3$ and $BaZrO_3$[12,13]. Hydrothermal synthesis is a process for crystallizing materials directly from aqueous solution by suitable control of temperature (> 25 °C) and pressure (> 1 atm) and precursor composition. Typically, a mixture of the reactants and a solvent is heated to the established reaction temperature in a sealed vessel under autogenous pressure. The product formation follows defined steps. Firstly, the reactants start to dissolve having a significantly higher solubility under hydrothermal conditions; secondly, the nuclei begin to form in the solution and finally they grow to larger crystallites by incorporation of material from the solution. All these sequential steps may be influenced by a large variety of reaction parameters like temperature, pressure, nature of the solvent, reaction time and surfactants. This allows control over the size, crystal morphology and stoichiometry of the resulting particles[14].

In this work, K- doped $BaZr_{0.9}Y_{0.1}O_{3-\delta}$ powders were synthesized by the hydrothermal technique in order to improve its sinterability and decrease the grain boundary surface. Pellets were sintered in air at different elevated temperature. In particular, it was used a solution of KOH in the aqueous solution both to control its pH but also to dope Ba with an alkali metal as potassium and therefore to affect the basicity of the perovskite. Indeed, the proton conductivity is reported in the literature to be enhanced by the basicity of the constituent oxides due to its influence on water uptake capacity[15, 16]. Introducing highly basic alkaline oxides should improve the conductivity, as also proved by A. S. Patnaik et al[17]. Potassium was chosen as dopant due to its matching ionic radius to that of Ba for a coordination number of twelve[18]. The aim of the work described in this chapter is to evaluate the structural and conductivity properties of $Ba_{1-x}K_xZr_{0.9}Y_{0.1}O_{3-\delta}$ and comparing its performance with that of $BaZr_{0.9}Y_{0.1}O_{3-\delta}$ (BZY91) and of $BaCe_{0.5}Zr_{0.4}Y_{0.1}O_{3-\delta}$ (BCZY541) obtained by solid state reactive sintering method. In addition, the objective is also to examine the conductivity and chemical stability of K- doped $BaZr_{0.9}Y_{0.1}O_{3-\delta}$ as possible electrolytes for the electrochemical conversion of CO_2 at elevated partial pressures of water vapour and of carbon dioxide and intermediate temperatures (T = 240 °C).

4.2 Experimental

4.2.1 Synthesis procedure

K-doped $BaZr_{0.9}Y_{0.1}O_{3-\delta}$ powders were synthesized by the hydrothermal method. In this process, a solution was prepared by dissolving barium nitrate (0.01 mol $Ba(NO_3)_2$ – Aldrich, 99.999 %) in distilled water. In parallel, zirconium nitrate (0.009 mol $ZrO(NO_3)_2$ – Aldrich, 99 %) and yttrium nitrate hexahydrate (0.001 mol $Y(NO_3)_3 \cdot 6H_2O$ – Aldrich, 99.8%) were dissolved in distilled water, obtaining a second solution. The two solutions were mixed and stirred in equal ratio to obtain a homogenized solution. Furthermore an aqueous solution of potassium hydroxide (16 M KOH – Alfa Aesar) was prepared separately. Equal volume of the homogenized solution and of the potassium hydroxide solution were blended and placed in a stainless steel autoclave with a Teflon-liner. Subsequently, the autoclave was heated to a temperature of 200 °C and maintained at this temperature for 72 h. After cooling, the obtained paste was washed with distilled water and ethanol and then dried at 80 °C. 1 wt% of ZnO (Aldrich, 99%) was added to the product as sintering additive and manually ground to obtain powder. To another batch was instead added 1 wt% of NiO (Alfa Aesar, 99% (metal basis)). Then the powder was used to produce cylindrical pellets, by uniaxial pressing under a pressure of 60 MPa. The pellets were placed on alumina crucibles covered by calcined 8YSZ and with an alumina cap to prevent contamination and to minimize the loss of potassium. The pellets were sintered in air at 1550 °C for 10 or 24 h or at 1670 °C for 10 h. The obtained pellets of $Ba_{1-x}K_xZr_{0.9}Y_{0.1}O_{3-\delta}$ sintered at 1550 °C for 10 h had a diameter of 8 ± 0.1 mm and a thickness of 2 ± 0.1 mm after polishing.

4.2.2 Characterization

XRD measurements were undertaken in air using a Bruker D8 X-Ray Diffractometer (Bruker-Siemens, Germany), using Cu Kα radiation, with an acceleration voltage of 40 kV and a filament current of 40 mA. TOPAS 3.0 software was used to perform Rietveld refinement of the lattice parameters and unit cell volume of the sintered compounds. SEM imaging was carried out on as synthesized powders and on fractured cross sections of tested and pristine pellets using a Zeiss SUPRA SEM. The powders and the fractured pellets were attached to a metal sample holder through a piece of carbon tape, and the pellets were also coated with a thin layer of carbon using a sputter coater. As synthesized powders of $Ba_{1-x}K_xZr_{0.9}Y_{0.1}O_{3-\delta}$ and sintered pellets were analyzed using inductively coupled plasma mass spectroscopy (ICP-MS, X Series II, Thermo Fisher Scientific, Waltham, MA) to evaluate their chemical compositions. Experiments were performed multiple times on a sample from the same batch to determine the uncertainty of the concentration of the cations. The relative density of the materials was determined from the mass and geometrical dimensions of the pellets, using 6 g/cm^3 as theoretical density.

4.2.3 Conductivity

Cells for conductivity measurements were made by painting Pt-ink (Ferro 308a, fritless, platelets) on each side of the electrolyte disc samples and fired in air at 900 °C for 4 h. The electrical conductivity of the materials was measured at 1 atm using a single atmosphere setup, which is constructed so that diluted H_2 in N_2 (maximum 9% H_2), N_2, air and O_2 and various humidity (from pH_2O < 0.001 atm up to pH_2O = 0.2 atm) can be used and mixed at temperatures ranging from room temperature up to 850 °C. Four samples can be tested in each test. For comparison, BCZY541 and BZY91 cells sintered by solid state reactive sintering and a BKZY91 cell were tested simultaneously. A Solartron 1260 frequency response analyzer (Solartron Analytical, UK) was used for electrochemical impedance spectroscopy (EIS) measurements. EIS measurements were performed using an AC signal with amplitude of 350 mV over a frequency range of 1 MHz down to 0.1 Hz. Data analysis was carried out using ZSimpWin 3.21 and Elchemea Analytical. During testing the material was exposed to a constant flux of gas (N_2), either dry (gases from the gas system, estimated pH_2O < 0.001 atm) or humidified (pH_2O = 0.038 or 0.1 atm). A humidity cycle was done at each temperature investigated, from 790 °C to 275 °C. The gas was humidified by bubbling through a water bottle at controlled temperature prior to entering the experimental setup. A pellet of $Ba_{1-x}K_xZr_{0.9}Y_{0.1}O_{3-\delta}$ was also tested in the high pressure electrochemical test station (limit: 100 bar, 300 °C), explained in detail elsewhere[19]. The AC conductivity test was performed along two consecutive sequences in high pH_2O and in high pCO_2, both at temperatures of 240 °C, as already described in Chapter 3.

4.3 Results

4.3.1 XRD and SEM characterization

After the sintering at high temperatures, the oxides showed a different mechanical stability dependent on the addition of 1 wt% of ZnO or NiO as sintering additive. The obtained pellets containing 1 wt% of NiO displayed formation of cracks on the surface and curved shape when increasing the sintering temperature to 1670 °C. Instead, pellets containing 1 wt% ZnO did not show mechanical instability and therefore they were the only to be analysed and tested. The relative density of the material before testing, estimated by the geometrical dimensions and mass of the pellets, was in the 87-90 % range for the samples sintered at 1550 °C for 10 h, and 93 % for the ones sintered at 1550 °C for 24 h. The pellets sintered at 1670 °C for 10 h showed the highest density, i.e. was in the 95-97 % range. ICP-MS analysis was used to verify the actual chemical composition of the as synthesized powders and the pellets sintered at various temperatures with respect to the nominal composition. In Table 4.1 are listed the mol% of the cations in the oxide (Ba, K, Zr, Y and Zn). Low concentration of potassium (ca. 0.5 mol %) was measured for pellets sintered at 1550 °C for 24 h. Only for the as synthesized powders and for the pellets sintered at 1550 °C for 10 h it was possible to detect significant presence of potassium. Therefore the final composition obtained after the sintering is $Ba_{0.92}K_{0.08}Zr_{0.9}Y_{0.1}O_{3-\delta}$. This composition is from now on referred to as BKZY91.

Table 4.1. Chemical compositions determined for $Ba_{1-x}K_xZr_{0.9}Y_{0.1}O_{3-\delta}$ powders and pellets sintered at 1550 °C for 10 h by ICP-MS.

Synthesized powder	**Sintered pellet at 1550 ^{0}C – 10 h**
Ba = 49.23 $\pm$ 2.46 mol%	Ba = 45.31 $\pm$ 2.25 mol%
Zr = 39.65 $\pm$ 1.98 mol%	Zr = 45.65 $\pm$ 2.28 mol%
Y = 7.26 $\pm$ 0.72 mol%	Y = 5.6 $\pm$ 0.28 mol%
K = 3.8 $\pm$ 0.38 mol %	K = 3.4 $\pm$ 0.34 mol%
	Zn = 0.048 mol%

Fig.4.1 shows the XRDs of the as synthesized powders of BKZY91 (pattern (a)) and of the powders obtained by grounding the sintered pellet of BKZY91 (pattern (b)). For comparison, also the powders of solid state reactive sintered BZY91 were investigated (pattern (c)). The sintering procedure of BZY91 is described in Chapter 3. In particular, 0.1 wt% of Si powder (Standard reference material 640c – NIST)[20] was added to both BKZY91 and BZY91 sintered powders, to determine accurately the lattice parameter of both compounds.

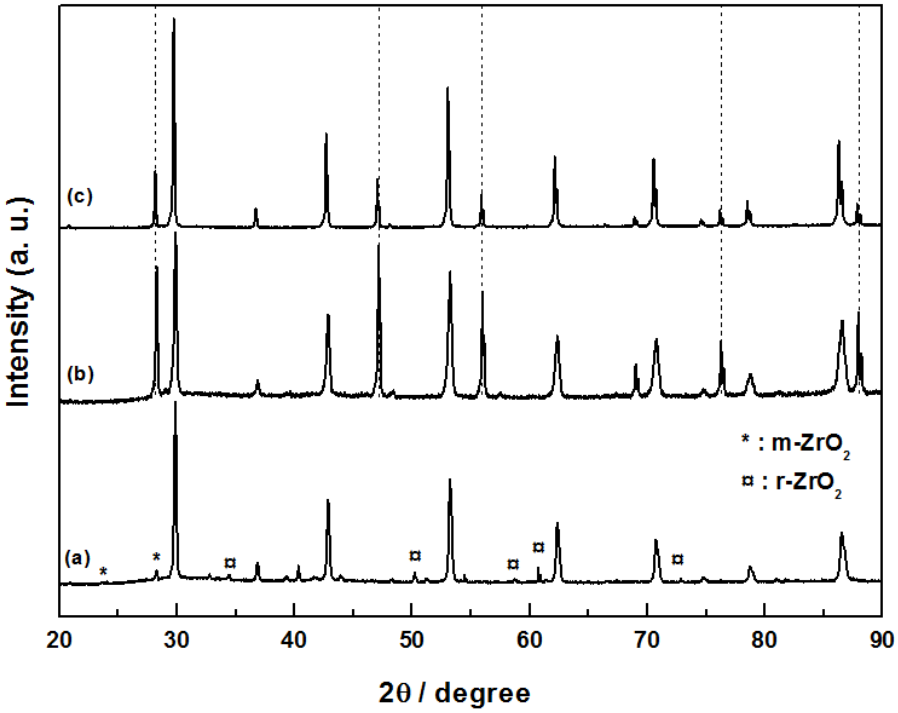

Fig.4.1. XRD of (a) as synthesized powders of BKZY91 prepared by hydrothermal synthesis, (b) powders of BKZY91 sintered at 1550 °C with added 0.1 wt% of Si powder as standard reference and (c) powders of BZY91 sintered by solid state reactive sintering at 1550 °C with added 0.1 wt% of Si powder as standard reference. The Si peaks position is indicated with dotted lines in pattern b) and c).

As synthesized powders of BKZY91 contains a detectable amount of extraneous peaks of monoclinic ZrO_2 (PDF 37-1484) and rhombohedral ZrO_2 (PDF 37-0031) and other second phases which could not be indexed. These peaks belonging to minor phases disappeared after sintering at 1550 °C for 10 h. In the patterns (b) and (c), dotted lines indicate the positions of Si peaks used as standard reference material, having a lattice parameter of 5.4311946 ± 0.0000092 Å[20], as indicated in the NIST certification. The lattice symmetry was found to be cubic (Pm-3m) for both BKZY91 and BZY91. The lattice parameter of BKZY91 (4.2048764 ± 0.0000915 Å) is close to the value estimated for BZY91 (4.208105 ± 0.0000678 Å). Both values were obtained from the XRD analysis done with the Rietveld refinement method. The XRD patterns of the sintered samples after electrochemical testing at ambient pressure are presented in Figure 4.2. Platinum peaks are due to platinum paint traces (contained in the electrodes) left on the material after testing. No extraneous peaks were detected.

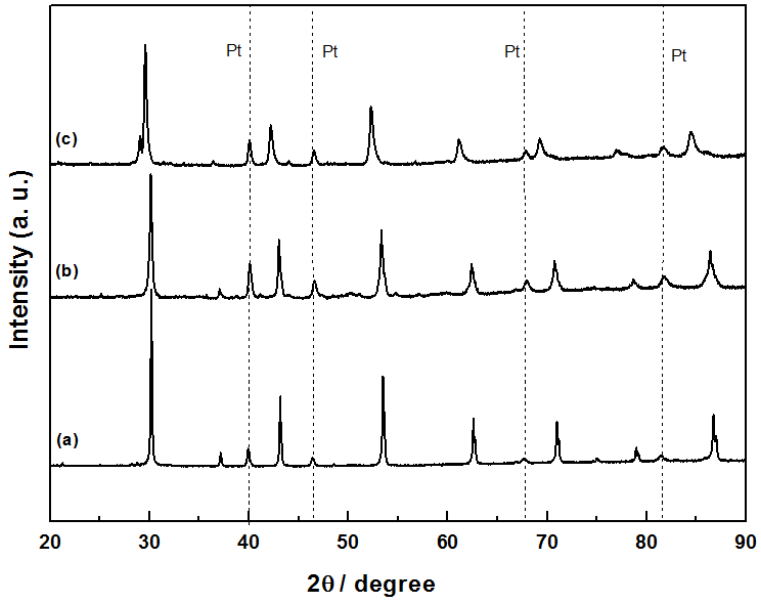

Fig.4.2. XRDs for the pellets of (a) BZY91, (b) BKZY91, (c) BCZY541 after the conductivity test in ambient pressure and various temperatures. Platinum peaks are due to traces of Pt paint (contained in the electrodes) left on the material after testing.

Furthermore, XRD analysis was undertaken on the electrolytes of the BKZY91 and BZY91 cells after the high pressure conductivity tests (sequences 1 and 2) were completed (Fig. 4.3).

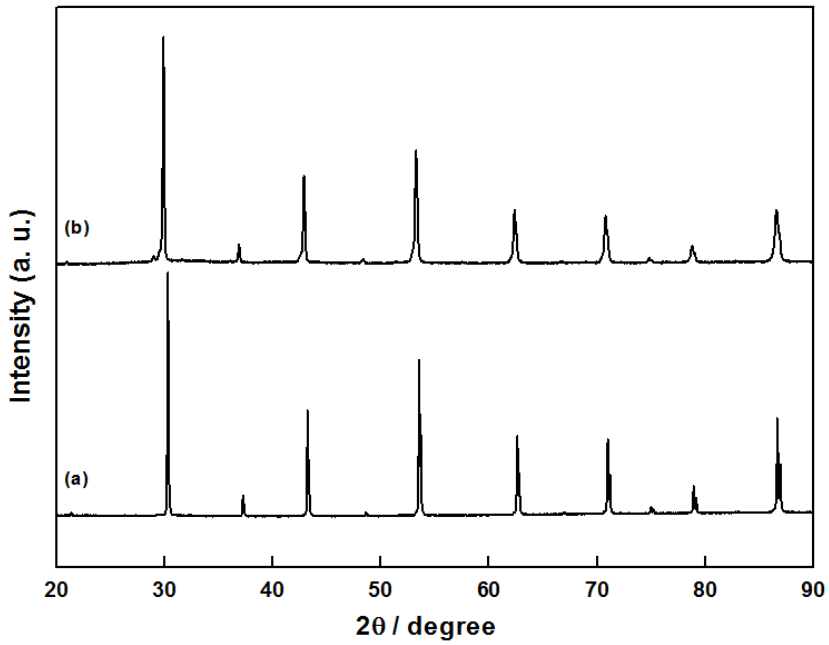

Fig. 4.3. XRDs for the pellets of (a) BZY91 and (b) BKZY91 after the conductivity test at 240 °C in high pH_2O and in high pCO_2.

SEM image of the as synthesized powders of BKZY91 is reported in Fig. 4.4. It is possible to observe that all particles appear uniform both in shape (decaoctahedron and spherical) and size (~ 2 to 3 μm in diameter). Furthermore, SEM images of BKZY91 sintered pellet were taken on the fractured area situated near the free surface of the untested and tested under high pressure pellets. Both sintered specimens were made from the same powder batch. The morphology of fractured surfaces of BKZY91 before and after the conductivity test under high pressure does not show any significant change (Fig. 4.5 a) and 4.5 b)). This is in agreement with XRD results, showing stable phase composition. For comparison, in Chapter 3 are reported SEM images taken on fractured area of BZY91 cell sintered by solid state reactive method. The estimated grain size of BKZY91 is on average around 2 to 3 μm, while BZY91 around 1 μm.

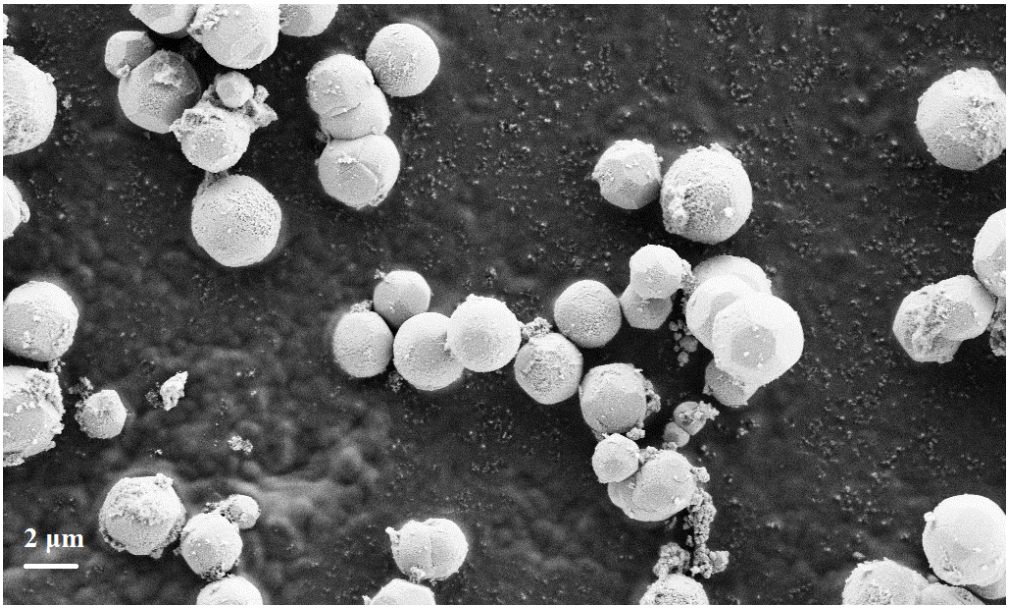

Fig. 4.4. SEM images of as synthesized $Ba_{1-x}K_xZr_{0.9}Y_{0.1}O_{3-\delta}$ powders obtained a hydrothermal treatment of 72 h at 200 °C.

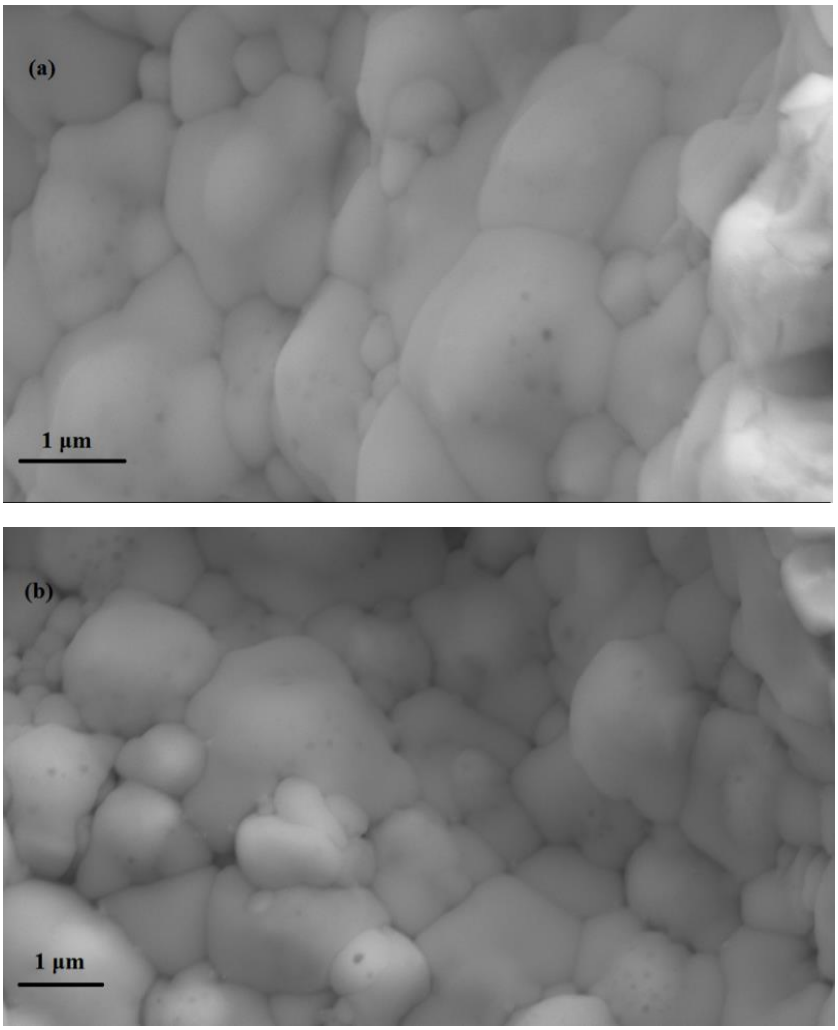

Fig. 4.5. SEM micrograph of the fractured cross section of: a) freshly sintered BKZY91 cell and b) BKZY91 cell tested under the 2 sequences of the high pressure conductivity test.

4.3.2 Conductivity characterization

EIS measurements were used to evaluate the electrical conductivity of BKZY91 electrolyte in comparison with BCZY541 and BZY91 electrolytes both in "dry" N_2 (pH_2O < 0.001 atm) and in wet N_2 (pH_2O = 0.1 atm). The EIS measurements were acquired in the 780-275 °C temperature range. A comparison between the AC spectra of BKZY91 and BZY91 recorded at 275 °C in wet N_2 (pH_2O = 0.1 atm) is presented in Fig. 4.6, showing a bigger contribution of the grain boundary of BZY91 to the total resistance. The bulk and the grain boundary contributions are modelled by two (RQ) circuits in series and were analysed using the *brick layer model*[21]. The bulk and the specific grain boundary conductivity are given by equations (4.1) and (4.2), respectively. δ and D are the grain boundary thickness and grain size respectively. *L* represents the thickness of the sample and *A* its surface, while R and C are the resistance and the capacitance of the bulk or of the grain boundary. The abbreviations *GB* and *sp.* indicates the grain boundary and specific terms. Since the dielectric properties of the bulk and grain boundaries are often similar, the specific grain-boundary conductivity of the specimens is calculated using equation (4.3).

$$\sigma_{bulk} = \frac{L}{A}\frac{1}{R_{bulk}} \tag{4.1}$$

$$\sigma_{sp.GB} = \frac{L}{A}\frac{1}{R_{GB}}\frac{\delta}{D} \tag{4.2}$$

$$\sigma_{sp.GB} = \frac{L}{A}\frac{1}{R_{GB}}\frac{C_{bulk}}{C_{GB}} \tag{4.3}$$

The impedance of the Q element (constant phase element) is given by $Z_q = [Y_0(j\omega)^n]^{-1}$ and $0 < n < 1$[22]. The bulk resistance is determined from the high frequency semicircle (pseudocapacitance of $8.5 \cdot 10^{-10}$ F/cm^2 for BKZY91 and $4.04 \cdot 10^{-10}$ F/cm^2 for BZY91), while the grain boundary resistance is deduced from the intermediate frequency semicircle (pseudocapacitance of ca. $8 \cdot 10^{-8}$ F/ cm^2 for BKZY91 and $5.5 \cdot 10^{-8}$ F/ cm^2 for BZY91) and the electrodes contributions give rise to the two low frequency arcs (pseudocapacitance of 10^{-6} F/cm^2 and 10^{-4} F/cm^2).

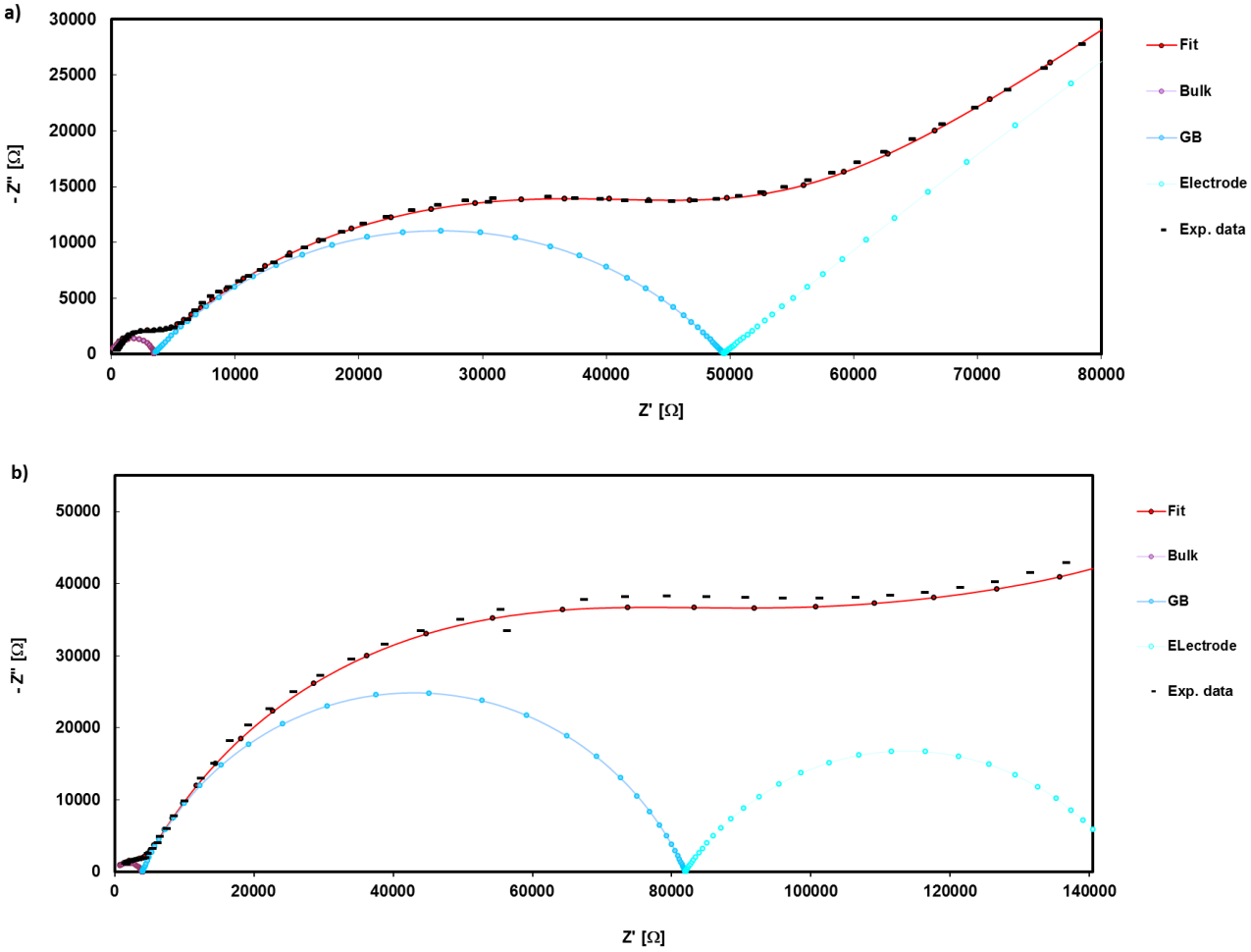

Fig.4.6. Nyquist plots recorded at 275 °C in wet N_2, pH_2O = 0.1 atm for (a) BKZY91 and (b) BZY91.

On all the BKZY91, BZY91 and BCZY541 impedance spectra recorded at 275 °C it has been possible to distinguish the contribution of the bulk and of the grain boundary to the total electrolyte resistance. The bulk contribution, instead, could not be clearly separated from the impedance spectra at 440 °C for all the three electrolytes, probably covered by the response from grain boundary. The dependence of the bulk, specific grain boundary and total conductivity as a function of time and pH_2O for both BKZY91 and BZY91 at 275 °C is shown in Fig. 4.7.

It can be noticed that the bulk conductivity values increased from $9.8 \cdot 10^{-5}$ S/cm to $1.2 \cdot 10^{-4}$ S/cm and from $8.5 \cdot 10^{-5}$ S/cm to $1 \cdot 10^{-4}$ S/cm for BKZY91 and BZY91 respectively, when increasing the pH_2O from $pH_2O < 0.001$ atm to $pH_2O = 0.1$ atm. The σ_{bulk} for both electrolytes is higher than that for the specific grain boundary. Therefore the total conductivity was dominated by grain boundary at 275 °C. In particular, the specific grain boundary conductivity increased from $4.8 \cdot 10^{-8}$ S/cm to $9.2 \cdot 10^{-8}$ S/cm and from $1.2 \cdot 10^{-8}$ S/cm to $4 \cdot 10^{-8}$ S/cm for BKZY91 and BZY91 respectively, when increasing the pH_2O from $pH_2O < 0.001$ atm to $pH_2O = 0.1$ atm. So the grain boundary conductivity of BKZY91 was higher compared to BZY91 along all the hydration process. The conductivity values obtained during the dehydration process were slightly higher if compared with the initial one at $pH_2O < 0.001$ atm.

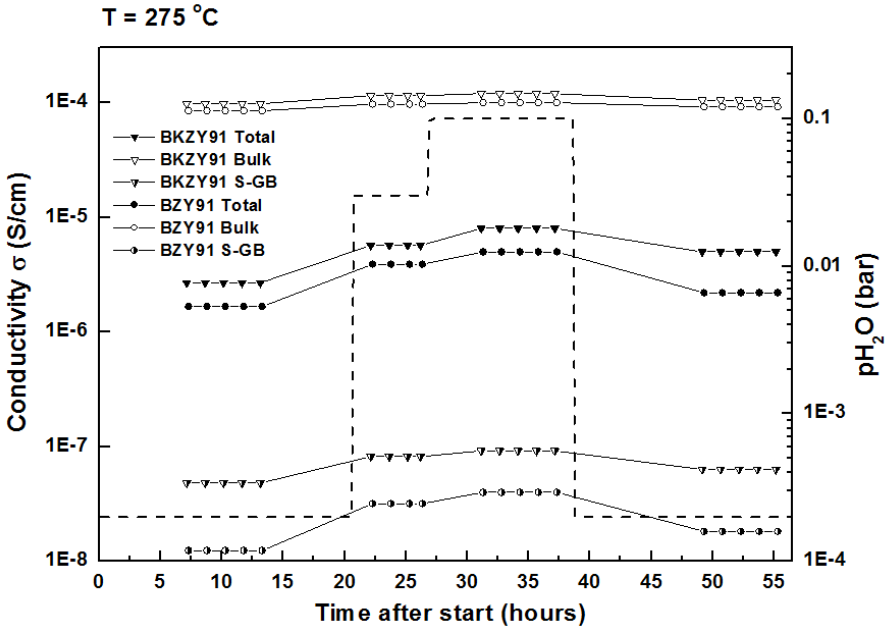

Fig. 4.7. Conductivity dependence curves of the bulk, specific grain boundary and total as a function of time at 275 °C in N_2 under varying pH_2O.

Fig. 4.8 shows the dependence of the total conductivity on different pH_2O at 440 °C for BCZY541, BZY91 and BKZY91. As expected from literature, the total conductivity is the highest for the electrolyte containing cerium. The conductivity upon exposure to wet atmosphere increased both at 440 °C and also at 275 °C (as can be seen in Figures 4.7 and 4.8). All the materials, including BCZY541, show the similar behavior upon changes of pH_2O.

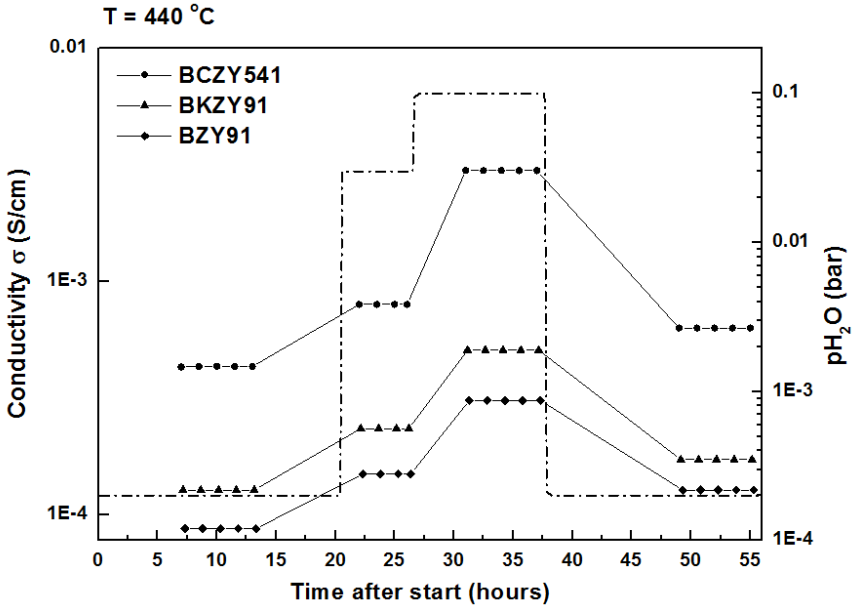

Fig. 4.8. Total conductivity of BZY91, BKZY91, BCZY541 as a function of time at 440 °C in N_2 under varying pH_2O.

Fig. 4.9 (a) and 9 (b) show the Arrhenius plot of total conductivity for the three oxides as a function of temperature for $pH_2O < 0.001$ atm and at $pH_2O = 0.1$ atm, respectively.

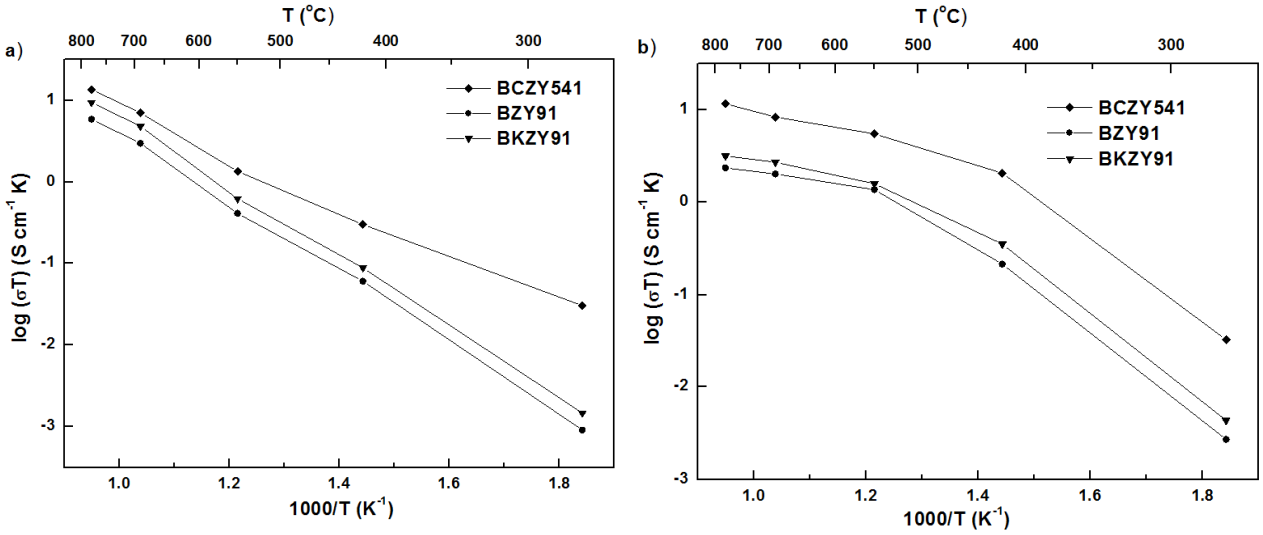

Fig. 4.9. Total conductivity of BZY91, BKZY91 and BCZY541 as a function of temperature in: a) dry N_2 ($pH_2O < 0.001$ atm) and b) wet N_2 $pH_2O = 0.1$ atm.

The total conductivity, in both atmospheres, was higher for BCZY541 and BKZY91 reported better values compared to BZY91, but lower than the compound containing cerium. The difference in conductivity was more pronounced for lower temperatures and for higher pH_2O, indicating proton conduction. Fig. 4.10 provides an overview of the trends in conductivity for both BKZY91 and BZY91 for $pH_2O < 0.001$ atm and at $pH_2O = 0.1$ atm, together with some conductivity values extrapolated from the data recorded at 300 – 700 °C by X.Xu et al.[23] and by A.S. Patnaik et al.[17] for analogous proton conductors.

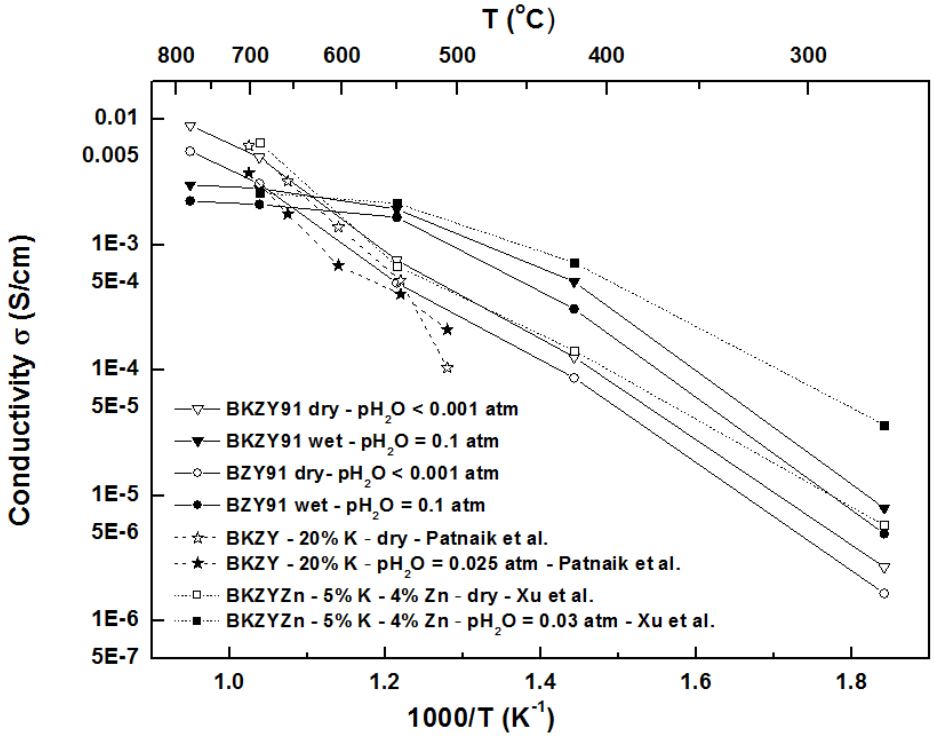

Fig. 4.10. Total conductivity of BZY91, BKZY91 as a function of temperature in dry N_2 (pH_2O < 0.001 atm) and wet N_2 (pH_2O = 0.1 atm). For comparison are reported data measured by X.Xu et al.[23] on a $Ba_{0.95}K_{0.05}Zr_{0.85}Y_{0.11}\ Zn_{0.04}O_{3-\delta}$ cell, and by A.S. Patnaik et al.[17] on a $Ba_{0.8}K_{0.2}Zr_{0.9}Y_{0.1}O_{3-\delta}$ cell.

The dependence of the bulk, specific grain boundary and total conductivity of BKZY91 on high partial pressure of H_2O at 240 °C is shown in Fig. 4.11. It was possible to identify the contribution of the bulk and of the grain boundary on the impedance spectra acquired for the last four values of pH_2O for BKZY91 (i.e. from 2.5 bar to 25 bar). For comparison, are reported also the conductivity data achieved by BZY91 electrolyte cell, as already presented in Chapter 3. In agreement with the results obtained by BZY91, the total conductivity increased by almost one order of magnitude upon increasing steam partial pressure from 10 mbar to 25 bar. Analysis of the EIS data suggests that the hydration process affected to a higher extent the specific grain boundary conductivity of BKZY91, which increased gradually from ≈ 1.1 $\cdot 10^{-6}$ S/cm at pH_2O of 2.5 bar to $5 \cdot 10^{-6}$ S/cm at pH_2O of 25 bar. The bulk conductivity contribution, instead, was almost independent on pH_2O ($\sigma_{bulk} \approx 2.4 \cdot 10^{-4}$ S/cm). A difference between the two electrolytes was observed for the grain boundary conductivity, in particular for lower pH_2O, i.e. at pH_2O of 5 bar. The bulk contribution of BKZY91 was two times higher than that obtained by BZY91 ($\sigma_{bulk} \approx 1.05 \cdot 10^{-4}$ S/cm).

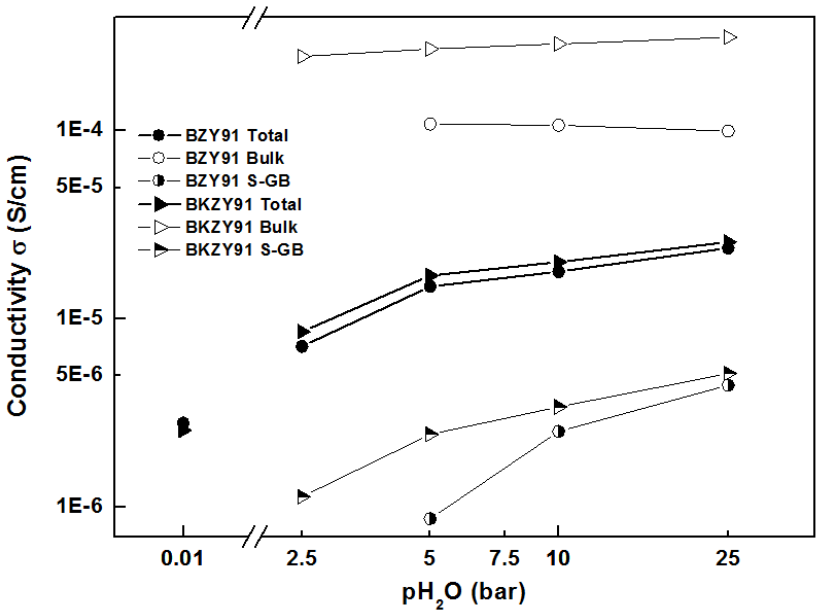

Fig. 4.11. Bulk, specific grain boundary and total conductivity dependence curves on increasing pH_2O at 240 ^0C at 50 bar in a wet mixture of 5 vol.% H_2 in N_2 and during the ramp down phase for BCZY541 cell.

The dependence of the conductivity on CO_2 partial pressure (Fig. 4.12) is analogous to the trend reported in Fig. 4.13 of Chapter 3. The conductivity values obtained in carbon dioxide rich atmospheres were slightly lower compared to the results obtained in high pH_2O. Nonetheless, it is interesting to observe that for low pCO_2 the conductivity of BKZY91 is as well almost constant or slightly decreasing and then for higher pCO_2 (≈ 4 bar) it shows a mild increasing tendency. The total conductivity varied from $1.5 \cdot 10^{-6}$ S/cm at pCO_2 of 0.5 bar, decreasing to $1.26 \cdot 10^{-6}$ S/cm at pCO_2 of 5 bar and finally increasing to $1.76 \cdot 10^{-6}$ S/cm at pCO_2 of 25 bar.

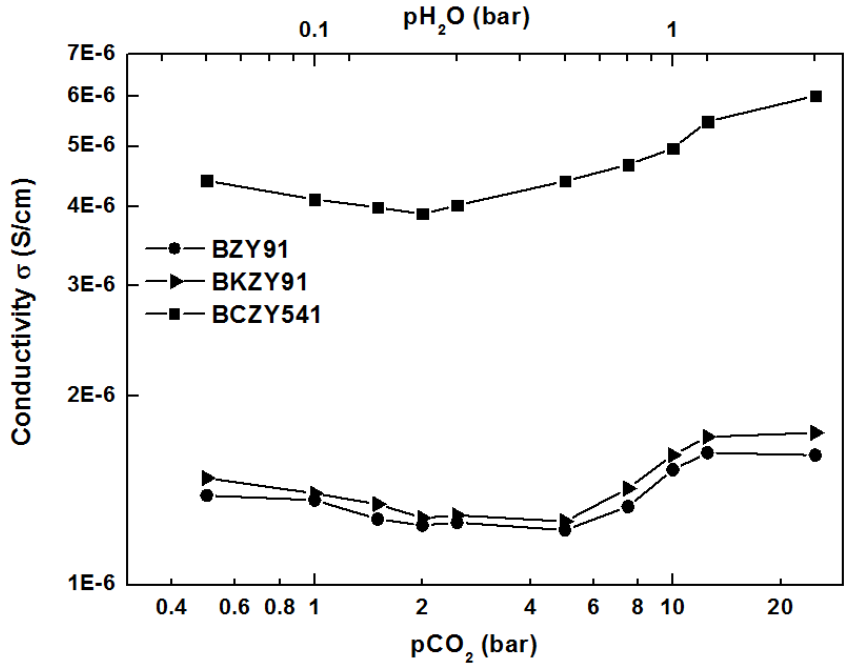

Fig. 4.12. Conductivity dependence on pCO_2 at 240 ^0C in the gas mixture: 50 vol.% CO_2, 5 vol.% H_2 and 45 vol.% N_2. The total pressure was between 1 bar and 50 bar. The pH_2O values given on top are the calculated equilibrium values of the gas mixture at 240 ^0C.

4.4 Discussion

4.4.1 Crystallographic structure

The results of this study demonstrate a novel-processing route to synthesize microcrystalline K-doped $BaZr_{0.9}Y_{0.1}O_{3-\delta}$ powder. To the best of the author's knowledge, the use of hydrothermal synthesis method for the production of $Ba_{1-x}K_xZr_{0.9}Y_{0.1}O_{3-\delta}$ has not been reported in literature.
The XRD diffractogram (Fig. 4.1 pattern (a)) undertaken on the as synthesized powders of BKZY91 revealed the presence of minor phases of monoclinic and rhombohedral ZrO_2. However, the XRD undertaken on BKZY91 pellets sintered at 1550 °C for 10 h (Fig. 4.1 pattern (b)) did not report the presence of any extraneous peaks. The formation of ZrO_2 secondary phases was also observed by Y. Pu et al.[12] in X-ray diffractograms of $BaZrO_3$ powders synthesized by hydrothermal synthesis at 120 °C for 8 h. Increasing the hydrothermal treatment temperature to 130 °C ensured them the synthesis of pure $BaZrO_3$ powders. Therefore, it might be possible to increase the hydrothermal treatment temperature of BKZY91 to values higher than that one used in this study (200 °C) to avoid formation of secondary phases also in the synthesized powders.
The presence of secondary phases cannot be explained only by the synthesis procedure used, since the formation of minor tetragonal ZrO_2 peaks was noticed also on potassium and yttrium-doped barium zirconate powders prepared by solid state reactive sintering, as reported by A. Patnaik *et al.*[17]. The refractory nature of yttrium barium zirconate leads to significant challenges to obtain a highly dense and pure compound, since high temperature and long sintering times are required because a long-distance diffusion of cations is required for the grain growth. [24]
The comparison between the lattice parameters of BKZY91 and BZY91, which was obtained by solid state reactive sintering, gave analogous values that might be justified by the similar ionic radius of Ba^{2+} (1.60 Å) and K^+ (1.60 Å) at 12 coordinates[18]. Moreover, this value is in line with published results determined from XRD using the same space group Pm3m. [25]
Surprisingly, the addition of 1 wt% of NiO as sintering additive did not improve the sinterability and the stability of BKZY91 pellets, since formation of cracks on the surface and curved shape were observed. However, 1 wt% of NiO is usually added to the mixture of precursors in the preparation of the yttrium-doped barium zirconate by solid state reactive sintering, as described in Chapter 3 and in several papers by S. Ricote *et al.* [26,27,28]. In this study, instead, mixing 1 wt% of ZnO to the synthesized powder of BKZY91 improved the sinterability and the density of the BKZY91 pellets sintered at 1550 °C for 10 h increased to up to 90%. Indeed, according to S. Tao *et al.*[29] with the addition of 1 wt% of ZnO as sintering aid, $BaZr_{0.8}Y_{0.2}O_{3-\delta}$ pellets may be sintered at a temperature as low as 1325 °C with a density up to 96%. They suggested as a possible explanation the similar ionic size of Zr^{4+} and Zn^{2+} ions, which might facilitate the insertion of Zn^{2+} into the $BaZrO_3$ lattice and ensuring a lower melting point. Operating at 1550 °C for 10 h gave the possibility to minimize the loss of potassium from the pellets after the sintering. Indeed, ICP results showed analogous mol% of potassium in the as synthesized powders and in the sintered pellets as reported in Table 4.1. Low concentration of potassium (ca. 0.5 mol %) was measured for pellets sintered at 1550 °C for 24 h and instead no traces of it for those sintered at 1670 °C for 10 h. Therefore both sintering time and elevated temperature influence the amount of potassium left as dopant in the A-site of the perovskite.

The stability of a proton conducting electrolyte is known to be a critical issue, thus XRDs were undertaken on sintered pellets after the electrochemical tests at ambient and at high pressure of H_2O and CO_2. As it is possible to see in Fig. 4.2 and Fig. 4.3, BKZY91 electrolyte did not report any secondary peaks after both experiments. The mechanical and chemical stability of BKZY91 and BZY91 pellets was not affected, since it didn't break in smaller pieces after the tests. This is also confirmed by the comparison between the SEM images taken before and after the electrochemical test at high pressure, which do not show any variation.
The particle's shape of the as synthesized powders was quite uniform and well defined, as shown in Fig. 4.4. On average, the smaller particles (~ 2 μm in diameter) reported a decaoctahedron shape composed of 18 regular crystal faces, comprising 6 squares and 12 hexagonal faces, as already observed by M.L. Moreira *et al.* in $BaZrO_3$ powders[30]. The decaoctahedron has the O_h octahedral group of symmetries. Instead, particles characterized by a bigger diameter (~ 4 μm) preferentially assumed a spherical shape. Z. Lu *et al.*[31] discussed the evolution of the morphology of barium zirconate from truncated dodecahedral to spherical shape by increasing the ethanol content in the water precursor solution. They claimed that it is possible to tune the size and shape of barium zirconate crystals by controlling the experimental conditions.

4.4.2 Conductivity

The two synthesis techniques used in the tested electrolytes, along with the diverse microstructural characteristics observed may help to explain the difference in measured grain boundary conductivities, in particular for the test at low steam partial pressure (pH_2O = 0.1 atm). The specific grain boundary conductivity of BZY91 increased from $1.2 \cdot 10^{-8}$ S/cm to $4 \cdot 10^{-8}$ S/cm with increasing pH_2O in the range < 10^{-3} atm – 0.1 atm, while for BKZY91 varied from $4.8 \cdot 10^{-8}$ S/cm to $9.2 \cdot 10^{-8}$ S/cm, as shown in Fig. 4.7. Also at high partial pressure of steam the specific grain boundary conductivity increased for both compounds when increasing pH_2O in the range 5 – 25 bar, as reported in Fig. 4.11. However, the bulk conductivity of BKZY91 and BZY91 measured at 240 °C in high partial pressure of steam (from pH_2O of 2.5 bar to pH_2O of 25 bar) was only weakly influenced by the increasing concentration of steam.
BKZY91 and BZY91 are expected to be almost fully hydrated already at the beginning of the conductivity measurements at 240 °C for a pH_2O of 10 mbar[7], thus the constant trend in bulk conductivity during the test at high partial pressure of steam could be explained.
The bulk conductivity for both compounds at 275 °C slightly increased when increasing the pH_2O from pH_2O < 10^{-3} atm to 0.1 atm, i.e. from $9.8 \cdot 10^{-5}$ S/cm to $1.2 \cdot 10^{-4}$ S/cm and from $8.5 \cdot 10^{-5}$ S/cm to $1 \cdot 10^{-4}$ S/cm for BKZY91 and BZY91 respectively. This was also observed by X. Xu et al.[23] when testing $Ba_{0.95}K_{0.05}Zr_{0.85}Y_{0.11}Zn_{0.04}O_{3-\delta}$ both in dry atmosphere (pH_2O ~ 10^{-6} atm) and wet atmosphere (pH_2O ~ 10^{-2} atm) for temperatures between 300 °C and 100 °C.
In particular, BKZY91 showed higher conductivity values both in wet and dry atmospheres if compared with BZY91 (Fig. 4.10). A possible explanation of the observed difference in conductivity may be related to the microstructures of the electrolytes. On average the grain size of BKZY91 electrolytes (~ 2-3 μm) is bigger than that of BZY91 (~1 μm), as observed in the SEM image in Fig. 4.5a). The difference in grain size and therefore in the grain boundary conductivity can be related to the specific preparation technique, as observed by S. Ricote et al.[32]. In addition, the

presence of an alkali dopant as potassium in the A- site of $BaZr_{0.9}Y_{0.1}O_{3-\delta}$ may affect not only the water uptake capacity, but also the composition and/or the structure of the grain boundary. This could modify the space-charge region and consecutively the concentration and conductivity across the grain boundaries[33]. The grain boundary conductivity might be affected by local changes in the composition in the ppm range or in the structure, as observed by Duval et al. [9]. Further investigations are required to better explain this behavior.

The EIS measurements done at 275 °C and 440 °C approached a condition of equilibrium during the holding time of each gas compositions. It was considered a minimum of 10 h waiting time between the measurements in wet ($pH_2O = 0.1$ atm) and dry ($pH_2O < 10^{-3}$ atm) atmospheres.

The total conductivity values obtained in dry atmosphere after the hydration treatment were higher compared to that reported at the beginning of the sequence at 440 °C always at $pH_2O < 10^{-3}$ atm. This might be related to a slower dehydration kinetic and also because even small amount of water contamination derived from the previous treatment in higher pH_2O could cause proton incorporation above ~ 400 °C [34].

The highest conductivity values were obtained by the electrolyte containing cerium (BCZY541), both in dry ($pH_2O < 10^{-3}$ atm) and in wet ($pH_2O = 0.1$ atm) atmospheres as shown in Fig. 4.9a) and 9b). Indeed, S. Ricote et al.[35] observed that the absolute value of the hydration enthalpy was increasing with cerium content, which indicated that at a fixed temperature the proton concentration increased with cerium concentration. In addition, barium cerate based electrolytes present a better grain boundary conduction since their grain boundary is less resistive compared to barium zirconate compounds [16, 36]. In Fig. 4.9 b), the dependence of conductivity on temperature shows a different trend for the compound containing cerium (BCZY541) when compared with the other two cerium free (BKZY91 and BZY91). The curves belonging to BKZY91 and BZY91 bend around 550 °C, possibly due to dehydration and therefore loss of proton carriers. This behavior is less evident for BCZY541, because compounds containing cerium showed also non-negligible oxide ion conductivity at temperatures around 600 °C[37]. For this type of cerate based material with a pH_2O of ca. 0.015 atm, proton conductivity reaches a maximum at around 700°C and then starts to decrease. At the same time the transport of oxide ions increases, leading to an increase in total conductivity [35].

The conductivity values reported for BKZY91 in Fig.4.10 in dry ($pH_2O < 10^{-3}$ atm) atmosphere are compared with that observed in air ($pH_2O \sim 8.4 \cdot 10^{-4}$ atm) condition by X. Xu et al. [23] and by A.S. Patnaik et al.[17]. The trends measured by X. Xu both in dry and in wet atmospheres are compatible with what was achieved experimentally in this study. Only at low temperatures the value obtained by X. Xu[23] are higher and this can be related to the difference in equilibration time between each variation in temperature. Conversely, the results of A.S. Patnaik[17] in wet atmosphere are lower along all the range of temperature, in spite that the mole fraction of potassium is higher. The presence of minor amounts of tetragonal ZrO_2 in $Ba_{0.8}K_{0.2}Zr_{0.9}Y_{0.1}O_{3-\delta}$ cell might affect and diminish the conductivity performance.

The addition of potassium into yttrium-doped barium zirconate resulted to be a good compromise for the performance in conductivity and for chemical stability even at high pressure. Overall, BKZY91 maintained slightly higher conductivity than BZY91 both in low and high steam partial pressures. They both preserved their morphology and structure during the high pressure test in CO_2.

4.5 Conclusions and outlook

Hydrothermal synthesis has proven to be a valid process to synthesize microcrystalline K- doped $BaZr_{0.9}Y_{0.1}O_{3-\delta}$ powder. It was time and cost efficient and allowed to obtain quite uniform and well defined particle's shape of the as synthesized powders, and most of all the incorporation of potassium in the perovskite structure. Further studies should be performed on the synthesis method varying the hydrothermal treatment temperature and time in order to observe possible variation in the particle sizes of the as synthesized powders. Smaller particles size might improve the sinterability of the ceramic compounds. The concentration of the potassium hydroxide solution should be varied to investigate the relation between the concentration of the solution and the mol% of potassium in the A-site of the perovskite.

The conductivity of $Ba_{0.92}K_{0.08}Zr_{0.9}Y_{0.1}O_{3-\delta}$ (BKZY91) and of solid state reactive sintered BZY91 and BCZY541 electrolytes was studied as a function of temperature (from 790 °C to 275 °C) and in different steam partial pressure ($pH_2O < 10^{-3}$ bar to 0.1 bar). The electrolyte containing cerium showed the best performance in all conditions tested. BKZY91 showed higher conductivity values both in wet and dry atmospheres if compared with BZY91 (Fig. 4.10). A possible explanation of the observed difference in conductivity may be related to the microstructures of the electrolytes. The better performance of grain boundary conductivity of BKZY91 might be connected to the specific preparation technique, which could influence the composition and/or the structure of the grain boundary. Investigation of the chemical composition of the grain boundaries of the two electrolytes based on yttrium doped barium zirconate needs to be performed with TEM imaging and/or atom-probe tomography. BKZY91 was also tested for the first time in wet H_2/N_2 and in $CO_2/H_2/N_2$ gas mixtures at a total pressure of up to 50 bar and temperature of 240 °C. The conductivity values obtained during the two sequences at high pressure were in line with the results registered with BZY91. An increase in grain boundary conductivity was observed when increasing the pH_2O from 2.5 bar to 25 bar, as shown in Fig. 4.11. The total conductivity registered at the end of sequence 1 was around $3 \cdot 10^{-5}$ S/cm for both BKZY91, while the best conductivity value achieved during sequence 2 was more than an order of magnitude lower (ca. $1.7 \cdot 10^{-6}$ S/cm) at a pCO_2 of 20 bar. BKZY91 could represent a suitable electrolyte for CO_2 reduction thanks to its stability during conductivity measurements (comparing XRD before and after conductivity testing). However, in order to be considered for implementation in full cells, the electrolyte should have showed a total conductivity of ca. 10^{-3} S/cm at intermediate temperature (below ~ 300 °C) and in high steam partial pressure.

This concludes that yttrium doped barium zirconate based electrolytes cannot be chosen as the candidate material for further studies in full cell cells for CO_2 reduction at intermediate temperature and high pressure.

References

[1] H. Iwahara, Solid State Ionics, 86-88 (1996) 9.
[2] T. Norby, Solid State Ionics, 125 (1999) 1.
[3] H. Iwahara, H. Uchida, I. Yamasaki, *International Journal of Hydrogen Energy*, 12 (2) (1987) 73-77.
[4] W. Grover Coors, *Journal of the Electrochemical Society*, 151 (7) (2004) A994-A997.
[5] K. Xie, Y. Zhang, G. Meng, J. T. S. Irvine, *Journal of Material Chemistry*, 21 (2011) 195.
[6] E. Fabbri, A. D'Epifanio, E. Di Bartolomeo, S. Licoccia, E. Traversa, Solid state ionics, 179 (2008) 558.
[7] K. D. Kreuer, *Annual Review of Material Research*, 33 (2003) 333.
[8] Y. Yamazaki, R. Hernandez-Sanchez, S.M. Haile, Chemistry of Materials, 21 (2009) 2755.
[9] S.B.C. Duval, P. Holtappels, U.F. Vogt, E. Pomjakushina, K. Conder, U. Stimmimg and T. Grauele, Solid state Ionics, 178 (2007) 1437.
[10] P. Babilo and S.M. Haile, Journal of American Ceramic Society, 88 (2009) 2362.
[11] J. Tong, D. Clark, M. Hoban, R. O'Hayre, Solid State Ionics, 181, 2010, 496.
[12] Y. Pu, H. Wu, K. Chen, Advanced Materials research 156 (2011) 988-991.
[13] S. Bhowmick, J. Basu, Y. Xue, C. Barry Carter, Journal of American Ceramic Society, 93 (2010) 4041-4046.
[14] H.L. Lin, R.K. Chiang, C.L. Kuo, C.W. Chang, Journal of non-crystalline solids, 353 (2007) 1188-1194.
[15] K.D. Kreuer, Solid state ionics, 97 (1997) 1.
[16] T. Norby, M. Wideroe, R. Glockner, Y. Larring, Journal chemical society, Dalton transaction, (2004) 3012.
[17] A. S. Patnaik, A. V. Virkar, Journal of Electrochemical Society, 153 (2006) 1397-1405.
[18] R.D. Shannon, C.T. Prewitt, Acta crystallographica, B 25 (1969) 925.
[19] C. Chatzichristodoulou, F. Allebrod, and M. Mogensen, *Review of Scientific Instruments*, 84 (2013) 054101.
[20] https://www-s.nist.gov/srmors/certificates/archive/640c.pdf
[21] J. R. Macdonald, *Solid State Ionics*, 13 (1984) 147.
[22] J.R. MacDonald, E. Barsoukov, Impedance Spectroscopy, J. R. MacDonald, Wiley and Sons, Second Edition, New York, 2005.
[23] X. Xu, S. Tao, J.T.S. Irvine, Journal of Solid State Chemistry, 183 (2010) 93-98.
[24] S. Imashuku, T. Uda, Y. Nose, and Y. Awakura, Journal of phase equilibria and diffusion, 31 (2010) 348-356.
[25] C.D. Savaniu, J. Canales-Vazquez, J.T.S. Irvine, Journal of Material Chemistry, 15 (2005) 598.
[26] S. Ricote, N. Bonanos, Solid State Ionics, 181 (2010) 694 – 700.
[27] S. Ricote, N. Bonanos, A. Manerbino, W.G. Coors, International Journal of Hydrogen Energy 37 (2012) 7954-7961.
[28] S. Ricote, N. Bonanos, P.M. Rørvik, C. Haavik, Journal of Power Sources, 209 (2012) 172-179.
[29] S. Tao, J.T.S. Irvine, Journal of Solid State Chemistry, 180, (2007), 3493-3503.

[30] M. L. Moreira, J. Andres, J. A. Varela and E. Longo, Crystal growth & design, 9 (2009) 833-839.
[31] Z. Lu, Y. Tang, L. Chen and Y. Li, Journal of Crystal growth 266 (2004) 539-544.
[32] S. Ricote, N. Bonanos, A. Manerbino, N. P. Sullivan and W.G. Coors, Journal of Materials chemistry A, 2, 2014, 16107.
[33] M. Shirpour, B. Rahmati, W. Sigle, P. A van Aken, R. Merkle, J. Maier, The Journal of physical chemistry C, 116 (2012) 2453-2461.
[34] H. G. Bohn, T. Schober, Journal of American Ceramic Society, 83, 2000, 768.
[35] S. Ricote, N. Bonanos and G. Caboche, Solid State Ionics, 180 (2009) 990-997.
[36] K. H. Ryu, S. M. Haile, Solid State Ionics, 125 (1999) 355 – 367.
[37] S. Ricote, N. Bonanos, H. J. Wang, R. Haugsrud, Solid State Ionics, 185 (2011) 11-17.

Chapter 5
Summary of Part II: Electrolytes

Different proton conducting oxides were synthesized and characterized with respect to phase composition, thermo-chemical stability and conductivity to be used as electrolyte materials. In order to be considered for implementation in a full electrochemical cell for reduction of CO_2, the materials should fulfil the following requirements. The conductivity should be $\sigma \geq 10^{-3}$ S/cm at temperatures below 300 ^{0}C. The materials have to be thermo-chemically stable in the same temperature interval as they exhibit high conductivity, i.e. the materials must not decompose during the electrochemical tests. Table 5.1 collects the tested solid proton conductor materials and indicates if their conductivity and thermo-chemical stability accomplished the requisites and therefore were worth to be implemented in a full electrochemical cell.

Table 5.1 Summary of the results for the different tested solid proton conductor electrolyte materials according to the relevant requirements for CO_2 reduction application.

Electrolyte Materials	**Temperature [^{o}C]**	**Conductivity [S/cm] @ pH_2O = 25 bar P_{tot} = 50 bar**	**Conductivity [S/cm] @ pH_2O = 0.1 bar P_{tot} = 1 bar**	**Thermo-chemical Stable**
BCZY541	240	$2\cdot10^{-3}$	-	no
BCZY262	240	$5\cdot10^{-6}$	-	yes/no
BZY91	240	$2\cdot10^{-5}$	-	yes
BKZY91	240	$3\cdot10^{-5}$	-	yes
BZY91	780	-	$2\cdot10^{-3}$	yes
BZY91	690	-	$2\cdot10^{-3}$	yes
BZY91	550	-	$1.8\cdot10^{-3}$	yes
BZY91	440	-	$4\cdot10^{-4}$	yes
BZY91	275	-	$5\cdot10^{-6}$	yes
BKZY91	780	-	$3\cdot10^{-3}$	yes
BKZY91	690	-	$3\cdot10^{-3}$	yes
BKZY91	550	-	$2\cdot10^{-3}$	yes
BKZY91	440	-	$6\cdot10^{-4}$	yes
BKZY91	275	-	$8\cdot10^{-6}$	yes

From the table above it is possible to see that BCZY541 would have been the best electrolyte candidate because of its low resistivity in high pH_2O even at temperatures as low as 240 °C. However, the instability in the acidic CO_2 gas atmosphere hinders practical application for carbon dioxide reduction at high pressure. BZY91 and BKZY91 could be suitable electrolytes for CO_2 reduction thanks to their stability, but the protonic conductivities at 240 °C were too low to be taken into consideration for implementation in full cells. These materials showed good conductivity at temperatures above 440 ^{0}C and at ambient pressure.

The study of proton conducting Y-doped $BaCeO_3$-$BaZrO_3$ solid solutions did not provide a clear electrolyte candidate, therefore aqueous alkaline based electrolytes were considered. As mentioned in Chapter 2, $KHCO_3$ is a well-known electrolyte for reduction of CO_2 both in ambient conditions and at elevated pressures[1]. Therefore it could represent a valid candidate as electrolyte.
In addition, P.L. Mollerup[2] investigated the potential of immobilized aqueous K_2CO_3 as a possible electrolyte for co-electrolysis of CO_2 and water at ca. 200 ^{0}C. This was done by studying the properties of pure aqueous K_2CO_3 and immobilized aqueous K_2CO_3 in porous ceramic matrixes. As shown in Fig. 2.2 and Fig. 2.4 the conductivities of both pure aqueous 10 wt% K_2CO_3 and immobilized 10 wt% aqueous K_2CO_3 were much higher than 10^{-3} S/cm at temperature below 200 ^{0}C and at 30 bar pressure. The lowest ionic conductivity value of 10 wt% aqueous K_2CO_3 immobilized in a porous $SrTiO_3$ pellet was ca. 0.05 S/cm at room temperature and at 30 bar pressure.
In conclusion, aqueous $KHCO_3$ and K_2CO_3 were the most promising electrolytes compared to the materials evaluated in Part II, and were therefore chosen as electrolytes for further studies in full electrochemical cells.

References

[1] Y. Hori, in Modern aspects of electrochemistry, ed. C. Vayenas, R. White, and M. Gamboa-Aldeco, Springer, New York, 2008, vol. 42, pp. 89-189.
[2] Pia Lolk Mollerup, "New Electrolytes for CO_2 Electrolysis cells", Department of Energy Conversion and Storage, Technical University of Denmark, December 2012.

Part III

ELECTRODES and CELL DEVELOPMENT

Chapter 6
CO_2 reduction on copper foam electrocatalyst at room temperature and ambient pressure.

Copper is the commonly used carbon dioxide reduction catalyst, and therefore a reasonable first candidate for this electrocatalyst screening analysis. CO_2 reduction reaction was studied on copper foam electrode in aqueous media (0.1 M $KHCO_3$ electrolyte) and at ambient condition. The identification and quantification of the reduction products as a function of the applied potential was the main focus of this Chapter.

Abstract

The potential dependent activity and selectivity of the electrochemical reduction of CO_2 on metallic copper foam surfaces was investigated under ambient conditions. This was enabled by the utilization of highly sensitive experimental methods for the identification and quantification of CO_2 electroreduction products. Copper foam was analysed across a range of potentials and it was observed a total of seven different CO_2 reduction products. In this study it is shown that both the number of products formed and their faradaic efficiencies differ from those obtained at smooth electropolished copper foil electrodes.

6.1 Introduction

As mentioned in Chapter 2, copper metal is the only known material capable of catalysing the formation of relevant quantities of hydrocarbons at high reaction rates over prolonged periods of time. On the other hand, a cathodic overpotential of ca. 1 V is necessary to obtain a wide variety of major and minor products such as formic acid, carbon monoxide, methane and alcohols at room temperatures and ambient pressure. In all cases aqueous inorganic salt solutions were utilized as the electrolyte[1,2,3,4]. The products distribution is largely related to the overpotential at the cathode copper electrode. Indeed hydrogen evolution is the main reaction taking place at lower overpotentials (-0.8 to -1 V vs. NHE), while for more negative overpotentials CO, hydrocarbons and alcohols are produced [1,5].
The overall chemical reaction taking place in the electrochemical device is:

$$CO_2 + H_2O \rightarrow C_xH_yO_z + O_2 \quad (6.1)$$

It represents the sum of two electrochemical half reactions. Water oxidation (oxygen evolution reaction, OER) taking place at the anode:

$$H_2O \rightarrow O_2 + 4H^+ + 4e^- \quad (6.2)$$

And carbon dioxide reduction taking place at the cathode:

$$CO_2 + 8H^+ + 8e^- \rightarrow CH_4 + 2H_2O \quad (6.3)$$
$$CO_2 + 6H^+ + 6e^- \rightarrow CH_3OH + 2H_2O \quad (6.4)$$
$$CO_2 + 2H^+ + 2e^- \rightarrow CO + H_2O \quad (6.5)$$

At the cathode electrode also the undesired hydrogen evolution reaction takes place (Eq. 6.6) since it is kinetically favoured compared to the other reactions.

$$2H^+ + 2e^- \rightarrow H_2 \quad (6.6)$$

Platinum foil was used for the anode, since it is a well-known and widely studied catalyst both for the oxygen evolution reaction[6, 7] and the oxygen reduction reaction[8]. While both the oxygen evolution reaction and the carbon dioxide reaction are necessary, this study focused only on the carbon dioxide reduction.

In this Chapter, the electrocatalytic activity of copper foam was investigated in aqueous media and at ambient condition for electrochemical reduction of CO_2. It represents a fundamental study of the copper foam electrode. The measurements were conducted at the laboratory of Prof. Thomas F. Jaramillo (Stanford University – Chemical Engineering Department), where it was possible to utilize an experimental setup with high detection sensitivity for minor products from the CO_2 reduction reaction. In particular, the results obtained with copper foam cathode electrode were compared to those reported on copper foil by K. Kuhl et al.[9] with the same electrochemical device.

6.2 Experimental

The electrochemical experiments were performed in a custom made two compartment electrolysis cell of polycarbonate which has been previously described by Kuhl et al.[9], shown in Fig. 6.1. The structure of the cell kept the working electrode parallel to the counter electrode to obtain a uniform voltage. The compartments were divided by an anion exchange membrane (Selemion AMV, AGC inc.) to reduce the transport of liquid phase products from the cathode electrode to the anode where they could be oxidized. The surface area of the electrocatalyst was of 4.5 cm^2 (3 cm x 1.5 cm) and the cell was designed to have a small electrolyte volume (8 ml) in each of the two compartments, a gas volume of ca. 3 ml above the electrolyte on each side of the membrane. The electrolyte was constituted by 0.1 M $KHCO_3$ (Sigma-Aldrich, 99.99% metals basis) and 20 ml/min of CO_2 was constantly flowing through the electrolyte during the electrolysis test. 30 minutes prior to start the experiments, CO_2 was flown through the electrolyte to obtain a stable pH of 6.8. This value was measured both before and after the electrochemical test. The gas outlet from the cathode electrode compartment was connected to a gas chromatograph (GC, SRI 8610C in the Multi-Gas #3 configuration) to analyze the gas phase products. For each electrolysis test the cell was constituted by copper foam (MMC Superalloy. 0.5 mm) as working electrode and platinum foil as counter electrode. As reference electrode an Ag/AgCl electrode (Accumet) was utilized. An aluminium foil

was put in contact with the copper foam cathode electrode to prevent electrolyte leakage, since the working electrode is highly porous with an average pore size of ca. 100 μm. Aluminum is inert under operating conditions for CO_2 electrolysis.

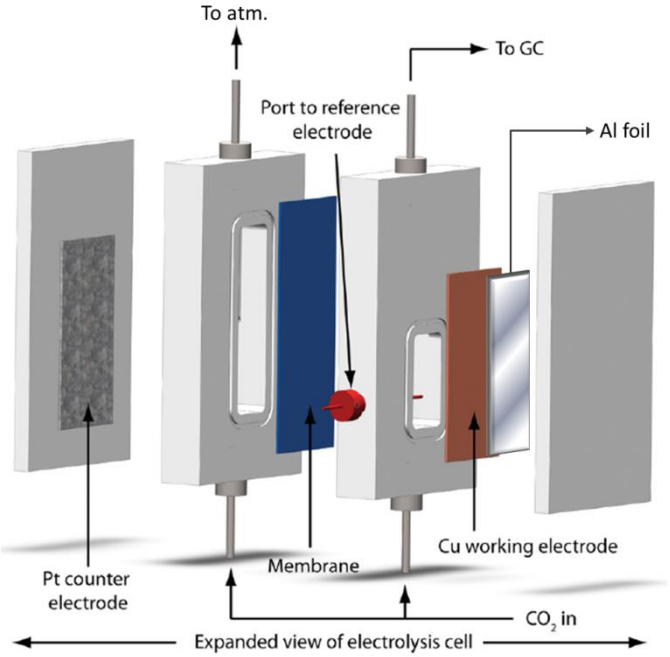

Fig. 6.1 . Schematic of the electrochemical cell and experimental setup used in electrolysis experiments.

Electrochemical experiments were carried out through a Biologic VMP3 potentiostat. The cell resistance was measured and 85% of the ohmic loss was compensated by the potentiostat for all the tests. The remaining 15% of the loss was manually corrected during the data analysis as indicated by K. Kuhl et al.[9]. The data collected vs. Ag/AgCl reference were then converted to a reversible hydrogen electrode (RHE) scale by $V_{vs.RHE} = V_{measured\ vs.Ag/AgCl} + 0.197 + 0.059 * 6.8_{(pH\ of\ sol)}$. The RHE is a subtype of the standard hydrogen electrodes which differs from it by the fact that the measured potential takes into account the pH value of the electrolyte.

All the potentials reported in the Chapter are *versus* RHE. The electrolysis potential (chronoamperometry) was applied for 1 h and three different potentials were tested: - 0.86 V, -0.93 V, -0.98 V.

The gas phase products were analysed and quantified with the GC after 5, 23, 41 and 59 minutes during the electrolysis test that lasting for one hour. The faradaic efficiency was determined by calculating the number of coulombs required to produce the measured quantity of each product and then dividing by the total charge passed during the time of the GC acquisition. Each potential was repeated three times, with a new and clean cathode electrode each time and its average is reported in the results below. The analysis of the liquid phase products was performed after the electrolysis experiments by running 1D ^{1}H NMR (600 MHz, Varian Inova) on the electrolyte sampled from the cathode electrode compartment. The surface of the copper foam cathode electrode was characterized before and after the one hour long electrolysis test at -0.98 V. Investigations of the

surface were performed by X-ray photoelectron spectroscopy (PHI VersaProbe Scanning XPS microprobe, Al-Kα radiation) and scanning electron microscopy (FEI XL30 Sirion SEM).

6.4 Results and Discussion

One-hour potentiostatic experiments were carried out at 3 different potentials between -0.85 to -1 V. The average current densities measured at each potential over the hour of electrolysis are reported in Table 6.1. The current remained stable along the one hour-long electrolysis test, suggesting little degradation of the copper foam electrode. For comparison, also the values obtained on copper foil by K. Kuhl are reported.

Table 6.1. Average current density measured during one-hour potentiostatic measurements at three different potentials. For comparison K. Kuhl data from dense copper foil electrodes are reported.

V vs. RHE	**Total average current density (mA/cm^2) Copper foam cathode**	**Total average current density(mA/cm^2), extra-polated from Kuhl et al.[9]**
-0.86	- 9.3	-1.3
-0.93	-10.2	-1.9
-0.98	- 15.7	-3.6

The range of current densities that could be investigated with the electrochemical device described above was between -0.5 to -20 mA/cm^2. Unfortunately, it was not possible to conduct tests at more negative potentials than -1 V since the current density started to decrease towards more negative values and the anion exchange membrane resulted to be damaged. As expected, the cathodic current density increased in magnitude with increasing cathodic overpotential. The current densities recorded with the foam based working electrode were higher compared to what obtained with the copper foil electrode. The values reported in Table 6.1 were obtained by dividing the total current by the surface area indicated in the experimental paragraph, i.e. 4.5 cm^2. On the other hand, it is relevant to consider that the copper foam was characterized by a rougher surface compared to the copper foil and therefore had a higher specific surface area. Considering the average pore size, the thickness of the foam and the roughness of the surface, the effective surface area is bigger than the value previously indicated. The SEM images taken on the copper foam and shown below were also used to roughly estimate the specific area as ca. 6 cm^2. However, since this value is not accurate enough to make a meaningful comparison, the value of surface area that will be used in the following results is 4.5 cm^2.

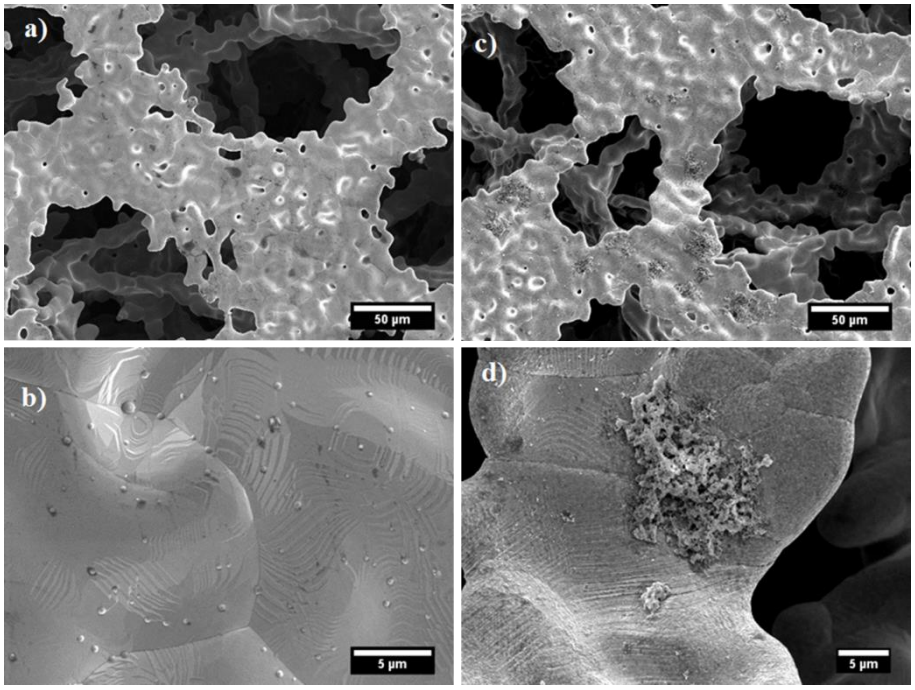

Fig. 6.2. SEM pictures of: a) and b) untreated copper foam; c) and d) after test copper foam. Note: the magnifications are different as indicated in the scale bars.

SEM images of the surface of the copper foam working electrode before and after an hour-long experiment at -0.98 V are shown in Fig. 6.2 a), b) and c), d). The pristine copper foam shows the presence of particles with a diameter of ca. 450 nm. The nature and composition of these impurities was not detected. The foam did not exhibit evident changes in the structures after the test. Comparing the images it is possible to notice the formation of clumps in the porous structures of the tested copper foam (Fig. 6.2 c) and d)). Their average size is of ca. 10 – 20 µm. Both SEM images show fairly rough surfaces.

XPS spectra carried out on the pre-run surface of the copper foam showed peaks which are attributable to Cu, O and C, as shown in Fig. 6.3 a) and their quantitative analysis is also listed. The O could be originated from a thin layer of copper oxide at the surface as well as from organics which could also explain the presence of C. Minor peaks are present in the XPS spectra between 300 and 500 eV, but it was not possible to identify their composition. XPS spectra (Fig. 6.3 b)) performed on the post-run surface of the copper foam revealed the presence of potassium which might explain the nature of the agglomerates observed by the SEM images. They most likely consist of $KHCO_3$ from the electrolyte.

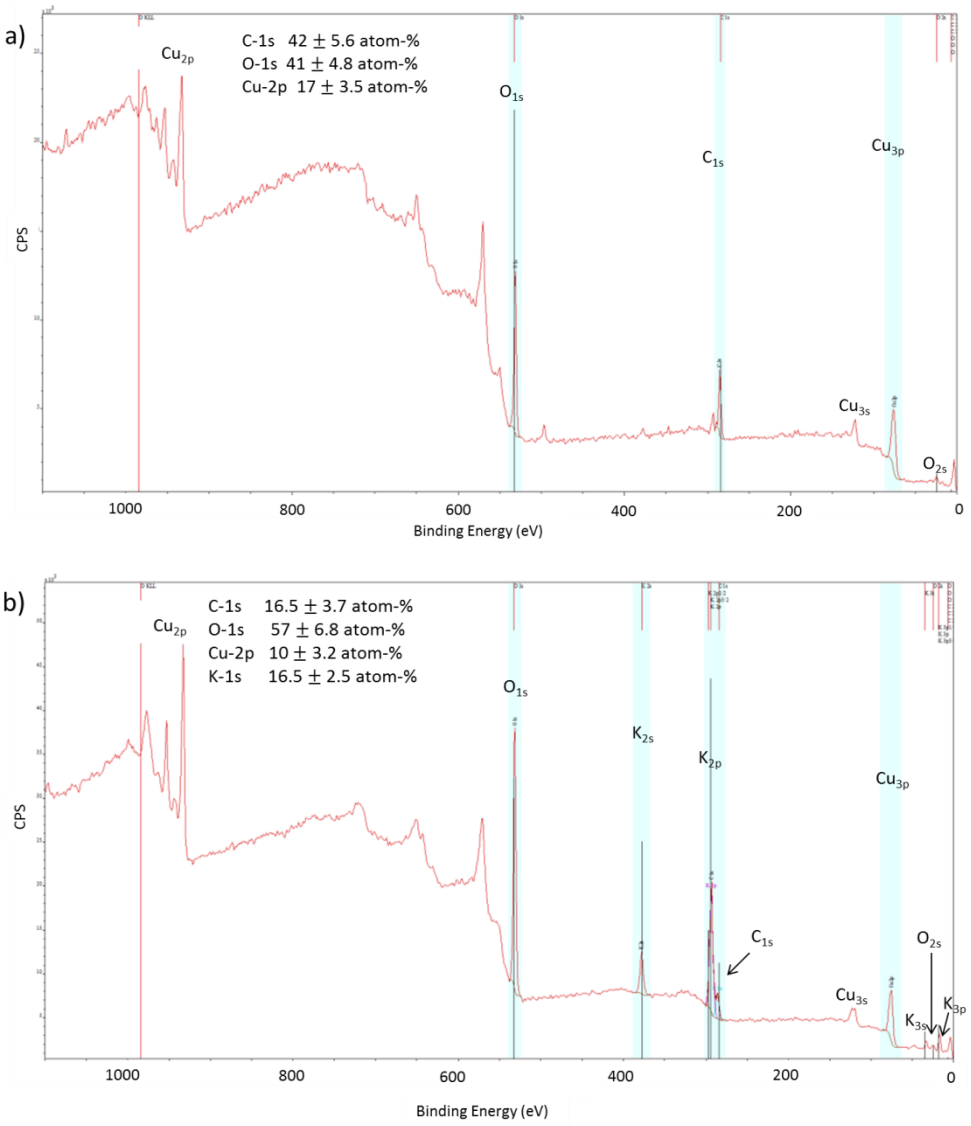

Fig. 6.3. XPS spectra of the copper surface: a) before the electrolysis experiment and b) after the electrolysis experiment at -0.98 V vs. RHE.

During the CO_2 electrolysis experiments, a total of seven reduction products were identified. The major products were H_2 and formate followed by CO, and interestingly four different minor products were detected: methane, methanol, ethylene and ethylene glycol. The faradaic efficiency of each product as a function of potential is reported in Fig. 6.4. For all the three potentials investigated the highest faradaic efficiency recorded was for H_2, with an almost constant trend close to 90 %. The data were compared with previously reported data from K. Kuhl et al. as shown as well in Fig. 6.4.

The faradaic efficiency of H_2 obtained with the copper foil cathode was significantly lower and it decreased moving towards more negative potentials, i.e. from ca. 45 % to 25 %. On the other hand, the faradaic efficiencies of formate, CO and methane obtained with the copper foil were higher, when compared to the copper foam electrode.

A possible explanation of this apparent discrepancy might be found in the significant difference of the surface structure and geometry of the two distinct copper electrodes investigated. Due to the porous structures of the copper foam, the applied overpotential is not constant throughout the thickness of the electrode. The overpotential drops in the electrolyte moving towards the inner parts of the pores, causing a gradient in the local electrode overpotential[10]. Therefore only a fraction of the high specific surface area of the foam is at the overpotential required for CO_2 reduction. This affects also the current, which decreases as a function of distance from the pore orifice.
Compared to the other reactions, H_2 evolution is both thermodynamically and kinetically favored at lower overpotentials. The production of CO slightly increased over the three potentials tested. Moving towards more negative potentials, the faradaic efficiency of formate started to decrease and simultaneously the faradaic efficiency of methane detected on copper foam electrode increased. Production of formate and CO which was observed at the lowest overpotential required only a two electron reduction. Exclusively at higher potential more reduced products can be formed. Indeed, at -0.93 V vs. RHE, methane and ethylene started to be observed followed by methanol and ethylene glycol at -1 V. Methane and methanol showed low faradaic efficiencies, lower than 1% for methane and around 0.04 % for methanol on the foam based copper electrode. The faradic efficiency of ethylene and ethylene glycol was ca. 0.01% and therefore is not reported in the plot of Fig. 6.4. The observation of methane and methanol at such small amounts and only at the highest overpotentials is likely related to the high number of proton and electron transfer steps needed for each of these products, i.e. 8 for methane and 6 for methanol.

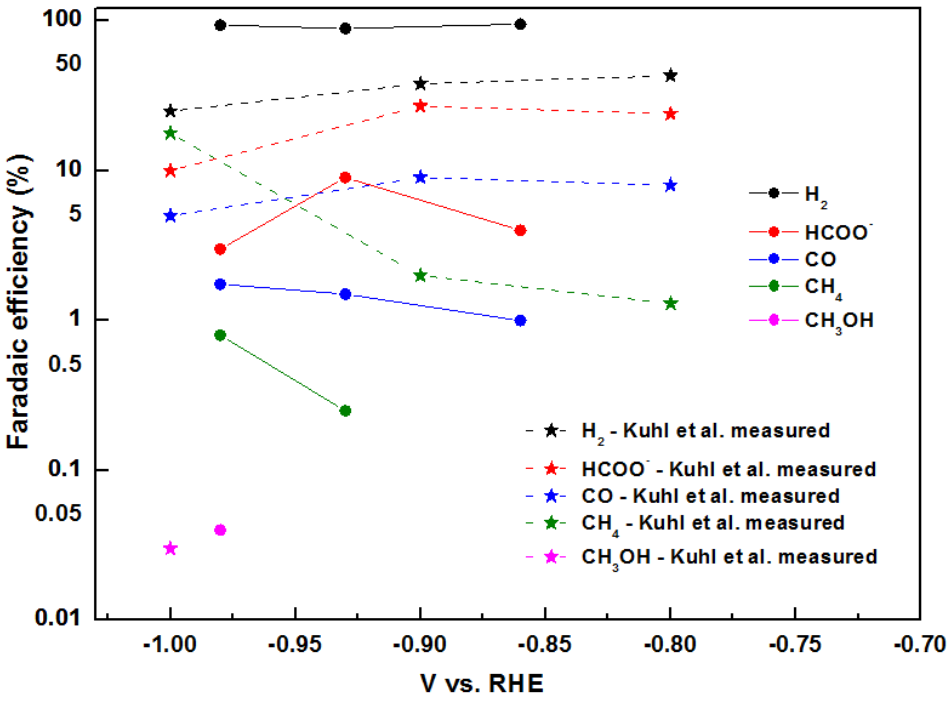

Fig. 6.4. Faradic efficiency for each product reduced as a function of potential on a copper foam electrode. For comparison also data reported by K. Kuhl et al.[9] on a dense copper foil electrode.

Also S. Sen et al.[11] observed that both the distribution of products formed from CO_2 reduction and their faradaic efficiencies were different when testing copper foams with hierarchical porosity instead of smooth electropolished copper electrodes. They claimed that the mechanism of CO_2 reduction was affected and altered by the nanostructure of electrodeposited copper foams. Indeed, they registered a higher faradaic efficiency for formate at all potentials suppressing H_2 evolution compared to the smooth copper electrode foil, a decreased faradaic efficiency for CO, methane and ethylene and formation of novel products C_3H_6. On the other hand in this Chapter, the highest faradaic efficiency was registered for hydrogen when testing copper foam with an average pore size of 100 µm. Therefore different average pore size of the foam electrodes can partially affect the products formed during the electrochemical reduction of CO_2. Also impurities present on the electrodes and different preliminary surface treatments may influence the selectivity of the catalyst. In Fig. 6.5 it is reported the partial current density required for the formation of each product as a function of potential. It was obtained by multiplying the total current density at a given potential by the faradaic efficiency for each product. The range of investigated potentials is unfortunately not sufficient to extrapolate and deduce a complete mechanistic study of CO_2 reduction on copper foam.

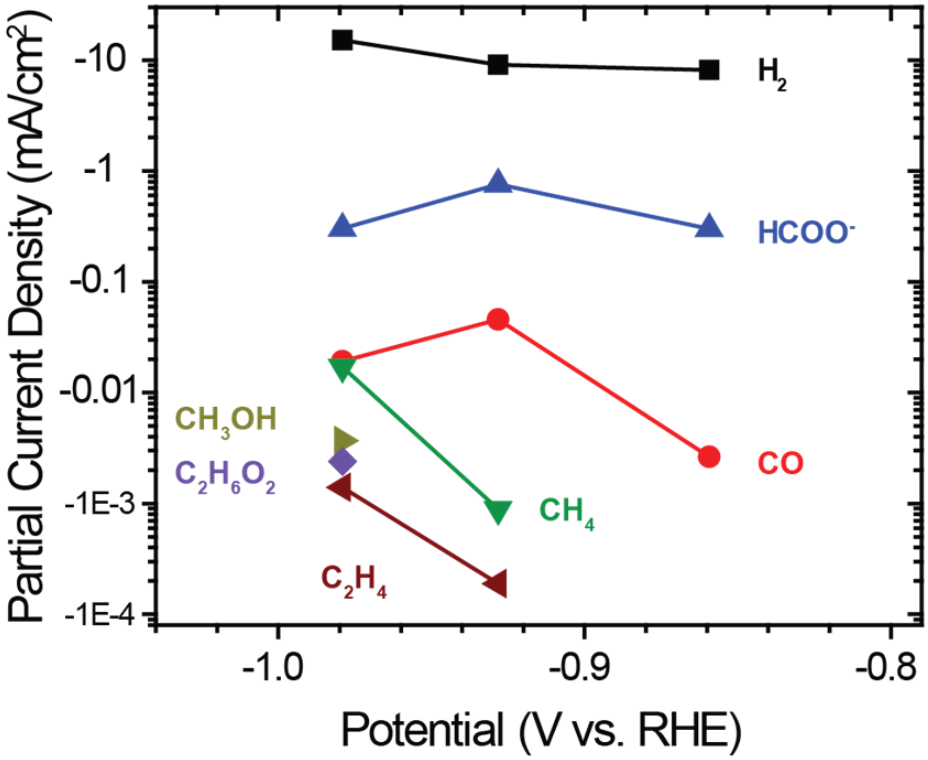

Fig. 6.5. Partial current density required for the formation of each product as a function of potential.

6.4 Conclusions

The aim of this study was to analyse the dependence of the applied potential on the catalytic activity of copper foams during CO_2 reduction at ambient conditions. In addition, a comparison between copper foam and a smooth electropolished copper electrode regarding the distribution of products formed from this reaction and their faradaic efficiencies was carried out.

The different roughness of the two electrode surfaces affected the current densities registered during the one hour long potentiostatic experiments. The current densities acquired on copper foams are ca. 5 times higher than the values obtained at the same potentials with smooth copper foil electrodes.

Accurate Brunauer–Emmett–Teller (BET) measurements of the effective surface area of copper foams are necessary to establish a fundamental comparison, i.e. is this a pure effect of surface area or is it also due to differences in surface structures. Traces of impurities on pristine copper foam electrodes, observed through XPS studies, suggest the need of improving and implementing cleaning procedures before the electrolysis tests. Seven products were identified on the copper foam electrode tested up to -0.98 V vs. RHE. H_2, formate and CO were the main products observed and in particular the faradaic efficiency of H_2 was ca. 90 %. The comparison with K. Kuhl results[9] suggested the idea that porous electrodes facilitate reaction pathways that are different from those that take place on smooth electrodes, due to graded electrical potential in the electrolyte through the Cu foam perpendicular to the electrode/electrolyte interface. The overpotential drops in the electrolyte in the pores when moving away from the main electrolyte causing a gradient in the local electrode overpotential. The products formed during the electrochemical reduction of CO_2 are affected by the electrode structure and design. Further studies that investigate how controlled variations in pore size, pore depth and effective surface area influence the products formed by the reduction of CO_2 are necessary. To realize this, it is also required to improve the electrochemical cell setup in order to sustain more negative current densities than -20 mA/cm^2.

References

[1] Y. Hori, A. Murata, R. Takahashi, Journal of the Chemical Society, Faraday Transactions 1: Physical Chemistry in Condensed Phases, 85 (1989) 2309-2326.

[2] H. Yano, F. Shirai, M. Nakayama, K. Ogura, Journal of Electroanalytical Chemistry, 519 (2002) 93 - 100.

[3] M. Gattrell, N. Gupta, A. Co, Journal of Electroanalytical Chemistry, 594 (2006) 1-19.

[4] Y. Hori, K. kikichi, S. Suzuki, Chemistry Letters, (1985) 1695 – 1698.

[5] M. Gattrell, N. Gupta, A. Co, Energy Conversion and Management, 48 (2007) 1255 - 1265.

[6] T. Reier, M. Oezaslan and P Strasser, ACS Catalysis *2* (8) (2012) 1765–1772.

[7] I.C. Man, H.Y. Su, F. Calle-Vallejo, H.A. Hansen, J.I. Martinez, N.G. Inoglu, J. Kitchin, T.F. Jaramillo, J.K. Nørskov, J. Rossmeisl, Journal of ChemCatChem 3 (2011) 1159-1165.

[8] J. Greeley, I. E. L. Stephens, A. S. Bondarenko, T. P. Johansson, H. A. Hansen, T. F. Jaramillo, J. Rossmeisl, I. Chorkendorff & J. K. Nørskov, Nature chemistry 1 (2009) 552-556.

[9] K. P. Kuhl, E. R. Cave, D. N. Abram and T. F. Jaramillo, Energy & Environmental Science, 5 (2012) 7050 – 7059.

[10] A. Lasia, Modeling of impedances of porous electrodes, in Modern Aspects of Electrochemistry, ed. by M. Schlesinger, vol. 43 (Springer, New York, 2009), pp. 67–138.

[11] S. Sen, D. Liu, G. Tayhas and R. Palmore, American Chemical Society Catalysis, 4 (2014) 3091-3095.

Chapter 7
CO_2 reduction on electrochemical cells using gas diffusion electrodes at elevated pressure.

The main aim of this study was to design and test a new electrochemical cell based on metal foam gas diffusion electrodes, as described in Chapter 2, able to reduce CO_2 in a single step process at elevated pressure. This chapter includes the results on the electrochemical performance and product selectivity of such newly designed cell. The evaluation and characterization of both microstructure and surface elemental composition of the different parts of the cells are included.

Abstract

An electrolysis cell for electrochemical reduction of CO_2 based on a new technology was developed. The aqueous electrolyte (0.5 M K_2CO_3) of the cell is immobilized by capillary forces in a ceramic porous structure (YSZ). Metal foam based gas diffusion electrodes were used to enhance the active surface area and three phase boundary length. The cells have been shown to operate at pressures up to 20 bar and to a maximum temperature of 50 °C. Copper and silver metal foams were studied as cathode, since they are promising electrocatalysts for CO_2 reduction. Nickel was chosen as anode, since it is a well-known catalyst for oxygen evolution reaction in alkaline electrolysis cell. The cells were tested by electrochemical impedance spectroscopy and chronoamperometric measurements across a range of applied voltages of -1.75 V, -2 V and -2.5 V. The total cell resistance was, for the cell with copper electrocatalyst and the lowest cell resistance, ca.14 $\Omega \cdot cm^2$ at an applied cell voltage of -2.5 V, 3 bar total pressure and ambient temperature. It exhibited a gradual degradation throughout the operation at high cell voltage. Gas chromatography measurements were conducted for the duration of the various tests. The only cathode products detected were CO, H_2 and methane when -2.5 V was the applied cell voltage. Scanning electron microscopy and X-ray photoemission spectroscopy analysis before and after the tests were used to investigate the degradation mechanism.

7.1 Introduction

Electrochemical CO_2 reduction research is driven by the aspiration to decrease reliance on fossil fuels and lower greenhouse gas emissions. Thanks to the electrocatalytic reduction process is possible to convert CO_2 and H_2O into alcohols and hydrocarbons such as methane and methanol that can eventually recover an important role in a CO_2 – neutral energy system[1]. Electrolysis can convert electrical energy produced by a renewable source into chemical energy in the form of syngas and hydrocarbons, and therefore could enable a shift to a sustainable energy economy and chemical industry. However, a key technological challenge to its utilization is the lack of efficient and selective electrocatalysts. Previous works in this area focused on ways to increase the energy efficiency of CO_2 reduction reaction and control other relevant aspects, such as selectivity and

production rates. The main contribution was given in 1985 by Hori et al.[2], when they showed on copper metal catalyst that the cathode overpotential contributes to control the product distribution. They discovered that hydrogen was the main product at low overpotentials followed by CO and $HCOO^-$ and thereafter evolution of hydrocarbons (CH_4 and C_2H_6) at even higher overpotentials. Since then, a number of scientific articles[3,4,5] have compared the activity of different transition metals and found that the products of the CO_2 reduction reaction depend on the binding energy of CO, which is believed to be a fundamental intermediate in the reduction of CO_2, to the transition metal catalyst used[3]. Metals that bind CO strongly produce few products during the reduction, because they are poisoned by CO or other intermediates that form along with the CO_2 reduction reaction. In particular, hydrogen is the main product observed from the competing water reduction. On the other hand, metals that bind CO weakly produce mainly CO as a product, because when CO_2 is reduced to CO, the CO is released from the surface and does not keep reacting to form more reduced products such as alcohols and hydrocarbons. Cu metal is characterized by an intermediate binding energy for CO, which is claimed to be the reason for its almost exclusive ability to catalyse the formation of more reduced products that need more than a two electron reduction. In addition, metallic silver exhibits low activity for the hydrogen evolution reaction and is characterized by a fairly weak CO binding energy, leading to a high selectivity of CO_2 reduction reaction for CO[6, 7]. Other aspects that affect the CO_2 reduction for experiments carried out at low temperatures and in aqueous electrolytes are slow kinetics and limited CO_2 solubility. The electrochemical rate limiting steps for the CO_2 reduction processes are strongly thermally activated[8], i.e. increasing the temperature helps in improving the electrode kinetics. This was recently demonstrated by E. J. Dufek et al[9] using a Ag based catalyst. They increased the electrolyser temperature from 18 °C to 70 °C and observed a reduction in the cathode overpotentials of ca. 0.3 V at 70 mA/ cm^2 /or an increase in current density of ca. 40 mA/ cm^2 at – 2V vs Ag/AgCl (3 M NaCl) reference electrode. In addition, a technology based on gas-diffusion electrodes (GDE) was proven to decrease mass-transport limitations across the gas-liquid interface to the electrocatalyst surface[10]. Furthermore GDEs can increase the active surface area of the electrode with possible extension of three-phase boundary[11] (active site where gas, electrode and electrolyte meet). The utilization of GDEs together with a pressurized testing system could enhance the solubility of CO_2 in liquid electrolytes. The advantages of performing the reduction at elevated pressure are manifold. Increasing the pressure increases the solubility of CO_2 according to Henry's law. In addition, a decrease in cell resistance will occur due to the frequency of reactants hitting the triple phase boundary, i.e. improved electrode kinetics and decreased diffusion resistance[12]. As a consequence, the rate of conversion to products enhances with increasing pressure. Operating the system at elevated pressure can enable to increase the operational temperature[13,14,15]. Various electrode surfaces have been already tested in highly pressurized reactors for CO_2 reduction [14, 16, 17] and a first attempt has been done to assemble a pressurized electrolysis system capable of producing syngas mixtures in continuous flow using silver as catalyst[18]. The work presented in this chapter utilized these previous investigations as the basis to develop a new type of electrolysis cell able to operate at high pressure and possibly at elevated temperature. In addition, the achievements obtained by F. Allebrod et al. with an innovative foam based alkaline electrolysis cells (FobAECs) capable of electrochemically splitting H_2O (g) into H_2 and O_2 at high efficiency at an elevated operating conditions of 250 °C and 42 bar

were also taken into consideration [19]. Therefore, a foam based electrolysis cell with gas diffusion electrodes and a ceramic porous structure in which the liquid electrolyte is immobilized by capillary forces was developed and tested up to 20 bar and to a maximum temperature of 50 °C. Potassium carbonate was selected as aqueous electrolyte. Copper and silver metal foam were tested as cathode, since they are promising electrocatalysts for CO_2 reduction. Nickel metal foam was chosen as anode because is widely used[20] and have been utilized as gas diffusion electrode both for the oxygen reduction reaction in an alkaline fuel cell[21] and in particular for oxygen evolution reaction in alkaline electrolysis[22]. This chapter presents the results of CO_2/H_2O electrolysis cell performance of cells made by a new production method for FobAECs. Moreover this work represents a first attempt to combine well known catalysts for CO_2 reduction with a new fabrication method. Finally, a comparison between the performances of the copper foam electrode achieved in aqueous media at ambient conditions (Chapter 6) and in the immobilized structure at high pressure is presented.

7.2 Experimental

7.2.1 Materials and cell fabrication

The foam based electrolysis cells were prepared and developed considering the earlier findings from the alkaline electrolyser cell designed and realized by Frank Allebrod. The electrochemical cell is constituted by metal foams as gas diffusion electrodes and by a porous electrolyte matrix tape of YSZ. Nickel foam (Alantum Europe GmBH) was used as anode, while copper and silver (MMC Super Alloy Corporation) were tested separately as cathode for carbon dioxide reduction. YSZ tape was carried out using tape casting technique. 300 g of YSZ powder (TZ-3Y, Tosoh) was added to 130 g Ethanol and then mixed with 40.4 g of Polyvinylpyrrolidone as binder. The slurry was processed by ball milling with 1000 g 3/8" balls for 72 h in a container at 50 rpm before adding 145.6 g of a suitable binder. Then the slurry was mixed for additional 24 h at 25 rpm. The obtained slurry was filtered and de-aired in vacuum and poured in the tape caster. A tape was produced with a speed of 20 cm/min and a doctoral blade height of 800 μm. The tape was ready to use after a drying time of additional 24 h, which led to a ca. 200 μm thick tape. The YSZ tape and the Nickel foam were cut in rectangular shape of ca. 20 x 40 mm^2 sizes. In particular, the Nickel based metal foam of a thickness of 1.5 mm and a porosity of ~ 95% were pressed in a hot press at 200 °C to decrease the thickness to ca. 0.5 mm. Two layers of the produced YSZ were placed on the pressed Ni metal foam and laminated together at 130 °C. The lamination was repeated for each half-cell at least 3 times, in order to achieve partial penetration of the foam into the YSZ tape. The half-cells were sintered in air at 200 °C, 420 °C and 600 °C for 4 h with a heating ramp of 15 °C / h followed by a second sintering step in 9% H_2/ Ar mixture at 1000 °C for 6 h with a heating and cooling ramp of 40 °C / h. Rectangular half-cells of ca. 19.5 x 39 mm^2 were produced. The thickness of the sintered half-cell was ca. 850 to 900 μm. Instead, the cathode electrode was obtained by cutting a rectangular surface of ca. 12.5 x 16 mm^2 of the copper and silver metal foams and then during the test it was put in contact with the YSZ side of the sintered half-cell. The thickness of the pristine metal foams of copper and silver was 0.5 mm. Before being tested, the metal foams were treated in reducing atmosphere (9 vol% H_2/ N_2) at 600 ^{0}C for 4 h. Photos representing both the half-cell and the electrodes were taken and shown in Fig.7.1.

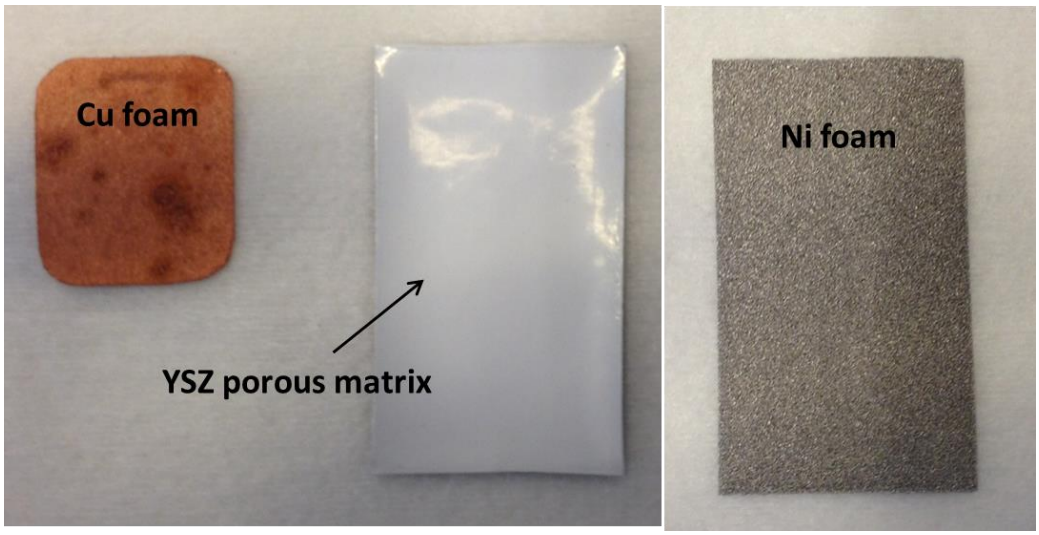

Fig. 7.1. Two photographs of the different part composing the electrolysis cell. Left: copper electrode foam and YSZ porous layers sintered on the nickel foam. Right: nickel foam.

The liquid electrolyte, immobilized in the sintered half-cell by capillary forces, was constituted by 0.5 M (6.5 wt%) K_2CO_3 (Sigma Aldrich, 99.99% metals basis). Deionized water was used in the preparation of the solution. The K_2CO_3 solution was pre-electrolyzed to remove any impurities (e.g. heavy metals, organic compounds) present in the aqueous electrolyte, which might deactivate the electrodes during CO_2 reduction. The pre-electrolysis was carried out in a clean container and the electrolyte solution was stirred at 100 rpm with a magnetic stirrer. Spirally coiled platinised Pt wires (Φ = 0.3 mm) were used as electrodes. Short circuiting of these electrodes was avoided by covering the part of the electrodes that was not immersed in the electrolyte with PTFE tapes. The electrodes were then immersed in the electrolyte solution separated at a distance of ca. 2 cm. One of the electrodes i.e., working electrode is negatively polarized at a constant voltage of 1.2 V for a period of 16 h using. During the entire pre-electrolysis process the electrolyte solution was bubbled with 80 ml/min of N_2 (99.998 % purity).

A custom cell holder of polytetrafluoroethylene (PTFE) was developed to carry out CO_2 electrolysis experiments on the foam based cell with immobilized liquid electrolyte (Fig.7.2). The holder was constituted by two separated pieces, i.e. a hollow cylinder with threads in only one of the two ends and a parallelepiped with one face attached to a cylindrical base. The first piece was screwed to the second to obtain a closed volume where to add a reservoir of 8 mL of liquid electrolyte. A Teflon O-ring was inserted between the two parts to avoid loss of liquid and improve the sealing. In particular, one face of the parallelepiped was modified by hollowing a smaller rectangular surface out. This was used as surface where to put the cathode (copper or silver foam) and a current collector mesh made of the same metal of the electrode tested. Moreover, two vertical sequences of small holes (diameter of ca. 1mm) were added on the excavated surface both to allow the CO_2 gas to flow in and also to the gaseous products of the reaction to flow out and be detected by the gas chromatograph. Indeed a capillary tube connected to the gas analysis system was inserted from the bottom of the sample holder to reach the empty volume near the cathode. Pieces of a Teflon O-ring

were inserted on the excavated surface to improve the contact between the metal foam and the ceramic porous matrix. A second O-ring was displaced along the perimeter of the surface to improve the sealing and to assure two distinct gas atmospheres in the cathode and anode side. Finally, the sintered half-cell and the cathode were located within two aluminium plates connected with insulating screws to improve the contact between the two parts of the electrochemical cell and the gas tightness, as shown in Fig. 7.2. The Ni foam was in direct contact with one of the aluminium plates, while the second plate faced the polytetrafluoroethylene (PTFE) holder as illustrated in Fig. 7.2. The sintered ceramic layers of YSZ laminated with the Ni foam happened to crack near the edges while assembling the different components and compressing them together. This might have an effect on the conductivity and on the mechanical stability of the cell depending on the size and position of the crack.

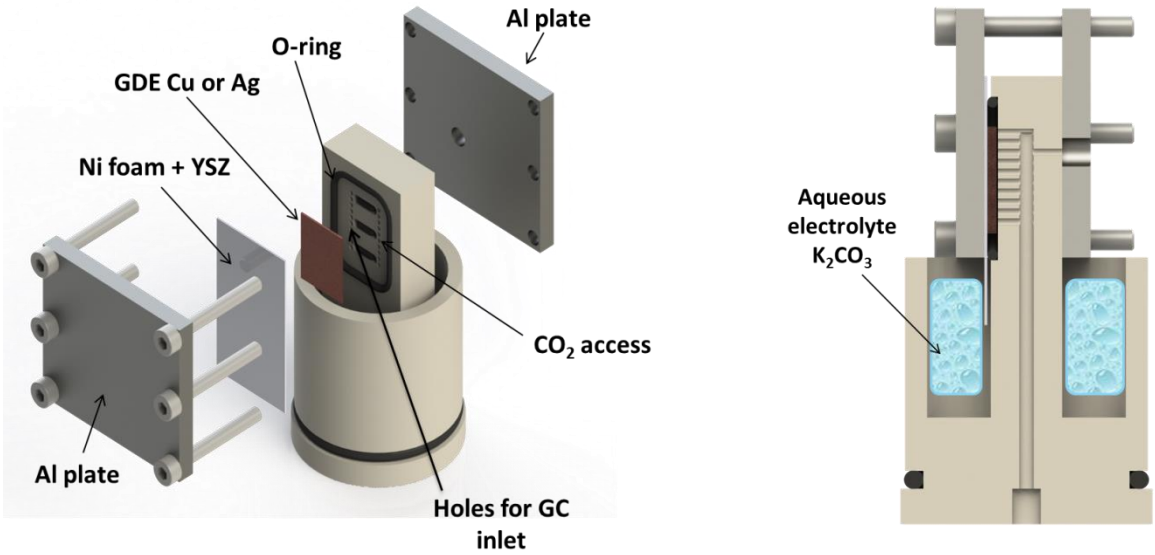

Fig. 7.2. Electrochemical cell holder for testing the foam based electrolyser cells. Left: Top-side view and Right: cross section view.

7.2.2 Characterization

The microstructure of the metal foams electrodes was investigated using a scanning electron microscope, SEM (Zeiss SUPRA), prior and after being tested electrochemically. In addition, X-ray photoelectron spectroscopy (XPS) was used to investigate the surface of pristine and electrochemically tested copper and silver foams. It was also studied by XPS the side of the ceramic porous electrolyte matrix in contact with the cathode to allow a better understanding of the reactions at the interface after the electrolysis test. The XPS analyses were performed on a K-alpha (Thermo Electron Limited, Winsford, UK) using a monochromatic Al-K_α X-ray source and a take-off angle of 90 from the surface plane. Atomic concentrations were determined from surface spectra (0–1350 eV, 200 eV detector pass energy, 50 ms dwell time, 3 scans) and were calculated by determining the relevant integral peak intensities using a Shirley type background. All XPS analyses were repeated three times on different surface locations. SEM and XPS analysis on pristine copper and metal

foams were performed two months after the reducing thermal treatment at 600 °C for 4 h in 9 vol% H_2/ N_2.

Mercury porosimetry analysis of the YSZ electrolyte matrix was performed by F. Allebrod[23] with an AutoPore IV 9500 porosimetry analyser, showing a mean pore size of 70 nm and a porosity of 45%.

Tests on different metal foams cathode were carried out in the high pressure electrochemical test station (limit: 100 bar, 300 °C), explained in detail elsewhere[24]. Electrochemical tests were usually performed at 25 °C and at pressures ranging from 2 bar to 20 bar, the duration of the test was approximately between 40 to 60 hours. In particular, copper metal foam electrode was also tested increasing the temperature from 25°C to 50 °C and in an interval of pressures from 2 bar to 5 bar. All the experiments were conducted in a gas configuration constituted by two separate atmospheres. The gas mixture present in the anode side (Ni-foam sintered with YSZ electrolyte matrix) was composed by N_2, H_2O (steam) and H_2. In order to avoid condensation of steam, inert gas as N_2 was introduced. In particular, the concentration of N_2 was modified from 83 vol% at a pressure of 2 bar, to 90 vol% at 20 bar. At the same time, H_2O concentration decreased from 5 vol% at 2 bar to 2 vol% at 20 bar and H_2 concentration from 12 vol% to 8 vol% within the same range of pressure. The total gas flow varied from 200 ml/min at 2 bar to 550 ml/min at 20 bar. The same ramping rate of 6 bar/h was set both for increasing and decreasing the pressure. In the cathode side (Cu or Ag foam) only CO_2 was present and the flow rate increased from 33 ml/min at 2 and 3 bar to 50 ml/min for higher values of pressure. All gas compositions, given in vol%, are presented as the inlet gas composition assuming no crossover of gases from one compartment to the other, i.e. a 100 % gas tight sealing and no mixing of gases.

The electrochemical measurements were performed using a Gamry reference 3000 potentiostat. Two-electrode mode experiments were carried out. The Cu or Ag electrode (the cathode when the cell is operating) was connected as the working electrode. The reference and counter potentiostat terminals were connected to the Ni electrode, which was intended as pseudo-reference electrode. The working electrode was negatively polarized compared to counter electrode. The voltage applied and the current densities obtained were therefore negative. Preparatory tests on symmetrical cells with nickel electrode foams were conducted at ambient temperature and increasing pressures from 2 to 20 bars to estimate the contribution of the polarization resistance. Electrochemical tests were performed at open circuit voltage and the same gas atmosphere at both electrodes was maintained. The gas mixture of N_2, H_2O (steam) and H_2 was varied with increasing pressure, as described above. Unfortunately, the recorded values of polarization resistance were not as small as expected, i.e. ca. 300 Ω cm^2 at 2 bar. A better pseudo-reference electrode could have been a platinum foam, but it was not available on the market. Therefore, it was decided to use nickel foam as anode electrode since it is widely used in analogous applications.
One measurement cycle was performed at each pressure and consisted of electrochemical impedance spectroscopy (EIS), cyclic sweep measurements (CV), chronoamperometry (CA) as well as measurements of the open circuit voltage (OCV). Table 7.1 and Table 7.2 present settings for the

EIS, CV, CA and OCV measurements performed during the different tests. Analysis of EIS data were carried out using ZSimpWin 3.21 and Elchemea Analytical.

Test 0 was conducted on copper foam increasing the pressure from 2 to 10 bar and for each value the cell was tested at three different potentials, i.e. -1.75, -2 and -2.5 V. Test 0 is described in Table 7.1. Afterwards, more detailed experiments were conducted both on copper and on silver only at -2.5 V, as reported in Table 7.2. Current density was expressed as the total current divided by the geometric surface area of the cathode (2 cm^2). Also the cells impedances were normalized by the same geometric surface area and expressed as $\Omega \cdot cm^2$.

Table 7.1. Summary of measurement types and settings used for measurements performed within each cycle during Test 0.

Step #	Measurement Type	Applied cell Voltage	Settings
1	**OCV**	--	30 minutes
2	**EIS**	OCV	100 kHz – 0.1 Hz AC amplitude 10mV
3	**CV**	OCV to -2.5 V	50 mV/s, 2 cycles
4	**CA**	-1.75 V	1.5 hours
5	**EIS**	-1.75 V	1 MHz – 0.1 Hz AC amplitude 10mV
6	**OCV**	--	15 mins
7	**CA**	-2 V	1.5 hours
8	**EIS**	-2 V	1 MHz – 0.1 Hz AC amplitude 10Mv
9	**OCV**	--	15 mins
10	**CA**	-2.5 V	1.5 hours
11	**EIS**	-2.5 V	1 MHz – 0.1 Hz AC amplitude 10Mv
12	**OCV**	--	15 mins

Table 7.2. Summary of measurement types and settings used for measurements performed within each cycle of test 1 to 3.

Step #	Measurement Type	Applied cell Voltage	Settings
1	**OCV**	--	1 hour
2	**EIS**	OCV	100 kHz – 0.1 Hz AC amplitude 10mV
3	**CV**	OCV to -2.5 V	50 mV/s, 2 cycles
4	**CA**	-2.5 V	2 hours
5	**EIS**	-2.5 V	1 MHz – 0.1 Hz AC amplitude 10mV
6	**OCV**	--	10 mins

Gas analysis was performed using a gas chromatograph (GC - Thermo Scientific, Trace 1300 Analyzer) equipped with thermal conductivity detectors (TCD). The autoclave was connected to the gas analysis system through a valve that could enable the operator to feed the GC with gas from the autoclave. Prior to introduction to the GC, the product flow from the cathode was passed through a gas/liquid separator (GLS) which condensed and separated any liquids from the gas stream. Inside the autoclave, a capillary tube was positioned next to the cathode to be in contact with the products of the CO_2 reduction. This capillary tube was also connected to the valve. Measurements were carried out continuously during all the duration of the test in order to control also the gas tightness between the two sides of the cell holder. The acquisition time of each chromatogram was of ca. 12 minutes. The aim was to determine the concentration of gaseous products such as hydrogen, CO, methane and other possible alcohols and hydrocarbons.

The faradaic efficiency (FE) of a gaseous product *x* was defined by the following equation:

$$FE(x) = \left(\frac{n_x \cdot F \cdot c_x \cdot f_m}{I}\right).$$

I represents the total current (in A), n_x is the number of electrons involved in the reduction, F is Faraday's constant, c_x is the mole fraction of the *x* product in the gaseous mixture examined (also equivalent to the volume fraction if gases are considered ideal), f_m is the molar flow rate in mol/s. The latter quantity is derived from the volume flow rate f_v by the equation $f_m = \frac{(p \cdot f_v)}{R \cdot T}$, with p equal to ambient pressure expressed in Pa, R the ideal gas constant and T the temperature expressed in K. The only cathode products detected were CO, H_2 and methane although it is anticipated that trace quantities of other products in the liquid phase were generated during the experiments. The standard deviation associated to the quantification of the faradaic efficiency for each condition analyzed was of ca. 10 % for hydrogen, while for CO and CH_4 it was of 2% relative to the reported values.

7.3 Results

7.3.1 Microstructure

SEM images of the pristine nickel, copper and silver foams are shown in Figures 7.3, 7.4 and 7.5, respectively. The pore size of the nickel is ca. 450 μm, the silver is ca. 150 μm and the copper is ca. 50 μm according to the manufacturer's specification. It can be seen that the surface of nickel foam is relatively smooth compared to the copper and silver foams.

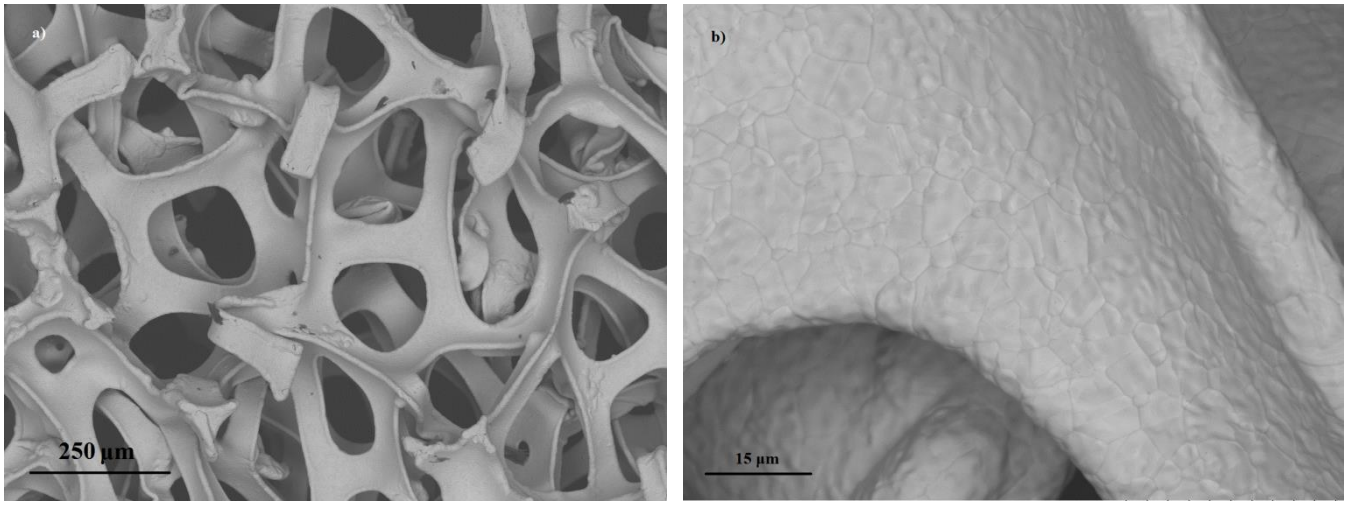

Fig. 7.3. SEM pictures of an untreated nickel foam. Note: the magnifications are different as indicated by the scale bars.

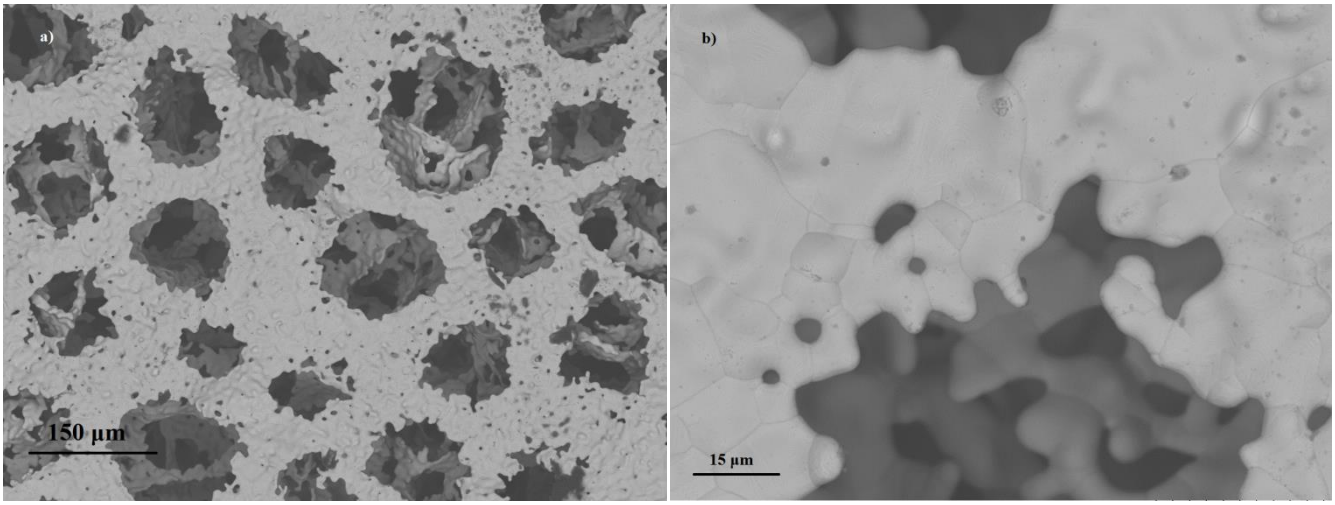

Fig. 7.4. SEM pictures of an untreated copper foam. Note: the magnifications are different as indicated by the scale bars.

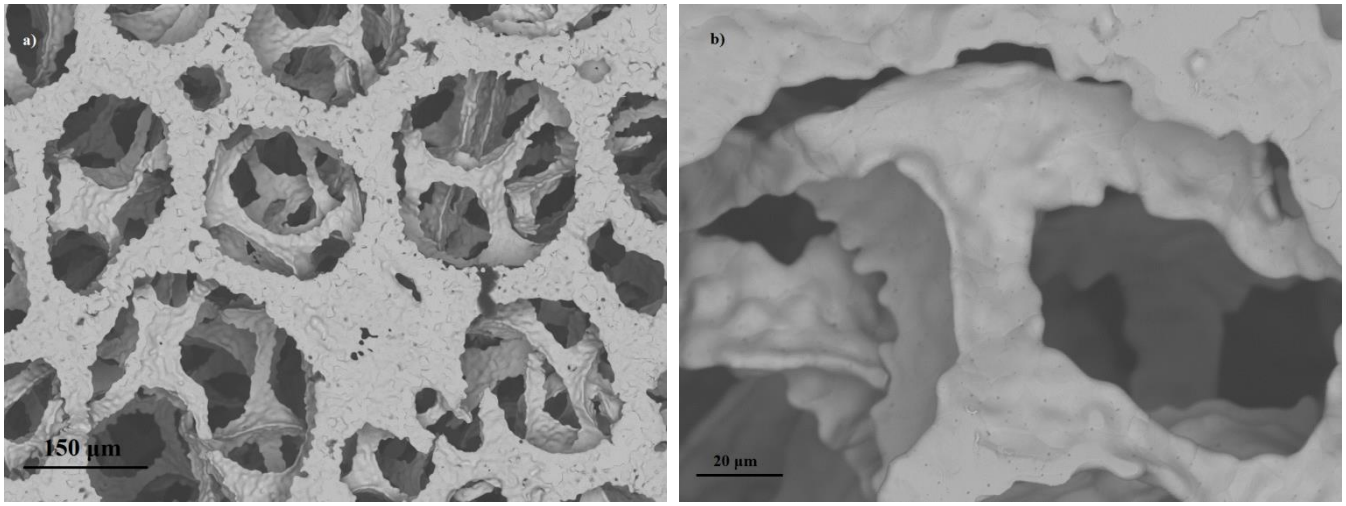

Fig. 7.5. SEM pictures of an untreated silver foam. Note: the magnifications are different as indicated by the scale bars.

In addition, X-ray photoelectron spectroscopy allowed a qualitative and quantitative analysis of the elements present in a thickness within 5 to 10 nm from the surface in the copper and silver pristine foams. Figs. 7.6 and Fig. 7.7 show XPS spectra recorded on pristine copper and silver foam, respectively. From the survey spectra, not shown here, it was possible to determine that the surface belonging to the pristine copper foam consisted of CuO that has a significantly different Cu-2p spectrum compared to Cu_2O and Cu[25]. However, for Ag pristine foam the photoelectron analysis was not sufficient to correctly identify its oxidation state. In addition, the quantitative surface region analysis specific of each foam is reported. The concentration of carbon can be explained by adventitious adsorbed hydrocarbon from ambient air, even after being introduced to the ultra-high vacuum chamber of the XPS. However, that should only account for 10-15 atom%, so the foams are unusually contaminated. The aspect that the other apparent contaminants are nitrogen, oxygen, sulphur and chlorine (on silver surfaces) suggests that the analysed surfaces were contaminated from sample handling, such as the thermal treatment in reducing atmosphere in tube furnaces.

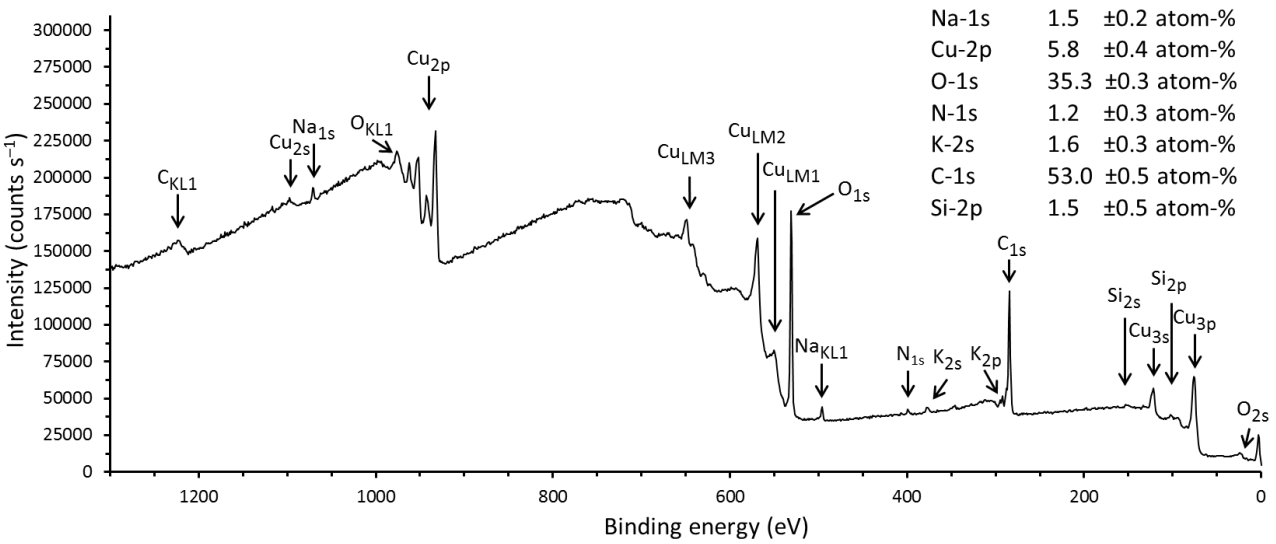

Fig. 7.6. XPS spectra of the pristine surface copper foam. It is also reported the quantitative analysis of the elements detected on the surface.

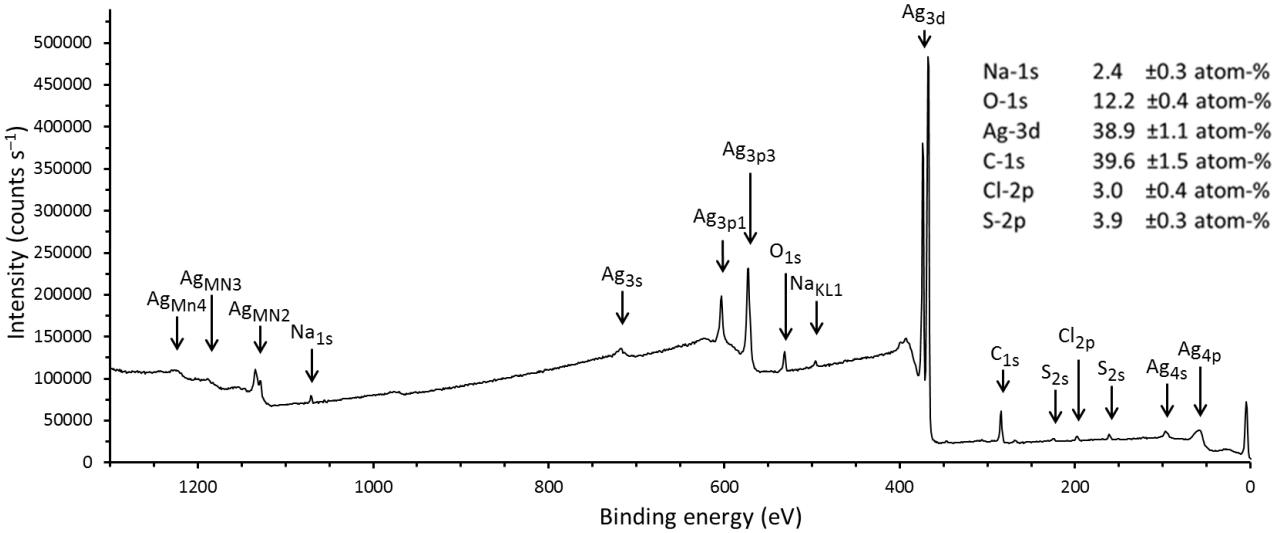

Fig. 7.7. XPS spectra of the pristine surface silver foam. It is also reported the quantitative analysis of the elements detected on the surface.

7.3.2 Electrochemical characterization

7.3.2.1 Copper

Results from electrochemical impedance spectroscopy measurements on the copper cathode foam are presented in Fig. 7.8 a), b) and c). These results were acquired during Test 0. Three different voltages were applied to the cell, -1.75 V, -2 V and -2.5 V at each different pressure from 2 to 10 bar.

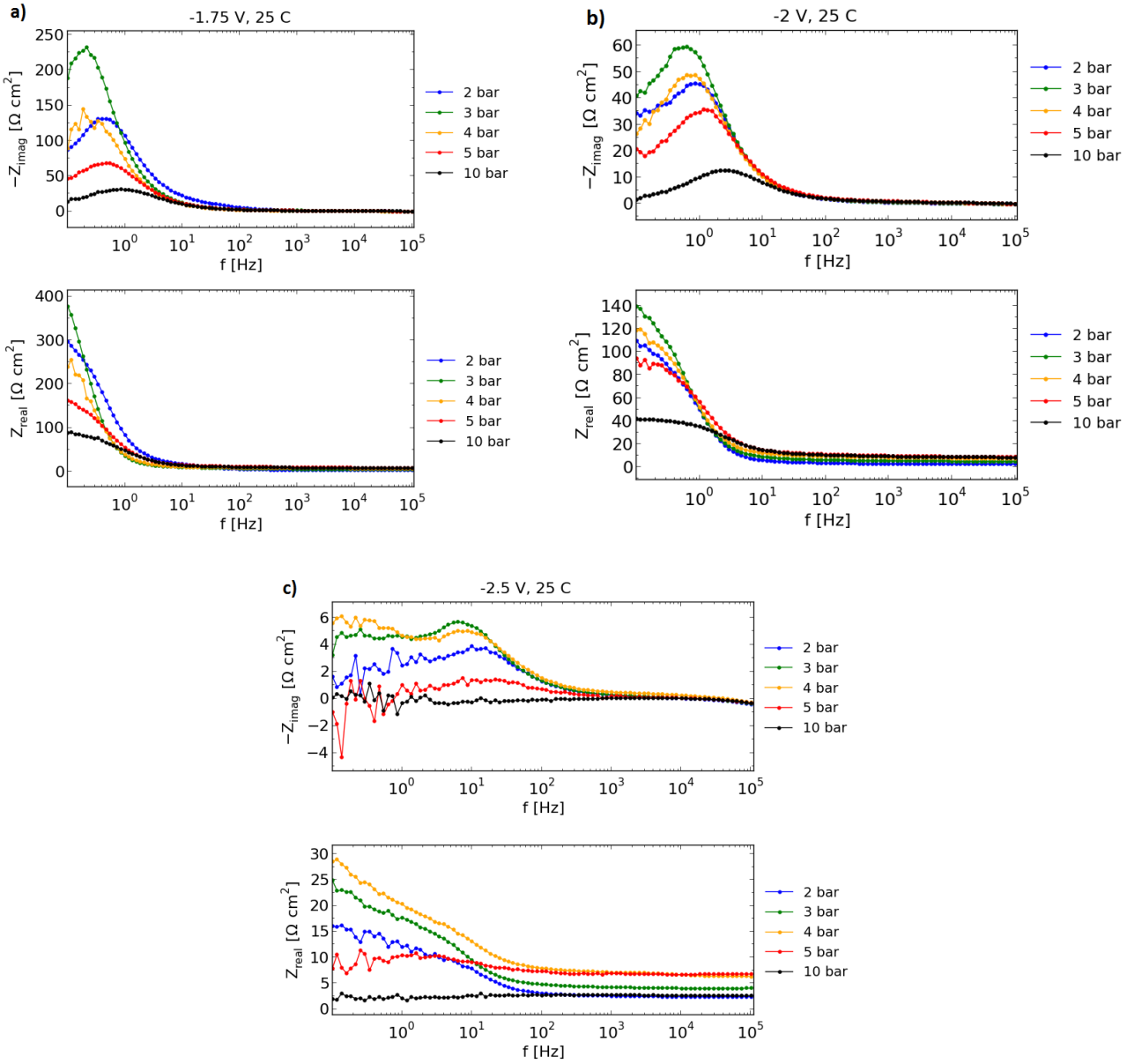

Fig. 7.8. Bode representation of EIS measurements performed on copper foam based cathode at pressures varying from 2 to 10 bar and different applied potential: a) -1.75 V , b) -2 V, c) -2.5V. The gas mixture present in the anode side was composed by N_2, H_2O (steam) and H_2 while on the cathode was only CO_2.

Table 7.1 reports the order and the type of measurements performed during Test 0. It is possible to observe how the total cell resistance ($R_{tot} = R_s + R_p$), the polarization resistance (R_p, electrode, mass transfer) and the serial resistance (R_s, ohmic resistance i.e. electrolyte and contact resistance) changed for increasing applied potentials (from -1.75 V, -2 V to -2.5 V) and increasing pressure. The highest values of R_p and therefore also R_{tot} were obtained for the EIS recorded at -1.75 V and -2 V. For impedance spectra recorded at -1.75 V and -2 V, the R_p significantly decreased while increasing the pressure from 2 to 10 bar, as it is possible to see in Fig. 7.8 a) and Fig. 7.8 b). Indeed, when applied -1.75 V, R_{tot} decreased from ca. 450 $\Omega \cdot cm^2$ at 3 bar to ca. 100 $\Omega \cdot cm^2$ at 10 bar. The R_s, instead, gradually increased when increasing the pressure. In particular, as shown in Fig. 7.8 a) and in Fig. 7.8 b) the R_s went from 2.5 $\Omega \cdot cm^2$ at 2 bar to 10 $\Omega \cdot cm^2$ at 10 bar when applied -1.75 and -2V. Conversely, the impedance spectra registered at -2.5 V exhibited the lowest values of R_{tot}, but it increased from 17 $\Omega \cdot cm^2$ at 2 bar to ca. 40 $\Omega \cdot cm^2$ at 4 bar, as shown in Fig. 7.8 c). Then the EIS measurements started to be unstable at 5 bar only when the cell was polarized to -2.5 V (Fig. 7.8 c)). However, the following EIS spectra acquired at 10 bar pressure and polarization of -1.75 and -2 V were still stable. The last EIS spectra at 10 bar and -2.5 V was totally unstable (Fig. 7.8 c).
The OCV measured at 2 bar, before polarizing the cell, was around + 450 $\pm$ 10 mV. The OCV acquired after the cell was polarized dropped to negative values as – 1100 $\pm$ 10 mV at 2 bar pressure (step #12 of the first cycle). During the OCV measurements at 3, 4 bar and up to 5 bar, the values recorded oscillated around – 1000 mV, except for the last OCV acquisition at 5 bar where the voltage decreased to less negative values, as ca. – 35 $\pm$ 5 mV. Along the OCV measurements at 10 bar the voltage went from -20 mV at step #1 to ca. -5 mV at step # 12.

Fig. 7.9 a), b) and c) show the current density vs. time profile of the different chronoamperometric measurements at the three polarization of -1.75, -2 and -2.5 V, respectively. The current remained stable when the applied voltage was -1.75 V and -2 V. The current density registered at -2.5 V at 5 and 10 bar increased significantly during the ninety minutes of chronoamperometric measurements. In particular, at 10 bar the current density varied from -30 mA/ cm^2 to -500 mA/ cm^2 when applying -2.5 V, but also for the other two values of voltages the current density increased. However, the high current density registered did not lead to an increase of production of hydrocarbons at the cathode electrode. The gas chromatograms reported CO production only during the last hour of chronoamperometry measurement at 2 bar and only when applying -2.5 V. H_2 evolution was always detected when applying -2 V and -2.5 V as electrolysis voltage and its highest concentration was obtained during the measurement at 2 bar and -2.5 V. The calculated faradaic efficiency at 2 bar and -2.5 V was: 9 % for CO production and 91% for H_2 evolution. At higher pressures (up to 10 bar) it was not possible to detect the production of any hydrocarbons, even if the current density was high.

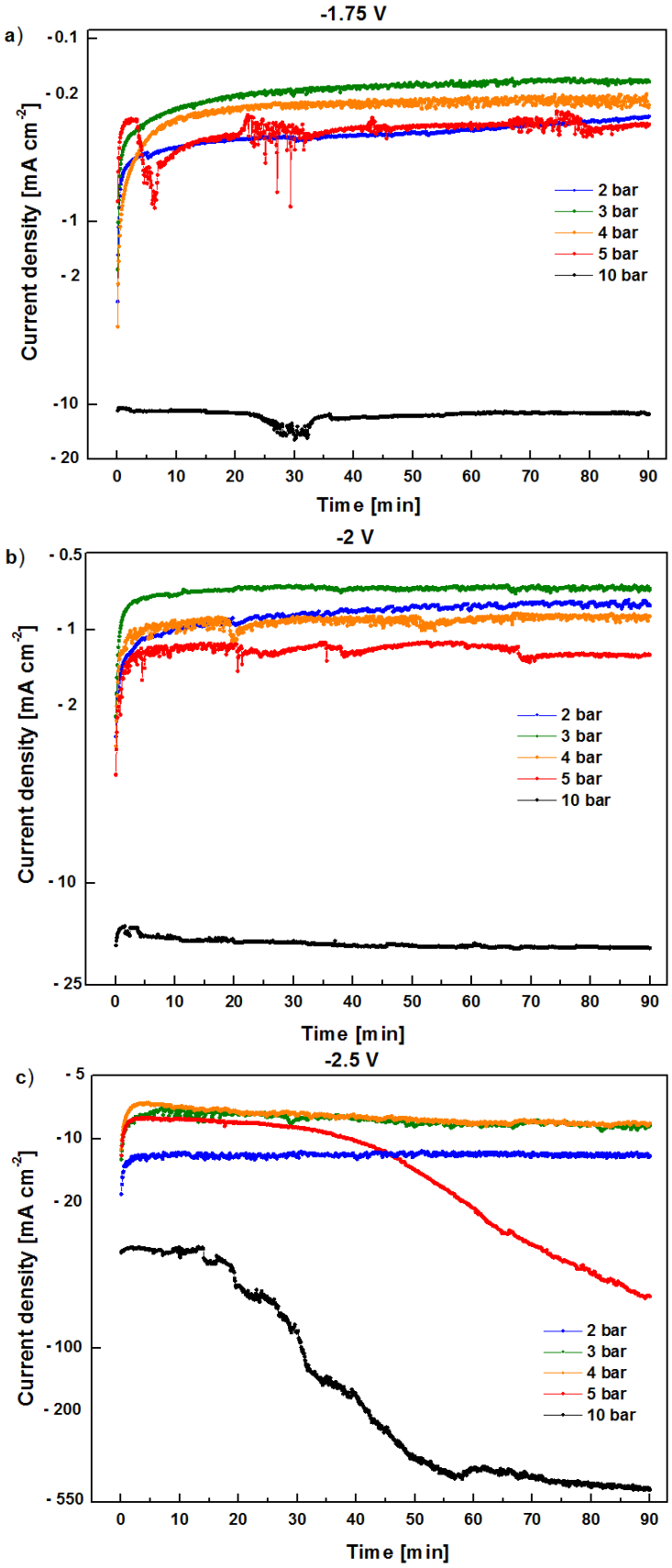

Fig. 7.9. CO_2 reduction current densities as a function of time at pressures from 2 to 10 bar and at different voltages: a) -1.75 V, b) -2 V and c) -2.5 V.

Other electrolysis tests were conducted using Cu foam cathodes. Firstly the pressure was increased from 5 bar to 20 bar and the temperature was maintained at 25 °C. For simplicity this test will be defined as Test 1 along the Chapter. Another test was performed in a different cell at the initial temperature of 25 °C and then was increased up to 50 °C. The pressure was raised from 2 bar to a maximum of 5 bar in each value of temperature. In this case, the test will be called Test 2. In both tests the cells were analysed only at the most negative voltage of -2.5 V, after taking in consideration the previous results. Table 7.2 reports the order and the type of measurements performed during Test 1 and Test 2. In Fig. 7.10 are shown the total cell resistance, the polarization resistance and the serial resistance reported both at OCV and when applied -2.5 V for the electrolysis test at high pressure, up to 20 bar and 25 °C (Test 1). After reaching 20 bar pressure, electrolysis measurements were done also decreasing the pressure to 10 bar, 5 bar and finally 2 bar. The values of R_s and R_{tot} were obtained by modelling the stable EIS spectra with a R_s in series with 3 (RQ) circuits.

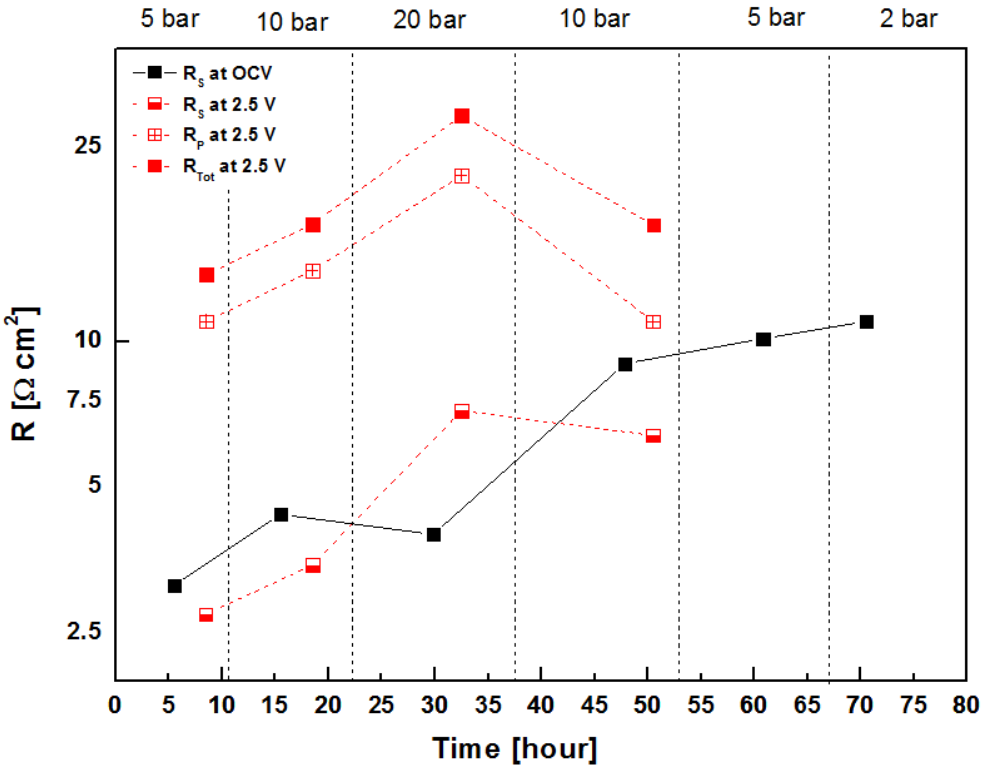

Fig. 7.10. Total cell resistance, serial resistance and electrode polarization resistance for EIS measurements showed in Fig. 7.11 a) and b), and additional measurements performed at OCV before each CA measurement. The y axis is plotted on a logarithmic scale.

From the EIS spectra acquired at 20 bar it was possible to observe an increase in R_s and also in R_p, compared to the previous values, as reported in Fig. 7.11 a). Then, during the ramp down phase from 10 bar to 2 bar, the EIS measurements started to be unstable as shown in Fig. 7.11 b). Since it was not possible to identify the R_{tot} and R_s values, they are not indicated in Fig. 7.10.

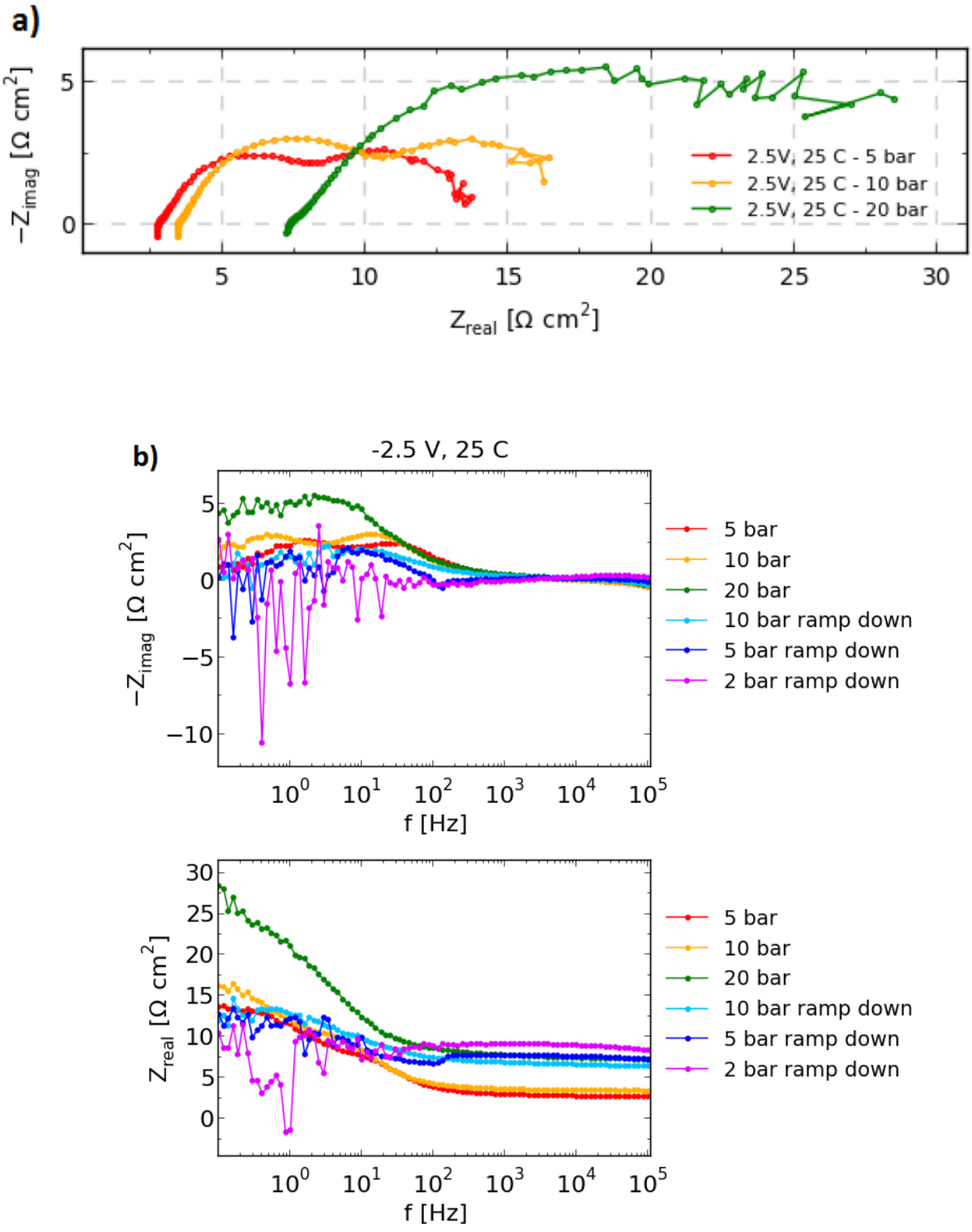

Fig. 7.11. Representation of EIS measurements performed on copper foam based cathode when applied a potential of -2.5 V and at pressures varying: a) from 5 to 20 bar (Nyquist plot) and b) from 10 to 2 bar (Bode plot).

The OCV measured at 5 bar, before polarizing the cell was ca. + 460 ± 10 mV. The measured OCV dropped to negative values as – 980 mV, -1060 mV and -1200 mV after the cell was polarized (step #6 of Table 7.2) and the pressure was of 5, 10 and 20 bar, respectively. Along the ramp down phase of pressure from 10 bar to 5 and then to 2 bar, the OCV acquisitions reported less negative values, as ca. -30 mV, -530 mV and – 20 mV, respectively.
In parallel, the current density registered during the two hours of chronoamperometry began to be not steady already at 10 bar during the decreasing phase of total pressure, as reported in Table 7.3.

Table 7.3. Average current density (mA/ cm^2) obtained from CA measurements performed for 2 hours at -2.5 V applied cell voltage and various pressures.

Applied cell voltage	*5 bar*	*10 bar*	*20 bar*	*10 bar*	*5 bar*	*2 bar*
-2.5 V	-14	-11	-9	-10 to -38	-25 to -56	-33 to -65

The gas chromatograms detected CO when the electrolysis voltage of -2.5 V was applied at 5 bar and 10 bar. On the other hand H_2 evolution was observed during all the different pressure conditions. The faradaic efficiency calculated at 5 bar is 4% for CO and 96% for H_2, while at 10 bar is 0.75% for CO and 99% for H_2. For the other values of pressure the only product detected was hydrogen, which decreased in concentration with decreasing pressure.

In Fig.7.12 are shown the total cell resistance, the polarization resistance and the serial resistance both at OCV and when applied -2.5 V for the electrolysis test at lower values of pressure, up to 5 bar and for two different temperatures, i.e. 25 °C and 50 °C (Test 2). The y axis is plotted on a logarithmic scale.

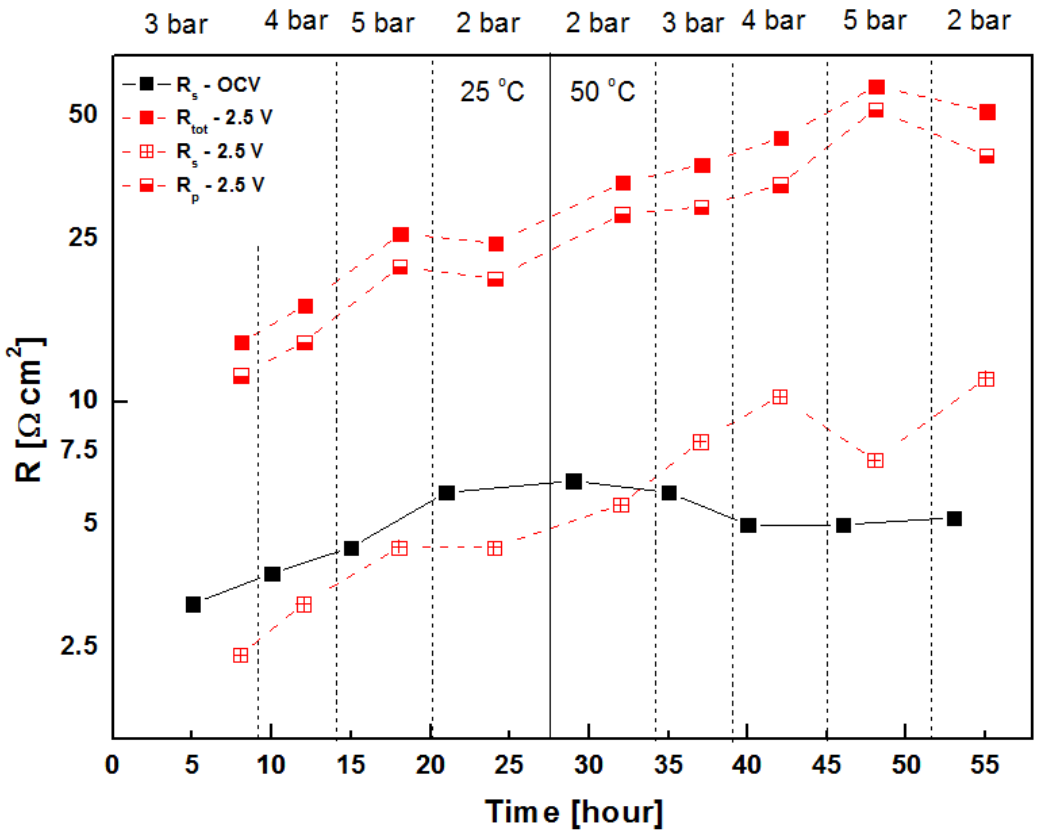

Fig. 7.12. Total cell resistance, serial resistance and electrode polarization resistance for EIS measurements showed in Fig. 7.13 a) and b), and additional measurements performed at OCV before each CA measurement.

The R_s and the R_p registered, when polarizing the cell, increased gradually with time while changing the pressure and the temperature. The values of R_s and R_{tot} were obtained by modelling the EIS spectra acquired at 25°C and at 50°C with a R_s in series with 3 (RQ) circuits. In particular, R_s went from 3 Ω·cm^2 at 3 bar and 25 °C to 10 Ω·cm^2 at 2 bar during the ramp down phase at 50 °C. The R_p, instead, increased from 12 Ω·cm^2 to 40 Ω·cm^2 for the same range of pressure and temperature. The R_s measured at OCV during Test 2 was almost constant, i.e. from 3 Ω·cm^2 to 5 Ω·cm^2. The EIS spectra acquired during the test at 25 °C are reported in Fig. 7.13 a) and for the measurements at 50 °C in Fig. 7.13 b).

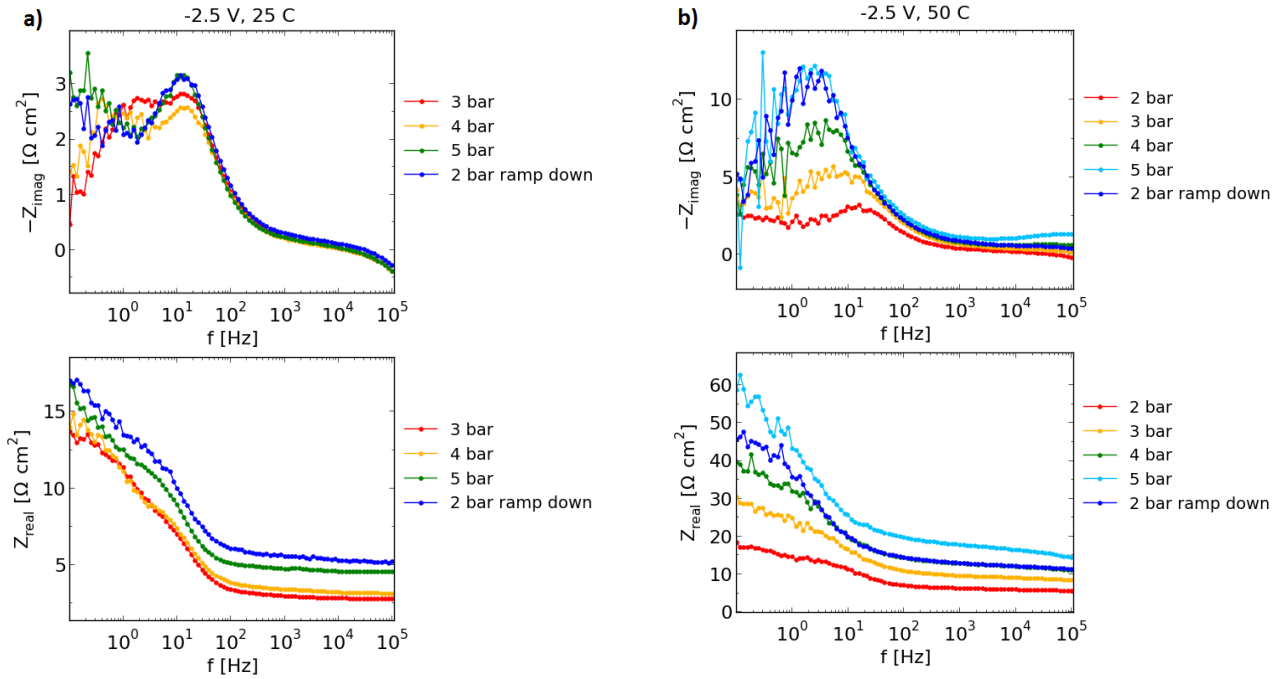

Fig. 7.13. Bode representation of EIS measurements performed on copper foam based cathode when applied a potential of -2.5 V and at pressures varying: a) from 3 to 5 bar and after the ramp down at 2 bar, and b) from 2 to 5 bar after the ramp down at 2 bar. The operational temperature was 25°C in a) and 50 °C in b).

The OCV measured at 3 bar and 25 °C, before polarizing the cell was ca. + 480 ± 10 mV. Then the OCV dropped (step #1) to negative values as – 550 mV, -680 mV and -800 mV for 4, 5 bar and 2 bar after the ramp down phase. When increasing the temperature to 50 °C the OCV maintained negative values varying from -770 mV at 2 bar to -1130 mV at 2 bar after the ramp down phase.
The EIS spectra recorded at 3 bar pressure and 25 °C is modelled by a resistor R_s in series with three (RQ) circuits, as shown in Fig. 7.14.

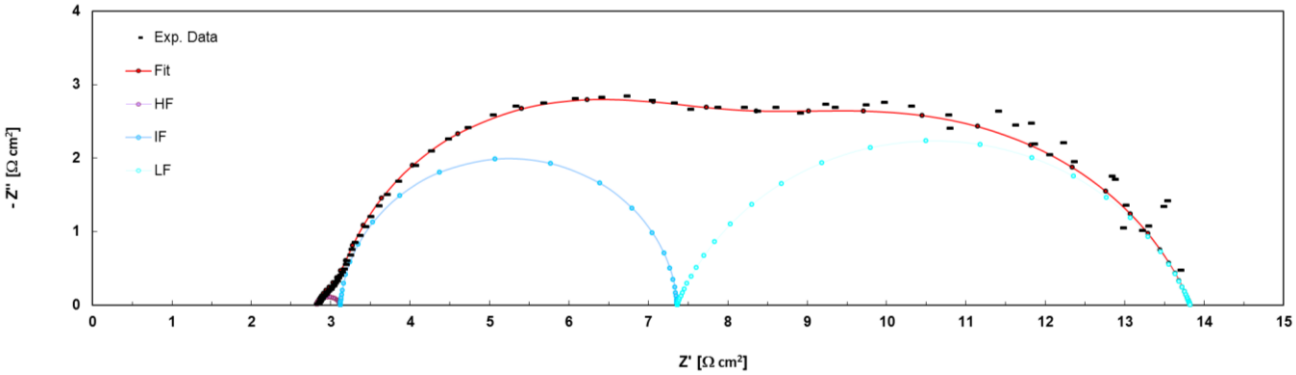

Fig. 7.14. Nyquist representation of EIS spectra performed when applying a cell voltage of -2.5V at 3 bar pressure and T = 25°C. Gas conditions: 86 vol % N_2 + 4 vol % H_2O + 10 vol % H_2 in the anode side and 100 vol % CO_2 on the cathode side.

The impedance of the Q element (constant phase element) is given by $Z_q = [Y_0(j\omega)^n]^{-1}$ and $0 < n < 1$[26]. The high frequency (HF) semicircle reported a pseudocapacitance of $6.6 \cdot 10^{-4}$ F/cm^2, a value of n equal to 0.8, while R was 0.3 Ω·cm^2. The intermediate frequency (IF) semicircle showed a pseudocapacitance of $2 \cdot 10^{-3}$ F/cm^2, n = 0.98 and R equal to 4 Ω·cm^2.The low frequency (LF) semicircle was characterized by a presudocapacitance of $1.68 \cdot 10^{-2}$ F/cm^2, n = 0.76 and R equal to 6.9 Ω·cm^2. The average error between fitted and measured data is less than 1%.
The chronoamaperometric measurements done at the different pressures reported stable values and the variation in current density among the various pressures was little, as shown in Table 7.4.

Table 7.4. Average current densities (mA/ cm^2) obtained from CA measurements performed for 2 hours at -2.5 V applied cell voltage and various pressures.

Applied cell voltage	*3 bar 25 °C*	*4 bar 25 °C*	*5 bar 25 °C*	*2 bar 25 °C*	*2 bar 50 °C*	*3 bar 50 °C*	*4 bar 50 °C*	*5 bar 50 °C*	*2 bar 50 °C*
-2.5 V	-15	-16	-12	-14	-15	-10	-10	-8.5	-8

The gas chromatograms detected CO when applying the electrolysis voltage of -2.5 V at 3, 4, 5 bar and 2 bar after the ramping down phase at 25 °C. In addition, CO was also detected at 2 and 3 bar when the temperature was increased to 50 °C. The concentration of CO was higher during the electrolysis conducted at 4 and 5 bar at 25 °C. On the other hand H_2 evolution was observed during all the different pressure conditions. In addition, CH_4 was detected during the measurement acquired at 2 bar and 25 °C. The faradaic efficiencies calculated at the different pressures are reported in Table 7.5.

Table 7.5. Average CO, H_2 and CH_4 faradaic efficiency during the 2 hours of CA measurements. The applied cell voltage was of -2.5 V.

Faradaic Efficiency (%)	*3 bar 25 °C*	*4 bar 25 °C*	*5 bar 25 °C*	*2 bar 25 °C*	*2 bar 50 °C*	*3 bar 50 °C*
CO	0.2	1.2	1.3	0.5	0.6	0.4
CH_4	-	-	-	3.38	-	-
H_2	99.8	98.8	98.7	96	99.4	99.6

7.3.2.2 Silver

Silver foams were also tested as gas diffusion cathode at high pressures, up to 20 bar and at 25 °C. In Fig. 7.15 are shown the total cell resistance, the polarization resistance and the serial resistance reported both at OCV and when applied -2.5 V for the electrolysis test at high pressure. After reaching 20 bar pressure, electrolysis measurements were done also decreasing the pressure to 10 bar, 5 bar and finally 2 bar. This test is called Test 3. Table 7.2 reports the order and the type of measurements performed during Test 3. The EIS spectra recorded at 3, 4 and 5 bar were stable, while the spectra acquired after were not, and it was not possible to identify the R_s and R_p when the cell was polarized to -2.5 V.

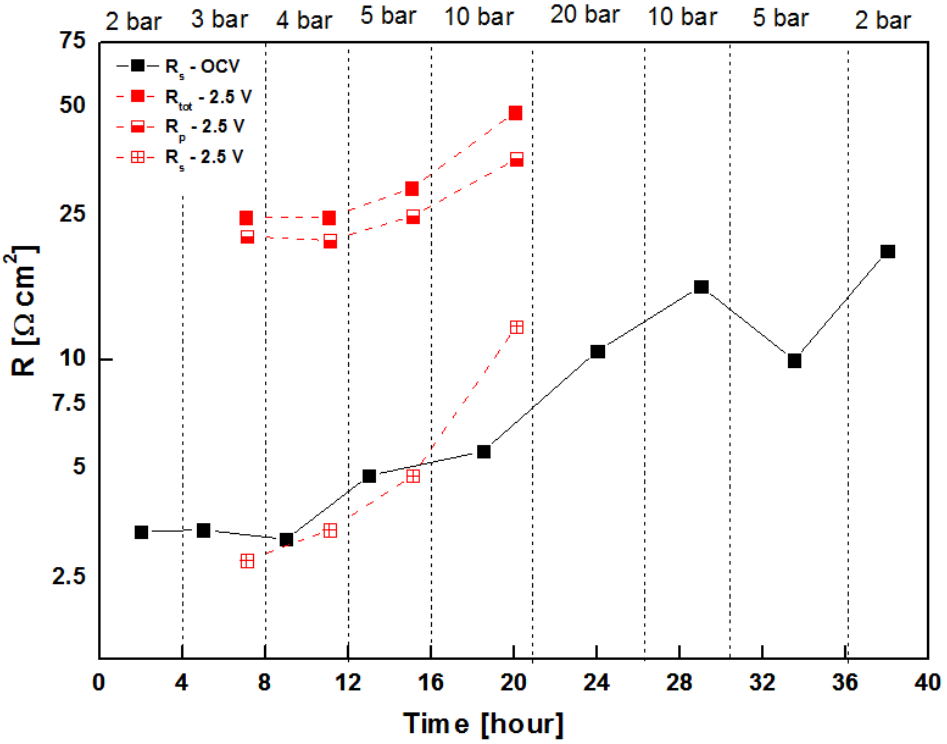

Fig. 7.15. Total cell resistance, serial resistance and electrode polarization resistance for EIS measurements showed in Fig. 7.16 a) and b), and additional measurements performed at OCV before each CA measurement. The y axis is plotted on a logarithmic scale.

The EIS spectra recorded at pressures up to 5 bar and when polarized the cell to -2.5 V are shown in Fig. 7.16 a) and b). Indeed, the R_s acquired at OCV increased with time from 3 $\Omega \cdot cm^2$ at 2 bar to 20 $\Omega \cdot cm^2$ at 2 bar after the ramping down phase from 20 bar pressure. The OCV measured at 3 bar, before polarizing the cell, was around + 220 $\pm$ 10 mV. As soon as the cell was polarized, the OCV acquired after the chronoamperometric tests (step #6) dropped to negative values as – 1300 $\pm$ 20 mV from 3 bar to 2 bar after the ramp down phase. On the other hand, the OCV measured before polarizing the cell (step #1) registered again positive values as +560 mV, +250 mV, +600 mV, +580 mV, +440 mV, +420 mV and + 20 mV from 4 bar to 2 bar after the ramp down phase in pressure.

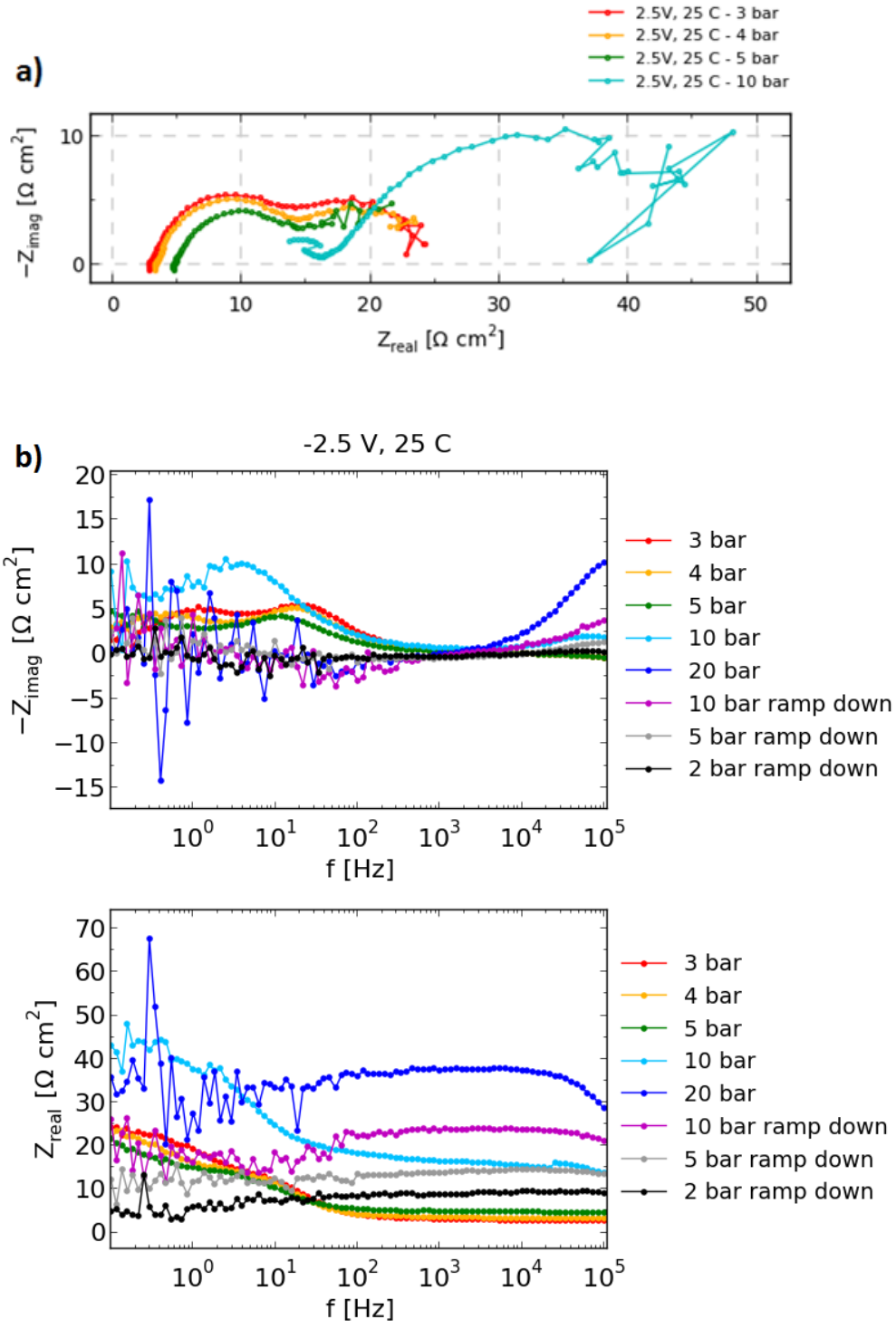

Fig. 7.16. Representation of EIS spectra performed on Ag based cathode foam when applied a potential of -2.5 V and at pressures varying: a) from 3 to 10 bar (Nyquist plot), and b) from 3 to 20 and along the ramp down phase to 2 bar (Bode plots).

The EIS spectra recorded at 3 bar pressure and 25 °C is modelled by a resistor R_s in series with three (RQ) circuits, as shown in Fig. 7.17. The impedance of the Q element[26] (constant phase element) is given by $Z_q = [Y_0(j\omega)^n]^{-1}$ and $0 < n < 1$. The high frequency (HF) semicircle reported a pseudocapacitance of $3 \cdot 10^{-4}$ F/cm^2, a value of n equal to 0.8, while R was 0.45 Ω·cm^2. The intermediate frequency (IF) semicircle showed a pseudocapacitance of $7 \cdot 10^{-4}$ F/cm^2, n = 0.95 and R equal to 9.6 Ω·cm^2.The low frequency (LF) semicircle was characterized by a presudocapacitance of $1.3 \cdot 10^{-2}$ F/cm^2, n = 0.8 and R equal to 11.6 Ω·cm^2. The average error between fitted and measured data is less than 1%.

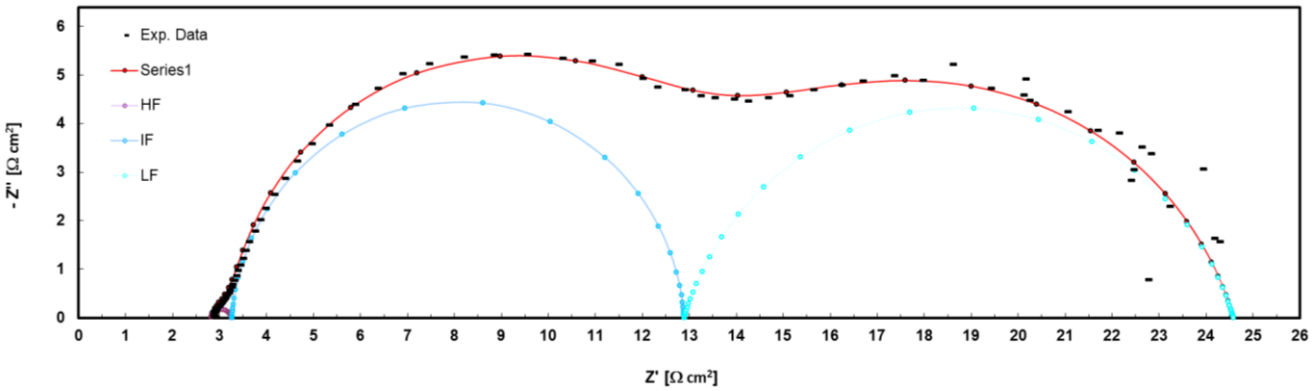

Fig. 7.17. Nyquist representation of EIS spectra performed when applying a cell voltage of -2.5V at 3 bar pressure and T = 25°C. Gas conditions: 86 vol % N_2 + 4 vol % H_2O + 10 vol % H_2 in the anode side and 100 vol % CO_2 on the cathode side.

The current density recorded during the chronoamperometry measurements started to be instable at 10 bar pressure of the ramping up phase and the instability become more severe with time and varying the pressure. The average current densities are reported in Table 7.6.

Table 7.6. Average current densities (mA/cm^2) from CA measurements performed for 2 hours at -2.5 V applied cell voltage and various pressures.

Applied cell voltage	*3 bar*	*4 bar*	*5 bar*	*10 bar*	*20 bar*	*10 bar*	*5 bar*	*2 bar*
-2.5 V	-7	-7.5	-8	-10 to - 5	-7to -30	-36to -50	-45to -135	-180 to - 200

The gas chromatograms detected CO when the electrolysis voltage of -2.5 V was applied at 3, 4 and 5 bar. On the other hand, H_2 evolution was observed during all the different pressure conditions. The faradaic efficiency calculated for H_2 and CO at the different pressures is reported in Table 7.7. For the other values of pressure the only product detected was hydrogen, which decreased in concentration over decreasing pressure.

Table 7.7. Average CO and H_2 faradaic efficiency during the 2 hours of CA measurements. The applied cell voltage was of -2.5 V.

Faradaic Efficiency (%)	*3 bar*	*4 bar*	*5 bar*
CO	38	50	20
H_2	62	50	80

7.3.3 Post mortem analysis

7.3.3.1 Scanning electron microscopy (SEM)

SEM images were taken both on the Ni foam and on the YSZ layer, and on the different cathode electrodes (Cu and Ag) after electrochemical testing in high pressure. In particular, micrographs taken on the cathode after Test 2 and Test 3 are reported in Fig. 7.17 and Fig.7.18, respectively.

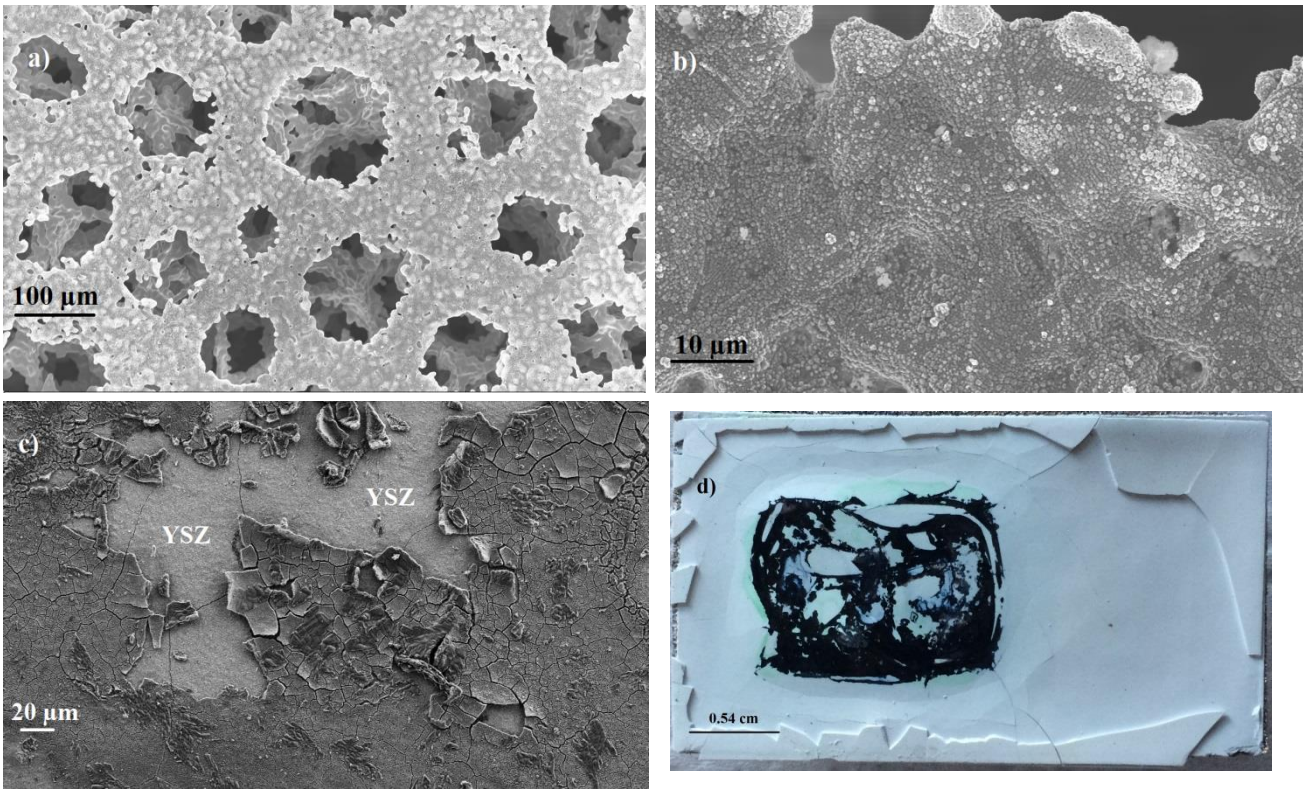

Fig. 7.18. Images taken on the electrolyser cell after Test 2. a) SEM image of the copper foam cathode, b) magnified SEM image of the copper foam, c) SEM image of YSZ layer in contact with the copper foam and d) photograph of the YSZ layer after the test; the black rectangular area corresponds to where the copper foam was put in contact.

The surface of the cathodes facing the ceramic porous layer was analysed. Copper foam used as cathode in Test 2 is shown in Fig. 7.18 a) and b). In Fig. 7.18 c) is possible to observe a micrograph taken on the YSZ porous matrix which was in contact with the copper foam during the test, while Fig. 7.18 d) shows an overview picture taken after the experiment. The surface of the YSZ matrix that had been in contact with the Cu foam was covered by a black layer. No major cracks in the contacted part of the YSZ matrix were observed. The pores of the copper foam cathode were still open and allowed proper gas diffusion. Comparing the images of the pristine copper foam (Fig. 7.4) and the tested one (Fig. 7.18), it is possible to observe the formation of particles having a diameter of ca. 0.5 μm after the electrochemical characterization. These particles were distributed along all the active surface of the tested copper foam. Anyway, the copper foam was still in fairly good condition after Test 2.

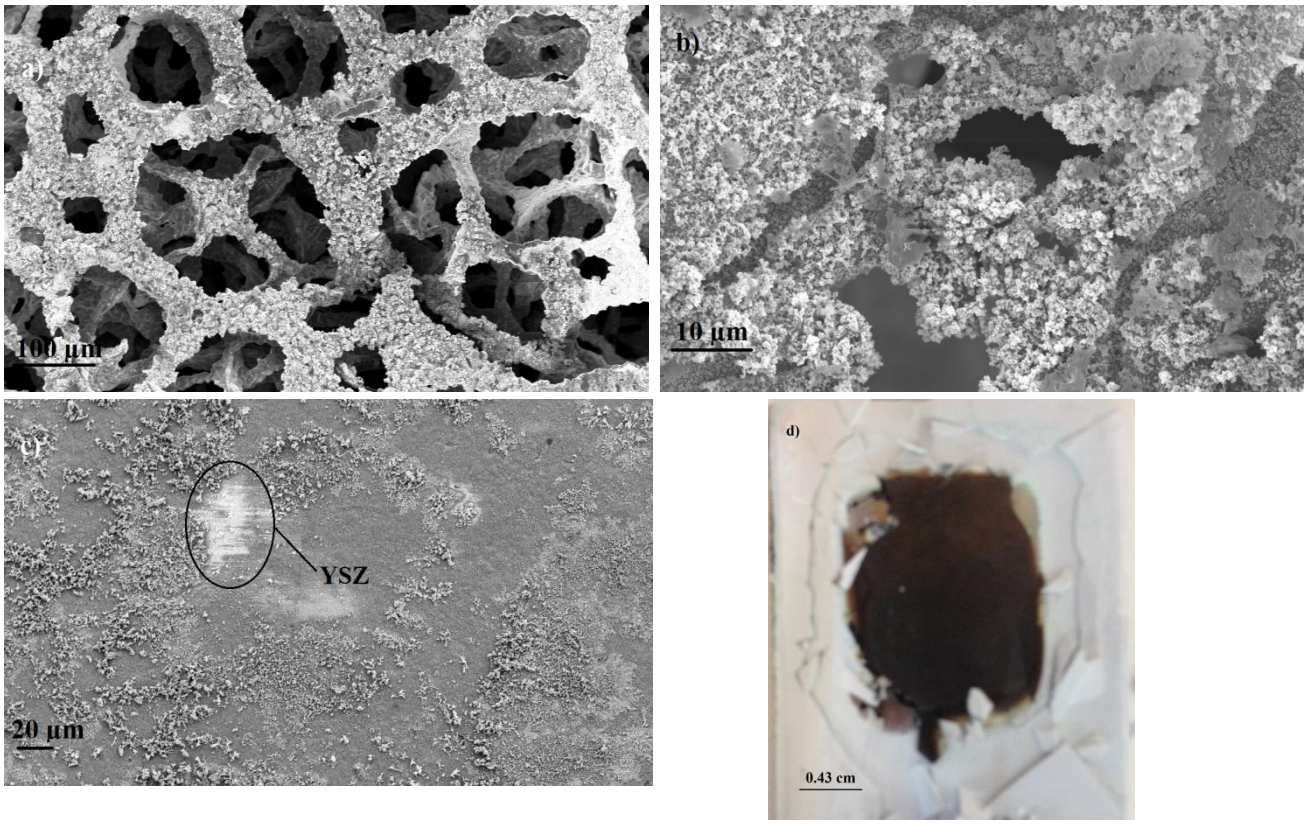

Fig. 7.19. Images taken on the electrolyser cell after Test 3. a) SEM image of the Silver foam cathode, b) magnified SEM image of the silver foam, c) SEM image of YSZ layer in contact with the silver foam and d) photograph of the YSZ layer after the test; the black rectangular area corresponds to where the silver foam was put in contact.

On the other hand, the silver foam after Test 3 appeared to be more affected by the electrochemical test. The edges of the Ag foam reported some etchings and cuts, as pointed out by Fig. 7.19 a). In addition, in Fig. 7.19 b) it is possible to notice the formation of a dense layer of agglomerated particles that covers the tested foam, and it was absent in the pristine Ag foam (Fig. 7.5 b)). Fig.

7.19 c) shows a micrograph taken on the YSZ porous matrix which was in contact with the silver foam during Test 3, while Fig. 7.19 d) shows an overview picture taken after the experiment. The contacted surface presented minor cracks but it was completely covered by a black layer.
The SEM study done on nickel foam, after Test 3, reveals severe degradation of its external surface. Ni foam presents deep cuts and etchings also in the more internal parts of the porous structure, as shown in Fig. 7.20 a). A higher magnification image (Fig. 7.20 b) exhibits the formation of a dense coating which was absent in the pristine nickel foam (Fig. 7.3). The nickel anode after the test became rough and scabrous. The pores appear to be partially closed and obstructed.

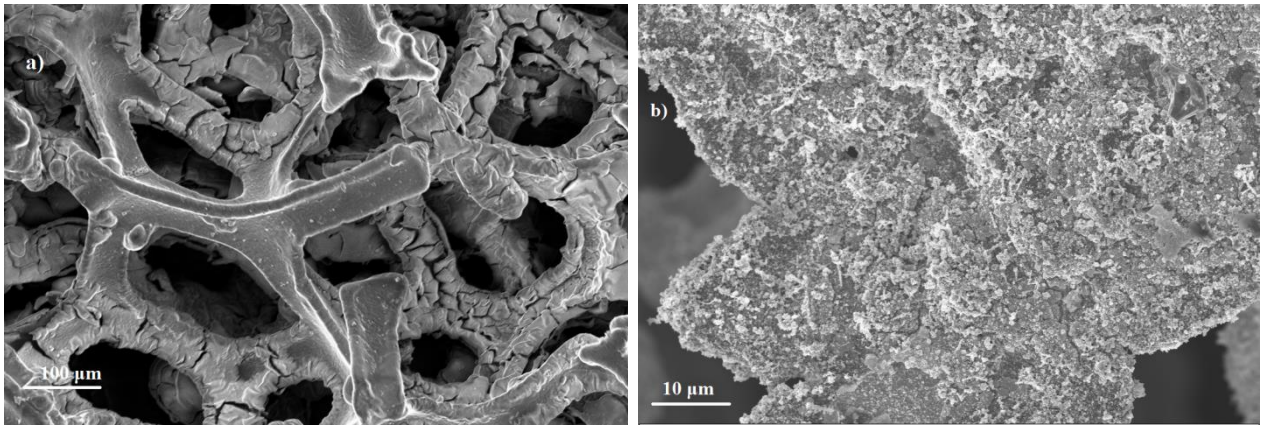

Fig. 7.20. Images taken on the electrolyser cell after Test 3. a) SEM image of the nickel foam anode, b) magnified SEM image of the nickel foam.

7.3.3.2 X-ray photoemission spectroscopy (XPS)

The surface composition of the tested cathode foams and of the YSZ layers (Fig. 7.18 (c) and Fig. 7.19 (c)) were analysed by XPS. In particular, the surface of the cathodes facing the ceramic porous layer was investigated. Fig. 7.21 a) shows the spectra of the tested copper foam after Test 2, and Fig. 7.21 b) shows its interval in binding energy from 885 to 845 eV which represents the Ni-2p high resolution region. The copper of the tested foam consisted of CuO. The quantitative analysis revealed, in particular, a minor amount of nickel (1.5 ± 0.3 atom %). In particular, the nickel consisted of $Ni(OH)_2$ and NiOOH (Fig. 7.21 b)). To understand the origin of nickel compounds in the copper foam was analysed also a piece of the YSZ layer that was facing the copper foam during Test 2 (Fig. 7.18 d)). In addition its XPS spectra is shown in Fig. 7.22, together with the Ni-2p high resolution spectra observed in the restricted range of binding energy. The quantitative study identified a higher concentration of nickel (6.2 ± 0.4 atom %), which formed $Ni(OH)_2$ and NiOOH.

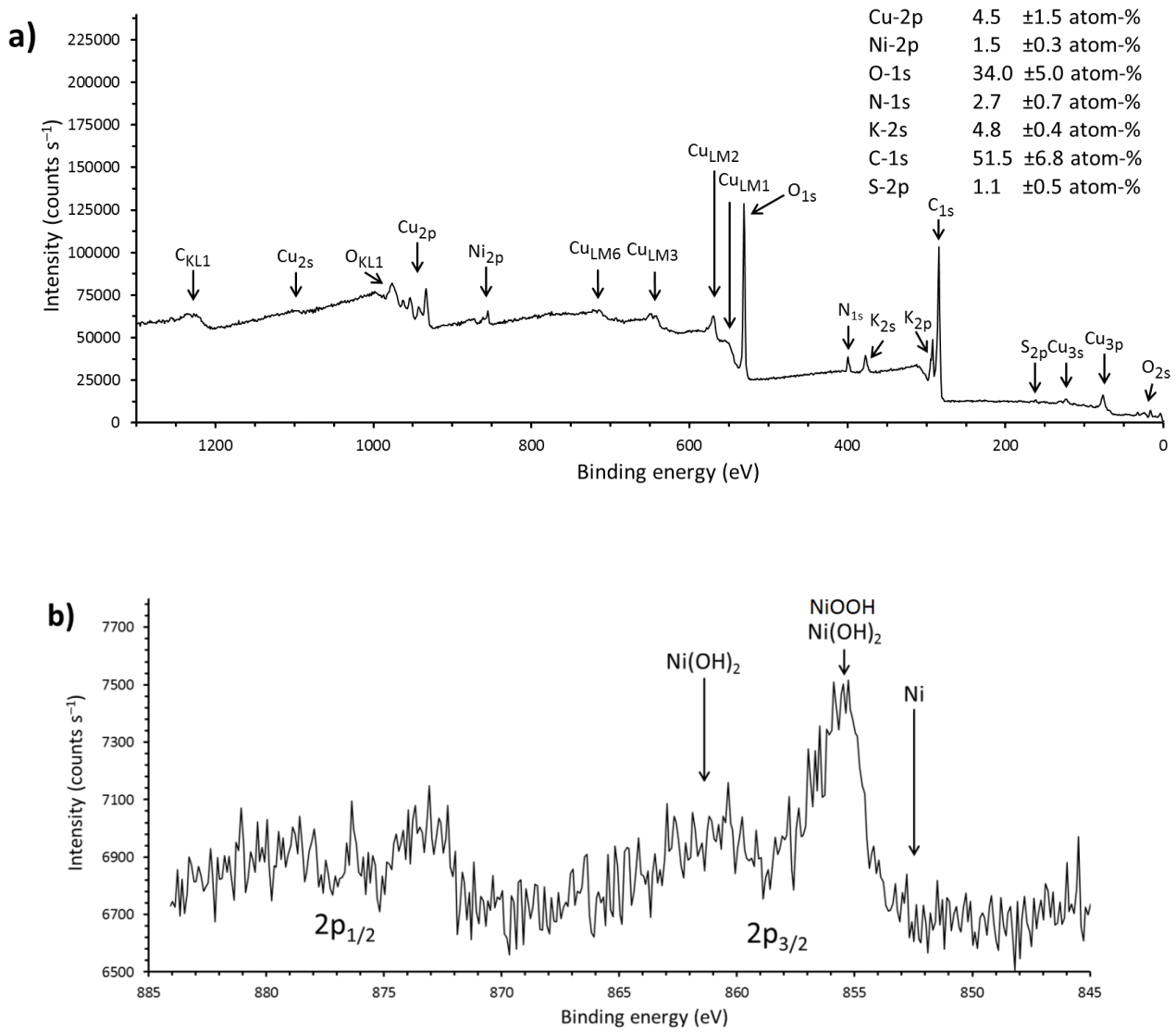

Fig. 7.21. XPS spectra of: a) the surface of Cu foam tested during Test 2. It also reports the quantitative analysis of the elements detected on the surface. b) XPS detailed region of Ni-2p detected on the Cu foam.

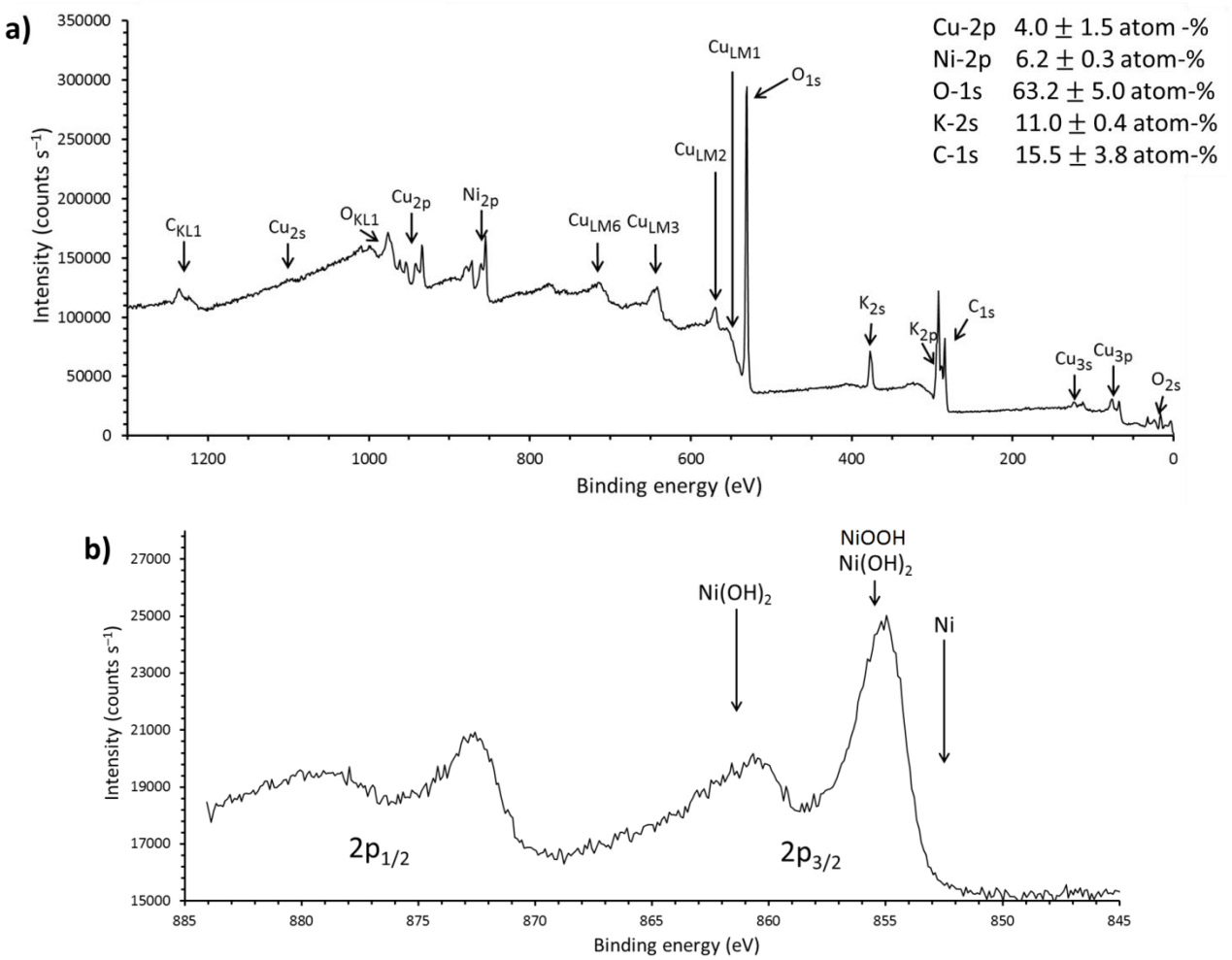

Fig. 7.22. XPS spectra of: a) the surface of YSZ layer in contact with the Cu foam tested during Test 2. It is also reported the quantitative analysis of the elements detected. b) XPS detailed region of Ni-2p detected on the YSZ layer.

Analogously, the Ag cathode foam and a piece of the YSZ layer that were in contact during the Test 3 were studied through XPS. However, for Ag pristine foam the photoelectron analysis was not sufficient to correctly identify its oxidation state. Fig. 7.23 shows both the spectra acquired on the surface of Ag foam and the Ni-2p high resolution spectra detected. The quantitative studies exhibited a high concentration of Ni also in the tested Ag foam (9.4 ± 2.9 atom %), which consisted of $Ni(OH)_2$ and NiOOH and also metallic Ni. The XPS investigation done on a piece of YSZ layer that was in contact with the Ag foam is represented in Fig. 7.24. It is also shown the Ni-2p high resolution spectra observed in the restricted range of binding energy (Fig. 7.24 b)). The quantitative analysis reported a high amount of nickel (10.2 ± 2.8 atom %) also on the part of YSZ studied. The presence of potassium on the tested foams and ceramic membranes are related to the immobilization of the aqueous K_2CO_3 electrolyte into the cells. The concentration of carbon detected on the tested foams is in line with the high values obtained on the pristine foams; therefore it cannot be related to the reactions taking place during the tests. Instead, the amount of carbon detected on the tested YSZ layers (15 atom-%) is in line with the quantity that can be explained by adventitious adsorbed hydrocarbon from ambient air. The presence of sulphur on the tested copper foam and of chlorine

on the silver foam and on its YSZ layer together with other apparent contaminants as nitrogen and oxygen suggests that the analysed surfaces were accidentally contaminated.

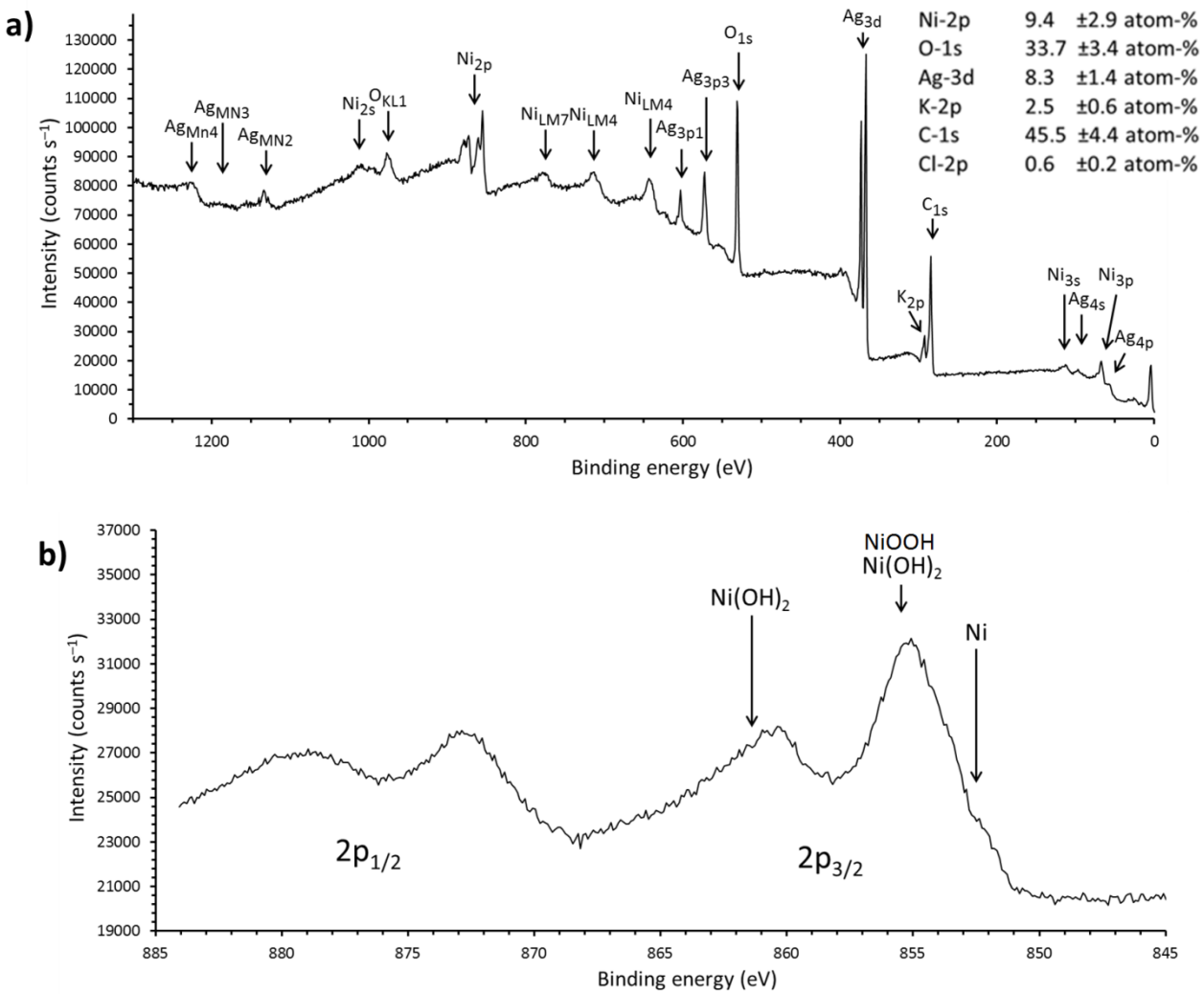

Fig. 7.23. XPS spectra of: a) the surface of Ag foam tested during Test 3. It is also reported the quantitative analysis of the elements detected on the surface. b) XPS detailed region of Ni-2p detected on the Ag foam.

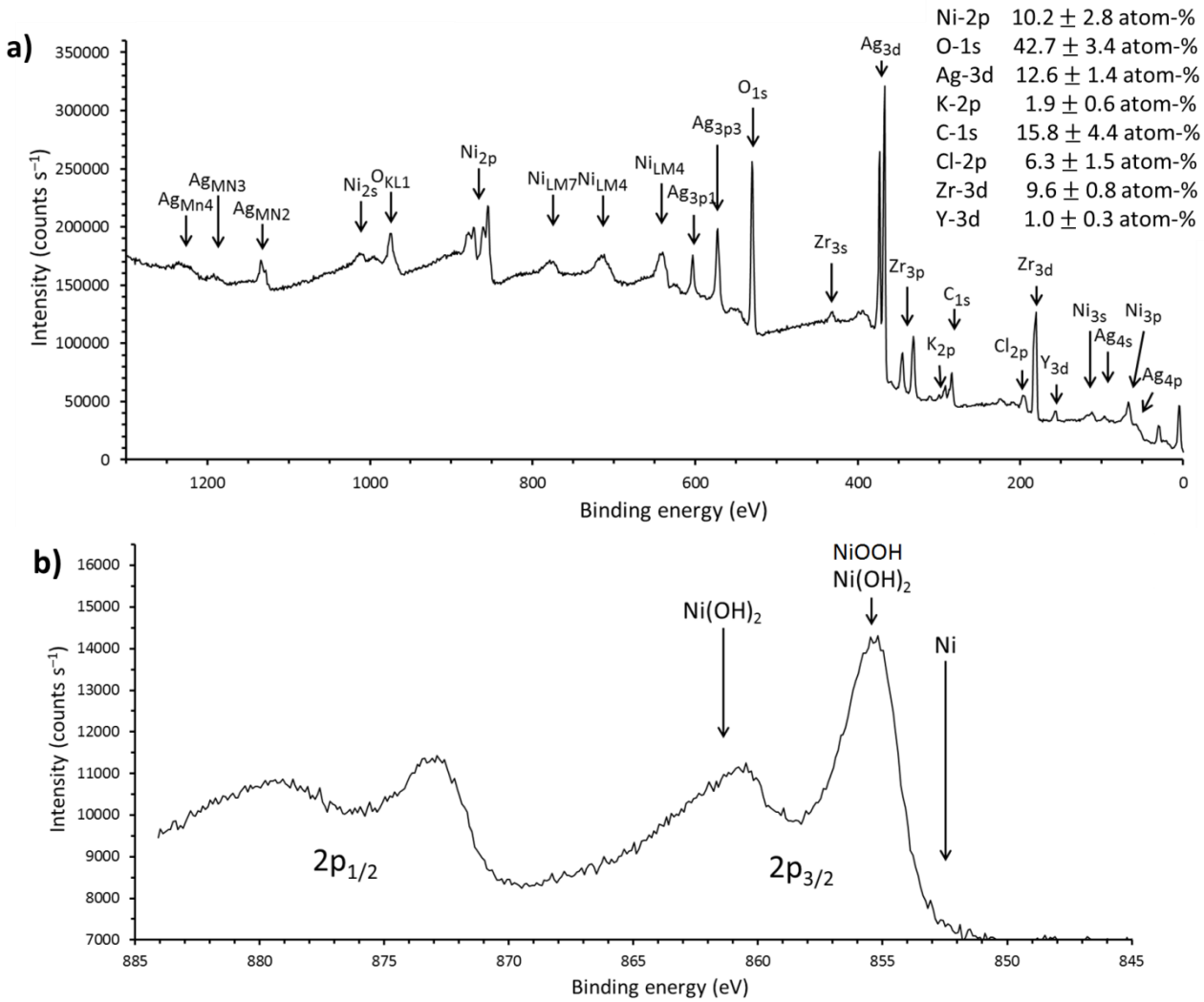

Fig. 7.24. XPS spectra of: a) the surface of YSZ layer in contact with the Ag foam tested during Test 3. It is also reported the quantitative analysis of the elements detected. b) XPS detailed region of Ni-2p detected on the YSZ layer.

7.4 Discussion

7.4.1 Electrochemical performance and microstructure

The tested cells were prepared to be identical, i.e. to have the same electrolyte matrix tape thickness and to be immobilized with the same aqueous electrolyte. Nonetheless a minor variation could be expected due to the usage of fabrication techniques as hot pressing of the nickel foam electrodes and lamination of the ceramic tapes which might not ensure identical cells. In addition, minor fractures of the YSZ tape could occur while setting the cell to the sample holder prior to be tested. Thus as expected, the initial values of the serial resistance, $R_{s,}$ were similar for the different cells tested at a given temperature as reported above. Indeed the first recorded R_s was ca. 2.5 $\Omega \cdot cm^2$ from the EIS spectra, when the cells were polarized at -2.5 V and at pressures of 3 bar and 5 bar. The following parameters were taken into account to estimate the value of the serial resistance: electrolyte matrix tape thickness of ca. 400 μm and a porosity of 45 %, conductivity (σ) of 0.5 M K_2CO_3 immobilized in similarly porous ceramic matrix of ca. 0.025 S/cm [27] as well as electrode thickness of ca. 500 μm both for the anode and for the cathode. Based on this R_s was calculated to be ca. 1 $\Omega \cdot cm^2$, according to the equation:

$R_s = \left(\frac{1}{\sigma}\right) \cdot \left(\frac{d}{A_{cell}}\right)$, in which *d* represents the thickness of the tape, σ the conductivity and A_{cell} the nominal are of the electrode (2 cm^2). The measured R_s were higher than the calculated value, as seen in Fig. 7.10, 7.12 and Fig. 7.15. One possible explanation could be poor percolation for the ionic and the electronic phases in the electrodes. Another reason could be related to a resistive contribution from the interface between the electrodes and the meshes used for current collection, i.e. contact resistance. In addition, the interface between the copper or silver foam electrodes and the ceramic matrix could represent another explanation, since the two parts were not sintered together. Indeed, ideally the foam electrodes should have been embedded in the YSZ matrix and then sintered together. Therefore, the ohmic losses can be reduced by improving the design and the fabrication of the cell and also by reducing the thickness of the porous structure. The evaluation of the conductivity of similar immobilized structures is relevant and was accomplished with the van der Pauw technique by F. Allebrod et al. [28] testing different concentration of KOH. EIS measurements showed that the serial resistance increased already during the first hours of all the tests at operating conditions. Indeed, during Test 0 the R_s increased gradually with time while increasing the pressure, until the EIS spectra started to be unstable at 5 bar and -2.5 V of applied voltage. The following EIS measurements at 10 bar and lower polarization of -1.75 V and -2 V were again stable, and it was still possible to quantify both R_s (ca. 15 $\Omega \cdot cm^2$) and the R_p. Conversely the last EIS spectra recorded at 10 bar and -2.5 V was unstable and no analysis was possible (Fig. 7.8 c)). A similar behaviour was observed in the EIS spectra recorded during Test 1 (Fig. 7.11 b)) and Test 3 (Fig. 7.16), in which only the highest polarization voltage was applied (-2.5 V). Only during Test 2 it was possible to quantify the R_s for polarized cell at -2.5 V until the end of the test, and it increased from ca. 2.5 $\Omega \cdot cm^2$ to approximately 10 $\Omega \cdot cm^2$ (Fig.7.12). Furthermore, the R_s measured at OCV both for Test 1 and Test 3 increased when the EIS spectra started to be unstable (Fig. 7.10 and Fig. 7.15). Also the polarization resistance was affected along the duration of the tests both by the high applied voltages and by the consequent deterioration of the electrodes.

As reported by the EIS acquired during Test 0 at -1.75 V (Fig. 7.8 a) and at -2 V (Fig. 7.8 b), the polarization resistance decreased with increasing pressure as it should. As mentioned in the introduction, at elevated pressure the electrode kinetics were expected to be enhanced due to the increased collision frequency of the reacting gas molecules at the triple phase boundary. This trend was not observed when the cells were polarized to -2.5 V (Fig. 7.8 c)), conversely to what expected by the R_p of gas diffusion electrodes[12,29]. The CA measurements carried out before the EIS spectra showed steady values for applied voltages of -1.75 V and -2 V (Fig. 7.10 a) and b)). The current densities registered at -2.5 V were higher, but at 5 bar and in particular at 10 bar it increased from 30 mA/cm^2 to 500 mA/cm^2 in two hours. Similarly, it occurred also during Test 1 (Table 7.3) and Test 3 (Table 7.6). Only during Test 2 the current densities were almost steady until the end of the test. The investigations of the tested foam electrodes and of the electrolyte porous matrix surfaces together with the analysis of possible reactions at the electrodes may help rationalize the electrochemical performances of the different tested cells in high pressure.

XPS analysis of the cells investigated during Test 2 and Test 3 indicated the presence of $Ni(OH)_2$ and NiOOH on the YSZ porous layers facing the copper and the silver foam. Also the SEM images confirmed the presence of an adjunctive black layer covering the YSZ surface (Fig. 7.18 c) and Fig. 7.19 c)). The mobility of nickel through the porous ceramic structure could be a consequence of formation of $Ni(OH)_2$ that would be dragged toward the interface when polarizing the cell[30]. In general, when a nickel metallic electrode is immersed in a aqueous alkaline solution, a film of the hydrous Ni(II) oxide species, α-$Ni(OH)_2$, is spontaneously formed[31]. By electrochemical means or by ageing (especially in more concentrated alkali solution) the α-$Ni(OH)_2$ can dehydrate and recrystallize as a largely anhydrous phase, denoted as β-$Ni(OH)_2$ [32] . According to B. Berverskog et al.[32] strong alkaline solutions corrode nickel by forming $Ni(OH)_3^-$, which is one of the hydrolysis products of Ni (II). The nickel foam anode looked heavily oxidized after the test. The SEM analysis could support the hypothesis of corrosion of the anodic nickel foam electrode, as shown in Fig. 7.20. It shows cuts and etchings on the frame even in the inner layers. The pores were partly blocked by grown oxide layers, affecting the ability of the electrode to work as a gas diffusion electrode. In addition the aluminum plate, used to improve the gas tightness, was in direct contact with the nickel foam and it showed corrosion due to the interaction with the liquid K_2CO_3 immobilized along the foam[33]. This aspect most likely worsened the contact in between the electrode and the current collector; the constant growth of the serial resistance supports this hypothesis. XPS investigations performed on the tested silver foam (Test 3) and on the YSZ surface facing the electrode itself showed a similar concentration of Ni based compounds, i.e. 9.4 atom % and 10 atom %, respectively. The binding energy registered for the Ni-2p peaks were associated to $Ni(OH)_2$ and NiOOH compounds. This result may help to justify the high current density observed during the CA measurements from 20 bar until the end of the Test 3 and the corresponding instable EIS spectra (Fig. 7.16 b)). Indeed, the presence of nickel based compounds from the anode side through the interface between the cathode and the electrolyte matrix layer and to the cathode surface itself could create a short circuit when polarizing the cell. This explanation can be valid also for the Test 0 and Test 1, in which copper was used as cathode and high current density and instable EIS spectra were recorded. In addition, for Test 0 and Test 1 the voltages recorded during the last OCV measurements were low and oscillating around -5 mV and -20 mV, respectively.

The Ni-2p high resolution XPS spectra carried out on the tested silver foam reported the presence of metallic nickel at 853 eV of binding energy (Fig. 7.23 b)), as expected after a cathodic reduction. On the other hand, the cathodic reduction did not completely reduce $Ni(OH)_2$ to Ni and after reduction $Ni(OH)_2$ was still present on the surface. This phenomenon was also observed and studied by W. Visscher et al.[34] who claimed that the conversion (recrystallization) from α-$Ni(OH)_2$ to β-$Ni(OH)_2$ might alter the reducibility of the passive $Ni(OH)_2$ film.

Conversely, XPS investigations on the copper foam used during Test 2 showed lower concentration (1.5 atom %) of Ni based compound compared to what recorded on the YSZ surface that was facing the electrode itself (6.2 atom %), as shown in Fig. 7.21 and Fig. 7.22 respectively. The binding energy registered for the Ni-2p peaks were associated to $Ni(OH)_2$ and NiOOH compounds. This observation indicated that the majority of nickel percolation through the cell stopped at the YSZ porous layer. Indeed, the current densities recorded during the CA measurements decreased moderately throughout the test and showed stable values. Also the OCV measured during Test 2 reported more negative values compared to the other tests, varying around ca. -800 mV to -1100 mV at 2 bar after the ramp down phase at 25 °C and at 50 °C, respectively.

The slow degradation of the cell was also observed by EIS spectra, which exhibited increasing values of serial and polarization resistance (Fig. 7.12). The formation and the gradual growth of the oxide layer from the nickel foam towards the ceramic matrix, which might be aggravated by the application of high voltages as -2.5 V, represent the main cause of degradation of the cell.

Using K_2CO_3 (aq) as electrolyte leads to the following equilibrium reactions in the electrochemical cell:

$$H_2O + CO_3^{2-} \leftrightarrow OH^- + HCO_3^-$$

$$CO_2 + OH^- \leftrightarrow HCO_3^-$$

These equilibrium reactions can also be written as:

$$CO_2 + H_2O + CO_3^{2-} \leftrightarrow 2\,HCO_3^-$$

This indicates that increasing the partial pressure of $CO_2$the equilibrium will be shifted to the right and therefore the amount of HCO_3^- ions will also increase. This also suggests that the CO_2 partial pressure can influence the possible charge carriers in the aqueous electrolyte.

The anode reaction (water oxidation) taking place on the Ni surface can be written as:

$$2H_2O \leftrightarrow O_2 + 4\,e^- + 4H^+$$

Or

$$4\,OH^- \leftrightarrow O_2 + 4\,e^- + 2H_2O$$

While at the cathode CO_2 is reduced and H_2O is involved as proton donor (OH^-) since the electrochemical reactions occur in an aqueous solution. If the products are CO or methane the reactions are as follows:

$$CO_2 + H_2O + 2e^- \leftrightarrow CO + 2\,OH^-$$

$$CO_2 + 6H_2O + 8e^- \leftrightarrow CH_4 + 8\,OH^-$$

At the same potential as CO_2 reduction reaction occurs, it is also possible for water to be reduced to make hydrogen, which is a concurrent reaction:

$$2H_2O + 2e^- \leftrightarrow H_2 + 2\,OH^- .$$

Electrochemical impedance spectroscopy was used as a sensitive tool in studying these possible reactions taking place on the gas diffusion electrodes. The most stable EIS spectra for both copper

and silver foams were recorded at 3 bar and 25 °C and were modelled by a resistor R_s in series with three (RQ) circuits, as shown in Fig. 7.14 and Fig. 7.17, respectively. In particular, the main focus was to rationalize the low frequency part of the EIS spectra, because it was affected first during the experiments. Post characterization of the nickel anode by SEM revealed that it had degraded significantly. This might have had an impact on the oxygen evolution reaction, which most probably takes place at the anode at high cell voltage/current densities. The oxidation reaction at the anode at lower current densities is oxidation of H_2 to H_2O. Therefore, it is possible to hypothesize that the low frequency semicircle of the EIS spectra could be related to oxidation/reduction reactions of the Ni oxidation products. On suitable polarization $Ni(OH)_2$ is oxidised to β-NiOOH[35] which is an electrocatalyst for the OER[36].

The pseudocapacitance describing the low frequency semicircle is estimated to be $4.8 \cdot 10^{-2}$ F/cm^2 for the copper foam tested during Test 2, and $4.3 \cdot 10^{-2}$ F/cm^2 for the silver foam of Test 3, using the method described by T. Jacobsen et al[37]. The nominal area of the electrode was of 2 cm^2. However, it is reasonable to consider that the effective area was significantly smaller, since the cathode foam was not embedded in the ceramic matrix. Here, due to different average pore size, 0.7 cm^2 and 0.6 cm^2 are assumed for copper and silver foams, respectively.

The estimated charge density involved in the $Ni(OH)_2$ oxidation is 41 C/cm^3, knowing that its cell unit has a volume of 39 Å^3 and assuming that with a 20 mV peak to peak amplitude only 1% of Ni(II) is available for charge transfer to Ni(III). With these assumptions, it is calculated that the thickness (t) of the passive oxide film formed by the oxidation of nickel hydroxides was 235 nm and 210 nm for copper and silver, respectively. Nickel passive layers have p-semiconductive properties[38]. It results from the high number of defects constituted by vacancies or inserted species as protons which can move in the lattice thanks to the ionic conduction of the layer. According to literature[39,40], the conductivity (σ) of Ni oxyhydroxide is ca. 10^{-5} S/cm at 25 °C. Therefore it is possible to calculate the passive layer resistances (R_l) on copper and silver electrodes according to the equation: $R_l = \left(\frac{1}{\sigma}\right) \cdot \left(\frac{t}{A_{eff}}\right)$, in which t represent the thickness of the layers and A_{eff} the effective area of the electrodes. The R_l of the passive oxide films are 3.3 Ω on copper foam and 3.5 Ω on silver foam electrodes. These R_l values are in agreement with the measured resistances associated to the low frequency semicircles, which are 3.4 Ω and 5.8 Ω for copper and silver as shown in Fig. 7.14 and Fig. 7.17, respectively.

7.4.2 CO_2 reduction products

Measurements with a gas chromatograph connected to the sample holder inside the test rig were performed, in order to identify gaseous products at the cathode as the cells were operated under applied cell voltages of -1.75 V, - 2 V and most of all at -2.5 V. Throughout the whole series of measurements acquired during Test 0 when applying a potential of -1.75 V no concentration changes or new compounds were detected with the gas chromatograph. In addition, only small concentrations of H_2 were detected when the applied voltage was changed to -2 V. A possible explanation to these results is that the cell was tested at relatively low applied cell voltages giving low overpotentials at the cathode. It has been reported in several scientific studies that low overpotentials favour hydrogen evolution[41]. Another reason could be that a product as formate ion

might have been produced in small concentration at low overpotentials, but not detected by the gas chromatograph. Only when polarizing the cell at -2.5 V it was possible to detect CO on copper cathode metal foams. The CO faradaic efficiency was the highest during the first electrolysis measurements as observed both for Test 0 and Test 1. Indeed, along Test 1 the FE of CO went from 4 % to 0.75 %, even if the pressure increased from 5 to 10 bar. According to the results obtained by K. Hara et al.[42] increasing the CO_2 pressure should increase the production efficiency of CO and/ or HCOOH. The cell tested along Test 1 degraded prior to have the possibility of observing this trend for the faradaic efficiency. Similarly it happened to the cell of Test 0. On the other hand, when the cell was more stable, as it happened during Test 2, the CO faradaic efficiency started to increase when increasing the pressure from 3 bar to 5 bar. In addition, CH_4 was detected at 2 bar and 25 °C, when the pressure was decreased from 5 bar. Increasing the temperature from 25 °C to 50 °C did not affect the faradaic efficiency of the products obtained. This might be explained by the too low difference in temperature and by the decreasing current density registered along the test conducted at 50 °C, due to degradation of the cell. On the other hand the main product obtained during the electrolysis test done on copper foam was H_2 produced by reduction of water at the cathode.

The performance of Ag cathode metal foam confirmed its higher selectivity for CO_2 reduction to CO. The highest CO faradaic efficiency (up to 50 %) was obtained at the beginning of the Test 3 during the chronoamperometric measurements at 3 and 4 bar of pressure and 25 °C, when the cell was stable. A further evaluation of this type of cell design is possible by considering the overall performance of the cell. To this end, it is relevant to calculate the energy efficiency ε, which is defined as the thermal energy obtained by the combustion of CO and H_2 over the electrical energy consumed during electrolysis.
The energy efficiency is defined as [10]
$\varepsilon = (\Delta r H^0_{CO} \cdot FE_{CO} + \Delta r H^0_{\mathrm{H2}} \cdot FE_{H2})/2F \cdot V$,

where $\Delta r H^0_{CO}$ and $\Delta r H^0_{H2}$ are the enthalpy changes of the following reaction:

$CO_2 \leftrightarrow CO + ½\ O_2$ with a $\Delta r H^0_{CO}$ = 283 kJ/mol

$H_2O \leftrightarrow H_2 + ½\ O_2$ with a $\Delta r H^0_{H2}$ = 286 kJ/mol

FE_{CO} and FE_{H2} is the faradaic efficiency of CO and H_2, while F is the Faraday constant and V the total cell voltage. During the initial chronoamperometric measurements at 3, 4 and 5 bar the energy efficiency was almost constant, ca. 0.58. Then it started to decrease as the current densities increased along the duration of the test.
The presence of impurities as silicon, sodium, nitrogen in pristine copper foam and of chlorine and sulfur in pristine silver foam might hinder and affect the selectivity for CO_2 reduction. Indeed, CO_2 reduction is highly surface sensitive reaction[7]. Therefore, this is pointing out the need for more specific precautions and attentions while handling the metal foams.
The formation of nickel based compounds on the surface of the cathode foam, as observed by XPS measurements, might influence the selectivity towards H_2 evolution. Nickel is a metal catalyst that binds strongly CO and therefore hydrogen from competing water reduction is the main product observed[7].

Unfortunately, it is not possible to correlate the present results with those reported in the literature for analogous catalysts and aqueous alkaline electrolytes, since the voltages applied in this study cannot be directly compared to the overpotentials measured in other work. Here, the correlation between the cathode and the anode overpotential is unknown and also the correlation between the cathode overpotential and the standard hydrogen electrode is unknown. This suggests the need for additional measurements using a three-electrode setup, which permits for individual characterization of the anode and the cathode overpotentials, respectively.

7.4.3 CO_2 reduction on copper foam electrodes: a comparison

Unfortunately it is not possible to do an accurate comparison between the performances obtained on the copper foam electrode in aqueous media at ambient condition and in the immobilized cell at high pressure. The electrochemical device, custom made by K. Kuhl et al.[43], allowed to carry out experiments with a three electrode cell setup, fundamental to determine the overpotential at which the different products of the CO_2 fixation were reduced. The tests in the immobilized cell at high pressure, instead, were conducted in a two electrode cell setup so it was unknown the correlation between the cathode overpotential and the reference electrode. Therefore it is not possible to compare the onset potentials of the different reduction products. In addition, the experimental method implemented by K. Kuhl et al.[43] for the identification and quantification of the gaseous and liquid products was highly sensitive. It allowed to detect sixteen different products on the copper foil electrode. This method, indeed, permitted to identify seven products on the copper foam electrode tested up to -0.98 V vs RHE. H_2, formate and CO were the main products observed and in particular the faradaic efficiency of H_2 was ca. 90 %. Similarly, the gas analysis performed during the tests on the immobilized cell at high pressure indicated a high faradaic efficiency for the evolution of H_2, i.e. between 92 to 99 %. The other products detected were CO and during one test also methane was identified. On the other hand it was not possible to analyse the aqueous electrolyte after the tests, therefore no information about formation of liquid products is available. Both testing methods utilized resulted in an elevated hydrogen faradaic efficiency, even though the experimental conditions were different. This might be explained by the porous structure of the copper foams utilized in both setups. The applied potential is not well defined throughout the thickness of the electrode, as already described in Chapter 6.

7.5 Conclusions

Electrochemical cells were realized by assembling metal foam based electrodes to a porous YSZ matrix. The cathode foams were not sintered together and therefore not embedded with the ceramic matrix. Potassium carbonate with a concentration of 0.5 M was immobilized in the porous YSZ layers to form the electrolyte matrix. Tests were conducted using copper and silver-foam cathodes and nickel-foam anodes and were performed generally at room temperature and at total pressures up to 20 bar in two distinct gas atmospheres on the cathode and anode side. The aim of the tests was not only to reduce CO_2/H_2O into syngas, hydrocarbons and alcohols, but also to collect results on the electrochemical performance of cells made by a new fabrication method. One test was carried out on copper foam cathode at three different voltages, i.e. -1.75 V, -2 V and -2.5 V, at ambient temperature and at pressure up to 10 bar (Test 0). The best performance in terms of current densities was obtained at the most negative voltage, but in parallel the degradation of the nickel foam anode occurred. SEM images support the hypothesis of corrosion of the anodic nickel foam electrode. Furthermore, with XPS spectroscopy it was possible to detect Ni based compounds, such as $Ni(OH)_2$ and NiOOH, from the anode side through the interface between the cathode and the electrolyte matrix layer and to the cathode surface itself. This could potentially create a short circuit when polarizing the cell. The gradual growth of this passive oxide film formed by the oxidation of nickel hydroxide had an effect both on serial resistance and on polarization resistance of the cells. For example, along Test 1 the R_s increased from 2.5 $\Omega \cdot cm^2$ to 7.5 $\Omega \cdot cm^2$ in ca. 50 hours, while increasing the pressure from 5 to 20 bar and then decreasing it to 10 bar and applying a potential of -2.5 V. Afterwards, the cell started to be unstable and it was not possible to identify both the R_s and the R_p. The test which gave the best performance in terms of cell stability was Test 2, since the cell was stable for more than 55 hours along the different pressures and also when increasing the temperature from 25 ^{0}C to 50 ^{0}C. In addition, also the average current density registered when polarizing the cell at -2.5 V was stable during the two hours of chronoamperometry.

Gas chromatography, electrochemical impedance spectroscopy and chronoamperometry were conducted in order to evaluate the cell performance with respect to the reduction of CO_2, and the evidence of it was found in all the tests when the most negative voltage was applied, i.e. -2.5 V. When copper was used as electrocatalyst, a high faradaic efficiency for the evolution of H_2, i.e. between 92 to 99 % was registered. The other products detected were CO and during one test (Test 2) also methane was identified. The performance of Ag cathode metal foam confirmed its higher selectivity for CO_2 reduction to CO. The highest CO faradaic efficiency (up to 50 %) was obtained at the beginning of the Test 3 at 3 and 4 bar of pressure and 25 °C, when the cell was stable.

The formation of passive oxide layers and the subsequent degradation of nickel foam electrodes, already at room temperature and after few hours of testing, clearly show the need for other electrodes materials suitable for oxygen evolution reactions.

References

[1] C. Graves, S.D. Ebbesen, M. Mogensen, K.S. Lackner, Renewable and Sustainable Energy Reviews, 15 (2011) 1-23.
[2] Y. Hori, K. Kikuchi, S. Suzuki, Chemistry Letters, 14 (1985), 1695-1698.
[3] M. Gattrell, N. Gupta, A. Co, Journal of Electroanalytical Chemistry, 594 (2006), 1-19.
[4] Handbook of Fuel Cells: Fundamentals, Technology and Application; Hori, Y., Ed.; VHC-Wiley: Chichester, 2003; Vol. 2.
[5] M. Jitaru, D.A.Lowy, M. Toma, B. C. Toma, L. Oniciu, Journal of Applied Electrochemistry 27 (1997), 875.
[6] K. Watanabe, U. Nagashima, and H. Hosoya, Chemical Physics letters, 209 (1993) 109-110.
[7] Y. Hori, in Modern aspects of electrochemistry, ed. C. Vayenas, R. White, and M. Gamboa-Aldeco, Springer, New York, 2008, vol. 42, pp. 89-189.
[8] M. Mogensen, ECS Transactions. 41 (2012) 3-11.
[9] E. J. Dufek, T. E. Lister, and M. E. McIlwain, Journal of Applied Electrochemistry, 41, 623 (2011).
[10] C. Delacourt, P. L. Ridgway, J. B. Kerr, and J. Newman, Journal of Electrochemical Society, 155, B42 (2008).
[11] D.T. Whipple, E.C. Finke, P.J. Kenis, Electrochemical and Solid-State Letters. 13 (2010) B109-B111.
[12] A. Momma, K. Takano, Y. Tanaka, T. Kato, A. Yamamoto, ECS Transaction, 57 (2013) 699.
[13] K. Hara, T. Sakata, Bull. Chem. Soc. Jpn. 70 (1997) 571-576.
[14] K. Hara, A. Kudo, T. Sakata, Journal of Electroanalytical Chemistry. 391 (1995) 141-147.
[15] K. Hara, A. Kudo, T. Sakata, M. Watanabe, Journal of Electrochemical Society, 142 (1995) L57-L59.
[16] S. Nakagawa, A. Kudo, M. Azuma, and T. Sakata, Journal of Electroanalytical chemistry, 308 (1991) 339.
[17] K. Hara, A. Kudo, and T. Sakata, Journal Electroanalytical Chemistry, 421(1–2), 1 (1997).
[18] E. J. Dufek, T. E. Lister, S. G. Stone, M. E. McIlwain, Journal of the Electrochemical Society, 159 (2012) F514-F517.
[19] F. Allebrod, C. Chatzichristodoulou, M.B. Mogensen, Journal of Power Sources, 229 (2013) 22-31.
[20] J. Banhart, Progress in Materials science, 46 (2001) 559-632.
[21] F. Bidault, D. J. L. Brett, P. H. Middleton, N. Abson, N. P. Brandon, International Journal of Hydrogen Energy, 34 (2009) 6799-6808.
[22] F. Allebrod, C. Chatzichristodoulou, M.B. Mogensen, Journal of Power Sources, 229 (2013) 22-31.
[23] F. Allebrod, C. Chatzichristodoulou, M. B. Mogensen, ECS Transactions, 64 (3) (2014) 1029-1038.
[24] C. Chatzichristodoulou, F. Allebrod, and M. Mogensen, *Review of Scientific Instruments*, 84 (2013) 054101.
[25] ref. http://xpssimplified.com/elements/copper.php
[26] J.R. MacDonald, E. Barsoukov, Impedance Spectroscopy, J. R. MacDonald, Wiley and Sons, Second Edition, New York, 2005.
[27] Pia Lolk Mollerup, "New Electrolytes for CO2 Electrolysis cells", Department of Energy Conversion and Storage, Technical University of Denmark, December 2012.

[28] F. Allebrod, C. Chatzichristodoulou, P. L. Mollerup, M. B. Mogensen, International Journal of Hydrogen Energy, 37 (21) (2012) 16505 – 16514.
[29] J. Nielsen, T. Jacobsen, M. Wandel, Electrochimica Acta 56 (2011) 7963–7974.
[30] A. Hauch, S. D. Ebbesen, S. H. Jensen, M. Mogensen, Journal of Electrochemical Society, 2008, 155, B1184.
[31] A. Seghiouer, J. Chevalet, A. Barhoun and F. Lantelme, Journal of Electroanalytical Chemistry, 442 (1998) 113.
[32] B. Beverskog, I. Puigdomenech, Corrosion Science, (1997) 39,5, 969-980.
[33] O. R. Brown, J. S. Whitley, Electrochimica Acta, 32 (1987), 545-556.
[34] W. Visscher, E. Barendrecht, Electrochimica Acta, (1979) , 25, 651-655.
[35] Miles, M. H., Kissel, G., Lu, P. W. T. and Srinivasan, S., Journal of the Electrochemical Society, 1976, 123, 332.
[36] Kibria, M. F. and Mridha, M. S. H., International Journal of Hydrogen Energy, 1996, 21, 179.
[37] T. Jacobsen, B. Zachau-Christiansen, L. Bay and S. Skaarup, Proceedings of the 17th Risø International Symposium on Materials Science — 1996, pp. 29 - 40.
[38] G. Barral, F. Njanjo-Eyoke and S. Maximovitch, Electrochimica Acta 40, 28 15 (1995).
[39] A. Motori, F. Sandrolini and G. Davolio, Journal of Power Sources, 48 (1994) 361-370.
[40] Ref. [8] in G. Barral, S. Maximovitch and F. Njanjo-Eyoke, Electrochimica Acta, 41 (1996) 1305-1311.
[41] Y. Hori, A. Murata, R. Takahashi, Journal of the Chemical Society, Faraday Transactions 1: Physical Chemistry in Condensed Phases, 85 (1989) 2309 – 2326.
[42] K. Hara, A. Tsuneta, A. Kudo, T. Sakata, Journal of Electrochemical Society, 141, (1994) 2097 – 2103
[43] K. P. Kuhl, E. R. Cave, D. N. Abram and T. F. Jaramillo, Energy & Environmental Science, 5 (2012) 7050 – 7059.

Part IV

OVERALL DISCUSSION, CONCLUSION AND FUTURE OUTLOOK

Chapter 8
Overall Discussion and Conclusions

The purpose of this exploratory thesis work was to develop and investigate electrolyte materials and electrodes for production of hydrocarbons and alcohols via electrochemical reduction of CO_2 at elevated pressure and temperatures below 300 ^{0}C.

8.1 Overall Discussion and Outlook

Two types of electrolytes were tried in this study. First, it was attempted to find a solid electrolyte with a conductivity of minimum 10^{-3} S/cm at the operation temperature below 300 °C. The reason for wishing a solid electrolyte is the simplicity solid – gas system with no need to handle a liquid, e.g. the demand to the gas diffusion electrode of being able to keep gas diffusion pathways free of liquid under all circumstance is removed. Next, as the work of developing a proper solid electrolyte was not successful, an immobilised liquid electrolyte was selected.
The solid electrolytes studied were $BaCe_{1-x-y}Zr_yY_xO_{3-\delta}$ (x; y) = (0.1; 0.9) – (0.1; 0.4) – (0.2; 0.6) electrolytes sintered by solid state reactive sintering and $Ba_{0.92}K_{0.08}Zr_{0.9}Y_{0.1}O_{3-\delta}$ electrolyte synthesized by hydrothermal method. The conductivity of these compounds was studied in wet H_2/N_2 and in $CO_2/H_2/N_2$ gas mixtures at a total pressure of up to 50 bar and temperature of 240 °C for the first time. The highest conductivity values were found for the compound with the highest Ce content (BCZY541), reaching a value of 10^{-3} S/cm at pH_2O = 25 bar. Increasing pH_2O from 10 to 25 bar resulted in almost one order of magnitude increase in the conductivity of BCZY541. On the contrary, the conductivity of BCZY262 dropped irreversibly by one order of magnitude for pH_2O > 5 bar. These changes are most probably associated with the formation of $Ba(OH)_2$ at the grain boundaries, which enhances the conducting properties of the BCZY541 cell, but decreases the conductivity of the BCZY262 cell due to the formation of micro-cracks. The resistivity of BZY91 and BKZY91 gradually decreased by increasing pH_2O, which was found to arise from a positive influence of increasing pH_2O on the grain boundary conductivity of both electrolytes. The total conductivity of BKZY91 measured at high steam partial pressures was slightly higher compared to the values obtained with BZY91. It went from $5.8\cdot10^{-6}$ S/cm to $2\cdot10^{-5}$ S/cm and from $7\cdot10^{-6}$ S/cm to $3\cdot10^{-5}$ S/cm for BZY91 and BKZY91 respectively, when increasing the pH_2O from 2.5 bar to pH_2O = 25 bar. BKZY91 showed higher conductivity compared to BZY91 also in ambient pressure. At temperature below 300 °C the highest conductivity was $8.3\cdot10^{-6}$ S/cm for BKZY91 and $5\cdot10^{-6}$ S/cm for BZY91, both at pH_2O of 0.1 bar. BKZY91 and BZY91 could represent a suitable electrolyte for CO_2 reduction thanks to their stability during conductivity measurements (comparing XRD before and after conductivity testing). However, in order to be considered for implementation in full cells, the electrolyte should have showed a total conductivity of ca. 10^{-3} S/cm at intermediate temperature (below ~ 300 °C) and in high steam partial pressure. This value in conductivity was reached by these electrolytes only at temperatures above 440 °C and at a pH_2O of 0.1 bar. On the other hand, conductivities above 10^{-3} S/cm for temperature below ~ 300 °C were obtained only in grain boundary – free Y doped barium zirconate films grown by pulsed laser deposition (PLD) on

single-crystal (100) - oriented MgO[1]. The non-conductive grain boundary region dominated the conductivity in both electrolytes, even if it was observed a better performance for BKZY91.
Investigations of the grain boundary chemical composition of the different tested electrolytes need to be performed with TEM imaging[2] and/or atom-probe tomography[3], in order to achieve a better understanding of the highly resistive grain boundary region. Hydrothermal synthesis has proven to be a valid process to synthesize microcrystalline K- doped $BaZr_{0.9}Y_{0.1}O_{3-\delta}$ powder. The motivation behind the decision to synthesize this compound was related to the fact that an alkali oxide should have been an effective dopant due to its high basicity[4], which is reported to enhance the water uptake capacity. Further studies should be performed to confirm this hypothesis via thermogravimetric analysis and also on the synthesis method varying the hydrothermal treatment temperature and time in order to observe possible variation in the particle sizes of the as synthesized powders. The concentration of the potassium hydroxide solution should be varied to investigate the relation between the concentration of the solution and the mol% of potassium in the A-site of the perovskite.
BCZY541 would have been the best electrolyte candidate because of its low resistivity in high pH_2O even at temperatures as low as 240 °C. However, the instability in the acidic CO_2 gas atmosphere hinders practical application for carbon dioxide reduction at high pressure.

The study of proton conducting Y-doped $BaCeO_3$-$BaZrO_3$ solid solutions did not provide a clear electrolyte candidate. Therefore a known aqueous alkaline based electrolyte was considered in order to make a full cell. Thus, the focus was moved to the selection of electrode materials and electrochemical characterization of cells and analysis of the CO_2 reduction products formed.

Aqueous 0.1 M $KHCO_3$ is a common electrolyte used for reduction of CO_2 in ambient conditions. It was also utilized as electrolyte in the highly sensitive experimental setup developed by K. Kuhl et al.[5], during the investigation of copper foams as electrocatalysts for CO_2 conversion. The identification and quantification of the reduction products as a function of the applied potential was the main focus of this study. The comparison between a copper foam and a smooth electropolished copper electrode revealed that the different roughness of the two electrode surfaces affected the current densities registered during the one hour long potentiostatic experiments. The current densities achieved on copper foams are ca. 5 times higher than the values obtained at the same potentials with smooth copper foil electrodes. Accurate Brunauer–Emmett–Teller (BET) measurements of the effective surface area of copper foams are necessary to establish a fundamental comparison, i.e. is this a pure effect of surface area or is it also due to differences in surface structures.
The products detected with a higher faradaic efficiency on the copper foam electrode tested to -0.98 V vs. RHE were H_2, formate and CO. In particular, the faradaic efficiency of H_2 was ca. 90 %. The comparison with K. Kuhl results suggested that the porous electrodes facilitate reaction pathways that are different from those that take place on smooth electrodes, due to graded potentials in the electrolyte through the Cu foam perpendicular to the electrode/electrolyte interface, and to possible differences in surface structure and purity. The products formed during the electrochemical reduction of CO_2 are affected by the electrode structure and design. Further studies that investigate

how controlled variations in pore size, pore depth and effective surface area influence the products formed by the reduction of CO_2 are necessary. To realize this, it is also required to improve the electrochemical cell setup in order to sustain more negative current densities than -20 mA/cm^2. Traces of impurities on pristine copper foam electrodes were observed through XPS studies. This suggests the need of implementing improved cleaning procedures before the electrolysis tests.

A new cell concept, based on metal foam gas diffusion electrodes and on aqueous 0.5 M K_2CO_3 electrolyte immobilized by capillary forces in a porous ceramic structure (YSZ) was developed in order to electrochemically reduce CO_2. Tests were conducted using copper and silver-foam cathodes, while nickel-foam was chosen as anode since is a common catalyst for oxygen evolution reaction in alkaline electrolysis cell. Tests were performed generally at room temperature and at total pressures up to 20 bar in two distinct gas atmospheres on the cathode and anode side. Two-electrode mode experiments were carried out.

One of the first tests was carried out on copper foam cathode at three different voltages, i.e. -1.75 V, -2 V and -2.5 V, at ambient temperature and at pressure up to 10 bar (Test 0).

The highest values of R_p and therefore also R_{tot} were obtained for the EIS recorded at -1.75 V and -2 V. For impedance spectra recorded at -1.75 V and -2 V, the R_p significantly decreased while increasing the pressure from 2 to 10 bar. Indeed, when applied -1.75 V, R_{tot} decreased from ca. 450 $\Omega \cdot cm^2$ at 3 bar to ca. 100 $\Omega \cdot cm^2$ at 10 bar. The R_s, instead, gradually increased when increasing the pressure. In particular, the R_s went from 2.5 $\Omega \cdot cm^2$ at 2 bar to 10 $\Omega \cdot cm^2$ at 10 bar when applied -1.75 and -2V. Conversely, the impedance spectra registered at -2.5 V exhibited the lowest values of R_{tot}, but it increased from 17 $\Omega \cdot cm^2$ at 2 bar to ca. 40 $\Omega \cdot cm^2$ at 4 bar, as shown in Fig. 7.8 c). Then the EIS measurements started to be unstable at 5 bar only when the cell was polarized to -2.5 V. The last EIS spectra at 10 bar and -2.5 V was totally unstable (Fig. 7.8 c). The highest values of current densities was obtained with the chronoamperometric measurements at the most negative voltage, but in parallel the degradation of the nickel foam anode occurred. Another cell of this type, but using silver foam cathode, was tested for 40 hours (Test 3) at applied cell voltage of -2.5 V, at ambient temperature and pressure increasing up to 20 bar. The R_s went from 3 $\Omega \cdot cm^2$ at 2 bar to 12 $\Omega \cdot cm^2$ at 10 bar in ca. 20 hours. Then the EIS spectra acquired started to be unstable. The R_p, indeed, increased from 25 $\Omega \cdot cm^2$ to 50 $\Omega \cdot cm^2$ for the same range of pressure.

SEM images support the hypothesis of corrosion of the anodic nickel foam electrode. Furthermore, with XPS spectroscopy it was possible to detect Ni based compounds, such as $Ni(OH)_2$ and NiOOH, from the anode side through the interface between the cathode and the electrolyte matrix layer and to the cathode surface itself. This could potentially create a short circuit when polarizing the cell. The gradual growth of this passive oxide film formed by the oxidation of nickel hydroxide affected both the serial resistance and the polarization resistance of the cells.

The formation of passive oxide layers and the subsequent degradation of nickel foam electrodes, already at room temperature and after few hours of running time hindered the possibility of testing the cells at higher temperatures. This made it impossible to pursue the aim of developing a cell able to produce hydrocarbons at temperatures below 300 °C.

Therefore more stable and corrosion resistant electrocatalysts for the oxygen evolution reaction, OER, need to be analyzed and identified. Noble metal catalyst as Ir-based dimensionally stable

anode supported on nickel mesh was used by E. Dukef et al.[6] in a pressurized electrochemical system operating at temperature between 60-90 °C. However less expensive materials should be utilized. It is unlikely that practical oxygen evolution anodes will be based on precious metals. Overpotential reductions obtained with Pt, Ir, or Pd, for example, have been modest[7]. The promising results obtained with far cheaper materials as mixed metal oxides, and especially spinel and perovskites, such as Co_3O_4, $NiCo_2O_4$[8], $La_{0.5}Sr_{0.5}CoO_3$, $SrCoO_3$ [9]and $Ba_{0.5}Sr_{0.5}Co_{0.8}Fe_{0.2}O_{3-\delta}$ [10] reduce the interest against the use of precious metals. Techniques to load and deposit the catalyst close to the three phase boundary should be investigated. Electrodeposition, spray pyrolysis, impregnation and coating are the most common methods to deposit catalysts on stable support. A valid solution could be achieved if the most active and corrosion resistant electrocatalyst was already present in the selected metal foams by customized coatings technique.

Gas chromatography measurements were conducted in order to evaluate the cell performance with respect to the reduction of CO_2, and the evidence of it was found in all the tests when the most negative voltage was applied, i.e. -2.5 V. When copper was used as electrocatalyst, a high faradaic efficiency for the evolution of H_2, i.e. between 92 to 99 % was registered. The other products detected were CO and during one test (Test 2) also methane was identified. The performance of Ag cathode metal foam confirmed its higher selectivity for CO_2 reduction to CO. The highest CO faradaic efficiency (up to 50 %) was obtained at the beginning of the Test 3 at 3 and 4 bar of pressure and 25 °C, when the cell was stable.

By increasing the CO_2 pressure should increase the reaction rates and therefore the formation efficiency of the different products. The cell tested along Test 1 degraded prior to have the possibility of observing this trend for the faradaic efficiency. Similarly it happened to the cell of Test 0. On the other hand, when the cell was more stable, as it happened during Test 2 and at the beginning of Test 3, the CO faradaic efficiency started to increase when increasing the pressure from 3 bar to 5 bar and from 3 to 4 bar, respectively.

Unfortunately, it is not possible to correlate the present results with those reported in the literature for analogous catalysts and aqueous alkaline electrolytes, since the voltages applied in this study cannot be directly compared to the overpotentials measured in other work. Here, the correlation between the cathode and the anode overpotential is unknown and also the correlation between the cathode overpotential and the standard hydrogen electrode is unknown. This suggests the need for additional measurements using a three-electrode setup, which permits for individual characterization of the anode and the cathode overpotentials, respectively.

On the other hand, the sintered ceramic 400 µm thick layer of YSZ laminated with the Ni foam is brittle and it happened to crack near the edges while assembling the different components and compressing them together. The cracks will most likely be filled with the aqueous electrolyte during operation and not compromise the electrochemical performance, but the cracks might have an effect on the mechanical stability and on the gas tightness of the cell depending on the size and position of the crack and might provide a potential channel for gas diffusion. This might dilute the gaseous products and affect the gas analysis results. Ideally, the foam electrodes should have been embedded in the YSZ matrix and then sintered together. A more compact cell design has to be developed.

8.2 Conclusions

The main purpose of this thesis was to search for materials necessary for making a cell, in which it is possible to electrochemically reduce CO_2 into hydrocarbons at elevated pressures and at temperatures below ~300 °C. The long term goal is to make a basis for manufacturing of commercially viable cells. This has been done by investigating and developing both electrolyte materials and electrodes.
The investigations on proton conducting Y-doped $BaCeO_3$-$BaZrO_3$ solid solutions did not give a clear electrolyte candidate, therefore aqueous alkaline based electrolytes were considered.

By testing copper foam as CO_2 reduction catalyst in a highly sensitive experimental setup it was possible to conclude that porous electrodes facilitate reaction pathways that are different from those that take place on smooth electrodes, due to graded electrical potential in the electrolyte through the Cu foam perpendicular to the electrode/electrolyte interface. The overpotential drops in the electrolyte in the pores when moving away from the main electrolyte causing a gradient in the local electrode overpotential[11]. The main part of the reaction takes place on the copper surface near the main electrolyte because that is giving the least loss in electrolyte resistance.
In addition, the impurities present on the catalyst surface might affect the product selectivity; therefore implementing improved cleaning procedures before the electrolysis tests is necessary.
Newly developed and fabricated cells based on aqueous K_2CO_3 electrolyte immobilized in a ceramic porous structure were tested during the study.
Gas diffusion electrodes as copper and silver foams were analysed as CO_2 reduction catalysts, while nickel foam was investigated as oxygen evolution reaction catalyst. The SEM analysis together with XPS results showed significant corrosion of the anodic nickel foam electrode. Degradation of the nickel foam anode compromised the electrochemical performance of the cells. The gradual growth of a passive oxide film formed by the oxidation of nickel hydroxide had an effect both on serial resistance and on polarization resistance of the cells.
The formation of CO during all the tests, when -2.5 V was the applied cell voltage, is the evidence for reduction of CO_2 on both copper and silver foams. In particular, methane was also detected on copper foam at 2 bar and 25 °C, after the ramp down phase in pressure. The degradation of the nickel electrode did not allow to study the effects of increasing operating pressures and temperature. The fast corrosion of the Ni anode and the migration of Ni-ions through the electrolyte remain the main problem to be solved and investigated.

References

[1] D. Pergolesi, E. Fabbri, A. D'Epifanio, E. Di Bartolomeo, A. Tebano, S. Sanna, S. Licoccia, G. Balestrino and E. Traversa, Nature Materials, 9 (2010) 846-852.
[2] F. Iguchi, T. Tsurui, N. Sata, Y. Nagao and H. Yugami, Solid State Ionics, 180 (2009) 563.
[3] S. Ricote, N. Bonanos, A. Manerbino, N.P. Sullivan and W. G. Coors, Journal of Materials Chemistry A, 2 (2014) 16107-16115.
[4] A. S. Patnaik, A. V Virkar, Journal of the Electrochemical Society, 153 (7) 1397-1405.
[5] K. P. Kuhl, E. R. Cave, D. N. Abram and T. F. Jaramillo, Energy & Environmental Science, 5 (2012) 7050 – 7059.
[6] E.J. Dufek, T.E. Lister, S.G. Stone, M.E. McIlwain, Journal of Electrochemical Society, 159 (2012) 514-517.
[7] D.E. Hall, Journal of Electrochemical Society, 132 (1985) C41-C48.
[8] M. Hamdani, R.N. Singh and P. Chartier, International Journal of Electrochemical Science, 5(4) (2010) 556-577.
[9] I.C. Man, H-Y. Su, F. Calle-Vallejo, H.A. Hansen, J.I. Martinez, N.J. Inoglu, J. Kitchin, T.F. Jaramillo, J.K. Nørskov, J. Rossmeisl, ChemCatChem, 3 (2011) 1355.
[10] J. Suntivich, K.J. May, H. Gasteiger, J.B. Goodenough, Y. Shao-Horn, Sicence, 334 (2011) 1383.
[11] A. Lasia, Modeling of impedances of porous electrodes, in Modern Aspects of Electrochemistry, ed. by M. Schlesinger, vol. 43 (Springer, New York, 2009), pp. 67–138.